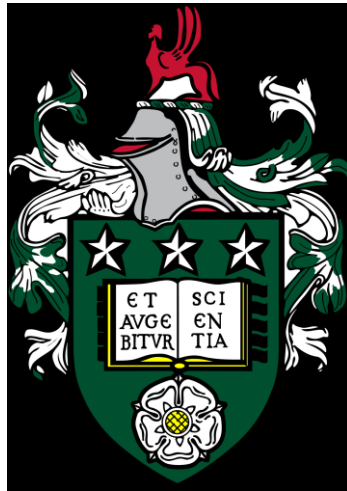


Impact of faults on fluid flow in carbonates



Ieva Kaminskaite

Submitted in accordance with the requirements for the degree of
Doctor of Philosophy

The University of Leeds
School of Earth and Environment

October, 2019

Declaration

The candidate confirms that the work submitted is her own, except where work which has formed part of jointly-authored publications has been included. The contribution of the candidate and the other authors to this work has been explicitly indicated below. The candidate confirms that appropriate credit has been given within the thesis where reference has been made to the work of others. Contributors to jointly-authored publication are outlined below.

Chapter Four

Reference: Kaminskaite, I., Fisher, Q.J. and Michie, E.A.H., 2019.

Microstructure and petrophysical properties of deformation bands in high porosity carbonates. *Journal of Structural Geology*, 119, pp.61-80.

Received 10 September 2018, Revised 28 November 2018, Accepted 6 December 2018, Available online 10 December 2018.

Authors:

I. Kaminskaite: principal investigator, collected and analysed all data on deformation bands and main author.

Q. J. Fisher: fieldwork assistance, thorough discussion, critical manuscript review.

E. H. Michie: fieldwork assistance, critical manuscript review.

This copy has been supplied on the understanding that it is copyright material and that no quotation from the thesis may be published without proper acknowledgement.

The right of Ieva Kaminskaite to be identified as Author of this work has been asserted by her in accordance with the Copyright, Designs and Patents Act 1988.

© 2019 The University of Leeds and Ieva Kaminskaite

Acknowledgements

Firstly, I would like to express my sincere gratitude to my enthusiastic supervisor Prof Quentin Fisher, who have been a tremendous mentor for me, guiding me through all the work and inspiring with his ambitious attitude towards research or, frankly, everything. I was extremely lucky to have him as my supervisor and having had an opportunity to work alongside of him, to travel so much and to meet so many new people through him. Thank you! I gratefully acknowledge the funding received towards my PhD as part of the Carbonate Fault Rock Group project from the ADNOC, ENI, OMV, Petrobras and Wintershall Dea.

The experimental part of this thesis would not have been possible without the help of my second supervisor Dr Carlos Grattoni and lab technician Dr Samuel Allshorn, who spent a great deal of time teaching and supporting me through all the experiments. Also, a huge thanks goes to Dr John Martin who gave me advice and constant provision through all the triaxial testing, and to Harri Williams, who was patient with me making hundreds of thin sections in his lab, helping and supporting me all the way through, and for all the laughs! I will forever be thankful to Dr Emma Michie for her help and teachings during the fieldwork and constructive reviews on my first manuscripts. Also, thanks go to Dr Ilan Fridman Rojas, Dr Sergio Gonzalez Lopez, Dr Mattia Miroballo and Andrew Cooke for their assistance and hard work with me in the field. I would have never brought back with me more than half a ton of samples if it weren't for you!

Finally, but by no means least, sincere thank you goes to my parents and grandparents, all of my sisters and, especially, to Adomas Baranauskas, for almost unbelievable support. They are the most important people in my world and I dedicate this thesis to them.

Conference abstracts

As part of the research work, several results were previously presented at conferences in posters and a talk:

Kaminskaite, I., Fisher, Q.J., Michie, E. and Yielding, G., 2017. Poster on “Microstructure of deformation bands in carbonates”. In *1st Joint Assembly of TSG – VMSG – BGA*.

Kaminskaite, I., Fisher, Q. and Michie, E., 2017. Poster on “Faults in High Porosity Carbonates”. In *AAPG Annual Convention and Exhibition*, Houston, Texas.

Kaminskaite, I., Fisher, Q.J., Michie, E., 2019. Talk on “Impact of laboratory-induced deformation and naturally-occurring faults on fluid flow in carbonates”. In *Fifth EAGE International Conference on Fault and Top Seals*, Palermo, Italy.

Abstract

To fully characterise the behaviour of carbonate rocks in the subsurface it is important to understand their textural heterogeneity, and how their textures may be modified by faulting. A number of fault zones were investigated in detail, firstly analysing the microstructural, petrophysical as well as mechanical properties of the host rocks. Secondly, describing the fault zone architectures by mapping fault rock distributions and fracture patterns. Lastly, correlating the deformation mechanisms forming the faults to the initial rock properties and the stress conditions during faulting. Moreover, triaxial laboratory deformation was performed on a large number of host rock samples covering all carbonate rock types, as well as the whole range of porosities (<1-52%). Deformation mechanisms that resulted in sample's failure were studied in order to compare them with the naturally-occurring deformation. Moreover, permeability changes were investigated induced both by natural faulting and laboratory deformation. The results proved to be comparable, and showed that simplified rules may be derived in terms of predicting hydraulic properties of deformed carbonates. For instance, permeability generally seems to decrease due to deformation for carbonates with porosity >10%, and may be either increased or decreased for lower porosity samples. Higher porosity (>10%) carbonates fail due to distributed or localized cataclastic flow or focused damage around the macropores, resulting in porosity reduction. Lower porosity (<10%) carbonates fail in a brittle manner due to brecciation and transitional- or brittle-shearing, leading to porosity increase. Significant reduction in permeability, however, may only be produced by diagenetic processes, such as recrystallization and cementation, or very high-strains, which are able to create

fine-grained cataclasites. However, even though these fault rocks gain very low permeability, they become prone to brittle deformation. Therefore, these potentially sealing fault rocks may be cut by open fractures if were subjected to further faulting or uplift, and hence, while creating permeability anisotropy in the reservoir, they may not form good seals. Nevertheless, several fault examples in this study showed fracture blunting at the surface of the fault rocks suggesting that fault sealing is possible both in highly-porous and very tight carbonates.

Table of Contents

Declaration.....	i
Acknowledgments.....	iii
Conference abstracts.....	iv
Abstract.....	v
Table of Contents.....	vii
List of Symbols and Abbreviations.....	xiii
List of Tables.....	xv
List of Figures.....	xvii
Chapter 1 Introduction.....	1
1.1 Background to research	1
1.2 Aims and objectives	4
1.3 Layout of thesis.....	5
Chapter 2 Properties of undeformed and faulted carbonates	8
2.1 Properties of carbonates.....	8
2.1.1 Carbonate rock types.....	8
2.1.2 Porosity.....	10
2.1.2.1 Porosity types.....	11
2.1.3 Diagenesis	12
2.1.3.1 Aggrading neomorphism.....	14
2.1.3.2 Dolomitization	15
2.2 Faults in carbonates.....	16
2.2.1 Fault zone elements	16
2.2.2 Fault zone architecture.....	17
2.2.2.1 Fault zone architectural controls	19
2.2.3 Fault zone scaling relationships	21

2.3	Fault rock classification	23
2.3.1	High-porosity carbonates	24
2.3.2	Low-porosity carbonates	25
2.4	Damage zone structures	27
2.5	Fault impact on permeability.....	28
2.5.1	Sealing faults	28
2.5.1.1	Static and dynamic sealing.....	33
2.5.2	Faults as conduits.....	35
2.5.3	Permeability anisotropy.....	35
Chapter 3	Methodology	37
3.1	Overview of the workflow	37
3.2	Fieldwork	38
3.2.1	Sampling locations.....	38
3.2.2	Field mapping and sample collection	39
	Sample preparation.....	42
3.3	42
3.3.1	CT-scanning and coring.....	42
3.4	Microstructural analysis.....	43
3.4.1	Optical microscopy	43
3.4.2	Scanning Electron Microscopy (SEM).....	44
3.4.3	Cathodoluminescence microscopy (CL)	44
3.5	Petrophysical property measurements	45
3.5.1	Porosity	45
3.5.2	Permeability	46
3.5.3	Mercury-injection (MICP).....	48
3.6	Triaxial testing	49
3.6.1	Experimental procedure	49

3.6.1.1	Hydrostatic tests	51
3.6.1.2	Multistage and continuous failure triaxial tests	52
Chapter 4	Banding in high-porosity carbonates	53
4.1	Introduction.....	53
4.2	Geological setting.....	61
4.2.1	Isle of Thanet	61
4.2.2	San Vito lo Capo and Favignana	61
4.2.3	Gargano promontory.....	62
4.2.4	Rhodes	62
4.3	Methodology	64
4.3.1	Sampling.....	64
4.3.2	Macrostructural analysis	64
4.3.3	Microstructural analysis	65
4.3.3.1	Optical microscopy	65
4.3.3.2	Scanning Electron Microscopy (SEM)	68
4.3.4	Petrophysical properties	70
4.4	Results.....	71
4.4.1	Host rock characteristics	71
4.4.1.1	Isle of Thanet	71
4.4.1.2	San Vito lo Capo and Favignana	72
4.4.1.3	Gargano promontory	72
4.4.1.4	Rhodes.....	73
4.4.2	Deformation band structure.....	74
4.4.2.1	Isle of Thanet	74
4.4.2.2	San Vito lo Capo and Favignana	74
4.4.2.3	Gargano	75
4.4.2.4	Rhodes.....	75
4.4.3	Deformation band pore types.....	77

4.4.3.1	Porosity	77
4.4.3.2	Intergranular macroporosity.....	78
4.4.3.3	Moldic porosity	80
4.4.3.4	Microporosity	81
4.4.4	Force chain stress analysis.....	82
4.4.5	Pore and particle analysis.....	84
4.4.5.1	Pore throat sizes.....	84
4.4.5.2	Grain size	88
4.4.6	Deformation-induced microstructural changes.....	90
4.4.7	Permeability.....	92
4.5	Discussion	93
4.5.1	Deformation band structure.....	93
4.5.2	Deformation mechanisms.....	94
4.5.2.1	Single deformation bands in chalk.....	95
4.5.2.2	Single deformation bands in bioclastic grainstones.....	96
4.5.2.3	Clustered deformation bands in bioclastic grainstones	97
4.5.2.4	Single cemented bands.....	97
4.5.3	Geomechanics of deformation band formation.....	99
4.5.4	Time-dependant evolution of deformation bands and its influence on their petrophysical properties	100
4.6	Conclusions.....	106
Chapter 5 Faulting in low-porosity carbonates: A case study from San		
Vito lo Capo, Sicily, Italy		
107		
5.1	Introduction	107
5.1.1	Tectonic setting of the study area	109
5.2	Samples and methods	111
5.2.1	Fault zone mapping.....	111
5.2.2	Microstructural analysis.....	112

5.2.3	Petrophysical analysis	112
5.2.4	Mechanical properties of the protoliths	112
5.3	Results.....	113
5.3.1	Host rocks	113
5.3.2	Fault zone architecture.....	113
5.3.2.1	Limestone.....	113
5.3.2.2	Dolomite	118
5.3.3	Fault rock microstructure	121
5.3.4	Fault petrophysical properties.....	125
5.4	Discussion.....	127
5.4.1	Fault zone evolution	127
5.4.1.1	Faults in limestone.....	127
5.4.1.2	Faults in dolomite.....	130
5.4.1.3	Fault zone evolution in the local tectonic context.....	131
5.4.1.4	Mineralogy impact on fault zone architecture.....	134
5.4.2	Impact of faulting on permeability	140
5.4.3	Application to other dolomite reservoirs	142
5.5	Conclusions	143
Chapter 6	Mechanical properties of carbonates	145
6.1	Introduction.....	145
6.1.1	Microstructural controls on deformation.....	147
6.1.2	Water weakening effect on deformation.....	148
6.2	Material and methods	149
6.2.1	Sample material.....	149
6.2.2	Sample preparation	155
6.2.3	Experimental procedure.....	155
6.2.3.1	Mechanical testing.....	155

6.2.4	Microstructural analysis.....	155
6.2.5	Petrophysical properties.....	156
6.3	Results.....	156
6.3.1	Mechanical experiments	156
6.3.1.1	Hydrostatic tests.....	156
6.3.1.2	Multiple and continuous failure state triaxial tests	158
6.3.2	Macroscopic deformation	164
6.3.3	Microscopical deformation	165
6.3.4	Microstructural texture impact on mechanical behaviour	172
6.3.5	Permeability	173
6.4	Discussion	174
6.4.1	Mechanical response to failure.....	174
6.4.2	Parameters controlling failure of carbonate rocks	177
6.4.3	Failure deformation mechanisms.....	182
6.4.4	Water weakening effect on deformation.....	183
6.4.5	Impact of deformation on permeability.....	184
6.5	Conclusions.....	186
Chapter 7	Discussion.....	189
7.1	Carbonate reservoirs	189
7.2	Permeability changes induced by faulting and laboratory-deformation	195
7.2.1	High-porosity carbonates	195
7.2.2	Low-porosity carbonates.....	197
7.2.3	Sealing faults or conduits to flow?	198
7.3	Fault/Fracture interaction.....	201
7.4	Fault sealing prediction in carbonates.....	206
Chapter 8	Conclusions	210

List of Symbols and Abbreviations

- σ_1 - maximum compressive stress (axial stress)
- σ_2 - intermediate compressive stress (radial stress)
- σ_3 - minimum compressive stress (radial stress)
- σ'_v – vertical stress (MPa)
- σ_u - uniaxial compressive strength (MPa)
- p_f – pore fluid pressure
- σ' - effective stress ($\sigma - p_f$)
- σ_h – horizontal stress (MPa)
- q - differential stress (MPa) ($\sigma_1 - \sigma_3$)
- p - mean stress (MPa) ($(\sigma_1 - 2\sigma_3)/3$), when $\sigma_2 = \sigma_3$)
- ϵ_v - volumetric strain (fraction)
- ϵ_r – radial strain (fraction)
- ϵ_a – axial strain (fraction)
- P^* - critical pressure under hydrostatic conditions (pre-consolidation pressure) (MPa)
- C' – yield stress indicating onset of dilatancy (MPa)
- C^* - yield stress indicating onset of inelastic compaction (MPa)
- P_c - confining pressure (MPa)
- E - Static Young's modulus (MPa)
- K – Bulk modulus (MPa)
- K – stress path coefficient ($K = \Delta\sigma_3/\Delta\sigma_1$)
- K_{IC} - critical stress intensity factor
- ν – Poisson's ratio
- λ - water weakening parameter (fraction)
- ρ - density (g/cm^3)
- g - gravitational force (9.80665 m/s^2)
- h - burial depth (m)
- k - permeability (mD)

k_{ap} - apparent permeability (mD)

ϕ – porosity (%)

μ - viscosity (Pa/s)

L - sample length (cm)

Q - flow rate at ambient conditions (cm³/s),

A - cross-sectional area of a sample (cm²)

P_1, P_2 - pressures at the upstream and downstream side of a sample, respectively (psi)

P - pressure (psi)

d - pore diameter (μm)

r – pore radius (μm)

γ - surface tension (mN/m)

θ - contact angle

V_1 - volume of a reference cell in helium porosimeter (cm³)

V_2 - volume of a cell containing a sample in helium porosimeter (cm³)

SS – Steady-State Permeability

PDP – Pulse-Decay Permeability

MICP – Mercury-Injection Capillary Pressure

CL - Cathodoluminescence Microscopy

SEM - Scanning Electron Microscopy

BSEM – Backscattered Scanning Electron Microscopy

IPS - Intergranular Pressure Solution

PS: Pressure Solution

PSs: Pressure Solution Seams

PWC - Petroleum-Water Contact

DB - Deformation Band

List of Tables

Chapter Four: Banding in high-porosity carbonates

Table 4.1. A compilation of documented examples of natural and laboratory-induced deformation bands in carbonate rocks, including the data collected during this study. PS: pressure solution; PSs: pressure solution seams.

Chapter Five: Faulting in low-porosity carbonates: a case study from San Vito lo Capo, Sicily, Italy

Table 5.1. Reference list of the compiled displacement and fault zone thickness data for carbonate rocks (**Figure 5-13**). Studied location, fault kinematics and fault-hosted carbonate protolith mineralogy are listed for each reference. Limestone+dolomite indicate mixed limestone and dolomite sequences, whereas limestone, dolomite shows that faults in the studied area occurred both in limestone and dolomite outcrops.

Chapter Six: Mechanical properties of carbonates

Table 6.1. Summary of sample data used in this study. The carbonate rock and pore types were described as explained in **Section 2.1.1** and **Section 2.1.2.1**, respectively. PS refers to pressure solution.

Table 6.2. Hydrostatic test results showing P^* values measured on dry and saturated samples on various carbonates. Samples were failed beyond the yield point, and deformation mechanisms which caused the macroscopical failure of the samples are indicated.

Table 6.3. Multistage-failure triaxial test results showing p-q values at yield point measured on dry and saturated samples on various carbonates at the confining pressure of 5 MPa. Samples were recovered after a few failure points, reaching confining pressures between 20 and 70 MPa. Friction coefficient and cohesion values determined from the Mohr circles are also indicated, as well as the deformation mechanisms which caused the macroscopical failure of the samples.

Table 6.4. Compilation of yield stress under various test conditions for carbonate rocks. C' denotes the onset of dilatancy, C^* denotes the onset of inelastic compaction, C is either C' or C^* (not defined in the literature), and P^* is the pre-consolidation pressure under hydrostatic conditions.

List of Figures

Chapter Two: Properties of undeformed and faulted carbonates

Figure 2.1. Examples of carbonate rock classification used in this study: based on depositional texture of the rock (Dunham, 1962) and the most common grains: a) peloids; b) corralinacean red algae; and c) ooids.

Figure 2.2. Statistical trends of average porosity values (%) of global petroleum reservoirs composed of sandstone (red) and carbonate (blue) plotted against depth (km) (after Ehrenberg and Nadeau, 2005).

Figure 2.3. Schematic illustrating the aggrading neomorphism process, during which micrite/carbonate mud is replaced by neomorphic microspar.

Figure 2.4. A schematic diagram showing established fault zone architectural models: a) single high-strain fault core surrounded by a damage zone, which exponentially decreases in deformation into the background protolith (modified from Chester and Logan, 1986; Caine et al., 1996); b) multiple high-strain cores, enclosing lenses of intensely fractured protolith (modified from Faulkner et al., 2003; Bauer et al., 2016).

Figure 2.5. Logarithmic graphs showing relationships between maximum displacement (m) and (a) fault zone, as well as (b) fault core maximum thickness (m) for carbonate rocks. Data is coloured based on fault kinematics.

Figure 2.6. Ternary diagram illustrating fault rock classification for carbonates (after Woodcock and Mort, 2008).

Chapter Three: Methodology

Figure 3.1. Graph showing workflow of the study.

Figure 3.2. Map showing locations of the study areas and sample collection.

Figure 3.3. Procedure of deformational structure mapping in an outcrop.

Figure 3.4. Schematic illustrating core plug and thin section orientation within the outcrop with respect to the fault plane and the apparent bedding plane.

Figure 3.5. Triaxial compression device with a Hoek-type cell in the Wolfson laboratory at the University of Leeds.

Chapter Four: Banding in high-porosity carbonates

Figure 4.1. Location (a) and local tectonic maps (b-f) of the studied areas. b) Isle of Thanet map modified after Ameen (1995); c) Favignana island map modified after Tondi et al. (2012); d) San Vito lo Capo peninsula map modified after Tondi et al. (2006b) and Todaro et al. (2012); e) Lindos area map in Rhodes modified after Hanken et al. (1996); and f) Gargano promontory map modified after Brankman and Aydin (2004) and Castiglioni and Sauro (2016). The studied areas are marked with a red hexagon.

Figure 4.2. Original optical images and their interpreted microstructural maps of the undeformed rocks from a-b) San Vito lo Capo, c-d) Favignana, e-f) Gargano, and g-h) Rhodes. Also note pressure solution (red) and force chain trajectories (yellow).

Figure 4.3. Original optical images and their interpreted microstructural maps of single deformation bands from a-b) San Vito lo Capo, c-d) Favignana, g-h) Gargano, and i-j) Rhodes; and clustered deformation bands from e-f) Favignana, and k-l) Rhodes. Also note pressure solution (red) and force chain trajectories (yellow).

Figure 4.4. Schematic diagram defining a force chain (yellow), which is a trajectory drawn perpendicular to a minimum of three sutured grain contacts (red). The angle between a force chain and the strike of the deformation band is marked in blue.

Figure 4.5. An example of dual porosity evaluation using Otsu's thresholding method on a BSE scan. The graph shows two thresholds dividing the histogram into three regions: resolvable pore space, microporosity and the solid region. The images at the bottom illustrate these regions (in red) and show at what percentage they compose the sample.

Figure 4.6. a) CT-scan of a core plug from Pegwell Bay containing deformation bands. b) Porosity values obtained from a 1-D vertical transect through the core (dotted line on the CT-scan). Note that the light-coloured deformation bands have a lower porosity than the undeformed chalk.

Figure 4.7. Micrographs of the protoliths from all studied locations: a) Isle of Thanet, b) San Vito lo Capo, c) Favignana, d) Gargano, and e) Rhodes. The pore space is highlighted by blue epoxy dye, and the most prominent characteristics are shown with the arrows. Micrographs f-g) show the syntaxial overgrowth cement under cross-polarized light and the encrusting dog-tooth cement, respectively.

Figure 4.8. Outcrop photographs of the studied single deformation bands from a) Isle of Thanet, b) San Vito lo Capo, c) Gargano, d) Favignana, and e) Rhodes; and clustered bands from f) Favignana, and g) Rhodes. Deformation bands are pointed with the blue arrows, and outlined with blue dotted lines where they are not erecting from the surface and are harder to pinpoint.

Figure 4.9. Boxplots showing mean and standard deviation values of the porosities (%) of all studied deformation bands (single – red; clustered – yellow) and their parent rocks (blue). The boxes represent interquartile range of the data; bars indicate minimum and maximum values; circles show outliers; and orange lines indicate mean values of the datasets. Number of measured values: host (26); single deformation bands (62), and clustered deformation bands (17).

Figure 4.10. Micrographs showing transects across single deformation bands and their host rocks and/or transition zones in a) San Vito lo Capo, b) Favignana, d) Gargano, and e) Rhodes; and clustered deformation bands and transition zones between individual bands in c) Favignana, and f) Rhodes. Deformation bands are outlined with dotted lines. Note porosity in blue.

Figure 4.11. Left: original BSE images of the chalk samples from Isle of Thanet containing deformation bands. Centre: maps showing microporosity; right: macroporosity. Note that deformation bands (marked with dashed

lines) contain far less intraparticle macroporosity due to collapse of the fossils.

Figure 4.12. BSE images showing matrix/cement of single deformation bands in a) Isle of Thanet, b) San Vito lo Capo, c) Favignana, e) Gargano, f) Rhodes; and clustered deformation bands in d) Favignana, and g) Rhodes. Red dashed lines separate bioclasts from the matrix. Note microporosity in black.

Figure 4.13. Rose diagrams of force chain orientations for the host (black), single (red) and clustered (yellow) deformation bands. Rose diagrams show data for the a) San Vito lo Capo; b) Favignana; c) Gargano, and d) Rhodes samples.

Figure 4.14. Graphs illustrating pore throat size distribution. Left: normalized intrusion pore throat size distribution curves; right: drainage curves for a,f) Isle of Thanet, b,g) San Vito lo Capo, c,h) Favignana, d,i) Gargano, and e,j) Rhodes samples. Blue illustrates undeformed host rock, red and black curves: single and clustered deformation bands, respectively.

Figure 4.15. Graphs illustrating grain sizes: cumulative frequency (left), and count number graphs (right) for a, e) San Vito lo Capo; b, f) Favignana; c, g) Gargano, and d, h) Rhodes samples. Undeformed sample data is plotted in blue, single and clustered deformation bands – in red and yellow colours, respectively.

Figure 4.16. Column graph showing the composition (%) of the deformed (single, clustered deformation bands marked as “single” and “clustered”, respectively) and undeformed (host) rock in all studied locations. Note the changes before and after banding (i.e., decrease of moldic porosity in Isle of Thanet; increase in cement in San Vito lo Capo and Gargano; increase in micrite in Favignana and Rhodes samples; and decrease in porosity in all samples).

Figure 4.17. Boxplots showing mean and standard deviation values of the permeabilities (mD) of all studied deformation bands (single – red; clustered – yellow) and their parent rocks (blue). The boxes represent interquartile

range of the data; bars indicate minimum and maximum values; circles show outliers; and orange lines indicate mean values of the datasets. Number of measured values: host (26); single deformation bands (62), and clustered deformation bands (17).

Figure 4.18. Yield surfaces in the p-q space, illustrating regimes, where studied deformation bands may have formed: brittle deformation regime (deformation bands in San Vito lo Capo and Gargano) and ductile deformation regime (deformation bands in Isle of Thanet, Favignana and Rhodes).

Figure 4.19. Schematic diagram illustrating evolution of the studied deformation bands, and their dependence on the sense of stress (dilation/compaction), peloid content and increasing magnitude of stress. Note how further diagenesis and grain dissolution might affect post-kinematic porosity.

Figure 4.20. Boxplots showing mean and standard deviation values of the permeabilities (mD) of all studied deformation bands (red) and their parent rocks (blue). The boxes represent interquartile range of the data; bars indicate minimum and maximum values; circles show outliers; and orange lines indicate mean values of the datasets. DBs: deformation bands.

Chapter Five: Faulting in low-porosity carbonates: a case study from San Vito lo Capo, Sicily, Italy

Figure 5.1. Left: geological map of San Vito lo Capo modified after Incandela et al. (1993). Studied fault outcrops are shown in black rectangles. Note that the inferred faults are indicated by red dashed lines, and observed faults are shown in red solid lines. Stereonets represent structural data for each study area. Right: interpreted cross-sections from North to South (top), and from West to East (bottom) of San Vito lo Capo peninsula (after Stead, 2018). Note that cross-section lines are marked on the geological map.

Figure 5.2. Micrographs of the two protolith rocks hosting the studied faults. Table displays main petrophysical and mechanical properties of the host rocks.

Figure 5.3. Structural maps (a-e) of faults in Mid-to-Upper Cretaceous limestone and representative outcrop photographs (f-k): their locations are marked on the maps in red rectangles. Note the fractured cataclasite walls (g, k) and weathered fault surfaces.

Figure 5.4. a) Structural map of the Torrazzo fault zone occurring within the Mid-to-Upper Cretaceous limestone. b) and c) show a close-up photograph and its structural interpretation of the fractures abutting against the fault core containing chaotic breccia, respectively. d) Photograph of the fault rocks: note white cataclastic layer on the left (west) that is adjacent to a cemented chaotic breccia (east).

Figure 5.5. a) Structural map of the Faro fault zone occurring within the Mid-to-Upper Cretaceous limestone. b) shows a close-up photograph and its structural interpretation of the crackle breccia layer against which fractures terminate. c) is an outcrop photograph of the damage zone typical for the fault zones in the tight limestone of San Vito lo Capo. Note long fractures with spacing of c.5-10 cm perpendicular to which are shorter fractures. d) Photograph of the main fault core, note the chaotic breccia layer along the fault in a creamy colour.

Figure 5.6. Representative maps and photographs of fault rocks and fracture patterns in dolomite of Pellegrino quarry. a) and b) show striated slip surfaces indicating vertical dip-slip and horizontal lateral slip, respectively. c) and d) show interpreted and photographed cataclasite band structures in the outcrop: note the anastomosing patterns and varying orientations forming a complex network of the bands. e) and f) structural map and original photograph of a representative close-up view of the slip surface and a cataclastic band network bounded by intensely fragmented rock within the Pellegrino fault zone. g) and h) show a vertical wider view of the Pellegrino quarry wall: note the complex network of cataclastic material and that only the dominant larger scale fractures are mapped.

Figure 5.7. Structural maps of Punta del Saraceno study area (a-b). Note that only large scale dominant fractures are mapped. Small scale fractures are shown in field photographs (c-d), they terminate at the cataclasite bands.

(e-g) show representative cataclasite bands, which are indicated by orange arrows. Photograph locations are marked on the structural maps.

Figure 5.8. Micrographs showing fault rock evolution in tight limestones and dolomites in San Vito lo Capo. The stained (pink) minerals indicate calcite, and unstained – dolomite. Note the pore space along the clast boundaries (o), and calcite cement in the crackle breccia open voids (n). Matrix is typically made up of fine cataclastic material, only the crackle and mosaic breccia in limestone is filled with calcite micritic cement (b,c), and crackle breccia in limestone (Faro fault) is filled with modern sedimentary matrix (h). Porosity is in blue.

Figure 5.9. Micrographs showing the partially dolomitized chaotic breccia found in limestone-hosted fault zones. Note the rhomboid dolomite shapes within the matrix and large partially dolomitized clast. Most clasts remain calcite and show stained pink colour.

Figure 5.10. Representative CL images of the fault rocks in both tight limestones and dolomites in San Vito lo Capo. Note the typically dark luminescence of a calcite (a,b,d,e) and bright orange luminescence of the dolomitized grains (e,f) and a calcite cement (a).

Figure 5.11. Porosity and permeability data for fault and host rock samples collected from tight carbonates in San Vito lo Capo combined with data from the literature. a-b) Porosity-permeability data is coloured in regard to mineralogy of the fault-hosted protolith rock, blue is the 1:1 line. c) Data is coloured in regard to the type of the fault rock. d) CT-scans of the fault rock core plugs. Note that porosity is in black and the higher the rock's density, the whiter the colour. All core plugs are 38 mm in diameter. e) Whole thin section BSEM scans of the fault rocks. Porosity is in black, and the width of the scan is 2.5 cm.

Figure 5.12. Conceptual models of the fault zone evolution in tight limestones and dolostones in San Vito lo Capo. Not to scale.

Figure 5.13. Logarithmic graphs showing relationships between maximum displacement and (a) fault zone and (b) fault core maximum thickness for

carbonate rocks from a variety of areas compiled from literature (Table 1) and this study. Data is coloured based on mineralogy of the fault-hosting rock and the source data came from. a) Number of data points (n)=403; b) n=607.

Figure 5.14. Photographs of fault zones observed in several dolomite outcrops in Europe: a) Gaaden Quarry, Austria; b) Sala Consilina Quarry, Italy; c) Padul Quarry, Spain. Note the intensely fragmented rock within the damage zone of all faults, and the white cataclasite rocks reminiscent to the ones in San Vito lo Capo.

Chapter Six: Mechanical properties of carbonates

Figure 6.1. Examples of the studied rock samples with the data collected on them: grain size distribution with an interpreted grain map; optical micrograph; and MICP data displaying pore throat size distribution with photographs of the core plugs and their CT-scan transects. Note that porosity on the CT-scans is in black, whereas grains are shown in white – the whiter the colour, the denser the grains. CT-scans and core plug photographs are 38 mm in width.

Figure 6.2. Examples of mechanical data for hydrostatic compression experiments on porous carbonates. These examples were chosen to show differences in failure mechanisms: a) Lower Pleistocene bioclastic grainstone was sheared or lost overall cohesion; b) Miocene corallinean grainstone failed due to compactive shear banding; whereas b) Planktonic foraminiferal wackestone showed compaction banding during the failure. Critical pressure, P^* , is marked with arrows on the stress-strain curves.

Figure 6.3. Examples of multistage-failure triaxial tests conducted on intermediate porosity limestone samples (c.14.4%) beyond failure. a) Mohr circles for one of the b) multistage-failure tests. Note that inflection points on effective mean stress-volumetric strain graph show a sudden volumetric increase when confining pressure was increased to the next higher increment. c) Mohr diagrams with shear failure envelopes for all d) multistage-failure tests done on the Tortorian bioclastic grainstone samples.

Numbers in the legend show porosity values (%). Photograph and CT-scan transect show macroscopical deformation of the samples. Micrographs illustrate dominant deformation mechanisms which caused the macroscopical failure of the samples: singular grain crushing and cracking across several grains. Both mechanisms are focused around the surfaces of the pores.

Figure 6.4. Examples of multistage-failure triaxial tests conducted on intermediate porosity limestone samples (c.7.5%) beyond failure. a) Mohr circles for one of the b) multistage-failure tests. Inflection points on effective mean stress-volumetric strain graph show a sudden volumetric increase when confining pressure was increased to the next higher increment. c) Mohr diagrams with shear failure envelopes for all d) multistage-failure tests done on the Tortorian bryozoan grainstone samples. Numbers in the legend show porosity values (%). Photograph and CT-scan transect show macroscopical deformation of the samples. Micrographs illustrate dominant deformation mechanisms which caused the macroscopical failure of the samples: brittle axial splitting with transformation to transitional-shear failure.

Figure 6.5. Examples of multistage-failure triaxial tests conducted on completely cemented limestone samples with porosity <13% beyond failure. a) Mohr circles for one of the b) multistage-failure tests. Inflection points on effective mean stress-volumetric strain graph show a sudden volumetric decrease and a strain hardening behaviour until the next increase in confining pressure. c) Mohr diagrams with shear failure envelopes for all d) multistage-failure tests done on the Jurassic oolitic biosparite samples. Numbers in the legend show porosity values (%). Photograph and CT-scan transect show macroscopical deformation of the samples. Micrographs illustrate dominant deformation mechanisms which caused the macroscopical failure of the samples: mechanical twinning of the cement and the grains, and intergranular cracks within the cement.

Figure 6.6. Examples of multistage-failure triaxial tests conducted on tight limestone samples (<1%) beyond failure. a) Mohr circles for one of the b) multistage-failure tests. Inflection points on effective mean stress-volumetric

strain graph show a sudden volumetric decrease followed by a flat line until the next increase in confining pressure. c) Mohr diagrams with shear failure envelopes for all d) multistage-failure tests done on the Cretaceous recrystallized packstone samples. Numbers in the legend show porosity values (%). Photographs and CT-scan transect show macroscopical deformation of the samples. Micrographs illustrate dominant deformation mechanisms which caused the macroscopical failure of the samples: brittle-shear plane at an angle of c.57° and axial cracks that terminate at the main shear plane.

Figure 6.7. Yield stress measured during the multistage-failure tests plotted against a) friction coefficient, and b) cohesion (MPa).

Figure 6.8. Micrographs showing examples of the dominant failure deformation mechanisms observed throughout the deformed carbonate rock samples. The pore space is highlighted by blue epoxy dye.

Figure 6.9. Yield stress at hydrostatic (a-c) and non-hydrostatic conditions (d-f) plotted against porosity (a,d), average grain diameter (b,e), and average pore radius (c,f) for all tested carbonate samples.

Figure 6.10. Permeability values (mD) before and after the triaxial loading coloured with respect to the initial porosity (%) of the samples. Blue line shows a relationship of 1:1.

Figure 6.11. Yield (MPa) at a) hydrostatic, and b) non-hydrostatic conditions as a function of initial porosity (%) for various carbonate rocks. Data was collected from the literature (Table 4) and combined with the results of this study (n=428). Data is coloured with respect to mineralogy or distinctive carbonate rock type. c-d) Yield stress in p-q space for all collected data, and e-f) results of this study only. d-e) Data is coloured with respect to confining pressure (MPa), and f) porosity (%). Stress path coefficients, K, are marked in blue, brittle-ductile transition $\sigma_1/\sigma_3 = 5$ (Mogi et al., 1966) is in red.

Figure 6.12. Schematic illustrating changes in failure deformation mechanisms in relation to initial porosity, as well as permeability changes

induced by deformation. Note how different failure deformation mechanisms impact the permeability.

Figure 6.13. Yield point as a function of porosity illustrating impact of the test conditions on the failure for a) our data only; and b) our data combined with the documented data from the literature. Lines show best exponential fit through the data for dry and saturated samples with water/oil.

Figure 6.14. a) Permeability values of fault and host rocks collected from the literature on various carbonate rocks (Bauer et al., 2016; Zambrano et al., 2016; Cooke et al., 2019) and combined with the data from **Chapter 4** and **Chapter 5**, and coloured with respect to porosity of the host rock. b) Permeability values of naturally-faulted rocks and their protoliths (green) combined with the permeability data measured in this study before and after the laboratory-induced deformation (yellow). Blue is the 1:1 line.

Chapter Seven: Discussion

Figure 7.1. World distribution of carbonate reservoirs (modified from Schlumberger Market Analysis, 2007) and a zoom in of the Mediterranean Sea region with the main carbonate hydrocarbon discoveries in the Central and Western parts (modified from Di Cuia and Riva, 2016).

Figure 7.2. Fractured reservoir types based on matrix character (modified from Nelson, 2001). Examples are given for each reservoir type: I) Very tight reservoir, where fractures provide both storage and fluid pathways; II) Tight reservoir: fractures provide flow pathways, but there is some contribution from the matrix; III) High matrix-porosity and low matrix-permeability reservoir (e.g., chalk): fractures provide flow pathways, production comes from matrix, these reservoirs are suitable for secondary and tertiary recovery; and IV) High matrix-porosity and high matrix-permeability reservoir: matrix provides storage and flow, fractures may enhance the permeability.

Figure 7.3. Permeability before and after (a-c) faulting and (d) lab-induced deformation. Note that CT-scans of core plugs are plotted instead of some data points, displaying internal views of the a) samples containing

deformation bands; b) cataclasites; c) breccias; and d) samples after the triaxial deformation (whenever the samples remained sufficiently intact).

Figure 7.4. Collection of permeability values from **Chapter 4** on deformation bands in porous carbonate outcrops, from **Chapter 5** on fault rocks in tight limestones and dolomites, and from **Chapter 6** on lab-deformed samples, combined with the permeability values collected from the literature on naturally-faulted rocks. a) illustrates the references for the data; b) shows the same data coloured in respect to initial porosity (%) of the host rock samples.

Figure 7.5. Outcrop photographs illustrating fault/fracture interaction along a cemented fault core in limestone-hosted rock (a-c), and cataclasite bands in dolomite-hosted rock (d-f) in San Vito lo Capo, Sicily, Italy. Note fracture blunting at the surface of the fault rock.

Figure 7.6. Outcrop photographs illustrating fault/fracture interaction along a dolomitized fault core in limestone-hosted rock in San Vito lo Capo, Sicily, Italy. Note how fractures cross-cut the fault rock, which shows yellow (a) and pink (b-c) colouration.

Figure 7.7. Photographs of a-b Dumpton Bay (Isle of Thanet, SE England) and c-g Vignagnotica (Gargano peninsula, Italy) cliff exposing a-d) open, and e-g) cemented faults. d) shows an interpretation of the slip surfaces (red) and fractures (blue) of an original image (c). f-g) are close-up photographs of a gravitational fault, a full image of which is showed in e). Note that the continuous layer of cement, formed along a slip surface, shows pink colouration, whereas the irregularly shaped brown patch in the footwall formed due to dolomitization. The host rock in Dumpton Bay (a-b) is Upper Cretaceous foraminiferal wackestone (chalk) with porosity of c.39.6%, and the host rock in Vignagnotica (c-g) is Tithonian–Aptian radiolarian mudstone with an average porosity of 8.8%.

Figure 7.8. Photographs of a quarry wall at St Margarethen, Austria, exposing a fault within coralline grainstone of Middle Miocene in age, with a host rock porosity of c.33%. a) Original image, and b) interpretation of the deformational structures. Note a thick deformation band zone (orange) in the hanging wall, forming along a principal slip surface (red) and cut by

fractures (blue). 1 indicates a fracture which cross-cuts the deformation bands; 2 shows a fracture blunting at the surface of the deformation band; 3 indicates a fracture which bypasses the deformation bands; and 4 shows a fracture which stops propagating at the slip surface.

Chapter Eight: Conclusions

Figure 8.1. Summary of the results of this work: graph illustrates permeability before and after the laboratory-induced deformation (green) and natural faulting (yellow). Deformation mechanisms, observed at both deformation conditions, which result in increase or slight decrease in permeability are coloured in blue, and mechanisms, which lead to significant permeability reduction and may act as potential fault sealing mechanisms, are coloured in red.

Chapter 1 Introduction

1.1 Background to research

It is well known that faults can act both as barriers and conduits to fluid flow in the subsurface (e.g., Knipe et al., 1998). Faults that act as barriers are often referred to as sealing faults. Fault sealing in siliciclastic reservoirs has been studied extensively. However, despite being the most important reservoir for geofluids (i.e., water, gas and oil), fault sealing in carbonates has not received significant attention in the literature. The reason for this could be that carbonates are commonly more reactive than siliciclastics, thus they more often lose porosity due to cementation and pressure solution at shallow depth, which makes them more susceptible to dilation and hence faulting tends to result in the formation of conduits to fluid flow rather than barriers. Moreover, many carbonate reservoirs are thought to be oil-wet or having intermediate/mixed wettability, thus they are not as effective capillary seals as siliciclastics, which tend to be more water-wet (e.g., Buckley and Liu, 1998; Høgnesen et al., 2004). However, quantitative data on fault properties, such as permeability and capillary pressure, are important for the petroleum industry because they affect the movement and distribution of hydrocarbons in the subsurface. Many fault-related conduits result in higher than expected recovery (Coney et al., 1993), although they may also lead to mud losses and early water breakthrough (Rawnsley and Wei, 2001). In contrast, fault-related barriers within reservoirs may reduce the rate of petroleum production and make reservoirs less economically viable to

exploit. Therefore, knowing the properties of the faults can help improve production forecasts and reserve estimates.

A number of studies increased in the past two decades analysing faults in carbonates, and several deformation mechanisms were found by which faults in carbonates may develop seal potential. For instance, mechanical smearing of sealing lithologies such as evaporites or clays (e.g., Honda et al., 1996; Aydin and Eyal, 2002; Cornet et al., 2004; Færseth, 2006; Bastesen and Braathen, 2010; Jeanne et al., 2012), cementation of faults (e.g., Mozley and Goodwin, 1995; Agosta and Kirschner, 2003; Agosta et al., 2007; Gaviglio et al., 2009), dynamic recrystallization and pressure solution (e.g., Dunnington, 1967; Nelson, 1981; Finkel and Wilkinson, 1990; Dutton and Willis, 1998; Alsharhan and Sadd, 2000; Kirschner and Kennedy, 2001; Hassan, 2007), pore collapse or development of low-permeability and high-capillary entry pressure carbonate cataclasites (e.g., Billi et al., 2003; Storti et al., 2003; Baxevanis et al., 2006; Micarelli et al., 2006a; Cilona et al., 2012; Tondi et al., 2012; Wennberg et al., 2013), and carbonate-carbonate juxtapositions that appear to be sealing over geological or production time scales (e.g., Bramwell et al., 1999). An extensive compilation of examples of apparent static and dynamic seal in faulted carbonate reservoirs put together by Solum and Huisman (2017) shows that the occurrence of apparent carbonate fault seal in the subsurface is sufficient to warrant the development of models and methodologies similar to those developed for predicting fault sealing within siliciclastics. Advanced tools have been developed for siliciclastic sediments to predict the distribution of fault rocks along faults and predict how these faults will impact fluid flow in the

subsurface: algorithms of Shale Gouge Ratio (Yielding et al., 1997); Clay Smear Potential (Bouvier et al., 1989); Shale Smear Factor (Lindsay et al., 1993); Probabilistic Shale Smear Factor (Childs et al., 2007); Effective Shale Gouge Ratio (Freeman et al., 2010); and softwares such as TrapTester –T7, TransGen, Fault Seal Plugin for Petrel. Each of the siliclastics-based models is based on estimating the clay concentration in the fault rocks, and while faulted carbonate sequences with shaley intervals may allow for the use of algorithms currently in place, they are not applicable to faulted carbonates where other fault seal mechanisms are important. Even though the number of studies on carbonate fault rocks is greatly increasing, a lot more work is required to create equivalent methodology to predict fault transmissibility multipliers for carbonate reservoirs, which will likely have to include cementation and diagenesis (Solum and Huisman, 2017).

There is a large variability in carbonate lithofacies and each undergoes intricate diagenetic processes resulting in heterogeneous and complex microstructures even within a single reservoir (Lucia, 1995; Lønøy, 2006). Moreover, these lithofacies acquire new textural and physical properties with time, burial depth and fault-related deformation. The variety of fault rock types will lead to a range of permeability values. The limited documented examples of the impact of faults on fluid flow in carbonates mean the estimated hydraulic behaviour of these faults within the subsurface is often inaccurate, compounded by the fact that the along-strike variation of fault rock permeability may be substantial. More detailed studies of the petrophysical properties of many carbonate fault rock types, in a range of tectonic regimes, in various carbonate lithofacies, with different deformation

and diagenetic histories will improve our capabilities to predict their hydraulic properties and to better simulate the effect of faulting on fluid flow.

1.2 Aims and objectives

The key aim of this work is to provide a quantitative understanding of how textural variations of differing carbonate facies affect extrinsic fault-related deformation, and the spatial predictions of petrophysical properties of faulted carbonates.

This project utilises a number of outcrops in Europe displaying various carbonate lithofacies. Low-displacement faults were studied in highly-porous rocks (porosity >38%), whereas intermediate- and high-displacement faults were analysed in very tight carbonates (porosity <2%). The main objectives of these analyses were to:

- 1) Determine the composition and textures of the host rocks and compare them with the microstructures of the fault rocks occurring within these lithofacies;
- 2) Measure porosity and permeability of the fault rocks and their protoliths, and investigate how different deformation mechanisms affect hydraulic properties;
- 3) Measure fault-scaling relationships in the field and produce detailed maps of deformational structures to investigate fault-fracture interactions, as well as fault zone architectures in different carbonate lithofacies;
- 4) Collect published fault-scaling data and compare that with the faults of this study.

Moreover, a large number of host rock samples were collected from various locations for mechanical testing including very porous, intermediate- and low-porosity carbonates. The tests were conducted in order to:

- 1) Deform the samples until they reach failure to find their yield point;
- 2) Investigate deformation mechanisms at failure;
- 3) Determine composition and textures, porosity, grain and pore sizes for all tested carbonates before the deformation, and derive relationships between the yield stress and textural as well as physical properties of the samples;
- 4) Investigate mechanical deformation impact on permeability.

The last objective was to compare permeability changes and deformation mechanisms induced both by naturally-occurring faults and mechanical laboratory deformation.

1.3 Layout of thesis

The thesis has been subdivided into eight chapters to analyse in detail the influence faulting has on the carbonate facies and impact on fluid flow. The main topics addressed are:

- Banding in high-porosity carbonates (**Chapter 4**)
- Faulting in low-porosity carbonates (**Chapter 5**)
- Mechanical deformation of various carbonates (**Chapter 6**).

Chapter 2 firstly describes general properties of carbonates, including their classifications, porosity types and the most common diagenetic processes.

Secondly, it talks about fault zone architectures in carbonates and their controlling factors, as well as fault rock classifications in porous and tight

carbonates. Lastly, it presents the known hydraulic behaviour of faults in carbonates and describes documented fault sealing mechanisms.

Chapter 3 describes the methods used during the research project.

Chapter 4 focuses on the small-throw faults in high-porosity (>38%) carbonates, which are referred to as “deformation bands”. It investigates the host rock composition impact on different fault rock textures, variability in deformation mechanisms and their expression in the hydraulic properties.

Chapter 5 analyses the faults in low-porosity (<2%) limestones and dolomites in the relatively small geographical area of San Vito lo Capo peninsula, Sicily, Italy, where these rocks underwent the same faulting events but show very different fault zone architectures. It investigates evolution of these fault zones in the local tectonic history context, as well as fault rock distribution and continuity, fracture patterns and their cross-cutting relationships, and examines how these structural features affect fluid flow.

Chapter 6 describes the extensive study done on mechanical deformation of 29 different carbonate lithofacies, which cover a full range of porosities: <1 - 52%. Samples were triaxially loaded beyond failure, and deformation mechanisms are analysed in relation to the initial textural and petrophysical properties of these samples. Deformation-induced permeability changes are investigated and compared to the naturally-occurring fault impact on permeability.

Chapter 7 discusses overall textural impact on fault rock formation both in natural and mechanical laboratory settings and their expression in the

petrophysical properties. It contains a comprehensive discussion of the results presented in **Chapter 4** to **Chapter 6**, and suggests what type of carbonate hydrocarbon reservoir studied outcrops would represent. Special emphasis is placed on fault-fracture interaction.

Chapter 8 summarises the results of this thesis and proposes suggestions for further work on this subject.

Chapter 2 Properties of undeformed and faulted carbonates

2.1 Properties of carbonates

Deposition in varying environments and intricate diagenetic processes lead to the heterogeneity and complex microstructures of carbonate rocks, which often pose a significant problem when it comes to understanding their reservoir quality (e.g., Lønøy, 2006). In order to fully characterize the behaviour of carbonate rocks in the subsurface it is important to understand their intrinsic properties and textural heterogeneity, and how their textures can be modified by faulting.

2.1.1 Carbonate rock types

Carbonate rocks may be classified based on:

- a) Chemical and mineralogical composition (e.g., Pettijohn, 1957; Füchtbauer, 1959; Chilingar, 1960);
- b) Physical parameters such as porosity (Choquette and Pray, 1970; Lønøy, 2006);
- c) Rock composition and textures: grains, matrix and/or cement (Folk, 1962; Dunham, 1962).

The latter carbonate rock type classification was used in this study.

Carbonates are composed of allochemical grains (grains produced by precipitation somewhere else and transported to the depositional site), fine micritic matrix (mud) and a crystalline cement of calcite or dolomite precipitated during diagenesis. Dunham's classification is based on the

depositional texture of the rock that is the amount of matrix surrounding the grains at the time of deposition (Dunham, 1962). Mud-supported rock consisting of less than 10% grains is called a mudstone, and with greater than 10% grains - a wackestone. Grainstone is a grain-supported, mud-free limestone and generally forms in settings where mud-grade matrix would have been removed. In the presence of 1% or more mud-grade matrix, the rock is called a packstone. If the original components were bound together (i.e., by corals or algae) at the time of deposition, the rock is characterized as a boundstone. Recrystallized rock, which has resulted in the original depositional fabric being destroyed to the extent that it is not identifiable, is called crystalline. The rocks are then further subdivided by means of their most common grains (e.g., peloidal bioclastic grainstone, corralinacean rudstone or cemented oolitic grainstone) when a more detailed description is needed (**Figure 2-1**). Cement types, fossils and other grains were interpreted based on the descriptions proposed by Flügel (2013). Structureless aggregates with an average size of 100-500 μm , and composed of microcrystalline carbonate, were classed as peloids (Tucker and Wright, 2009).

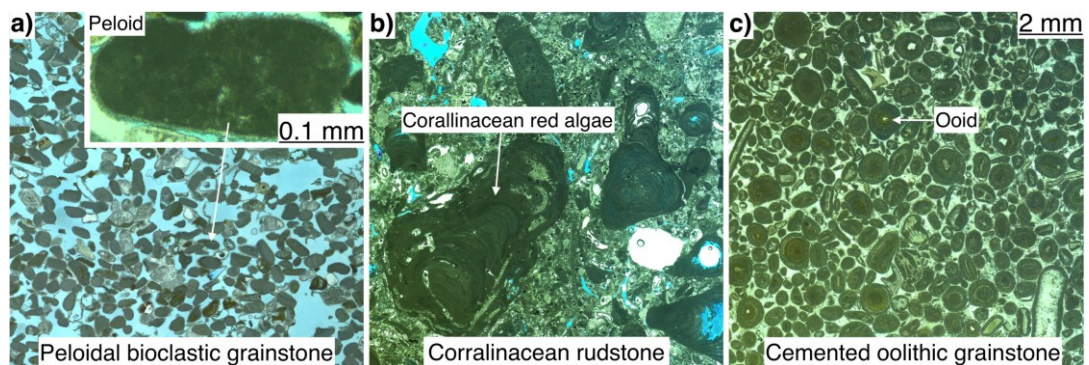


Figure 2-1 Examples of carbonate rock classification used in this study: based on depositional texture of the rock (Dunham, 1962) and the most common grains: a) peloids; b) corralinacean red algae; and c) ooids.

2.1.2 Porosity

A large difference between siliciclastic and carbonate reservoirs occurs due to the way in which their porosity varies as a function of burial depth (**Figure 2-2**). Carbonate rocks experience more rapid rates of porosity reduction compared to sandstones because they contain minerals that are prone to alteration (Ehrenberg and Nadeau, 2005). In carbonate grainstones, early pre-compactional cementation may result in a porosity reduction of up to 37% (Kupecz et al., 1997). The authors also suggest that surface exposure of carbonates may lead to karstification and meteoric cementation, with significant redistribution of porosity and alteration of permeability. Marine diagenesis may reduce their relative porosity further down by up to 70% during shallow burial (<1 km). Therefore, c.50% of carbonate reservoirs have a porosity of <16% by the time they are buried to 0.75 km, whereas c.50% of siliciclastic reservoirs have a porosity of >15% until they are buried to >3.25 km (Ehrenberg and Nadeau, 2005). The consequence of this is that carbonates are more likely to deform in a brittle-dilatant manner compared to siliciclastic reservoirs. However, this is not a scenario for all carbonate rock types. In the case of the chalk reservoirs from the North Sea, it has been argued that high porosity was preserved by a combination of high overpressures or the suppression of diagenesis by early oil emplacement (e.g., Ruddy et al., 1989; Mallon and Swarbrick, 2002; Goult, 2003; Keszthelyi et al., 2016).

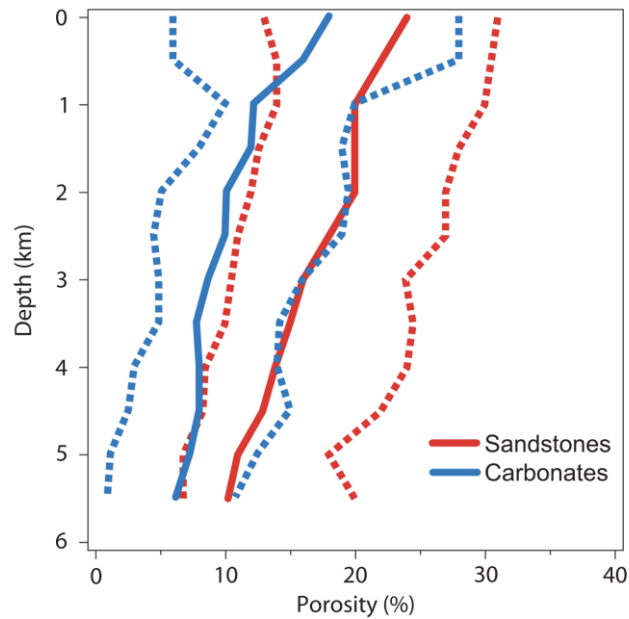


Figure 2-2 Statistical trends of average porosity values (%) of global petroleum reservoirs composed of sandstone (red) and carbonate (blue) plotted against depth (km) (after Ehrenberg and Nadeau, 2005).

2.1.2.1 Porosity types

Varying depositional environments, differences in the shapes of grains and fossils as well as complex diagenetic alterations of carbonates often result in multimodal pore-size distributions. Therefore, several types of porosity may coexist in a carbonate reservoir, ranging from microscopic to cave-sized (e.g., Anselmetti et al., 1998; Choquette and Pray, 1970; Pittman, 1971). In this thesis, pore types were classified according to the porosity classifications of Lønøy (2006) and Choquette and Pray (1970), and included intergranular, intragranular, intercrystalline, microporosity, moldic, vuggy and fracture porosity types. Intergranular porosity is porosity between grains, whereas intraparticle is porosity within individual grains. Intercrystalline porosity forms between the crystals in cemented carbonates. Porosity formed by selective removal of an individual constituent of the rock is called moldic. It is typically formed by dissolution due to rock-fluid interactions.

Pores larger than 1/16 mm in diameter and somewhat equant in shape are called vuggy porosity and are typically irregularly distributed throughout the rock. Porosity formed by fracturing is called fracture porosity. Microporosity contains pores which are $<10\ \mu\text{m}$ in diameter, and may be found within micritic matrix or microporous grains (Rahman et al., 2011). Identifying and understanding the distribution of micro-, meso- and macropores as well as their effect on production is a key aim of integrated reservoir studies (e.g., Akbar et al., 2000). The authors suggest that micropores with pore-throat sizes of $<0.5\ \mu\text{m}$ typically contain mostly irreducible water and little hydrocarbon. Mesopores, with pore-throat sizes between 0.5 and $5\ \mu\text{m}$, contain significant amounts of oil or gas. Macropores with pore-throats $>5\ \mu\text{m}$ are accountable for prolific production rates, but often provide permeability for early water breakthrough, leaving substantial gas and oil behind in mesopores.

Another porosity term used in the text is “minus-cement porosity”. The “minus-cement porosity” concept was first introduced by Rosenfeld (1949), and is a sum of void space and cement volume within a rock. It is used to determine the porosity prior to cementation (e.g., Exner et al., 2013; Lommatzsch et al., 2015).

2.1.3 Diagenesis

Carbonates are chemically very reactive so diagenesis plays an equally important role while analysing the properties of carbonates as the description of depositional facies. The most important diagenetic processes occurring in carbonates are pressure solution/dissolution, cementation and

recrystallization. The rock becomes cemented when mineral-enriched water is carried through porous spaces of a rock chemically precipitating to form new crystalline material within those pores binding the grains together. Cementation by calcite or dolomite may occur rapidly after deposition (e.g., Mallon and Swarbrick, 2002). Characterizing carbonate cementation several factors should be taken into account: the rate and total volume of water movement, timing of cementation relative to hydrocarbon generation, fluid chemistry, the effect of pH, CO₂ activity, temperature and pressure on mineral solubilities (Harris et al., 1985). Cementation may take place in many settings: marine environment during the deposition of the sediment, in a near-surface setting with freshwater penetration, in a subaerial setting produced by a sea-level fall, in a mixing zone between waters of varying chemistries, or in brines of the deeper subsurface. Cementation may also be related to pressure solution. The calcite dissolved by pressure solution migrates away from its source and precipitates as a cement in the adjacent rock (e.g., Garrison, 1981). Pressure solution processes may release sufficient amounts of calcium carbonate to explain cementation of some carbonate formations (Heydari, 2000). Therefore, the amount of cement may vary both regionally and locally due to the flowing water through the sediments or through re-precipitation of calcite due to pressure solution. On the other hand, dissolution by water or aggressive fluids may create extremely high-permeability layers (Schmoker and Halley, 1982; Brown, 1997).

Recrystallization is a process that occurs under temperature and pressure where atoms of a mineral are reorganized by diffusion and/or dislocation

glide that change the size and/or shape of crystal formations.

Recrystallization may occur in many forms and encompass one of the following (Machel, 1997):

1. Textural changes, i.e., changes in crystal size and shapes, such as from non-planar to planar. Often, this form of recrystallization is termed “neomorphism”, and it may be either aggrading or degrading;
2. Structural changes, i.e., changes in ordering and strain. For instance, strain-recrystallization is when a strained calcite lattice transforms to a mosaic of new unstrained calcite crystals;
3. Compositional changes, such as dolomitization or inversion, where, for instance, aragonite changes to calcite, or calcite is replaced by dolomite.

Two of the recrystallization mechanisms were encountered during this study and are described in more detail below: aggrading neomorphism and dolomitization.

2.1.3.1 Aggrading neomorphism

Neomorphism is a textural change of the crystals and is considered aggrading when recrystallization results in an increase in crystal size, i.e., carbonate mud develops to a microspar. Aggrading neomorphism affects both the matrix and the particles: granular calcite replaces the fine micrite and at least the margins of the grains (e.g., Flügel, 2013). Folk (1965, 1974) used the term “microspar” to describe the neomorphic fabric that formed by the recrystallization of micrite with an average size between 4 to 30 μm . The neomorphic microspars are formed of rounded calcite crystals with constant

size and wavy, curved or irregular intercrystalline boundaries (**Figure 2-3**). They often show cloudy appearance and exhibit dark edges due to the impurities that have been pushed aside during recrystallization (El Ghar and Hussein, 2005). The authors suggest that some micritic relics may be observed within the uniform equant microspars indicating the incompleteness of the recrystallization process.

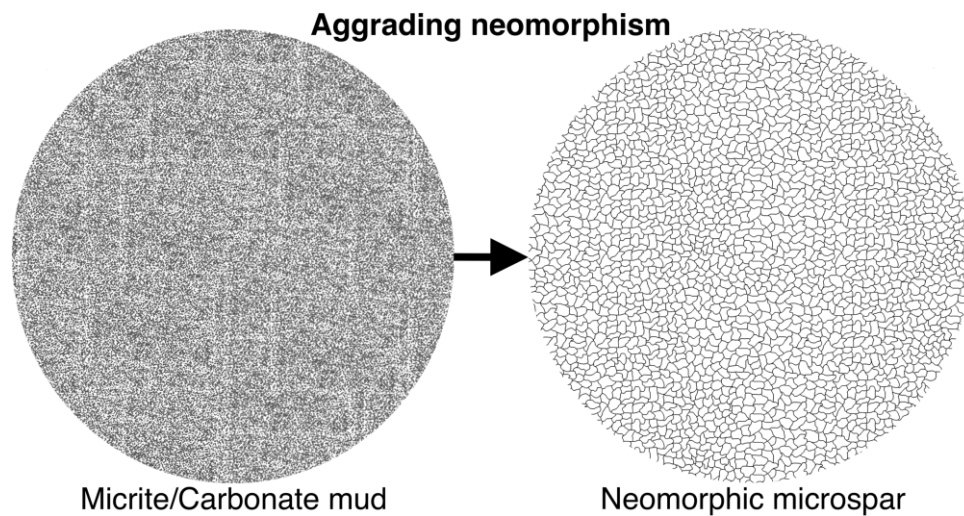


Figure 2-3 Schematic illustrating the aggrading neomorphism process, during which micrite/carbonate mud is replaced by neomorphic microspar.

2.1.3.2 Dolomitization

Dolomitization is a process when limestone comes into contact with magnesium-rich water and Mg^{2+} ions replace Ca^{2+} ions, forming dolomite from calcite. Dolomite may form in many ways: as a primary precipitate, diagenetic replacement, or a hydrothermal/metamorphic phase (Mehmood et al., 2018). Permeability and a sufficient supply of magnesium are required for a dolomite to form. It has been argued that dolomitizing fluids may come from seawater, continental waters, mixing of basinal brines or hypersaline brine with seawater, mixing of seawater with meteoric water, or via the cooling of basinal brines (Mehmood et al., 2018). The only abundant source

of Mg^{2+} ions for near-surface dolomitization is seawater. In low-porosity sedimentary basins, permeability is mostly created by faults and fractures which provide pathways for dolomitizing fluids, thus fault-related dolomitization is a widely known process (López-Horgue et al., 2010; Sharp et al., 2010; Lapponi et al., 2011; Swennen et al., 2012; Hendry et al., 2015; Hollis et al., 2017; Korneva et al., 2018). Unlike most of the near-surface dolomitization processes that tend to form strata-bound diagenetic geobodies, fault-related and fracture-related dolomites typically form geobodies that cross-cut stratigraphy and are geometrically constrained by tectonic structures. Dolomitization affects the distribution of petrophysical rock properties and may enhance or degrade porosity (Lucia and Major, 1994; Purser et al., 1994; Lucia, 2004).

2.2 Faults in carbonates

2.2.1 Fault zone elements

In tectonically active settings, carbonates are characterized by the development of wide zones of distributed strain due to pervasive fracturing and fragmentation, and narrow zones of localized strain along the main slip surfaces showing more intense deformation due to rock comminution, fragmentation, cataclasis and dissolution/precipitation (Agosta and Kirschner 2003; Billi et al., 2003; Agosta and Aydin 2006; Billi, 2007; Bussolotto et al., 2007; Gaviglio et al., 2009; Mitchell and Faulkner 2009; van Gent et al., 2010; Aydin, 2000; Faulkner et al., 2010; Bense et al., 2013; Michie et al., 2014). Tectonic movements thus form fault zones that are made of a fault core and a damage zone. The fault core is defined as a fault rock accommodating most of the slip and is composed of highly altered and

strained rocks where protolith fabric is mostly or completely obliterated (e.g., Sibson, 1977; Chester and Logan, 1986). The damage zone consists of brittle fractures and secondary faults that do not completely destroy the protolith fabric (Cowie and Scholz, 1992). The outer boundary of the damage zone is where the density of damage structures becomes similar to a background density of regional fracturing (e.g., Vermilye and Scholz, 1998; Cello et al., 2001; Wilson et al., 2003; Agosta and Kirschner, 2003; Micarelli et al., 2006b; Agosta et al., 2007; Mitchell and Faulkner, 2009). Damage zones are often divided into two domains associated with different deformation intensity: intensely deformed damage zone (IDDZ), and weakly deformed damage zone (WDDZ) (e.g., Micarelli et al., 2006b, Chambon et al., 2006).

2.2.2 Fault zone architecture

Several models have been proposed to explain the structure of fault zones in carbonates (**Figure 2-4**). A popular model is that they are composed of a fault core surrounded by a fractured damage zone (e.g., Chester and Logan, 1986; Caine et al., 1996; Agosta and Aydin, 2006). The fault core is typically made up of a gouge zone and an adjacent breccia zone: on one side the fault core is bounded by the slip surface, and on the other side by an abrupt boundary between the breccia zone and the damage zone (e.g., Billi et al., 2003). Increased displacement may lead to a more complicated structure containing numerous strands of fault rocks and second-order slip surfaces (e.g., Billi et al., 2003; Agosta and Aydin, 2006; Billi, 2010). Progressive slip may also result in widening of the fault core, forming younger fault rocks next to the slip surface (Chester et al., 2004), or reworking of the pre-existing fault

rocks, creating a mixture of old and young fault rocks. Alternatively, older fault rock may be replaced by younger fault rocks, representing only the last slip event (Chester et al., 1993). Recently, Bauer et al. (2016) observed a difference in fault zone architectures in low-porosity limestones and dolomites and proposed a new model for dolomites. The authors noted that faults in limestone are consistent with the single-stranded fault core model (**Figure 2-4a**). However, faults in dolostones are made up of far wider damage zones which contain widely distributed discontinuous multiple-stranded cataclastic fault cores which partially link up to an anastomosing network (**Figure 2-4b**). The model is supported by the observations made by Schröckenfuchs et al. (2015), as well as by Antonellini and Mollema (2000) who suggest that fault rocks in tight dolomites are reminiscent to the cataclastic shear bands. Moreover, even though most carbonate reservoirs are fractured, the fracture intensity is normally higher in dolomites than in limestones (Stearns and Friedman, 1972; Safko and Hickey, 1992; Nelson and Serra, 1995; Hanks et al., 1997; Cantrell et al., 2004). In mixed dolomite/limestone sequences, fault rocks are largely restricted to dolomites (House and Gray, 1982; Frost et al., 2009; Bauer et al., 2016).

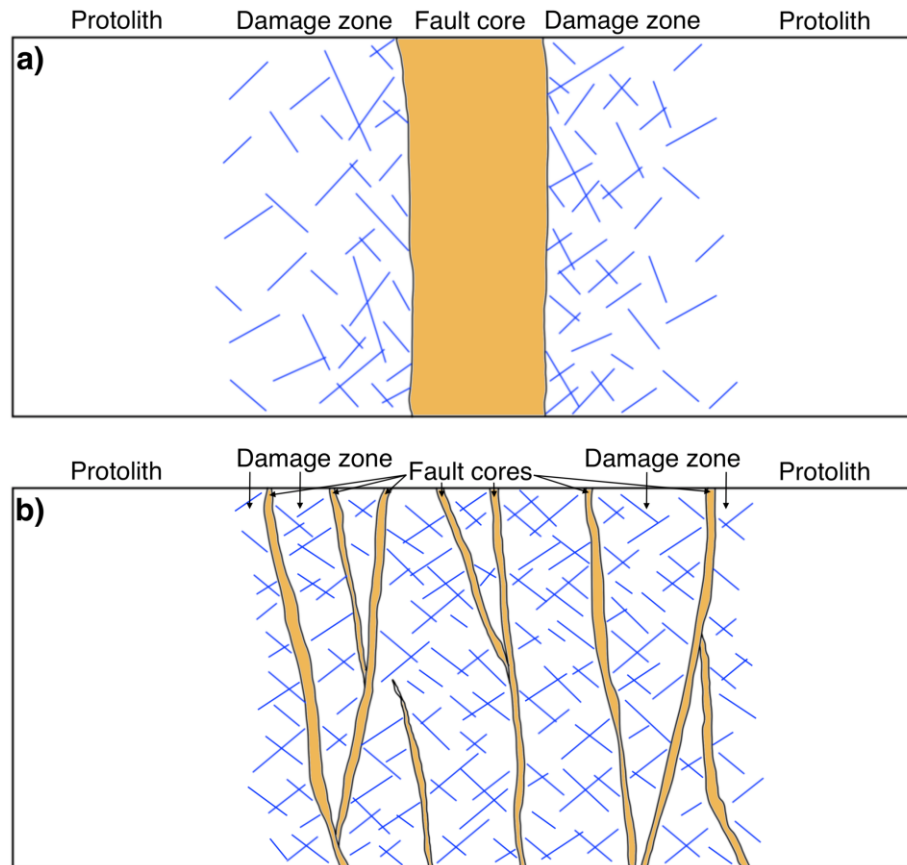


Figure 2-4 A schematic diagram showing established fault zone architectural models: a) single high-strain fault core surrounded by a damage zone, which exponentially decreases in deformation into the background protolith (modified from Chester and Logan, 1986; Caine et al., 1996); b) multiple high-strain cores, enclosing lenses of intensely fractured protolith (modified from Faulkner et al., 2003; Bauer et al., 2016).

2.2.2.1 Fault zone architectural controls

There are several controls on the production of fault zone elements, which can cause formation of different fault zone architectures and significant heterogeneity of fault rocks. First, mechanical stratigraphy has an impact on fault zone architecture and width. For instance, faults in a dominantly competent stratum (strong, brittle) will form narrow fault zones, whereas thick incompetent (weak, soft) layers retard initial fault propagation and initiate folding before faulting. Hybrid competent and incompetent strata exhibit wide complex fault zones (Ferrill and Morris, 2008; Matonti et al., 2012; Michie et

al., 2014). Moreover, faults propagate laterally rapidly within competent layers where pre-failure strains are small (Ferrill and Morris, 2008).

Carbonates containing phyllosilicate-rich material form very wide fault zones with anastomosing strands of fault gouge containing lenses of a country rock (Faulkner et al., 2003). Generally, fault architecture complexity increases as the heterogeneity of the host carbonate increases (Micarelli et al., 2005, 2006b).

Fault zone architecture also varies depending on its position along the fault plane (Peacock, 2002; Kim et al., 2004; Wibberley et al., 2008; Eichhubl et al., 2009; Matonti et al., 2012). In particular, in a relay zone breaching of relay ramps and the shearing of surface asperities often lead to increased complexity and widening of the fault zone (Childs et al., 1997). A fault tip is characterized by branching subsidiary faults (Chinnery, 1966; Kim et al., 2004).

Fault zone architecture also depends on the porosity of the protolith because variations in porosity may create different deformation structures to accommodate the strain. The type of deformation influences whether the damage zone will be dispersed or localised (Shipton and Cowie, 2001; 2003; Riley et al., 2010). For instance, high-porosity rocks tend to have a localized grain-crushing deformation, whereas low-porosity rocks fracture and disperse the damage (Groshong, 1988; Shipton and Cowie, 2003; Agosta et al., 2010; Faulkner et al., 2010; Agosta et al., 2012; Jeanne et al., 2012).

The other controls impacting fault zone architecture are depth at the time of faulting (stress/temperature), the presence and pressure of fluids, variations

in fault structure (e.g., dip angle of the slip surface(s) that produce fault jogs, oversteps and bends), displacement, differential movement of the footwall and hanging wall, and differing stress states (Sibson, 1977; Caine et al., 1996; Zhang and Sanderson, 1996; Wilson et al., 2003; Kim et al., 2004; Bussolotto et al., 2007; van Gent et al., 2010). Any variation in these controls will create different fault zone architectures.

2.2.3 Fault zone scaling relationships

Knowledge of fault rock thickness is crucial for modelling the impact of faults on fluid flow. Many studies have tried to define general scaling relationships between displacement and fault zone thickness. Solum and Huisman (2017) compiled the data focused solely on carbonates and other fracture-based lithologies. They found that fault zone architecture is highly heterogeneous at displacements less than c. 10 m. Both total fault zone width and fault core thickness plateau at displacements of c. 100 – 300 m, but there are examples of large faults with thin fault cores. Fault zone and fault core widths are plotted against displacement in **Figure 2-5** using a revised compilation of that of Solum and Huisman (2017), including the kinematics of the faults. Overall fault zone thickness scales linearly with displacement for all types of faults. However, this is not a rule applicable to all faults, as there is a high degree of overlap between the fault core and total fault zone thicknesses for the same displacement.

Damage zone thickness is thought not to evolve any more after a time-space threshold represented by the development of the main fault plane (Bussolotto et al., 2007, 2015). However, Mayolle et al. (2019) show that

fault damage zone thickness in carbonates scales linearly for displacements <100 m, above which damage thickness tends to remain constant.

The scaling relationships between displacement and fault zone thickness do not take into account the continuity of the fault rocks, which is an extremely important control of fluid simulation in the subsurface. It is generally thought that fault rock continuity evolves with displacement, and that fault core production initiates after a certain threshold after which a continuous fault core is observed (e.g., Cooke et al., 2018). However, there is no single critical value of displacement at which faults will form continuous fault cores. Instead, different values have been recorded in different study areas: between 1.5 and 5 m for faults in southern Sicily (Micarelli et al., 2006a), >60 m for faults in Malta (Michie et al., 2014), and >100 m displacement for faults in Northern Alps, Austria (Bauer et al., 2016). However, at the moment fault rock thickness is the best available proxy for fault rock continuity. Even though fault displacement is not sufficient to predict seal potential, the ability to use it to make predictions of fault zone architecture is important as displacement can routinely be measured from subsurface data.

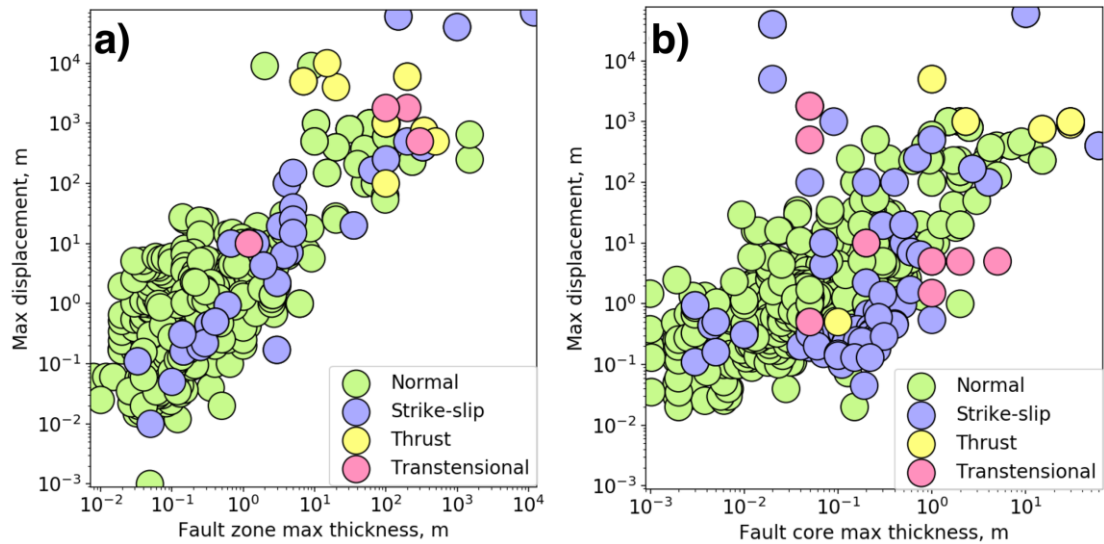


Figure 2-5 Logarithmic graphs showing relationships between maximum displacement (m) and (a) fault zone thickness, as well as (b) fault core maximum thickness (m) for carbonate rocks. Data is coloured based on fault kinematics. References are listed in **Table 5-1**.

2.3 Fault rock classification

Fault cores are comprised of highly altered and strained rocks, which are referred to as “fault rock”. There are several fault rock types including indurated gouge, cataclasite and mylonite (Higgins, 1971; Engelder, 1974; Sibson, 1977; Caine et al., 1996; Evans et al., 1997; Chester et al., 2004; Berg and Skar, 2005; Agosta and Aydin, 2006; Mitchell and Faulkner, 2009; Faulkner et al., 2010). Several different fault rock types may occur within a single fault core, e.g., layers of cataclasites and breccia ponds. This may be controlled by the intensity of deformation, where increased stress conditions and continued displacement create finer fault rock (Engelder, 1974). Other parameters may also cause significant heterogeneity of the fault cores. These include: mechanical properties of the faulted lithofacies, presence or absence of fluids, pressure/temperature and differing stress states (Sibson, 1977; Bussolotto et al., 2007). Different fault rocks occur within highly-porous and tight carbonates.

2.3.1 High-porosity carbonates

Low-displacement (in a range of millimetres to a few centimeters) faults in highly-porous granular rocks form structures commonly referred to as “deformation bands”. These are tabular strain localization structures and are typically characterized by particle size reduction and increased resistance to weathering compared to a parent rock (Fossen et al. 2007, and references therein). Deformation bands may be classified as “single” if they formed as individual bands and “clustered” if formed as several closely spaced individual bands (e.g., Fossen and Hesthammer, 1997), where distance between the individual bands is less than a few cm and typically within the mm-length range. Deformation bands generally do not represent a slip surface. Slip surfaces may form within bands or along/within zones of deformation bands, but this represents a more mature stage in the evolution of faults. Deformation bands are generally precursors to faults and typically start out as single structures, develop into clustered zones prior to the formation of a through-going slip surface. However, deformation bands were the most commonly observed structures within the highly-porous carbonates, thus most analyses in this study will be on the deformation bands (**Chapter 4**). Mature bands and the fault with a slip surface were encountered only in one outcrop located in St Margarethen, Austria, thus it will only briefly be described in **Section 7.3**.

Deformation mechanisms occurring within the evolving deformation bands in porous carbonates are widely reported in the literature, and typically start from mechanical grain reorganisation and pore collapse (e.g., Tondi, 2007; Agosta et al., 2010; Rath et al., 2011; Rustichelli et al., 2012; Cilona et al.,

2012, 2014; Rotevatn et al., 2016). Secondly, they evolve to form intergranular pressure solution surfaces and pressure solution seams (e.g., Tondi et al., 2006a, 2016; Antonellini et al., 2008; Cilona et al., 2012, 2014). The latest stage of deformation band formation is accommodated by grain-scale cataclasis (e.g., Tondi et al., 2006a, 2016; Rath et al., 2011; Cilona et al., 2012; Rotevatn et al., 2016; Tavani et al., 2016). Cementation has also been reported within the compactive shear bands in carbonates to accompany grain translation, rotation, granular flow, pore collapse or cataclasis (e.g., Rath et al., 2011; Zambrano et al., 2017; Cooke et al., 2018). In the literature, pure dilation bands have been reported only in sandstones (e.g., Du Bernard et al., 2002; Exner et al., 2013; Lommatzsch et al., 2015). These studies showed porosity increase caused by dilation and reported minus-cement porosity values varying between 4 and >7%. Porosity increase in these dilation bands is typically followed by carbonate cementation (Exner et al., 2013; Lommatzsch et al., 2015), authigenic clay mineral growth (Du Bernard et al., 2002; Lommatzsch et al., 2015), and dissolution of detrital grains (Exner et al., 2013). Dilational bands have not been reported in porous carbonate outcrops.

2.3.2 Low-porosity carbonates

In low-porosity carbonates, dominant deformation mechanism occurring during faulting is fracture-derived cataclasis. Depending on the intensity of cataclasis, different fault rocks may develop (**Figure 2-6**). In this study, fault rock in tight carbonates is primarily defined by the grain size: fault rock is classified as breccia if >30% of its volume comprises clasts at least 2 mm in diameter, and cataclasite if <30% of its volume comprises clasts at least 2

mm in diameter (Higgins, 1971; Sibson, 1977; Woodcock and Mort, 2008). Matrix between the clasts may be cement or fine cataclastic material of a size of <0.1 mm (**Figure 2-6**). The brecciated fault rock types are subdivided into crackle, mosaic and chaotic breccia with bounds at 75% and 60% clast content (Woodcock et al., 2006; Woodcock and Mort, 2008). Fault rock textures may be described by embryonic, intermediate and mature cataclastic fabrics defined by Billi (2010). Crackle and mosaic breccias show embryonic fabric and consists of an assemblage of large fractured angular grains, which are in contact with one another. Chaotic breccia indicates intermediate fabric and consists of an assemblage of several large grains, which are partly in contact with one another and partly surrounded by a fine matrix, and are less angular than those observed in the embryonic fabric. Cataclasites show mature fabric and consists of an assemblage of few large grains surrounded by a well-developed fine matrix. Cataclasis in tight carbonates includes at least three main physical processes of grain size reduction: intragranular extension fracturing (e.g., Gallagher et al., 1974; Hadizadeh and Rutter, 1982), chipping, and shear fracturing (Billi, 2010).

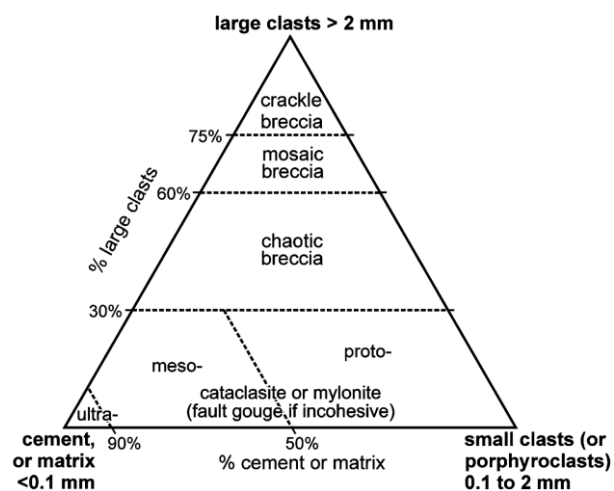


Figure 2-6 Ternary diagram illustrating fault rock classification for carbonates (after Woodcock and Mort, 2008).

2.4 Damage zone structures

Damage zones are characterized by relatively low strain and less intense deformation compared to the fault core. Even though processes such as precipitation/dissolution may affect both damage zone and a fault core (Kim et al., 2004; Agosta et al., 2007), in tight rocks, damage zones generally exhibit brittle deformational features, i.e., joints, tension gashes and secondary small-scale faults (e.g., Pollard and Aydin, 1988; Billi et al., 2003; Faulkner et al., 2010). In describing the structural fabric of damage zones, the term “fracture” is used to include all brittle structures. In high-porosity rocks, deformational features generally observed within the damage zones are deformation bands (e.g., Schueller et al., 2013; Qu and Tveranger, 2016). There is a general trend of deformation structures (i.e., fractures, deformation bands) to increase towards the fault core (e.g., Chester and Logan 1986; Caine et al., 1996; Faulkner et al., 2003; Johansen and Fossen, 2008; Giuffrida et al., 2019). However, different stages of deformation do not always follow this principle (e.g., Mitchell and Faulkner 2009). Inherent lithological variability may control deformational mechanisms, influencing the location and density of the damage (Hugman and Friedman 1979). Moreover, damage may occur at different locations around the fault, such as around fault bends, linkage zones, fault tips and areas of recurrent slip (Peacock and Sanderson, 1991; Shipton and Cowie, 2003; Schöpfer et al., 2006). Stresses may also create anisotropic deformation structures within the damage zone by controlling their orientation (Hancock, 1985; Sibson, 1994).

2.5 Fault impact on permeability

Petrophysical characterization of fault zones is crucial for reservoir exploitation, because they may behave either as seals or as conduits to fluid flow.

2.5.1 Sealing faults

Even though very few sealing faults have been documented within producing hydrocarbon reservoirs in carbonates (e.g., Johnson et al., 2002; Bockel-Rebelle et al., 2004; Cornet et al., 2004; Whitaker et al., 2007), in theory, several mechanisms have a potential to form low-permeability seals to geofluids in carbonates:

- i. **Juxtaposition of hydrocarbon-bearing rocks against extremely low-permeability rocks.** Juxtaposition seals are formed when faulting juxtaposes lithologies with different sealing capacities or capillary entry pressures, such as in carbonate/shale or carbonate/evaporate cross-fault (e.g., Knott, 1993). Moreover, tight carbonates of extremely low permeability may also act as a sealing rock (e.g., Bramwell et al., 1999). However, they generally make poor seals because they are prone to fracturing (Downey, 1984).
Halokinetic and tectonic movements may also create stratigraphic hydrocarbon traps. One of the most common stratigraphic traps in the North Sea, Persian Gulf and offshore Brazil are salt diapir traps, where hydrocarbon-bearing rocks are terminated against the salt diapirs, and hence form low permeability juxtaposition seals.
- ii. **Pressure solution.** Pressure solution reduces porosity by a combination of processes, such as vertical shortening of a rock,

intergranular pressure solution (IPS) and cementation (Heydari, 2000). Vertical shortening occurs due to mechanical compaction, IPS is caused by pressure-induced dissolution along grain contacts, and cementation occurs when dissolved material precipitates in pore spaces adjacent to pressure solution surfaces. Therefore, pressure solution is capable of decreasing the rock's porosity to as low as 0%. The main controls on pressure solution are effective differential stress and elevated pore fluid pressure (Croizé et al., 2013). Pressure solution rates also depend on a grain size – with the rate of pressure solution being inversely related to grain size (Zhang and Spiers, 2005). Pressure solution surfaces tend to form parallel to the bedding due to overburden stress, however tectonic activity may be reflected in structures oblique or perpendicular to the bedding (e.g., Peacock et al., 1998; Peacock, 2001; Antonellini et al., 2008). Stylolites are known to act as barriers to vertical fluid flow (e.g., Dunnington, 1967; Nelson, 1981; Burgess and Peter, 1985; Finkel and Wilkinson, 1990; Dutton and Willis, 1998; Alsharhan and Sadd, 2000; Hassan, 2007) due to their planar horizontal fabric and concentration of clay minerals (Koepnick, 1987). However, a few studies showed different results and suggested that stylolites do not have a significant impact on permeability (e.g., Lind et al., 1994; Heap et al., 2014).

- iii. **Smearing of clay- or evaporate-rich layers along the faults.** Clay may be smeared along a fault plane from source layers in both the hanging wall and the footwall, resulting in a low-permeability zone (e.g., Aydin and Eyal, 2002; Færseth, 2006; Bastesen and Braathen,

2010; Jeanne et al., 2012). Clay-smear continuity depends on the competency contrast between faulted layers (Sperrevik et al., 2000). The authors thus suggested that clay smears may be more effective in interbedded carbonate-shale sequences compared to interbedded sand-shale layers. If carbonates are interbedded with evaporates, faulting may cause entrainment of evaporates along the fault plane, which would act in the same way as clay smears. Evaporates, in fact, make better seals than clays due to their higher ductility (Downey, 1994).

- iv. **Cementation along the fault plane.** These seals may be restricted to the areas where deformation allows local dissolution and reprecipitation of soluble material, or may be associated with the extensive infiltration and precipitation of externally derived cements along or adjacent to the faults (e.g., Perez and Boles, 2004; Eichhubl et al., 2009). Numerous cemented faults have been documented in the literature having their porosity reduced to as low as 0-5% due to cementation (e.g., Mozley and Goodwin, 1995; Honda et al., 1996; Celico et al., 2006; Agosta et al., 2007; Hamaker and Harris, 2007; Gaviglio et al., 2009). Those faults typically form as brittle-dilatant faults and later on they become completely cemented. Therefore, the timing of cementation relative to hydrocarbon maturation and migration is extremely important. It determines whether the fault acts as a conduit to fluid flow or a barrier to fluid flow. Despite the dilatational cemented faults in low-porosity carbonates, cementation may also

accompany faults forming in a compactional manner, such as in very porous rocks (e.g., Matonti et al., 2012).

Once the timing and other factors of cementation allows the formation of a trap for hydrocarbons, cementation represents an extremely good seal, because it is able to hold a few hundred meters of hydrocarbon in height, similar to the sealing capacity of clay smears (Knipe, 1992). However, despite the high sealing capacity of the cements, cemented faults may not be sufficiently continuous on a larger scale, thus their sealing capacity also depends on the petrophysical properties of the uncemented parts of the fault (Fisher and Knipe, 1998).

Cementation is likely to be much more common in carbonate fault zones compared to siliciclastics given the greater reactivity of carbonate minerals, suggesting that seal-breaching fractures in the subsurface may be healed by mineralization. However, these healed fractures may be re-fractured by later tectonic activity (e.g., Li et al., 2003; Vidale and Li, 2003; Wilkins and Naruk, 2007) making the prediction of hydraulic properties of these fault zones more difficult.

- v. **Fracture-derived cataclasis.** Faults in tight carbonates are dominated by fracturing until they are brecciated to the extent that they are capable of rolling, at which point they can deform cataclastically. Cataclasis involves fine-scale fracturing, movement along those fractures, and fragment rotation and abrasion. The opening of fractures results in dilatancy, as does the subsequent fragment rotation (Hancock, 1994). In tight carbonates, which have no significant matrix porosity and permeability, fault-related fracturing

may enhance the permeability of reservoirs, which is essential to hydrocarbon and water storage and production. However, evolving deformation may form cataclasites, which have porosity and permeability similar or even lower to that of the host matrix (Cello et al., 2001; Rawling et al., 2001; Agosta and Kirschner, 2003; Géraud et al., 2006; Agosta, 2008; Bense et al., 2013). Therefore, documented examples suggest that large-displacement continuous fault cores formed due to cataclasis are potential permeability barriers (Solum and Huisman, 2017, and references therein).

- vi. **Grain-scale cataclasis.** Unlike fracture-derived cataclasis, grain-scale cataclasis may cause porosity collapse, and hence compaction. Grain-scale cataclasis is fragmentation of individual grains by microcracking and rigid-body rotations of the grains. Cataclastic deformation results in grain-size reduction (Wong et al., 2004) and often creates a rock with a broader grain-size distribution than the host rock (Blenkinsop and Rutter, 1986), which restricts the pore throat diameters. Grain-scale cataclasis occurs in highly porous granular rocks, and is responsible for significant porosity destruction during faulting (e.g., Tondi et al., 2006b, 2016; Rath et al., 2011; Cilona et al., 2012; Rotevatn et al., 2016; Tavani et al., 2016). Fault-related cataclasis is therefore known to create potential baffles to fluid flow both in sandstones (e.g., Pittman, 1981; Hardman and Booth, 1991; Shipton et al., 2005) and in carbonates (e.g., Rath et al., 2011; Antonellini et al., 2014a; Tondi et al., 2016). However, the fact that carbonate reservoirs tend to lose porosity at a faster rate than

siliciclastic reservoirs may suggest that barriers formed by cataclastic faults in high-porosity carbonates are less likely than in siliciclastic reservoirs.

Faults studied during this work occur within a single lithology with negligible clay content and no alternation with other lithofacies. Therefore, investigation of sealing mechanisms such as juxtapositions against other lithologies as well as clay/evaporite-smears were beyond the scope of this work. This thesis investigates faults with displacements ranging from a few millimetres to a few hundred metres occurring in high- and low-porosity carbonates. Therefore, sealing mechanisms such as pressure solution, cementation, as well as grain-scale and fracture-derived cataclasis are the most likely sealing mechanisms of the studied faults.

2.5.1.1 Static and dynamic sealing

There are two types of seals: static seals that are completely sealed and capable of trapping hydrocarbon columns over geological time; and dynamic seals in which a fault might leak on geological time-scales, but prevents cross-fault flow at commercial production rates (e.g., Jolley et al., 2010). Evidence for fault seal prediction include cross-fault differences in petroleum-water contact (PWC), cross-fault pressure differences and differences in fluid flow density and composition. These properties dissipate as a result of advective and diffusional processes and may equilibrate at very different rates (e.g., Smalley et al., 2004). For instance, pressure differences within aquifers may equilibrate very rapidly (e.g., 10 years), whereas fluid properties such as the isotopic composition of pore fluids may take tens of

millions of years to equilibrate throughout a reservoir. Therefore, some fluid properties may be slow to equilibrate even in uncompartimentalized reservoirs, thus evidence should be weighted with caution in terms of implications for fault-related compartmentalization (e.g., Fisher and Jolley, 2007). Despite having a fault present within a reservoir, variations in contacts may be explained by perched aquifers, hydrodynamically tilted contacts (e.g., Zawisza, 2004; Fabricius and Rana, 2010), palaeo-contacts associated with deformation after the trap was filled or variations in reservoir or fluid properties (e.g., Stenger et al., 2001). The most realistic evidence of fault-related compartmentalization may be provided by examples where water gradient lies on the same depth trend, whereas petroleum gradient lies on a separate trend, indicating a possible membrane seal between the compartments.

It has been argued that faults in carbonates may form both static and dynamic seals. Several faults with carbonate reservoir–reservoir juxtapositions have been documented in the literature, which are thought of being capable to support hydrocarbon columns on a geological timescale (Solum, 2015). Some faults at the Wafra Field between Kuwait and Saudi Arabia are reported to be capable of a dynamic fault seal of c.100-130 psi (Whitaker et al., 2007). A field from onshore UAE is documented to show cross-fault production-induced pressure difference of up to c.1000 psi (Johnson et al., 2002; Bockel-Rebelle et al., 2004). Moreover, c.100 psi cross-fault water pressure difference was estimated for the Aigion Fault in Greece (Cornet et al., 2004).

2.5.2 Faults as conduits

Overall, faults in carbonate reservoirs are perhaps less likely to act as barriers to fluid flow compared with faults in siliciclastics. This is because carbonates tend to become stronger at a shallower burial depth, which would make them more brittle and hence more susceptible to dilatant deformation than siliciclastic rocks buried under equivalent conditions. Therefore, fault zones in carbonates are most often dominated by open faults and fractures and are known to act as preferential pathways for fluid flow (e.g., Davidson and Snowdon, 1978; Litsey et al., 1986; Dunham, 1988; O'Neill, 1988; McCaig et al., 1995; Zeybek et al., 2002; Ferrill and Morris, 2003; Al-Obaid et al., 2005). Moreover, even though some of the faults in carbonates are composed of a sealing inner core, they are typically surrounded by a damage zone, which forms additional routes for the fluid to flow, resulting in an overall increased bulk permeability of the reservoir (e.g., Billi and Salvini, 2001; Banik et al., 2007; Ozkaya and Minton, 2007; Agosta et al., 2010; Giorgioni et al., 2013; Guerriero et al., 2013; Sagi, 2014).

2.5.3 Permeability anisotropy

Fluid transmissibility in a fault zone may show a high level of anisotropy due to the presence and orientation of different deformation features resulting from faulting (Guéguen and Sarout, 2009; Healy, 2009). In particular, fault zones in carbonates exhibit increased permeability parallel to the fault due to increased fracturing in the damage zone and reduced permeability perpendicular to it due to low-permeability material in the fault core (Géraud et al., 2006; Micarelli et al., 2006b; Ran et al., 2014). However, even though fracture networks may strongly enhance fluid flow in fault damage zones,

other, deformation features, such as stylolites, veins or deformation bands, may retard flow. Fluid flow in the fault core may be enhanced in fault-parallel directions in fault breccias, but strongly retarded in across-fault directions by cataclasites, clay smears or cementation surfaces along the fault planes.

Overall, the mixture of initial high porosities and brittle behaviour of diagenetically modified carbonate rocks results in complex sealing/transmissive behaviour of the fault rocks with respect to fluid flow.

Caine et al. (1996) classified faults into four categories: distributed conduits, localized conduits, localized barriers and combined conduit–barrier systems. Faults in carbonates will likely be either distributed conduits or combined conduit–barrier systems (Solum and Huisman, 2017). Fracture-dominated fault zones which have no fault core will most likely be distributed or localized conduits unless cementation is pervasive. Fault zones that contain fault cores may form a barrier at least in the direction perpendicular to it, but whether they seal or not will depend on the permeability/threshold entry pressure and continuity of those fault cores.

Chapter 3 Methodology

3.1 Overview of the workflow

The methods used in this work include extensive structural geological field studies, carried out in outcrop analogues, and laboratory analyses. The work was carried out in systematic steps, which are summarised in **Figure 3-1**.

First, a literature review was conducted to identify suitable outcrops for the study. Fieldwork was then carried out in these locations, which included detailed mapping of the deformational structures, such as faults and fractures, and samples representative for these structures were collected. The samples were CT-scanned to identify their internal structure and best position for drilling and thin section preparation. The laboratory testing on fault and host rock samples included petrophysical property and microstructural analysis. Host rock samples were then triaxially loaded beyond failure and the cycle of laboratory analysis was repeated.

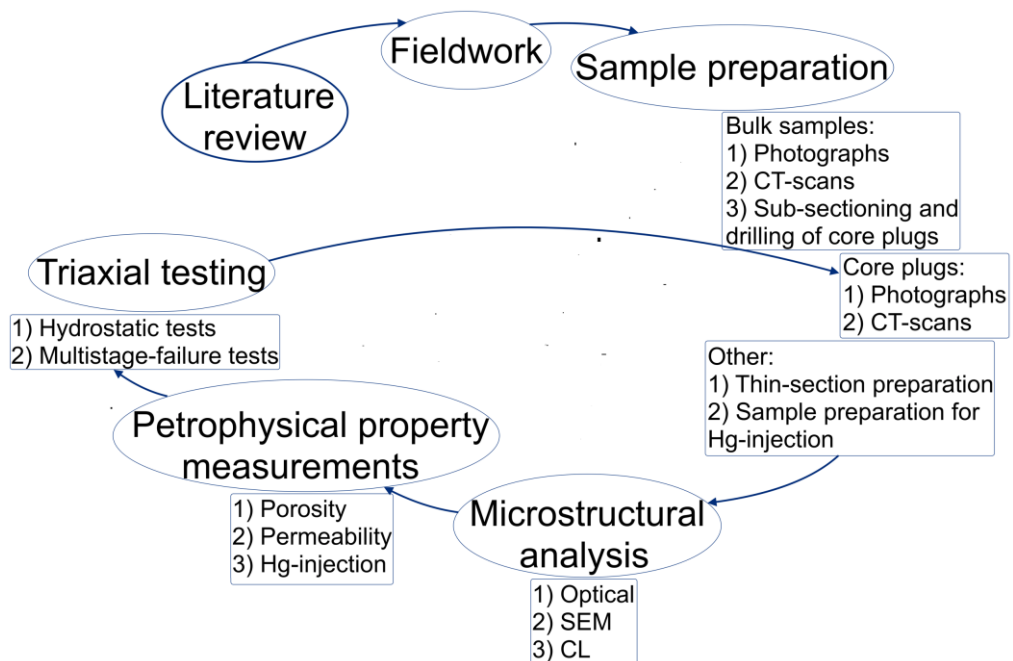


Figure 3-1 Graph showing workflow of the study.

3.2 Fieldwork

3.2.1 Sampling locations

Samples were collected from a number of locations across Europe (**Figure 3-2**):

- 1) Dumpton Bay (51.348922; 1.4407253) and Pegwell Bay (51.328392; 1.3843686) in Kent; Cleeve Hill in Gloucestershire (51.936700; -2.0119973); North York Moors (54.379014; -0.61649521) and Flamborough Head (54.118131; -0.082702533) in Yorkshire; Lulworth Cove (50.619602; -2.2489020) and Isle of Wight (50.669701; -1.5118217) in southern England, UK;
- 2) St Margarethen (47.803910; 16.633431) and Gaaden (48.066082; 16.231730) quarries close to Vienna, Austria;
- 3) Molinella (41.908771; 16.151933) and Vignanotica (41.759628; 16.164129) in Gargano promontory; Sala Consilina (40.391048; 15.612020) in Salerno province; San Vito lo Capo peninsula (38.108033; 12.717297) and Favignana island (37.935498; 12.344805) in Sicily, Italy;
- 4) Kallithea (36.377845; 28.239766), Kamiros (36.273146; 27.824165), Lindos beach (36.096743; 28.085502) and St Paul's Bay (36.088292; 28.087934) in Rhodes, Greece;
- 5) Cacín (37.005003; -3.9007693), Alfacar (37.243152; -3.5609592) and Padul quarry (37.027044; -3.6070561) in Granada basin, Spain;
- 6) Ghar Lapsi (35.826878; 14.423034) and Blue Grotto (35.821123; 14.456187) in Malta island; Gozo island (36.027675; 14.321415).

The main study area of this work was Favignana island and San Vito lo Capo peninsula in Sicily, Italy, where the most detailed and systematic field analyses were done. Deformation bands were also thoroughly studied in Kent, UK; Lindos beach and St Paul's Bay in Rhodes, Greece; and Molinella in Gargano, Italy. The rest of the outcrops were only used for comparison with the aforementioned faults or for host rock collection used for triaxial testing.

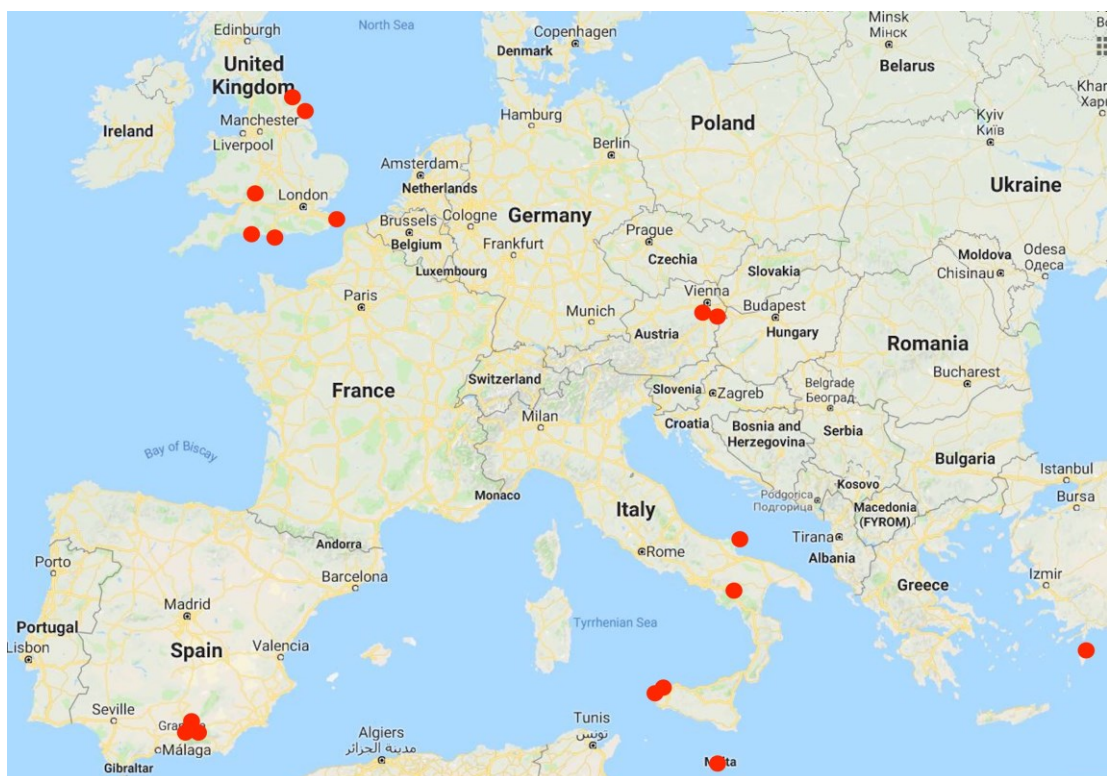


Figure 3-2 Map showing locations of the study areas and sample collection.

3.2.2 Field mapping and sample collection

Each study area was photographed using a Nikon Coolpix L340 camera. Georeferenced aerial photographs were taken at Favignana and San Vito lo Capo outcrops from 50 m height with a DJI Phantom 3 professional drone along automated flight paths with 65% overlap of the images. Photographs were then stitched together using DroneDeploy mapping platform to make a

high-resolution aerial view of each studied location (**Figure 3-3**). Structural features such as slip surfaces, deformation bands, cataclasite and breccia strands, as well as fractures were mapped in the field. The sketches were combined with the drone images to produce detailed maps illustrating fault rock distributions and fracture patterns (**Figure 3-3**). The maps were analysed in terms of width, internal architecture, heterogeneities of fault rocks, and aperture, spacing and cross-cutting relationships of fractures. Samples were collected along fault strike at intervals of c. 1-3 m for each fault zone with accessible outcrop to represent any heterogeneity present within the fault zone while collecting protolith samples for comparison.

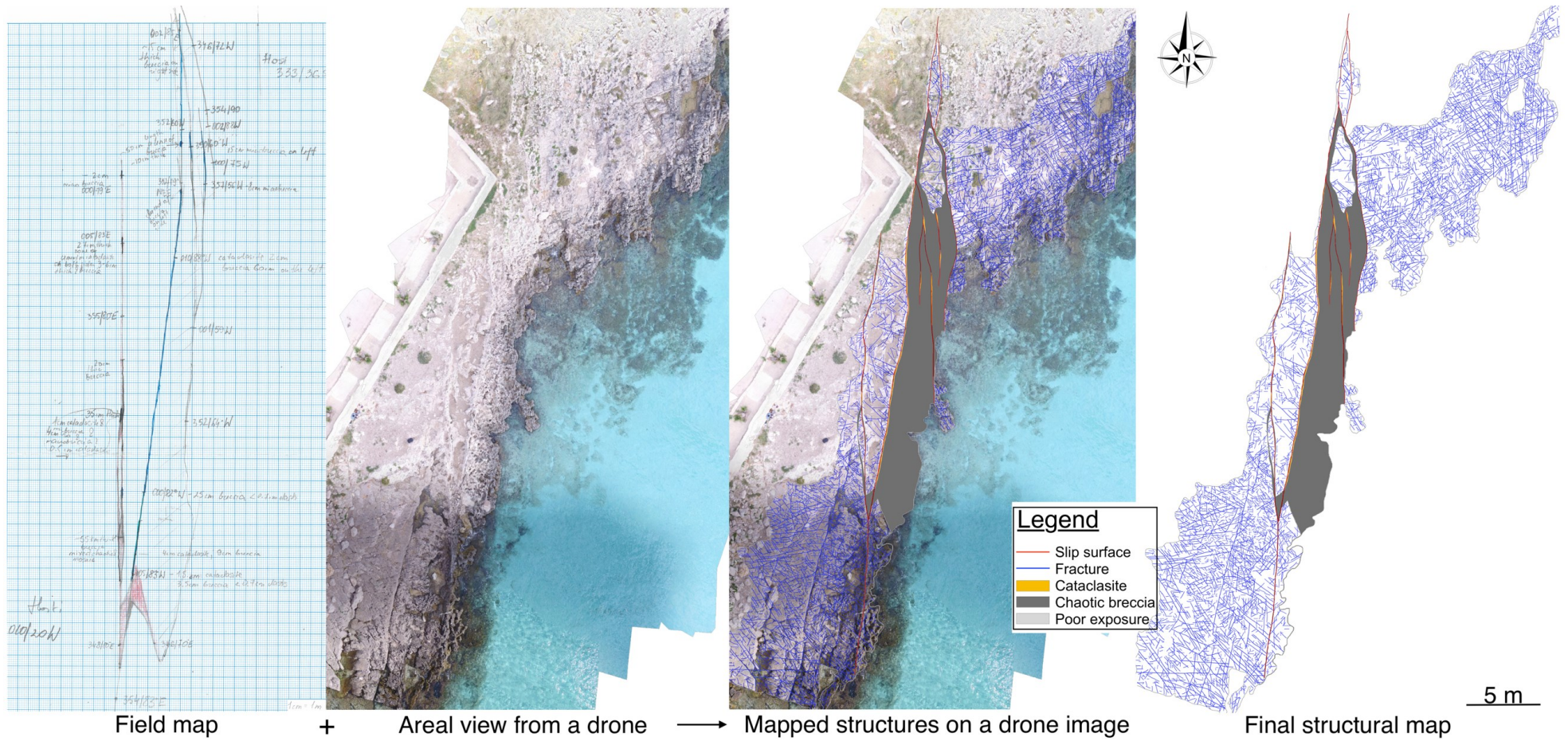


Figure 3-3 Procedure of deformational structure mapping in an outcrop.

3.3 Sample preparation

3.3.1 CT-scanning and coring

The internal structure of the collected bulk samples was determined using a GE Bravo 385 medical-style CT scanner. Each CT image contains 512 x 512 pixels, with a pixel size of 200 x 200 μm^2 . These scans were used to identify the best position for drilling core plugs. Core plugs of 38 mm in diameter were drilled from the bulk sample blocks in a direction perpendicular to the apparent bedding plane for the host rock, and perpendicular to the strike of the fault for the fault rock (**Figure 3-4**). Plugs were cleaned for salt by refluxing them with deionised water saturated with a powder of the same sample to prevent dissolution of grains. This process was continued until the conductivity of the refluxed liquid became the same as of the liquid used to clean the samples. Cleaned samples were oven dried for at least a week at 65°C until their weight stopped changing.

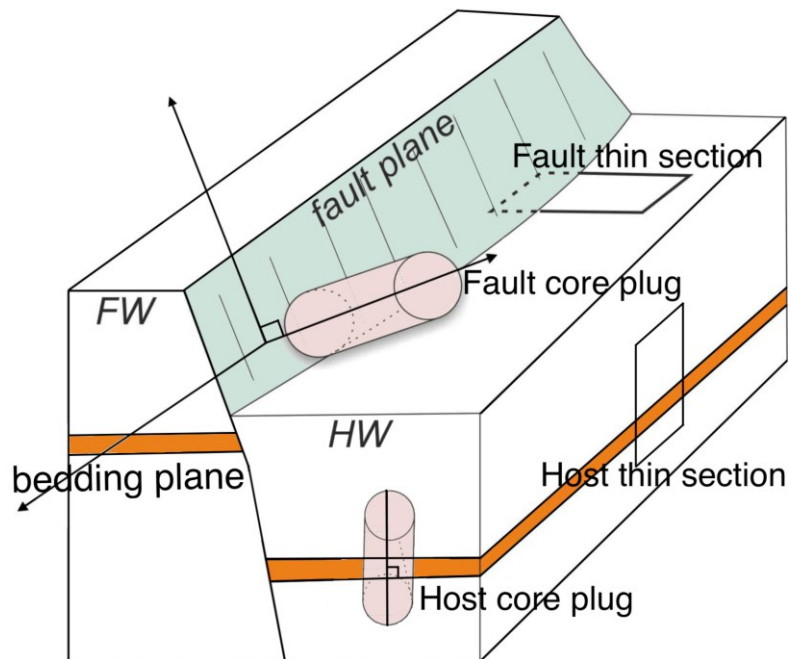


Figure 3-4 Schematic illustrating core plug and thin section orientation within the outcrop with respect to the fault plane and the apparent bedding plane.

3.4 Microstructural analysis

3.4.1 Optical microscopy

Small (2 x 4 cm) blocks were cut from all the samples at an orientation perpendicular to the fault for the deformed samples, and perpendicular to the bedding for the undeformed samples (**Figure 3-4**). Blue-dyed epoxy-impregnated polished thin sections were prepared for the microstructural analysis. Thin sections were stained with Alizarin Red-S and Potassium Ferricyanide to distinguish between dolomite and iron content, respectively. Calcite was distinguished from dolomite as calcite stains in pink, whereas dolomite does not stain.

By means of petrographic thin section observations, performed by using an optical polarizing microscope, the composition and textures of the fault and host rocks were assessed. Over a hundred images were taken for each thin section at a magnification of 4x. The images were stitched in Image Composite Editor to make images covering large areas of the thin sections. These optical images were then used to make microstructural maps by outlining the grains on the photo editor software GIMP. A computer-based quantitative image analysis was carried out on the interpreted microstructural maps using the ImageJ 1.32 software. Particle analysis was carried out to determine the grain size distribution from the mean of the minimum and maximum diameters. Also, the percentage of different rock components (i.e. grains, pores and matrix) was quantified.

3.4.2 Scanning Electron Microscopy (SEM)

Scanning Electron Microscopy was used for porosity evaluation, which at a right resolution and magnification is able to capture all pore sizes (e.g., Haines et al., 2015). A FEI Quanta 650 FEG-ESEM environmental SEM with Oxford Instruments INCA 350 EDX system 80 mm X-Max SDD detector was used for backscattered imaging (BSE) at a resolution of 0.52 pixels per μm with a pixel size of 1.92 μm . Tescan VEGA3 XM was used for the whole thin-section BSE scanning, obtained at a resolution of 81.3 pixels per mm, with a pixel size of 12.3 μm . Images were saved in the 8-bit format, which allocates each pixel to 1 of 256 levels on the grey-scale (0 corresponds to black, and 255 – to white). Studied carbonates are generally composed of calcite or dolomite (>95%), thus they are considered as monomineral, and hence their atomic number as constant. Taking that into consideration, the local grey-levels are proportional to the local mineral density (2,711 kg/m^3 for a calcite, and 2,899 kg/m^3 for a dolomite), and hence the porosity.

3.4.3 Cathodoluminescence microscopy (CL)

A CL microscope was used in the School of Earth, Atmospheric and Environmental Sciences Department at the University of Manchester. The instrument used was a CITL cold cathode luminescence 8200 mk3 fitted on a Nikon Optiphot microscope with 5x, 10x, 20x and 40x objectives. The camera fitted on the microscope was a ProgRes C10plus.

The different luminescence of the crystals under the CL microscope reflects temporal geochemical changes allowing variations in incorporation of Mn^{2+} (a CL-exciting ion) and Fe^{2+} (a CL-quenching ion). The low overall concentrations of Fe and Mn imply precipitation under oxidizing conditions

(Kim et al., 2007). Cathodoluminescence microscopy offers the possibility to examine fabrics, diagenetic phases, replacement, recrystallization and cement relationships.

3.5 Petrophysical property measurements

3.5.1 Porosity

Porosity was calculated from measurements of bulk volume, V_b , and grain volume, V_g , made on the core plugs using the equation:

$$\phi = 100\left(\frac{V_b - V_g}{V_b}\right)$$

where ϕ is porosity (%), V_b is bulk volume (cm^3), and V_g is grain volume (cm^3).

Grain volume was measured with a helium pycnometer using Boyle's Law Double-Cell method (API, 1998). The law states that when the temperature is held constant, the volume of a given mass of ideal gas varies with its absolute pressure as:

$$\frac{V_1}{V_2} = \frac{P_2}{P_1}$$

Gas is admitted into a reference cell of known volume (V_1) at a predetermined reference pressure ($P_1 = 15$ psi). The reference cell gas is then vented into a connected chamber of known volume containing a sample (V_2). This results in a lower equilibrium pressure (P_2), from which grain volume is calculated. Bulk volume was calculated from measurements of the length and diameter of core plugs using a digital calliper. The measurements were repeated three times each to reduce experimental error. The porosities

quoted later in the text are the arithmetic mean values of these three porosity measurements. In terms of accuracy, a well calibrated system provides grain volume measurement within $\pm 0.2\%$ of the true value (API, 1998).

3.5.2 Permeability

Helium permeability was obtained on the core plugs using a CoreLab 200 PDP pulse-decay permeameter. The permeameter has been adapted at the University of Leeds so that it can perform either steady-state (SS) or pressure pulse decay (PDP) axial flow permeability measurements depending on the permeability of the sample. Permeabilities were measured using a PDP technique (Brace et al., 1968) for samples with permeabilities < 0.1 mD and a SS technique (API, 1998) for more permeable samples. A confining pressure was applied to give the same mean effective stress as was estimated to have been experienced by the sample when at its maximum burial depth:

$$P_c = \rho gh$$

where P_c is the confining pressure (Pa), ρ is density of the formation (kg/m^3), g is gravitational force ($9.80665 m/s^2$), and h is burial depth of the sample (m).

The PDP-200 permeameter is composed of an upstream test gas reservoir (V_1), a high-pressure core-holder, a downstream gas reservoir (V_2), a differential pressure transducer and a second transducer for the downstream pressure's monitoring. The gas permeability using the PDP technique is obtained by saturating the sample to a set pore pressure and then transmitting a pressure pulse through the sample and monitoring the

pressure transient at the upstream (P_1) and downstream (P_2) pressures (Brace et al., 1968). The pressure transients were used to calculate permeability using the method of Jones (1997). Gas permeability using the SS technique (based on the Darcy's law) is obtained by establishing the steady-state flow rate of a gas through the specimen. The permeability is calculated from the measured flow rate and pressure gradient using the following equation:

$$k_{ap} = \frac{2000\mu L Q P_{atm}}{A(P_1^2 - P_2^2)}$$

where k_{ap} is apparent permeability (mD), μ is gas viscosity (cP), L is sample length (cm), Q is flow rate at ambient conditions (cm^3/s), P_{atm} is atmospheric pressure (*atmospheres absolute, atms, =1*) A is the cross-sectional area of the sample (cm^2), and P_1 and P_2 are the pressures at the upstream and downstream side of the sample, respectively (*atms*).

The Klinkenberg correction (Klinkenberg, 1941) was measured for each sample to take into account gas slippage effects. Apparent permeability, k_{ap} , was measured at 5 different gas pressures so that the absolute (Klinkenberg corrected) permeability could be obtained from plots of $1/P$ vs. k_{ap} as described in API (1998).

In permeability measurements, it is hard to define a precise accuracy of the measured values due to a number of parameters which may produce a slight error (e.g., system leakage, sample bypass, pressure transducer and flow meter errors, ambient temperature variations, etc.). Therefore, confidence intervals are often used for reporting core analysis results. Thomas and

Pugh (1989) reported that in the confidence interval of 95%, steady-state gas permeability in a range of 0.01-0.1 mD may provide accuracy of $\pm 16\%$; in a range of 0.1-1 mD - accuracy of c.16%; in a range of 1-50 mD - accuracy of c.10%; and permeability in a range of 50-1.000 mD would give accuracy of c.6%.

3.5.3 Mercury-injection (MICP)

Mercury-injection analysis was undertaken on c.1 cm³ sub-samples.

Samples containing a fault rock were cut so that the fault was in the centre of the cube parallel to two of the faces. Five surfaces were then coated with resin so that mercury was forced to flow across the fault. Host rock samples were not coated with the resin. Samples were oven dried at 65°C for 48 hrs.

Mercury porosimetry is based on the capillary law governing liquid penetration into smaller pores. This law, in the case of a non-wetting liquid like mercury and assuming cylindrical pores is expressed by the Washburn equation:

$$D = \frac{4\gamma\cos\theta}{P}$$

where D is the pore diameter (μm), P is the applied pressure (psi), γ is mercury-air surface tension (484 mN/m), and θ is mercury-air-rock contact angle (140°).

The measurements were carried out using a Micrometrics series IV mercury-injection porosimeter. This equipment is capable of injecting mercury into an evacuated and cleaned extracted sample as the pressure is increased in step-like increments up to pressures of 413 MPa. The volume of mercury

intruded after reaching equilibrium at each pressure increment is recorded. The pressure is then plotted against the mercury saturation readings to produce an injection curve. The raw data was conformance corrected and incremental intrusion was plotted against pore throat diameter.

The throat and pore sizes may be correlated, a ratio of c.2-11 between the pore and throat diameters have been inferred from MICP and microstructural data on carbonate and clastic rocks (Wardlaw et al., 1987, 1988; Churcher et al., 1991). Data in this study was converted to pore size distribution as described in ASTM D4404-84 (2004)

3.6 Triaxial testing

3.6.1 Experimental procedure

The triaxial compression tests were conducted with the aim of determining the yield stress of the samples. Multiple and continuous failure state triaxial, as well as hydrostatic tests were conducted on dry and water-saturated core plugs. For the dry experiments, samples were oven dried for a week at 65°C. For the drained tests, samples were saturated with CaCO₃ equilibrated distilled water under vacuum for 24 hrs. The core plugs were placed in a Hoek-type cell (**Figure 3-5**). The cell used for the current series of triaxial tests is designed for 38 mm diameter core plugs with a length at least twice that of the diameter. The ends of the samples were ground flat to ensure they were perfectly parallel to the loading surfaces. The confining pressure was applied up to a maximum of 70 MPa by a hydraulic pump via a rubber sleeve surrounding the circumference of the rock cylinder. The axial stress was applied using a calibrated universal compression/tension loading frame

at a strain rate of 10^{-5} s^{-1} . The upper limit of the applied axial stress is 250 MPa for 38 mm diameter core plug. Stresses for these samples are measured with an accuracy of 0.1 MPa.

The axial strain was measured using an axial linear variable differential transformer (LVDT) sensor, which is attached to the loading ram through aluminium mobile supports. The lateral strain was measured using two diametrically opposed gauges, mounted horizontally on the sample. The confining pressure was recorded by a pressure transducer, which was positioned on the inlet line for the confining fluid into the triaxial cell. The axial load was obtained using the load sensor, which is installed between the lower loading ram and the piston. The sensor consists of a bridge mounted on a piece of metal that deforms elastically when force is applied. This is a strain gauge-based load sensor, therefore the load is determined from the strain. The axial stress was calculated as the load divided by the cross-sectional area of the sample. For conventional triaxial loading, the maximum and minimum stresses are along the axial and radial directions of the sample, respectively, which are referred to as σ'_1 and σ'_3 (with $\sigma'_2 = \sigma'_3$). These are effective pressures, as pore pressure was kept at zero during all the experiments. Effective mean stress, p , was calculated using the relation, $p = (\sigma'_1 + 2\sigma'_3)/3$, and differential stress, q , as $q = \sigma'_1 - \sigma'_3$. Volumetric strain, ε_v , was calculated using the relation for axisymmetric samples, $\varepsilon_v = 2\varepsilon_r + \varepsilon_a$, where ε_r and ε_a are radial and axial strains, respectively. The convention was adopted that compressive stress and compactive strain (i.e., shortening and volume reduction) are positive. The axial loads, confining pressures as well as the axial and radial strains were plotted in real-time to allow the

identification of incipient failure. The yield point was determined from strain gauge volumetric data only, as it was not possible to directly measure the porosity change during the tests. This method for determining yield stress has been used successfully in previous studies (e.g., Cuss et al., 2003; Dautriat et al., 2011).

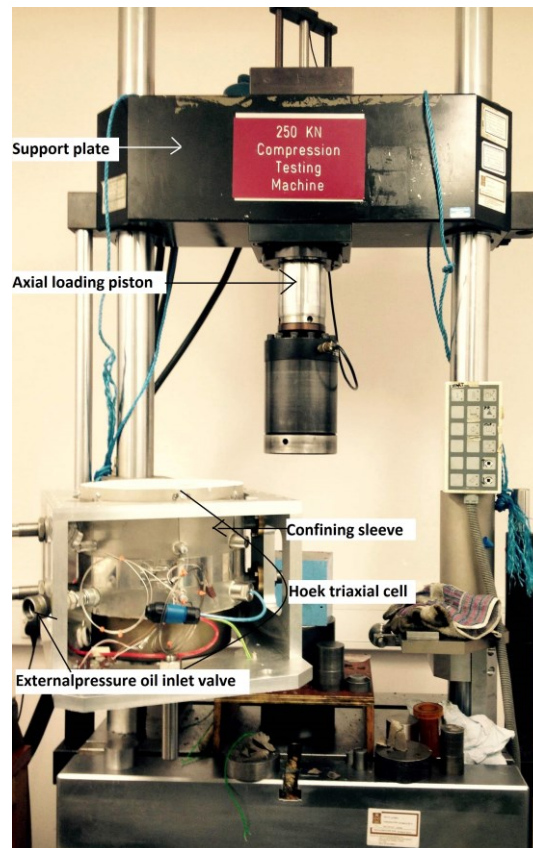


Figure 3-5 Triaxial compression device with a Hoek-type cell in the Wolfson laboratory at the University of Leeds.

3.6.1.1 Hydrostatic tests

The axial stress and confining pressure were increased at the same rate during the hydrostatic test. The sample was unloaded at the same strain rate when maximum confining pressure of 70 MPa was reached. The water was allowed to drain through ports in the steel end platens during the drained experiments.

3.6.1.2 Multistage and continuous failure triaxial tests

During the multistage and continuous failure state tests, the axial stress and confining pressure were increased hydrostatically until the level of the first confining pressure of 5 MPa was reached. The confining pressure was then held constant whilst the axial stress was increased. The confining pressure was increased to the next higher level (5 MPa higher) as soon as an inflection was identified that corresponded to yield. The procedure was repeated several times to provide the residual strength envelope.

Chapter 4 **Banding in high-porosity carbonates**

4.1 Introduction

Over the last four decades, extensive studies were conducted on deformation bands in siliciclastic sediments. The results indicate that such structural elements may form barriers to cross-flow as a result of: i) grain reorganisation, ii) cataclasis, and iii) cementation (e.g., Fisher and Knipe, 1998, 2001; Ogilvie and Glover, 2001; Fossen et al., 2007 and references therein). The former two mechanisms occur during faulting, whereas the latter mechanism can occur as a post-deformational process that tends to occur during mesodiagenesis at temperatures higher than 90°C (Fisher and Knipe, 1998, 2001), or between two consecutive slip events (Petit et al., 1999). Although the literature on deformation bands in carbonates is not as extensive as for siliciclastics, several publications on the subject emerged in the last two decades (**Table 4-1**). The most studied examples are from outcrops in Italy (e.g., Tondi et al., 2006a,b; Tondi, 2007; Antonellini et al., 2008; Agosta et al., 2010; Cilona et al., 2012; Rustichelli et al., 2012; Tondi et al., 2012; Antonellini et al., 2014a,b; Cilona et al., 2014; Tavani et al., 2016; Zambrano et al., 2017, 2018). However, other examples are also reported from Malta (Rotevatn et al., 2016; Cooke et al., 2018), Austria and Hungary (Rath et al., 2011), Norway (Wennberg et al., 2013; Wennberg and Rennan, 2018) and Spain (Tavani et al., 2017; Robert et al., 2018, 2019). Carbonates have higher chemical reactivity than siliciclastic rocks, and are therefore more susceptible to early diagenetic processes such as

cementation, dissolution and pressure solution. Furthermore, they often have complex pore geometries (e.g., Choquette and Pray, 1970; Lucia, 1995), thus the formation of deformation bands within carbonate rocks is likely to differ from that of siliciclastics.

In carbonate hosted deformation bands, it is common to observe grain crushing and cataclasis occurring at shallower burial depths than siliciclastics (e.g., Micarelli et al., 2006a; Tondi et al., 2012; Cilona et al., 2012; Michie, 2015; Rotevatn et al., 2016). It has been argued that grain crushing and cataclasis in natural deformation bands is usually facilitated by pressure solution (e.g., Tondi et al., 2006a). However, plastic deformation becomes a dominant deformation mechanism in rocks made up of a high percentage of micritic peloids (>60%) as a result of smearing and mixing (Antonellini et al., 2014b). Crushing of bioclastic grains and pressure solution becomes negligible in these rocks. Generally, the burial depth necessary to initiate pressure solution in carbonates is around 10 times shallower than in siliciclastics (Tada and Siever, 1989). In particular, grain contact quartz dissolution/pressure solution does not occur until a temperature of around 90°C (i.e. >3 km under a geothermal gradient of 30°C/km) and its rate is not thought to be dependent on the effective stress conditions (Bjørkum, 1996; Walderhaug, 1996). Pressure solution in carbonates may occur at depths as shallow as 30 to 40 m (e.g., Morawietz, 1958; Engelhardt, 1960). Tada and Siever (1989) suggest that temperature and minimum effective pressure required for pressure solution to occur in skeletal limestones is 6-25°C and 2-4 MPa, respectively. Pressure solution might occur as a combination of plastic deformation at the grain-to-grain contact and free face dissolution at

the edge of the contact (Tada and Siever, 1986; Karcz et al., 2006). However, deformation bands produced in laboratory experiments experience grain crushing and fracturing, as well as mechanical twinning, with no pressure solution when formed under confining pressures ranging between 5 and 435 MPa (e.g., Vajdova et al., 2004; Arroyo et al., 2005; Baxevanis et al., 2006; Baud et al., 2009; Vajdova et al., 2010; Zhu et al., 2010; Cilona et al., 2012; Vajdova et al., 2012; Brantut et al., 2014; Cilona et al., 2014; Ji et al., 2014; Baud et al., 2017; Tarokh et al., 2017). The time-dependent dissolution–precipitation processes are not yet well understood or quantified, because their very slow rates make them difficult to investigate under laboratory conditions. Therefore, specific rate-controlled creep tests at a single contact and in the presence of a pore fluid are usually performed to study pressure solution at grain contacts (e.g., Zubitsov et al., 2005; Croizé et al., 2010).

Deformation bands within carbonates have been documented to have a negative impact on fluid flow (e.g., Antonellini et al., 2014a; Tondi et al., 2016). Therefore, they may form barriers to fluid flow in groundwater aquifers or petroleum reservoirs. Rath et al. (2011) found that the permeability of compactive shear bands within the coralline limestone is reduced by up to 4 orders of magnitude in the direction normal to the band with respect to the host rock. Tondi et al. (2016) measured around 2 orders of magnitude reduction in permeability across the compactive shear bands both in the Upper Cretaceous Orfento rudist limestone from central Italy and porous grainstone from Favignana. Reduction in permeability measured from the host rock to the single and clustered deformation bands in porous

grainstones in San Vito lo Capo was reported to be only around 1 order of magnitude (Antonellini et al., 2014a).

Table 4-1 A compilation of documented examples of natural and laboratory-induced deformation bands in carbonate rocks, including the data collected during this study. PS: pressure solution; PSs: pressure solution seams.

Publication	Location	Formation	Host rock description	Porosity (%)	Deformation band type	Field data	Transition zone	Deformation mechanism
NATURAL DEFORMATION BANDS								
Agosta et al., 2010	Majella anticline, Central Italy	Bolognano Fm		<30	1) Bed-parallel compaction bands; 2) Oblique to bedding shear bands	Thickness 1) 0.5-3mm; 2) Single bands <2mm; zones of bands 5-10 cm	N/A	Particulate flow (grain translation & rotation with pore collapse)
Antonellini et al., 2008	Majella anticline, Central Italy	Orfento Fm		1) >15; 2) >10	1) Bed-parallel compaction bands; 2) Cross-cutting shear bands/zones of shear bands with associated PS seams	Spacing 1) 0.05-1.5 m; 2) 3-5 cm	N/A	PS and cataclasis. PS seams occurred along older shear bands which facilitated cataclastic faulting
Antonellini et al., 2014a	San Vito lo Capo and Favignana, Sicily, Italy	Lower Pleistocene grainstones	Grainstones consisting of bioclasts (i.e. Vermetus, Serpula, lamellibranches, echinoids, algae and corals) ranging in size from sub-mm to a cm. Intragranular and intergranular porosities, the latter reaching up to a few mm in diameter	25-45	1) Single compactive shear bands; 2) Zones of compactive shear bands	Used field data from Tondi et al. (2012)	Y	
Antonellini et al., 2014b	Cingoli anticline, N Italy	Calcare Massiccio Fm	Grainstone consisting of c.60% peloids. Grain-size c.128 µm; pore size c.70 µm	>17-27	Compactive shear bands	Spacing 1-5 cm; zone of bands thickness 0.5-15 cm; 1 band c.1 mm thick; offset 1-2 mm	Y	Plastic smearing and squashing of peloids with rare grain crushing & sparse PS
Cilona et al., 2012	Majella anticline, Central Italy	Orfento Fm	Mostly composed of rudist fragments and intraclasts; Rudist shells can be partially replaced by micrite or detrital sparry calcite. Rare echinoids	<32	1)Compaction bands; 2)Compactive shear bands		Y	Pore collapse, Hertzian cracks, PS → Grain dissolution, PSs growth → Shearing of PS, cataclasis, tail PSs development
Cilona et al., 2014	Majella anticline, Central Italy	Bolognano Fm	Shallow water skeletal grainstones & packstones, containing benthic forms, bryozoans, red algae, lamellibranches, echinoids	<32	Compaction bands		Y	Grain rotation, sliding, crushing, pore collapse and prevailing intergranular PS
Cooke et al., 2018	Qala Point region of Gozo, Malta	Upper Coralline limestone	Coralline algal limestone	25-35	Compactive shear bands		N/A	Grain translation, granular flow, minor PSs and PS around individual fossil clasts, cementation
Rath et al., 2011	Eisenstadt-Sopron Basin, Austria-Hungary	Leitha limestone	Mainly composed of Corallinacea, also contains forams, oysters, pectinids, echinoids	22-35	Compactive shear bands	<2 cm displacement; 4 m spacing	Y	Grain translation, rotation & pore collapse → cementation → cataclasis
Rotevatn et al., 2016	Maghlaq Fault, Malta	Globigerina limestone Fm	Mostly composed of planktonic forams, bivalve, echinoids. Pore sizes are mainly <100 µm, and do not exceed 200 µm	17-25	1) Bed-parallel compaction bands; 2) PS-dominated compactive shear bands; 3) Cataclasis-dominated compactive shear bands	1) 750-1500 µm thick; 0.5-2 m long; 2-3) Single bands 1-4 mm thick; clusters of bands <20 cm thick; anastomosing swarms 0.5-5 m thick. <few 10s of cm long, when undisturbed by other bands <10 m long	Y	1) PS, mechanical grain reorganization; 2) Grain reorganization, intergranular PS; 3) Cataclasis & grain crushing (fractured echinoids but intact forams)
Rustichelli et al., 2012	Majella anticline, Central Italy	Bolognano Fm	Mostly composed of benthics, bryozoans, red algae, lamellibranches, echinoids	15-35	Bed-parallel compaction bands	<25 cm long; 0.5-5 mm thick	Y	Grain rotation, translation & fracturing. The thickest bands show PS at grain contacts with minimal internal pores (echinoids) & microsparry cementation
Tavani et al., 2017	Cotiella Thrust, Spanish Pyrenees	Paleocene quartz-rich bioclastic calcarenites	Peloidal grainstone/packstone with minor echinoderm fragments, red algae, hyaline and agglutinated forams, quartz, K-feldspar, plagioclase and phyllosilicate material	N/A	1) Compactive shear bands; 2) Bedding-perpendicular compaction bands	1) Mm-thick anastomosing bands. Spacing: 5-50 cm; 2) Mm-thick bands	N	1) Increased concentration of quartz due to pressure-enhanced dissolution of calcite; quartz grains fragmentation with no significant clasts rotation and translation; insoluble material accumulation forming thin seams; pressure solution at grain contacts (sutured contacts between quartz grains); 2) N/A
Tavani et al., 2016	Lattari Mts., southern Apennine belt, Italy	Shallow-water dolomitic Jurassic-Cretaceous limestone	Made up of micritic calcite and dolomite crystals (the size of the latter ranges between 50 and 250 µm) and ≤0.97 % of clay	≤0.82	Hybrid bed-parallel compaction-solution bands	Few mm-2 cm thick bands with wavelengths of tens of cm and amplitudes of a few cm	N/A	Development of PSs due to stress-enhanced dissolution of calcite → concentration of less-soluble dolomite crystals due to dissolved calcite → collision, crushing and fragmentation of the concentrated dolomite crystals

Tondi, 2007	Castelluzzo, San Vito lo Capo, Sicily, Italy	Lower Pleistocene grainstones	Grains are made up of fragments of carbonates, marls and shales 0.05-1 mm in diameter; The matrix consists of bladed and sparry calcite cement and carbonate and marl fragments <0.05 mm	19-30	Compactive shear bands	Single bands 1-2 mm thick; zones of bands 2 mm - 20 cm thick	Y	Grain translation & rotation with pore collapse, PS, precipitation of solved solids in the transition zone, dilatant microcracking
Tondi et al., 2006a	Majella anticline, Central Italy	Orfento Fm	Consist fragments of rudists 0.05-0.4 mm in size	15-28	1) Compaction bands; 2) Compactive shear bands	1) 1-5 mm thick, discontinuous; 2) Single bands 1-2 mm thick, offset 1-2 mm; zones of bands 2 mm - 5 cm thick, offset 2 mm - 5 cm	Y	Particulate flow (grain translation & rotation with pore collapse) → PS → Cataclasis
Tondi et al., 2012	Favignana, Sicily, Italy	Lower Pleistocene grainstones	Consist vermetus, serpula, lamellibranches, echinoids, algae and corals	30-50	1) Single compactive shear bands; 2) Zones of compactive shear bands	1) Single bands 30-100 cm long, 4-6 mm thick, offset 2-4 mm; 2) Zones of bands <5 m long, <10 cm thick, offset <10 cm	N/A	
Tondi et al., 2016	1) Majella anticline, Central Italy; 2) Favignana, Sicily, Italy	1) Orfento Fm; 2) Lower Pleistocene grainstones	1) Dominant microporosity; 2) Dominant large intergranular pores	1) 31-32; 2) 45-50	Compactive shear bands	1) Offset 10-90 cm; 2) Offset 10-200 cm, 0.1-1 m thick, 8-100 m long	N/A	Particulate flow → PS → Cataclasis
Wennberg et al., 2013	Shetland Group of the Oseberg field, North Sea, Norway	Danian chalk	Mostly comprises of coccoliths, grain-size 2-10 µm	30-40	Compactive shear bands	0.05-0.5 mm thick	Y	Closer packing of coccolith grains, no fragmentation of grains
Zambrano et al., 2017	Favignana Island and San Vito Lo Capo Peninsula, Sicily, and the Abruzzo Region, Maiella Mt., Italy	Early Pleistocene: 1) San Vito Lo Capo Grainstone; 2) Favignana Island Grainstone; (Campanian to Maastrichtian: 3) Orfento Fm. Grainstone	1) Consists of fragments of carbonates, marls and shales with 0.05-1.0 mm diameters. Matrix is made up of bladed and sparry calcite cement; 2) Consist of bioclasts (i.e., Vermetus, Serpula, bivalves, echinoids, red algae and corals) ranging in size from sub-mm to cm. Cement is limited to the grain contacts, around echinoids, or within intragranular pores; 3) Composed of fragments of rudists	1-2) 25-30; 3) 15-32	Compactive shear bands (single or clustered)		Y	1) Compaction, cataclasis, channelized solution-enlarged stylolites; 2) Dissolution and cementation; 3) Cementation
This study	Isle of Thanet, Kent, UK	Upper Cretaceous chalk	Mostly composed of micritic matrix with around 15% of bioclasts such as foraminifera. Average grain diameter 1.25 µm. Pore-throat diameter 0.3-0.7 µm	<45	Compactive shear bands	Single bands <1mm thick, however, they typically form up to a m-scale anastomosing swarms	Y	Pore collapse (foraminifera), closer packing of grains
This study	San Vito lo Capo, Sicily, Italy	Lower Pleistocene grainstones	Mostly composed of peloids, algae, vermetus, foraminifera (millionids, fusulinids), serpula, corals, lamellibranches and echinoids. Average grain diameter 185 µm. Pore-throat diameter 0.4-12 µm	40-47	Dilation bands	<4 cm thick, <15 m long	Y	Cementation, dissolution of peloids
This study	Favignana, Sicily, Italy	Lower Pleistocene grainstones	Mostly composed of peloids, algae, vermetus, foraminifera (millionids, fusulinids), serpula, corals, lamellibranches and echinoids. Average grain diameter 236 µm. Pore-throat diameter 0.12-12 µm	52	1) Single compactive shear bands; 2) Clustered compactive shear bands	1) <5 cm thick, may be >60 m long, but generally less; 2) <70 cm thick, >50 m long	Y	1) Low-stress cataclasis/disintegration of peloids → neomorphism of loose peloids → dissolution of scarce grains; 2) High-stress cataclasis → dissolution of scarce grains
This study	Gargano promontory, Italy	Gravina calcarenite	Mostly composed of lamellibranches, gastropods, sea urchins, bryozoans, algae. Average grain diameter 126 µm. Peak-throat diameters 2.68, 7.2 µm	38	Dilation bands	2-3.5 cm thick, may be >30 m long, but generally less	Y	Cementation
This study	Rhodes, Greece	Cape Arkhangelos calcarenite	Mostly composed of peloids, benthic forams, echinoids, serpulids and red algae. Average grain diameter 138 µm. Peak-throat diameter 0.9-9 µm	43	1) Single compactive shear bands; 2) Clustered compactive shear bands	1) <2-4 cm thick; 2) <60 cm thick, >50 m long	Y	1) Low-stress cataclasis/disintegration of peloids; 2) High-stress cataclasis
LAB-INDUCED DEFORMATION BANDS								
Arroyo et al, 2005		1) Gravina calcarenite 2) Artificial conchiliades (shells cemented with lime and water	1) Bioclasts cemented with calcite 2) Average shell size is 7 mm		Compaction bands			1) N/A 2) Shell breakage (average shell size is 3 mm)
Baud et al., 2017	Hummel quarry, St. Margarethen/Burgenland, Austria	Leitha limestone – bioclastic grainstone of	Mostly composed of corallinean algae, bryozoans, foraminifers, bivalve and gastropod fragments, and echinoid debris. Average grain diameter is 360-480 µm,	1) 31 2) 21	1) Diffuse compaction band 2) Compactive shear band			1) Hertzian fractures emanating from bioclast contacts; intense grain crushing and pore collapse; distributed cataclastic flow;

		Middle Miocene age	porosity mostly consists of macropores, which are 30-500 μm in diameter, pore-throat diameters are $>50 \mu\text{m}$					2) Propagation and linkage of pore-emanated cracks, localized cataclasis and fracturing of neighbouring grains. Mechanical twinning of cement overgrowth occurred in both types of DBs
Baud et al., 2009	1) Majella anticline, Central Italy; 2) Saint-Maximin limestone	1) 2) Saint-Maximin limestone	Pore size 1) c.16.2 μm ; 2) c.140 μm	1) 30; 2) 37	Compactive shear bands			Grain crushing, microcracking (mostly from grain contacts)
Baxevanis et al., 2006		Tuffeau de Maastricht			1) Dilatant shear bands in brittle faulting regime; 2) Compactive shear bands & compaction bands in transitional regime between brittle faulting and cataclastic flow			Grain crushing and pore collapse
Brantut et al., 2014	South England	Purbeck limestone	It comprises peloids (size c.100-500 μm), microcrystals of calcite surrounded by sparry calcite crystals (typically $>100\mu\text{m}$). Quartz occurs as polycrystalline nodules (20% of the rock)	13.8	Conjugate shear bands.			Twinning and thin, straight, intragranular fracturing of large calcite crystals; tortuous intergranular cracking within peloids; most cracks in the cement terminate at the interface with peloids
Cilona et al., 2012	Majella anticline, Central Italy	Orfento Fm		<32	1) Compaction bands; 2) Compactive shear bands	$<0.5 \text{ mm}$ thick		1) Particulate flow; 2) Hertzian cracks & mechanical twinning \rightarrow comminution, crack growth & linkage \rightarrow wing cracks & cataclasis, shearing of cracks
Cilona et al., 2014	Majella anticline, Central Italy	Bolognano Fm		<32	Compactive shear bands	$<3 \text{ mm}$ thick		Grain crushing, mechanical twinning. Forms within layers of better grain sorting, larger pores, richer in bryozoans
Ji et al., 2014	Madonna delle Mazze quarry, Apennines, Central Italy	Majella limestone	Half of bulk rock volume is made up of allochems (mostly rudist fragments), and half of bladed sparry calcite cement and microspherules of silica cement	32.6	Increasing confinement: 1) planar shear band \rightarrow 2) curvilinear band \rightarrow 3) diffuse multiplicity of bands \rightarrow 4) delocalized cataclastic flow			
Tarokh et al., 2017	Mons basin, Belgium	Chalk		43-45	Compaction bands			Grain fracture and pore collapse
Vajdova et al., 2004		1) Indiana limestone; 2) Tavel limestone	Grain-size 1) c.300 μm ; 2) c.5 μm	1)14.6-20; 2)9.5-11.3	Shear enhanced compaction			Mechanical twinning, dislocation slip, cataclasis
Vajdova et al., 2012		1) Indiana limestone; 2) Majella limestone	1) Grain-size 5-300 μm , mostly skeletal grains, ooids, peloids; 2) Grain-size 50-400 μm , mostly rudist shells	1) 14-16; 2) 30	Shear enhanced compaction			Twinning, microcracking, pore collapse, cataclasis. In Indiana limestone high porosity layer that outlines allochems attracts microcracks
Vajdova et al., 2010		Tavel limestone	Sparry grains ($>10 \mu\text{m}$ in size) embedded in a microcrystalline matrix. Mostly microporosity, few larger pores	10-14	Shear enhanced compaction			Cataclasis, twinning of sparry grains. Microcracks initiate as pore-emanated cracks from micropores¯opores alike; macropores drive the crack propagation leading to crack coalescence

More microstructural studies are needed to better understand the parameters controlling deformation and/or diagenetic mechanism(s) acting during and following deformation of porous carbonate rocks. Moreover, understanding how these different deformation modes may affect permeability is important in predicting fluid flow in porous deformed carbonate reservoirs. Therefore, during this study, deformation bands were investigated from five locations across Europe: Isle of Thanet, Kent, United Kingdom; San Vito lo Capo peninsula and Favignana Island in Sicily, Italy; Gargano promontory, Italy; and Rhodes, Greece. The lithofacies within these localities vary from micritic chalk to peloidal or peloid-free grainstones; their porosities ranging between 38 and 52%. A broad spectrum of deformed lithofacies was studied to better understand the deformation band evolution and their controlling parameters. To achieve that, the bands were analysed at the macro- and micro-scale, thus the study includes observations of the deformed outcrops in terms of architecture of the deformation bands, and their basic dimensional parameters, such as length, thickness and, where applicable, displacement. The microstructures were analysed using optical and scanning electron microscopy (SEM), and 2-D microstructural mapping was conducted to provide quantitative analysis of the grains within the deformed and undeformed rock. Lastly, petrophysical property analysis was undertaken on the samples to investigate how deformation bands are likely to impact fluid flow.

4.2 Geological setting

4.2.1 Isle of Thanet

Pegwell Bay and Dumpton Bay are located in the SE of England on the coast of the Isle of Thanet (**Figure 4-1b**). The Isle of Thanet consists of a shallow monocline of Upper Cretaceous Chalk. It formed by initiation of a forced fold by draping and differential compaction of the chalk over a pre-existing basement fault scarp (Ameen, 1995). The monocline was deformed in two successive extensional stress fields with a minimum stress first E-W, and later NE-SW during late Cretaceous and Tertiary inversion (e.g., Bergerat and Vandycke, 1994; Vandycke, 2002).

Kennedy and Garrison (1975) suggested that the chalk cliffs were buried to a maximum of 300 m. However, porosity–depth trends for normally compacted chalk from the North Sea (Mallon and Swarbrick, 2002) suggest a maximum burial depth of around 500 m (Welch et al., 2015).

4.2.2 San Vito lo Capo and Favignana

North-West Sicily (**Figure 4-1c & d**) is part of the emerged western edge of the Sicilian-Maghrebian fold-and-thrust belt, and is characterised by stacking of SE-verging overthrust tectonic units in the Middle-Upper Miocene. Strike-slip and normal faults formed during the Upper Pliocene and the Lower Pleistocene; whereas brittle deformation corresponding to a relatively high-rate of uplift took place during the Middle and Late Pleistocene (e.g., Catalano et al., 1985). Studied deformation bands form a network comprised of high-angle structures oriented either W-E or NW-SE. The latter is parallel to the current regional stress field, which shows a principal horizontal compression oriented in the NW-SE direction (e.g., Giunta et al., 2004).

The studied outcrops are within bioclastic grainstones of Upper Pliocene-Lower Pleistocene in age. Their units in both Favignana (**Figure 4-1c**) and San Vito lo Capo (**Figure 4-1d**) have a thickness of around 10-60 m, and were buried to a maximum of 50 m depth (Abate et al., 1997).

4.2.3 Gargano promontory

Tectonic structures of the Gargano promontory (**Figure 4-1f**) are mostly pronounced by the Mattinata Fault System (MAFS). Chilovi et al. (2000) suggested that two kinematic episodes occurred related to the MAFS: first left-lateral motion started in Late Miocene-Early Pliocene, and second right-lateral motion, causing cumulative displacement of more than 15 km, started in Late Pliocene. The peninsula is cross-cut by several E-W, NE-SW and NW-SE trending steep to sub-vertical normal and strike-slip faults. Tondi et al. (2005) documented geomorphic and structural features indicating dextral shear as the most recent kinematic motion in the area.

The studied outcrops are within the Gravina calcarenite succession, which corresponds to sedimentation in a shallow neritic environment under a subsidence regime, and forms a 10-30 m thick unit (Casolari et al., 2000), which has been buried to >350-400 m depth (Tropeano and Sabato, 2000).

4.2.4 Rhodes

The Aegean Sea started to collapse due to Arabian-Eurasian plate collision during the Pliocene, and Rhodes was then exposed to tectonics controlled by sinistral strike-slip faults because of an increasing curvature of the plate boundary (ten Veen et al., 2002; **Figure 4-1e**). Moreover, Rhodes underwent

an anti-clockwise rotation phase after 1.8 Ma, and some significant vertical motions, which are still active today (Duermeijer et al., 2000).

The protolith of the studied deformed outcrops is the Cape Arkangelos calcarenite formation. It was deposited in Rhodes during a major forced regression and forms large asymptotic clinoforms, the vertical thickness of which is 20–30 m (Hanken et al., 1996). The total sea-level fall is at least 520 m, given that the lowermost visible part of the formation is situated at present-day sea level (Cornée et al., 2006).

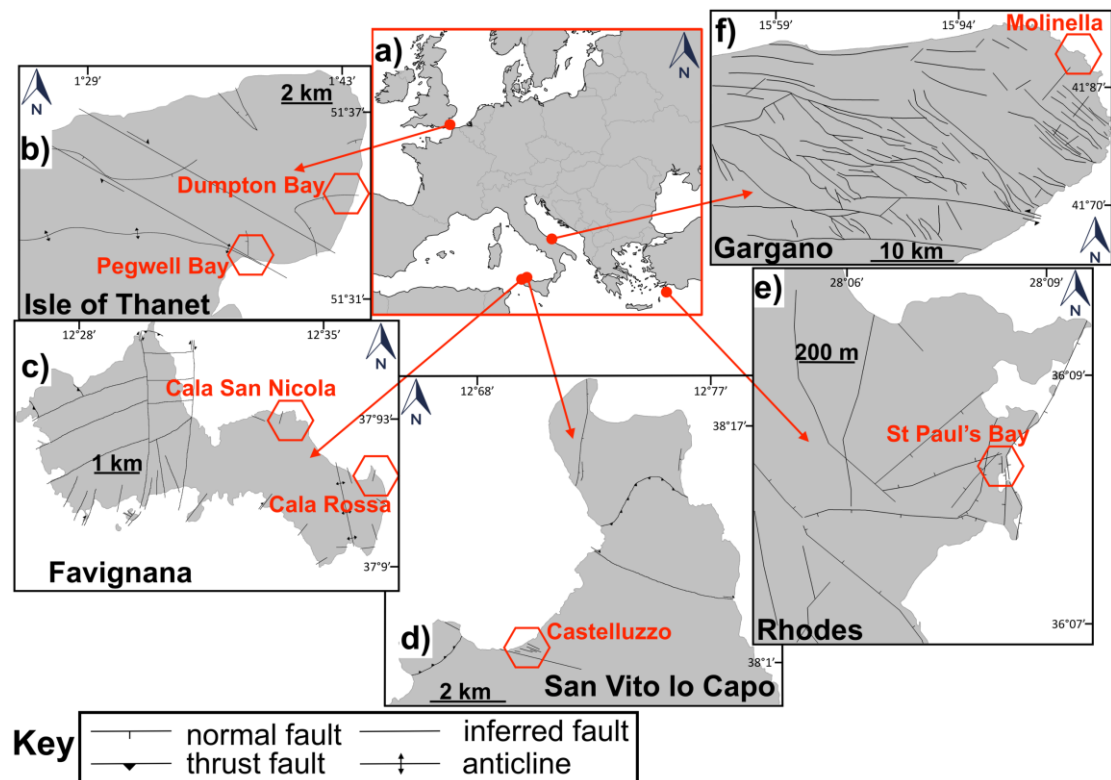


Figure 4-1 Location (a) and local tectonic maps (b-f) of the studied areas. b) Isle of Thanet map modified after Ameen (1995); c) Favignana island map modified after Tondi et al. (2012); d) San Vito lo Capo peninsula map modified after Tondi et al. (2006b) and Todaro et al. (2012); e) Lindos area map in Rhodes modified after Hanken et al. (1996); and f) Gargano promontory map modified after Brankman and Aydin (2004) and Castiglioni and Sauro (2016). The studied areas are marked with a red hexagon.

4.3 Methodology

4.3.1 Sampling

A total of 41 representative bulk samples containing deformation bands (c.30 x 20 x 20 cm in size) were collected throughout the studied locations. The number of samples collected at each location varied depending on deformation band variation in thickness and architecture. Samples were collected from both single and clustered deformation bands, and two representative host samples were taken from each location.

4.3.2 Macrostructural analysis

In each location, the thickness of the deformation bands was measured along their strike at regular intervals of c.1 m, where the exposure was accessible. Deformation bands in Isle of Thanet are very thin and all below 1 mm in thickness, but form very dense arrays throughout the outcrop, thus their mean area (the area taken by deformation bands/the total area of the outcrop) was calculated from the line drawings of the outcrop. The deformation bands were classified as “single” if they formed as individual bands and “clustered” if formed as several closely spaced individual bands (e.g., Fossen and Hesthammer, 1997), where distance between the individual bands is less than a few cm and typically within the mm-length range. Note that these deformation bands have no apparent slip surface thus deformation mode during which they were formed will be referred to as “banding” as opposed to “faulting” (Tondi et al., 2012).

4.3.3 Microstructural analysis

4.3.3.1 Optical microscopy

Small blocks were cut from all the samples at an orientation perpendicular to the deformation band for the deformed samples, and perpendicular to the bedding for the undeformed samples. Blue-dyed epoxy-impregnated polished thin sections were prepared for the microstructural analysis of all samples except chalk, for which SEM was used because the grains within its matrix are below the resolution of optical microscopy. In total, 113 thin sections were made from deformation bands, and 25 from the host rocks. For microstructural mapping, the most representative thin section was chosen of each deformation band type and undeformed rock for every locality, which would show the most common textures for that particular band and lithofacies type. Over a hundred images were taken for each thin section manually at a magnification of 4x using an optical microscope at a resolution of 0.688 pixels per μm with a pixel size of 1.45 μm . The images were stitched in Image Composite Editor to make an image covering 20 x 10 mm area of each thin section. These optical images were used to make a microstructural map by manually outlining the grains, using the photo editor software GIMP (**Figure 4-2 & Figure 4-3**). Processed images were imported into the image analysis software ImageJ and the Lazy Whatever Map macro was used for particle analysis to determine the grain sizes before and after deformation and to quantify the amount of cataclasis (Heilbronner and Barrett, 2013). The upper limit of the long axis of the mapped grains is 10 μm . The data were plotted as grain area (mm^2) versus cumulative frequency and count number. The maps were also used for rock composition analysis (%), as different

colours were used to distinguish different types of grains (skeletal grains, peloids), cement (interparticle, moldic, encrusting, syntaxial), pores (interparticle, moldic) and matrix (loose, neomorphosed) (Figure 4-2 & Figure 4-3). “Minus-cement” porosity was measured on 6 thin sections of cemented deformation bands and compared to the results derived from 4 thin sections of the host rock.

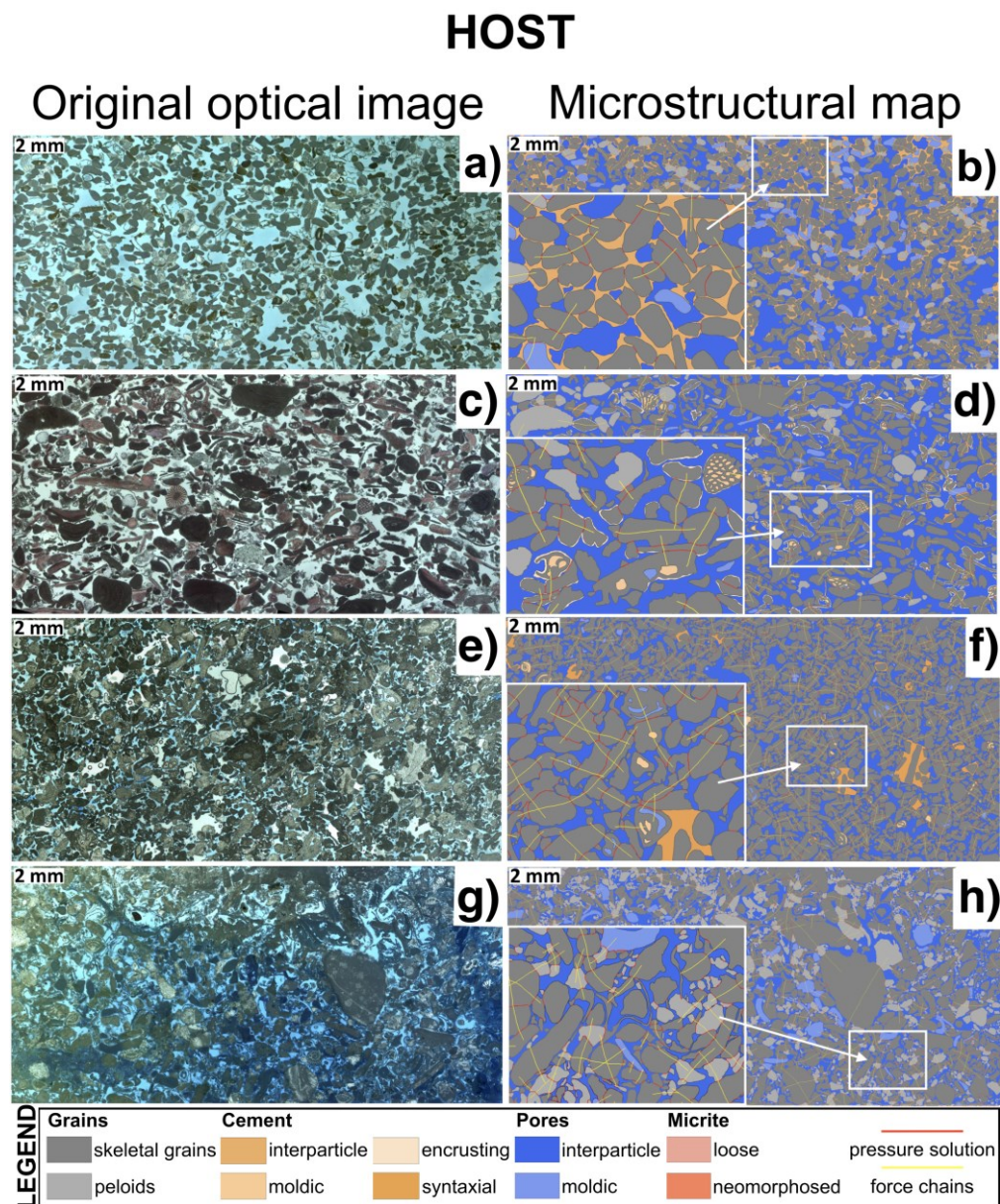


Figure 4-2 Original optical images and their interpreted microstructural maps of the undeformed rocks from a-b) San Vito lo Capo, c-d) Favignana, e-f) Gargano, and g-h) Rhodes. Also note pressure solution (red) and force chain trajectories (yellow).

DEFORMATION BAND

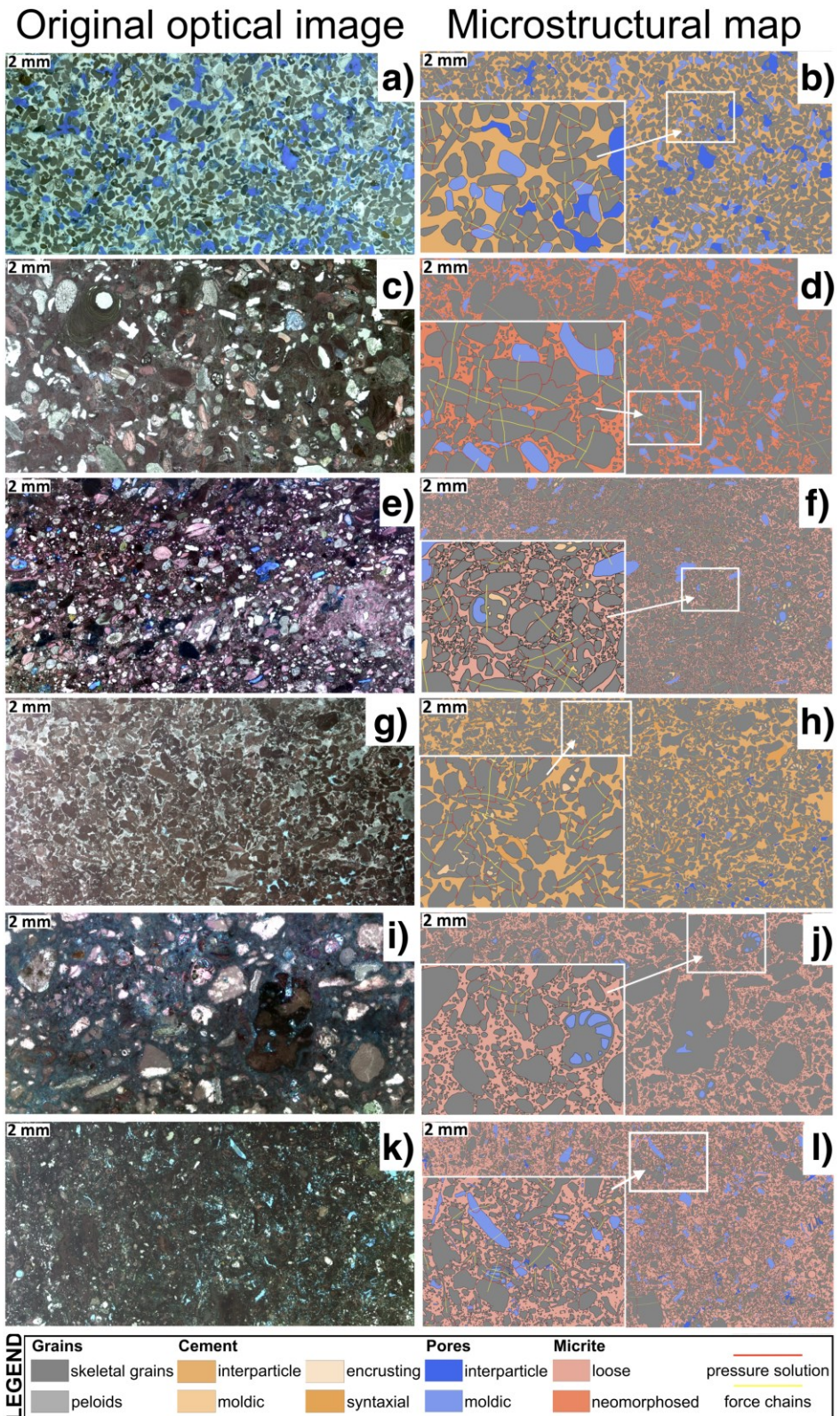


Figure 4-3. Original optical images and their interpreted microstructural maps of single deformation bands from a-b) San Vito lo Capo, c-d) Favignana, g-h) Gargano, and i-j) Rhodes; and clustered deformation bands from e-f) Favignana, and k-l) Rhodes. Also note pressure solution (red) and force chain trajectories (yellow).

Pressure solution surfaces were traced along the sutured grain contacts no shorter than 15 μm , and force chains were then constructed for a minimum of three contacting grains, perpendicular to the pressure solution surfaces (**Figure 4-2 - Figure 4-4**). Force chains are a 2-D proxy for the orientation of the load-bearing framework in the 3-D granular aggregate, thus indicating the direction of maximum principal stress (Eichhubl et al., 2010). The angle of the force chains was measured using the ImageJ software with respect to the strike of the deformation bands (**Figure 4-4**) and plotted as rose diagrams to highlight the frequency distribution of azimuths of force chains. Azimuthal bins were organised into 10-degree increments, and the radial distance from the centre of the graph shows the percentage of force chains that indicate a given direction.

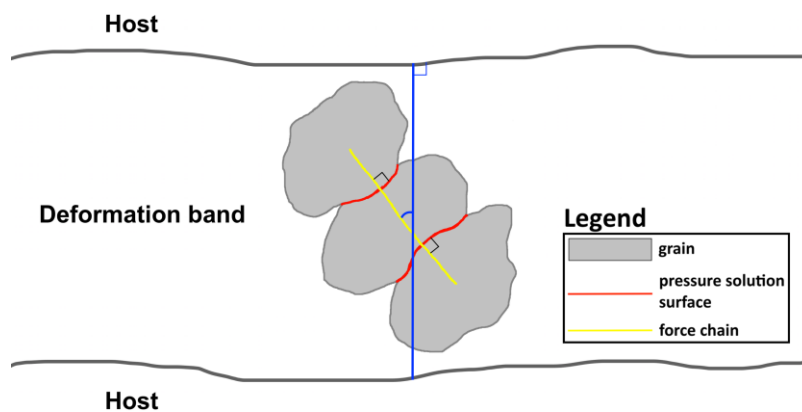


Figure 4-4 Schematic diagram defining a force chain (yellow), which is a trajectory drawn perpendicular to a minimum of three sutured grain contacts (red). The angle between a force chain and the strike of the deformation band is marked in blue.

4.3.3.2 Scanning Electron Microscopy (SEM)

Optical microscopy is good for quantifying large pores, which can be impregnated with blue dyed epoxy resin (Grove and Jerram, 2011).

However, it is not reliable for microporosity studies, because resin does not completely fill the smaller pores. Therefore, SEM was used for porosity

evaluation, which is able to capture all pore sizes (e.g., Haines et al., 2015). A FEI Quanta 650 FEG-ESEM environmental SEM with Oxford Instruments INCA 350 EDX system 80mm X-Max SDD detector was used for backscattered imaging (BSE) at a resolution of 0.52 pixels per μm with a pixel size of 1.92 μm . Tescan VEGA3 XM was used for the whole thin-section BSE scanning, obtained at a resolution of 81.3 pixels per mm, with a pixel size of 12.3 μm . Images were saved in 8-bit TIFF format, which allocates each pixel to 1 of 256 levels on the grey-scale (0 corresponds to black, and 255 – to white). Whole thin-section BSE scans were used for dual porosity evaluation (**Figure 4-5**). First, the scans were cropped to a rectangle of 1860 x 1260 pixels (20 x 15 mm) to remove edge artefacts appearing in the corners of the scans. Second, the scans were characterized by bimodal grayscale histograms, where two thresholds were determined using Otsu's thresholding method (Otsu, 1979) and dual porosity model (Ji et al., 2012) that divided the histogram into three phases: resolvable pore space, microporosity, which is at scales below the resolution of the scan, and the solid region. Studied carbonates are mostly composed of calcite (>99%), thus they are considered as monomineral, and hence their atomic number as constant. Taking that into consideration, the local grey-levels are proportional to the local density, and hence to porosity. However, considering the age of these rocks, there is a possibility that they also contain aragonite, which would slightly change the density of the minerals (from c.2.71 g/cm^3 for the calcite to c.2.94 g/cm^3 for the aragonite). It should be noted that the derived porosity fractions are limited by the size of the scans, thus larger pores or vugs may have been underestimated. Pore connectivity was determined by

visual inspection of 2-D SEM images by deciphering larger pore connectivity, however, the conclusion may not be brought through to the 3-D pore space.

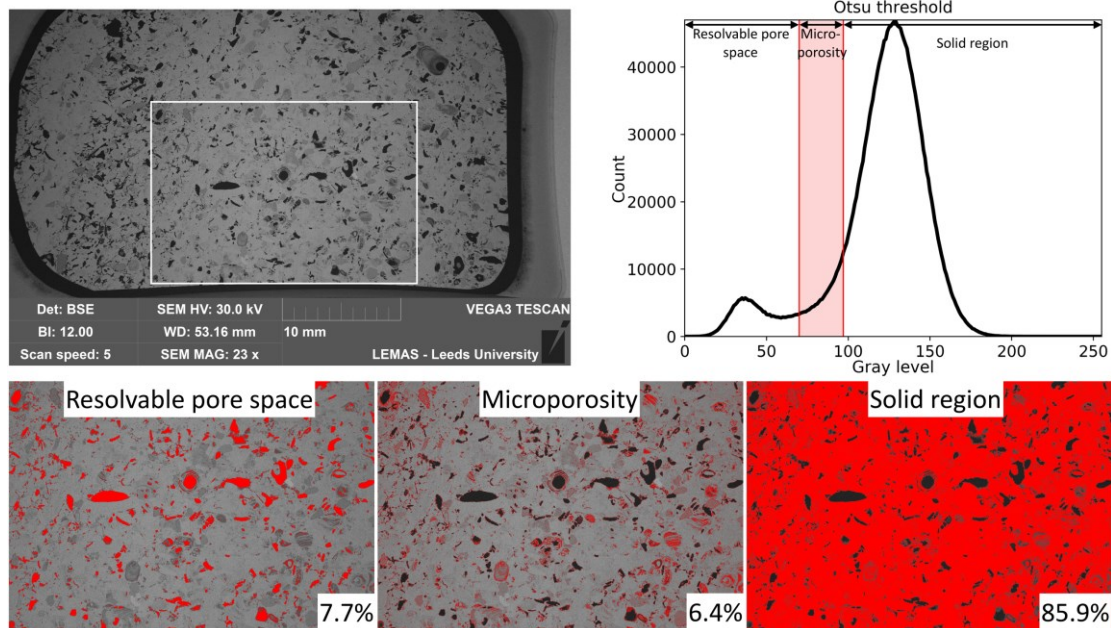


Figure 4-5 An example of dual porosity evaluation using Otsu's thresholding method on a BSE scan. The graph shows two thresholds dividing the histogram into three regions: resolvable pore space, microporosity and the solid region. The images at the bottom illustrate these regions (in red) and show at what percentage they compose the sample.

4.3.4 Petrophysical properties

Bulk porosity of the samples was measured as explained in **Section 3.5.1**.

All the core plugs were scanned using a GE Bravo medical-style CT scanner.

The scans showed that some of the core plugs containing deformation bands also consist of a host rock. For these samples, porosity of the bands was determined from the CT-scans (**Figure 4-6**). The Hounsfield units (HU) at each pixel on a transect was recorded so that density and hence porosity distribution along the sample could be calculated (e.g., Davis et al., 1992).

Porosity was estimated using the measured (HU) number of pure calcite (3071) within a cemented fracture.

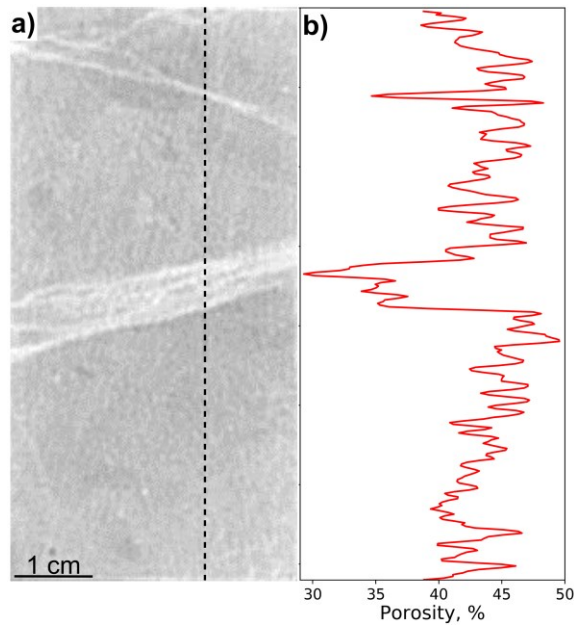


Figure 4-6 a) CT-scan of a core plug from Pegwell Bay containing deformation bands. b) Porosity values obtained from a 1-D vertical transect through the core (dotted line on the CT-scan). Note that the light-coloured deformation hands have a lower porosity than the undeformed chalk.

Permeability measurements of the core plugs were carried out as described in **Section 3.5.2**. For the plugs containing deformation bands and a proportion of a host rock, true permeability of the bands was deconvolved from the absolute permeability using a method based on work by Cardwell and Parsons (1945).

Pore throat sizes of the host rocks and the deformation bands were found as explained in **Section 3.5.3**.

4.4 Results

4.4.1 Host rock characteristics

4.4.1.1 Isle of Thanet

The Upper Cretaceous chalk in the Isle of Thanet has porosity ranging from 39 to 45%. The chalk is composed predominantly of a micritic matrix with around 15% of bioclasts such as planktonic foraminifera (**Figure 4-7a**). These

bioclasts have intragranular porosity. Average grain size of this chalk is c.2 μm .

4.4.1.2 San Vito lo Capo and Favignana

Host lithofacies in San Vito lo Capo and Favignana are bioclastic grainstones. They contain skeletal grains of algae, vermetus, foraminifera (millionids, fusulinids), serpula, corals, lamellibranches and echinoids (Tondi et al., 2012). The other grains are peloids, which comprise up to a half of the overall grains (**Figure 4-7b**). Elongate sutured grain contacts are common (**Figure 4-7c**). Syntaxial overgrowth cement is present on the plates and spines of echinoids, whereas other skeletal grains are encrusted by dog-tooth cement (**Figure 4-7g**). Grains within the San Vito lo Capo host rock are also partially cemented by granular calcite. Most of the porosity is intergranular, but a small percentage of moldic porosity also exists due to preserved micrite envelopes, where grains have been dissolved, or within the chambers of bioclasts. Average porosity is around 43% and 52% for the San Vito lo Capo and Favignana grainstones, respectively.

4.4.1.3 Gargano promontory

Host lithofacies in Gargano promontory are a bioclastic grainstone, composed of fossils such as bryozoans, red algae, gastropods, serpulids, corals, crinoid plates, echinoderms, bivalves and benthic foraminifera (**Figure 4-7d**). Most of the porosity is intergranular, and a majority of the moldic porosity is filled with cement. Syntaxial overgrowth cement is present around plates and spines of echinoderm fragments (**Figure 4-7f**). Pressure solution

textures at grain contacts are well developed. Arithmetic mean porosity is around 38%.

4.4.1.4 Rhodes

Cape Arkhangelos calcarenite in Rhodes is a bioclastic grainstone, composed of skeletal grains such as benthic foraminifera, echinoids, scleractinians, serpulids, red algae, gastropods, bivalves, scaphopods, polyplacophorans and brachiopods (**Figure 4-7e**). It also contains a high percentage of peloids, >50% of which have been broken down and in places fills the interparticle pore space as a micritic matrix. Porosity, which averages around 43%, is mostly intergranular (c.21%), however, molds also make up a high percentage of porosity due to preserved micrite envelopes (c.17%).

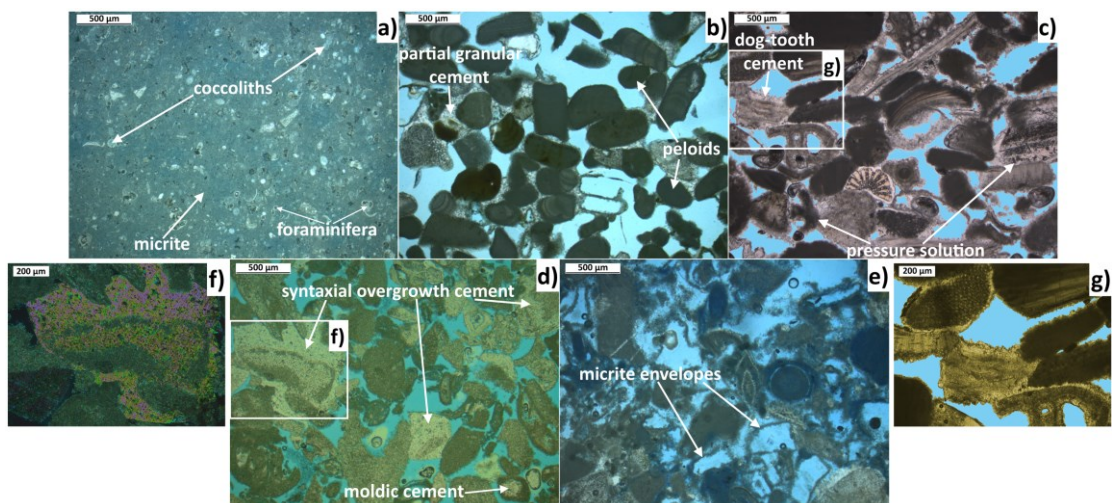


Figure 4-7 Micrographs of the protoliths from all studied locations: a) Isle of Thanet, b) San Vito lo Capo, c) Favignana, d) Gargano, and e) Rhodes. The pore space is highlighted by blue epoxy dye, and the most prominent characteristics are shown with the arrows. Micrographs f-g) show the syntaxial overgrowth cement under cross-polarized light and the encrusting dog-tooth cement, respectively.

4.4.2 Deformation band structure

4.4.2.1 *Isle of Thanet*

Deformation bands have the same colour as the undeformed rock, thus they are difficult to identify in most of the cliff sections. However, they can easily be recognised in the cliff on the shore line because they protrude from the rock due to being slightly more resistant to erosion than the undeformed chalk (**Figure 4-8a**). The deformation bands in The Isle of Thanet form parallel and sub-perpendicular to the bedding. The latter are mostly dipping at angle $>55^\circ$ to NE and displace the former by up to c.2 cm. Individual bands are <1 mm in width, however they typically form up to meter-wide anastomosing swarms. The mean area of the deformation bands calculated from the line drawings of the outcrops is c.6.5%. These exposures may be a few metres long, although due to weathering and vegetation it is difficult to assess the continuity of the deformation bands.

4.4.2.2 *San Vito lo Capo and Favignana*

Deformation bands in San Vito lo Capo are sparse and have a NW-SE orientation, which is the same as for the open fractures observed within these outcrops, following at the tips of the deformation bands or going parallel to them. They are highly altered by pedogenic processes, and features such as root structures are common. These bands are relatively curvilinear and may be as long as 15 m, and up to 4 cm thick (**Figure 4-8b**). They show no apparent offset in the field.

Single deformation bands in Favignana may be classified into two groups: the main group oriented WNW-ESE, and discontinuous secondary bands

cross-cutting the first group striking WNW to ESE. The former bands are continuous and relatively straight; they may be longer than 40 m and up to 5 cm thick (**Figure 4-8d**). Clustered deformation bands in Favignana form anastomosing deformation band zones up to 70 cm in width (**Figure 4-8f**). They are oriented in two directions: the dominant, trending N-S, and a cross-cutting group from NW to SE. These deformation bands form continuous zones >50 m in length. Based on available outcrop data, the displaced cross-cutting single bands suggest that the maximum offset is c.5 cm, and the clustered bands may reach a displacement >20 cm.

4.4.2.3 Gargano

The Gravina calcarenite in Gargano is cross-cut by intersecting deformation bands oriented N-S and WSW-ENE, and occur as single bands with thicknesses varying between 2 to 3.5 cm (**Figure 4-8c**). These bands are continuous and are often longer than 30 m. They show no visible shear displacement in the field.

4.4.2.4 Rhodes

Cape Arkhangelos calcarenite in St. Paul's Bay contains continuous clustered deformation band zone oriented in the N-S direction. It is up to 60 cm in width and may be longer than 50 m (**Figure 4-8g**). Cross-cutting single deformation bands are oriented either N-S or NNE-SSW. They are up to 4 cm thick and are found around 10 m radius from the clustered deformation band zone and are absent further away (**Figure 4-8e**). Single deformation bands on Lindos beach form in the same orientations as the ones in St. Paul's Bay, and are 2 to 3 cm in width.

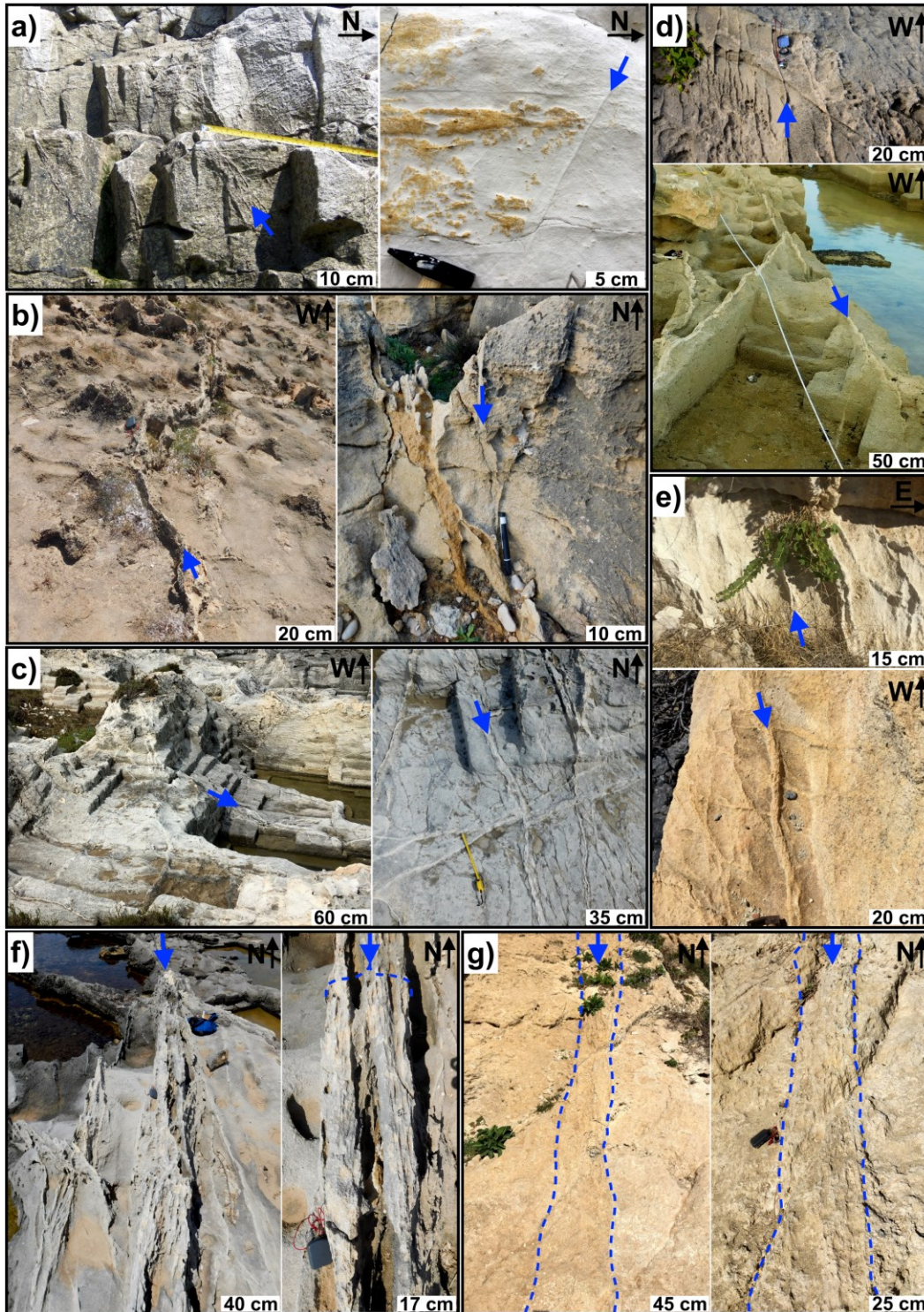


Figure 4-8 Outcrop photographs of the studied single deformation bands from a) Isle of Thanet, b) San Vito lo Capo, c) Gargano, d) Favignana, and e) Rhodes; and clustered bands from f) Favignana, and g) Rhodes. Deformation bands are pointed with the blue arrows, and outlined with blue dotted lines where they are not erecting from the surface and are harder to pinpoint.

4.4.3 Deformation band pore types

4.4.3.1 Porosity

All studied deformation bands show a significant reduction in porosity compared to their parent rock (**Figure 4-9**). Porosity of the deformation bands in the Isle of Thanet is c.30%. Irregularly cemented single deformation bands in San Vito lo Capo have a porosity ranging between 13 and 30%, and the bands in Gargano may have a porosity as low as 4% for the highly cemented parts. Porosity of the single deformation bands in Favignana range between 9 and 26%, whereas those in Rhodes are larger (25-33%). Porosities of the clustered deformation bands in the latter locations are on average lower than that of the single bands: c.17% and c.20%, respectively. These are the measured overall porosity values, which have been subdivided into intergranular macroporosity, moldic porosity and microporosity. The intergranular and moldic porosities were determined from the microstructural maps (**Figure 4-2 & Figure 4-3**), whereas microporosity was estimated from the BSE images (**Figure 4-5**).

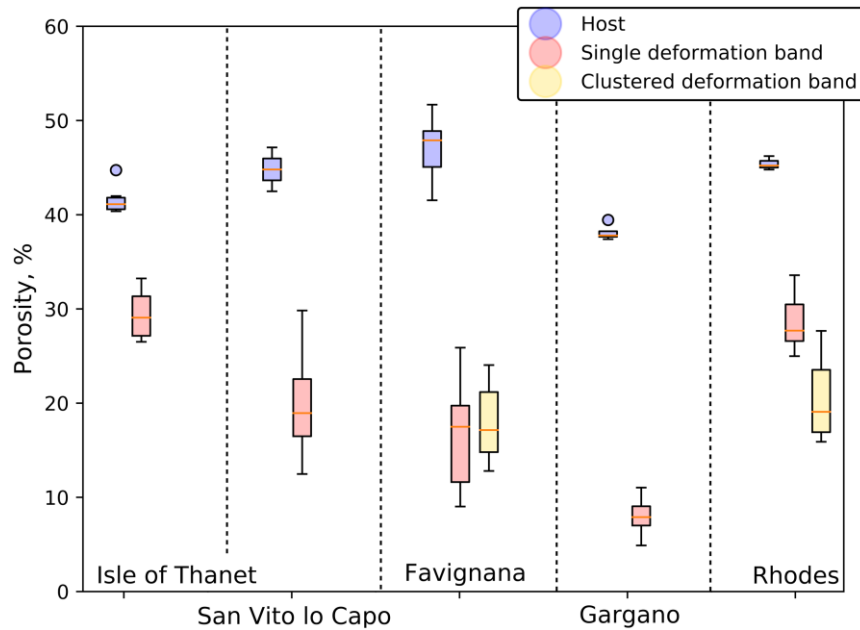


Figure 4-9 Boxplots showing mean and standard deviation values of the porosities (%) of all studied deformation bands (single – red; clustered – yellow) and their parent rocks (blue). The boxes represent interquartile range of the data; bars indicate minimum and maximum values; circles show outliers; and orange lines indicate mean values of the datasets. Number of measured values: host (26); single deformation bands (62), and clustered deformation bands (17).

4.4.3.2 Intergranular macroporosity

Intergranular macroporosity is generally absent within the studied deformation bands (**Figure 4-10**). Interparticle space within the deformation bands in Favignana and Rhodes is filled with micritic matrix and is generally <5% (**Figure 4-10b,c,e,f**), whereas those in San Vito lo Capo and Gargano are partially filled with sparry calcite cement (**Figure 4-10a,d**). Intergranular macroporosity within the San Vito lo Capo bands is very heterogeneous; large parts remain uncemented irregularly throughout the bands, and on average is around 12%. Gargano bands are highly cemented. Both of these cemented bands have a transition zone of increasingly less cemented parts into the uncemented adjacent host rock.

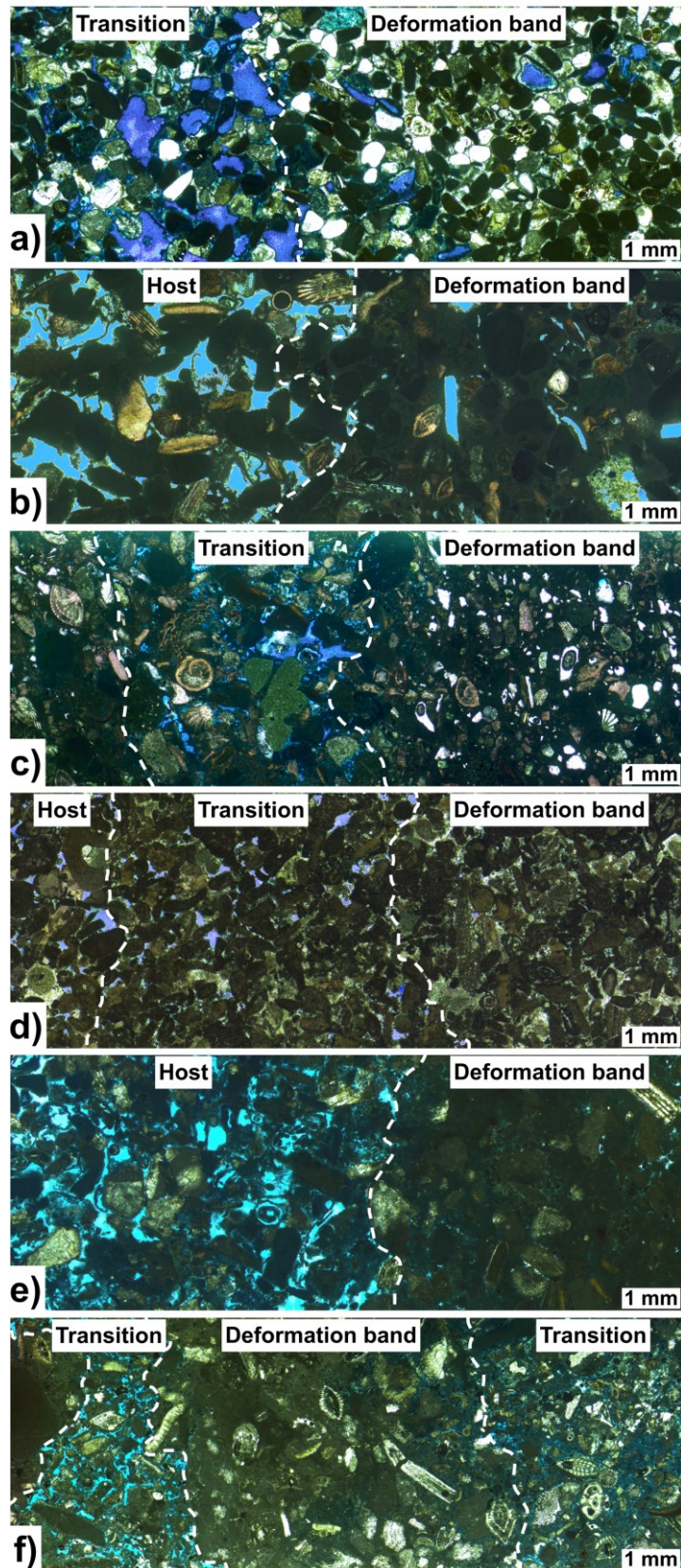


Figure 4-10 Micrographs showing transects across single deformation bands and their host rocks and/or transition zones in a) San Vito lo Capo, b) Favignana, d) Gargano, and e) Rhodes; and clustered deformation bands and transition zones between individual bands in c) Favignana, and f) Rhodes. Deformation bands are outlined with dotted lines. Note porosity in blue.

4.4.3.3 Moldic porosity

Some of the studied deformation bands are highly affected by post-kinematic grain dissolution compared to their undeformed rock. The molds within the bands make up to 20% porosity in San Vito lo Capo compared to c.13% within the host rock, and <18% and <8% in single and clustered bands in Favignana, respectively, compared to c.5% within the parent rock. The molds within the bands in Gargano are filled with sparry calcite cement. The deformation bands in the Isle of Thanet show fewer molds as compared to the undeformed chalk (from c.25 to c.2%) due to collapse of porosity within foraminifera; there is no evidence of post-kinematic dissolution (**Figure 4-11**). The molds within the single bands in Rhodes make up to 16% porosity and c.4% in the clustered bands, compared to c.18% within the parent rock.

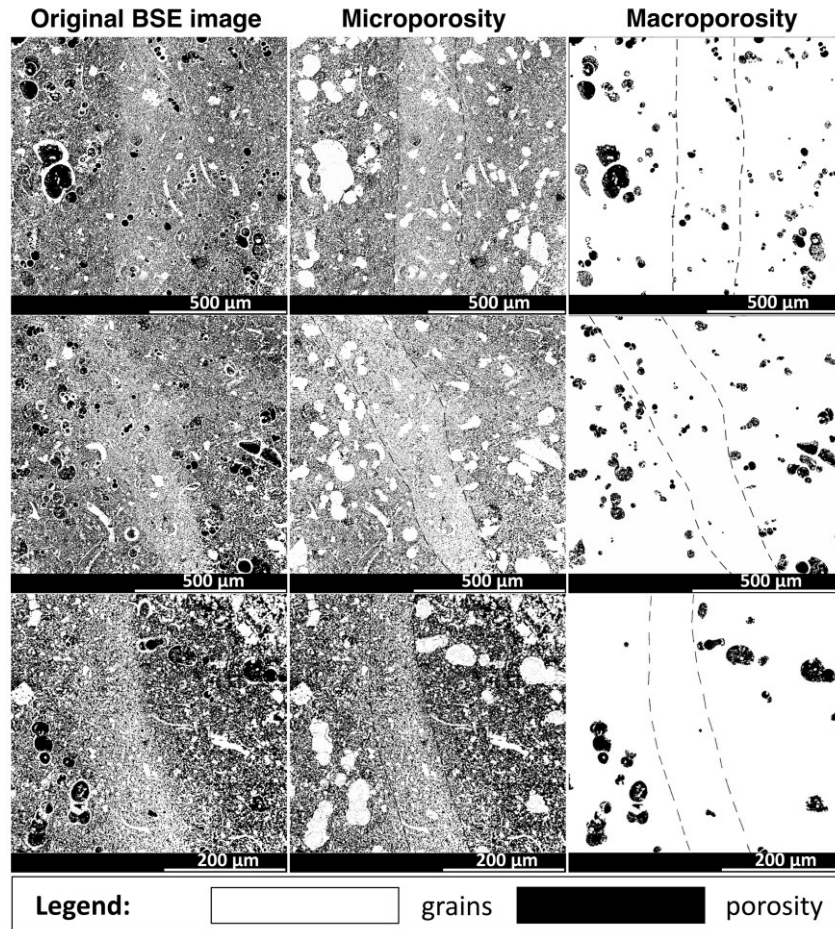


Figure 4-11 Left: original BSE images of the chalk samples from Isle of Thanet containing deformation bands. Centre: maps showing microporosity; right: macroporosity. Note that deformation bands (marked with dashed lines) contain far less intraparticle macroporosity due to collapse of the fossils.

4.4.3.4 Microporosity

Examples of BSE images, used for quantifying matrix microporosity, are represented in **Figure 4-12**. The results show that average microporosity within the Isle of Thanet deformation bands is 32% and it is well-connected (**Figure 4-12a**). Irregular cement filling of the interparticle porosity within the San Vito lo Capo deformation bands shows disconnected intercrystalline microporosity, not reaching more than 9% (**Figure 4-12b**). Matrix (neomorphosed micrite) within single deformation bands in Favignana has a microporosity of <4%, which is disconnected in 2-D, whereas clustered

bands show connected microporosity of <17% within its micritic matrix (**Figure 4-12c & d**, respectively). Disconnected intercrystalline microporosity within the cemented Gargano deformation bands does not exceed 10% (**Figure 4-12e**). Micritic matrix within the Rhodes deformation bands forms a well-connected network of microporosity, which is on average c.22% within the single bands (**Figure 4-12f**), and c.20% within the clustered deformation bands (**Figure 4-12g**). Microporosity also occurs within peloids and echinoderm, algae and bryozoan fossils throughout all the samples.

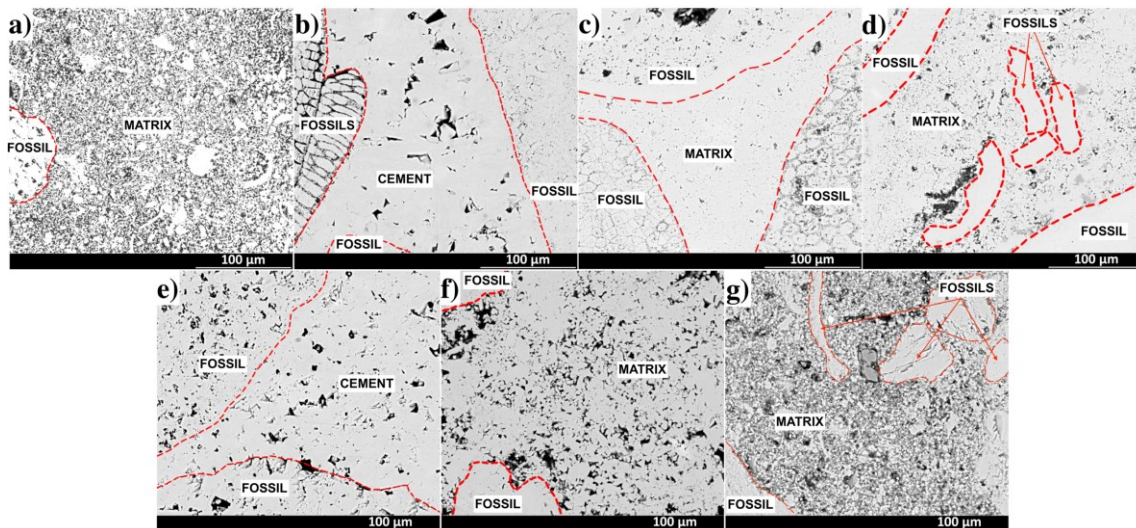


Figure 4-12 BSE images showing matrix/cement of single deformation bands in a) Isle of Thanet, b) San Vito lo Capo, c) Favignana, e) Gargano, f) Rhodes; and clustered deformation bands in d) Favignana, and g) Rhodes. Red dashed lines separate bioclasts from the matrix. Note microporosity in black.

4.4.4 Force chain stress analysis

Rose diagrams presenting the angle of force chains for deformed and undeformed samples are shown in **Figure 4-13**. Although the data is relatively scattered a few trends may be observed. The protolith within San Vito lo Capo show more than 70% of its force chain values falling between 65-85° and 270-315° normal to the bedding, whereas force chains within the single deformation bands show no particular trend (**Figure 4-13a**). The host

rock in Favignana shows the most frequent force chain angles at an interval of 60-75°, whereas both single and clustered deformation bands have most of their values falling perpendicular to the host and between 295 and 345° normal to the strike of the deformation band (**Figure 4-13b**). However, the number of drawn force chain trajectories for a single Favignana band is relatively low compared to the clustered bands (**Figure 4-13b**). Force chain orientations in deformed and undeformed rocks in Gargano look very scattered (**Figure 4-13c**). However, trends can still be seen: for the single deformation bands more values fall between 340-350°, and 40-50°, 300-330° for the host. The host rock in Rhodes shows very scattered force chain angle values, although a peak may be noted at 300-320° (**Figure 4-13d**). The single deformation band has very few values with most frequent between 35-40° and 270-275°, whereas clustered deformation bands have most of their values falling between 0 and 10°, and 40-60° normal to the strike of the deformation band. Furthermore, the number of force chains for the single and clustered bands in Rhodes show a significant difference: 46:369.

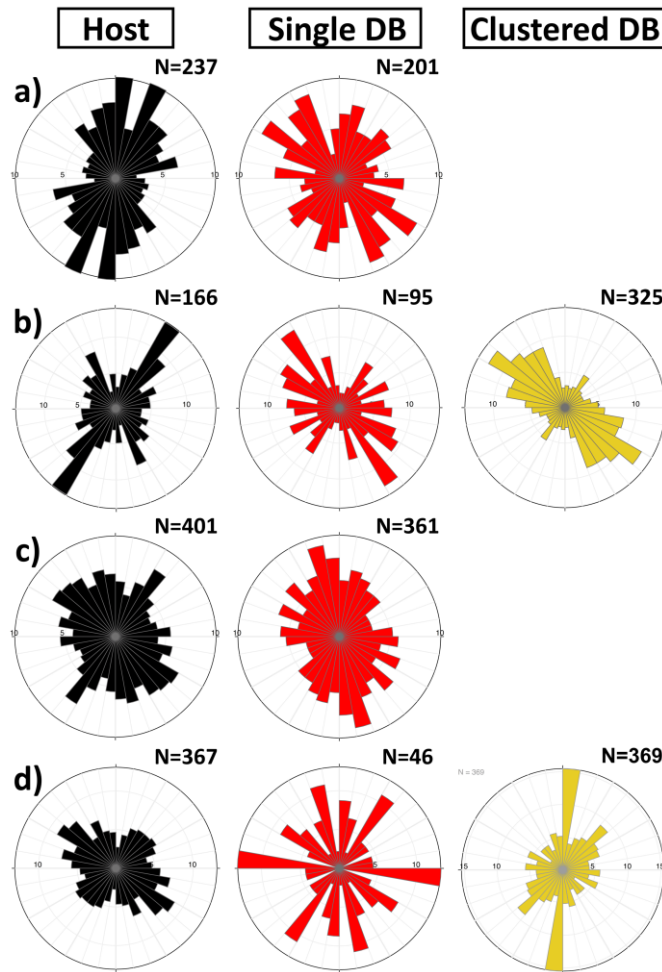


Figure 4-13 Rose diagrams of force chain orientations for the host (black), single (red) and clustered (yellow) deformation bands. Rose diagrams show data for the a) San Vito lo Capo; b) Favignana; c) Gargano, and d) Rhodes samples.

4.4.5 Pore and particle analysis

4.4.5.1 Pore throat sizes

Pore throat diameters from mercury injection capillary pressure (MICP) tests are plotted as incremental intrusion curves in **Figure 4-14**. Pore throat diameters were compared between deformed (red curves - single; black - clustered deformation bands) and undeformed porous carbonates (blue). In general, host rocks have one or two distinct pore throat diameter peaks and higher values than the ones for the deformed samples. Deformation bands in San Vito lo Capo, Favignana and Gargano show a wide range of pore throat

diameters, whereas deformation bands in Isle of Thanet show only a slight variation from the host rock. Clustered deformation bands in Favignana and Rhodes have smaller pore throat diameters than the single ones.

MICP data from Isle of Thanet samples (**Figure 4-14a**) reveal that the host rock and samples containing deformation bands have a single pore size distribution with a peak pore throat sizes between 0.3 and 0.7 μm . Some of the samples containing the deformation bands have slightly smaller pore sizes than the samples without the deformation bands. However, there is a considerable overlap between the pore size distribution of the undeformed chalk and the samples containing the deformation bands.

Pore size distribution curves for the San Vito lo Capo undeformed and deformed samples show a notable pore size reduction due to banding. The pore throat diameter varies between 0.012 and 9 μm for the deformation band, and 0.4 to 12 μm for the surrounding host rock (**Figure 4-14b**).

MICP data from the Favignana samples (**Figure 4-14c**) show a progressing decrease in pore sizes from host to single bands, and from single to clustered deformation bands. Host rock has pore throat sizes varying in their diameter from 0.12 to 12 μm , with peaks at 2.6 and 12 μm ; single bands show pore throat size distribution between 0.026 and 12 μm , with peaks at 0.12, 0.23 and 12 μm (**Figure 4-14c**, red), and clustered bands have pore throat sizes varying between 0.012 and 9 μm , with a peak at 0.12 μm (**Figure 4-14c**, black).

Gargano host pore throat size distribution curve (**Figure 4-14d**) reveals a bimodal porosity with peak pore throat sizes at 2.68 and 7.2 μm . Its

deformed counterpart shows multiple peaks between 0.026 and 22.6 μm , with most of the values falling between 0.1-0.6 μm .

Rhodes samples suggest a dominating single pore throat peak for a host rock as well as single and clustered deformation bands with only a few smaller peaks (**Figure 4-14e**). There is a shift in the main peak pore throat size from 7.5 μm for the host rock to 2.6 μm for the deformation bands. Host rock also shows a peak at 9 μm , which is reduced for the single deformation bands and is non-existent for the clustered deformation bands.

Mercury-injection drainage curves indicate that all studied deformation bands would hold higher hydrocarbon column heights compared to their protoliths (**Figure 4-14f-j**). However, threshold pressures (inflection points on the drainage curves) for the Isle of Thanet samples range between c.200 and 400 psi both for the host rock and the samples containing the deformation bands. Therefore, even though threshold pressures are overall higher for the deformed samples, there is a considerable overlap between the threshold pressures of the undeformed chalk and the samples containing the deformation bands. In all the examples, threshold pressure is higher for the clustered deformation bands compared to the single deformation bands formed within a given lithology (**Figure 4-14h,j**).

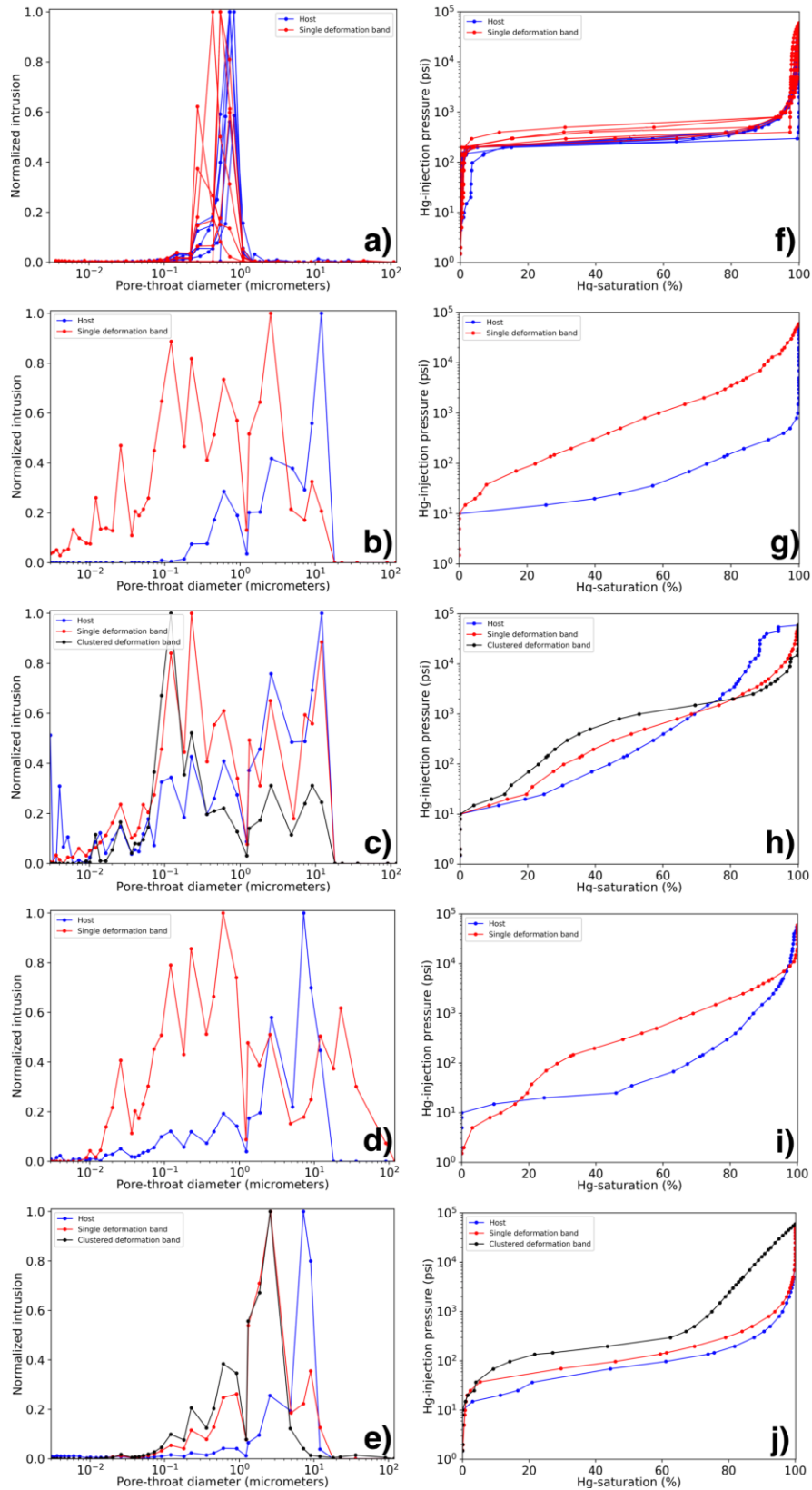


Figure 4-14 Graphs illustrating pore throat size distribution. Left: normalized intrusion pore throat size distribution curves; right: drainage curves for a,f) Isle of Thanet, b,g) San Vito lo Capo, c,h) Favignana, d,i) Gargano, and e,j) Rhodes samples. Blue illustrates undeformed host rock, red and black curves: single and clustered deformation bands, respectively.

4.4.5.2 Grain size

Grain size results are displayed as grain area (mm^2) versus cumulative frequency (**Figure 4-15a-d**) and count number graphs (**Figure 4-15e-h**). The given data reveal that deformation bands in Favignana and Rhodes (**Figure 4-15b,d**) have reduced grain sizes as compared to their undeformed counterparts. The bands in San Vito lo Capo and Gargano (**Figure 4-15a,c**) show very little difference between the deformed and undeformed rocks.

Grain diameter for the Favignana host rock is on average $240\ \mu\text{m}$, compared to $70\ \mu\text{m}$ for the single deformation bands, and $30\ \mu\text{m}$ for the clustered bands. Rhodes host rock shows an average grain diameter around $140\ \mu\text{m}$, compared to $50\ \mu\text{m}$ for the single deformation bands, and $40\ \mu\text{m}$ for the clustered bands. Gargano host rock has grains c. $130\ \mu\text{m}$ in diameter, whereas the deformation bands show values around $100\ \mu\text{m}$. The average grain size within deformation bands at San Vito lo Capo hardly differ from the surrounding host rock (both are around $190\ \mu\text{m}$). Grain-size determination is not accurate for small grains (long axis $<10\ \mu\text{m}$), and hence for the matrix within the samples. Slight variations in grain-size between the deformed and undeformed rocks may occur due to poor sorting of the rocks, particularly within Favignana, Gargano and Rhodes lithologies.

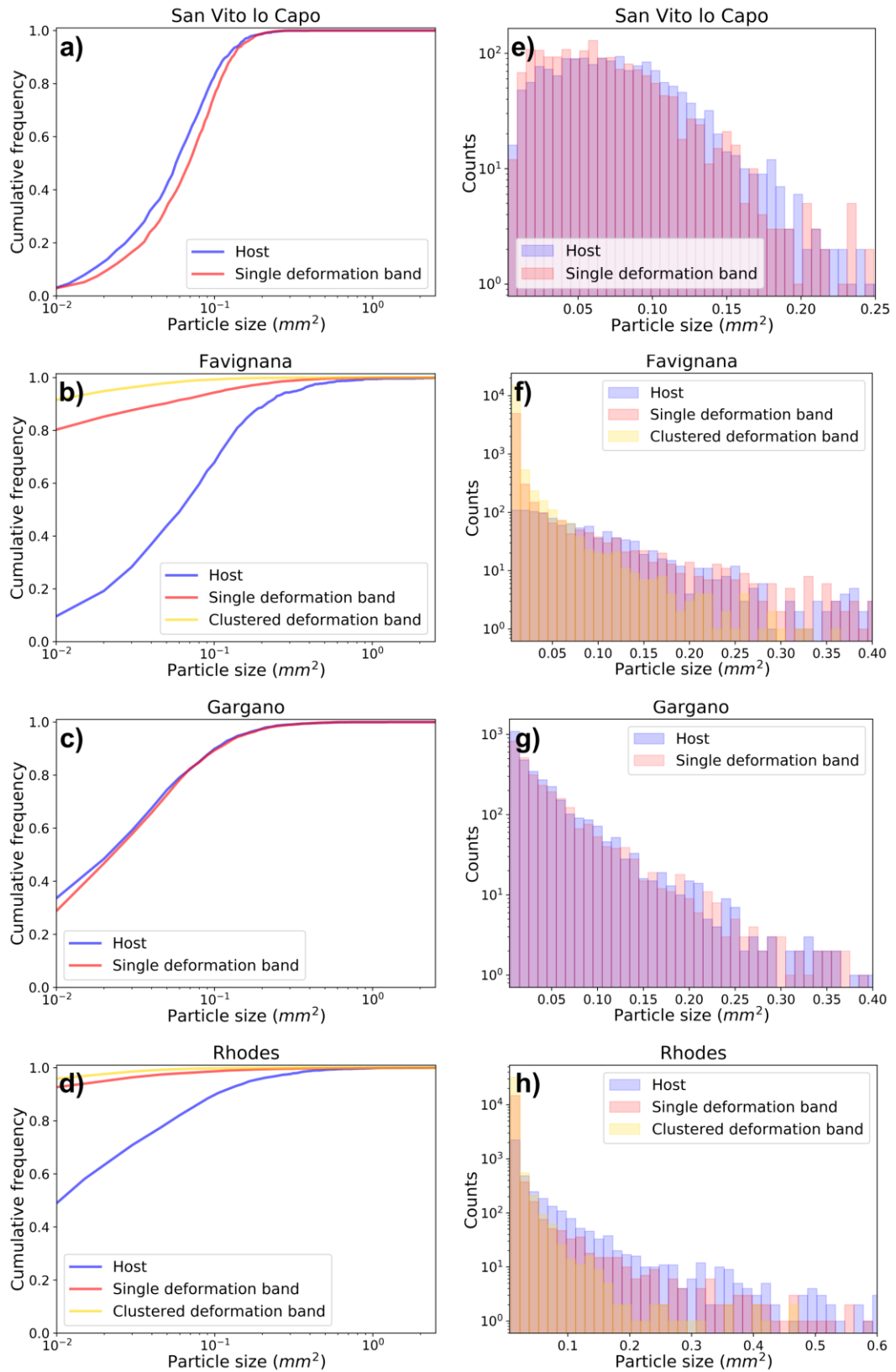


Figure 4-15 Graphs illustrating grain sizes: cumulative frequency (left), and count number graphs (right) for a, e) San Vito lo Capo; b, f) Favignana; c, g) Gargano, and d, h) Rhodes samples. Undeformed sample data is plotted in blue, single and clustered deformation bands – in red and yellow colours, respectively.

4.4.6 Deformation-induced microstructural changes

The microstructure of the undeformed and deformed rock was compared for samples from all 5 locations in a column diagram in **Figure 4-16**, and the main differences are as follows:

- I. Deformation bands in the Isle of Thanet chalk have fragmented foraminifera creating elongated angular clasts with smaller clast size. Microfossils (coccoliths)/micrite remain intact and hence the same size inside and outside the bands (**Figure 4-11**, middle);
- II. Deformation bands in the San Vito lo Capo grainstone show a slight increase (c.2%) in minus-cement porosity, and blocky calcite spar with a drusy mosaic infilling interparticle pore space. Peloids are often absent in deformation bands, instead moldic porosity from dissolved peloids is observed. All other grains remain intact; they show no signs of fracturing/fragmentation or pressure solution at grain contacts compared to the host rock;
- III. Deformation bands in the Favignana grainstone show disintegration of intact peloids and increase in loose or neomorphosed micrite as compared to their undeformed counterparts. The clustered bands show intense cataclasis, forming a high percentage of fragmented, broken angular fossil fragments, which greatly reduces the grain size;
- IV. Deformation bands in the Gargano grainstone contain interparticle and moldic blocky pore-filling cement, which is nearly absent in the undeformed rock. Moreover, they show a slight increase in minus-cement porosity (c.3%) and only a minor reduction in grain size due to fragmentation as compared to their host rock;

V. Single deformation bands in the Rhodes grainstone show the disintegration of intact peloids and increase in loose micrite as compared to their protolith. No differences in microstructures have been identified between the bands in St. Paul’s bay and Lindos beach.

The clustered deformation bands show intense cataclasis, forming a high percentage of broken skeletal grains and micrite filling most of the interparticle pore space.

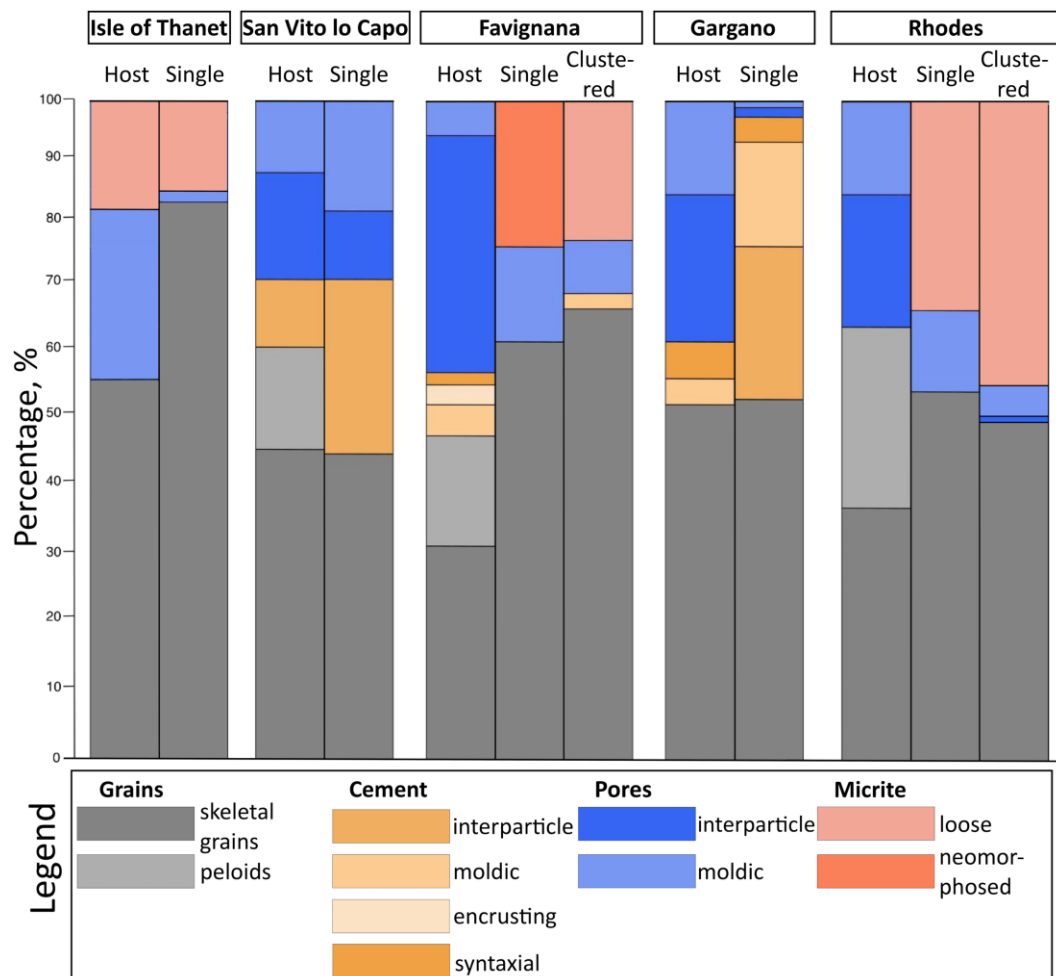


Figure 4-16 Column graph showing the composition (%) of the deformed (single, clustered deformation bands marked as “single” and “clustered”, respectively) and undeformed (host) rock in all studied locations. Note the changes before and after banding (i.e., decrease of moldic porosity in Isle of Thanet; increase in cement in San Vito lo Capo and Gargano; increase in micrite in Favignana and Rhodes samples; and decrease in porosity in all samples).

4.4.7 Permeability

All studied deformation bands have a negative impact on permeability, with its reductions down to 6.5 orders of magnitude relative to their parent rock (**Figure 4-17**). However, the data are very scattered. The smallest effect on permeability occurs in the deformation bands in the Isle of Thanet – the values of the deformed rock are only slightly smaller or overlap with the undeformed rock. Single deformation bands in San Vito lo Capo and Favignana show a wide variation in permeabilities; from $8 \cdot 10^{-3}$ mD to $1.7 \cdot 10^3$ mD, which are lower than the $2.8 \cdot 10^3$ mD of the host rock. Clustered deformation bands in Favignana show slightly smaller range: 10^{-2} - $2.3 \cdot 10^2$ mD. Single deformation bands in Gargano may have a permeability as low as $3 \cdot 10^{-3}$ mD, the lowest values corresponding to the completely cemented parts of the deformation bands, and higher values – for the less cemented parts (transition zone). Single and clustered deformation bands in Rhodes may reduce the permeability by up to 2 and 3 orders of magnitude, respectively.

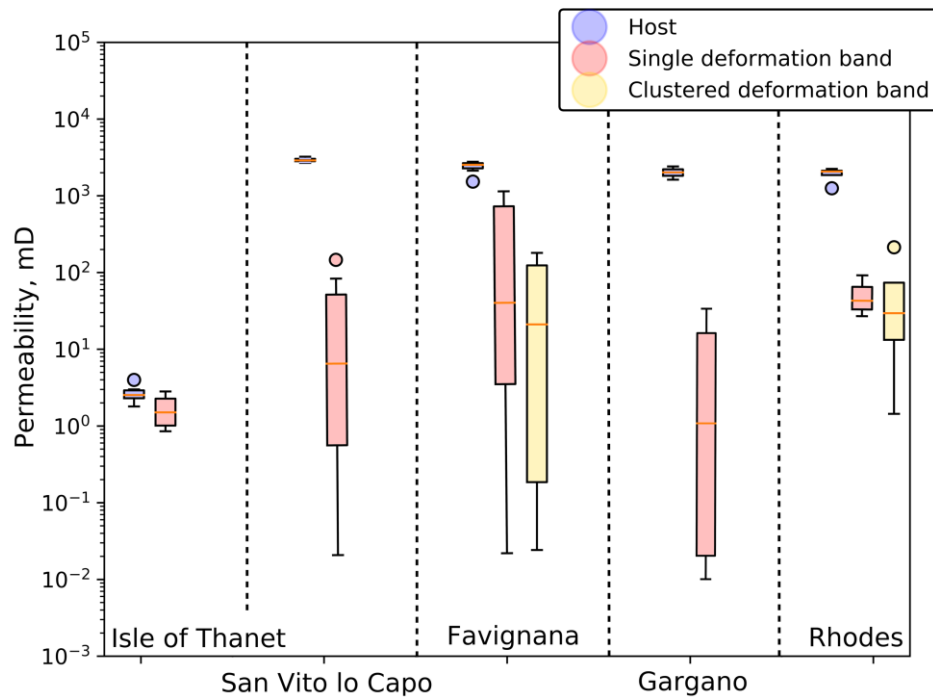


Figure 4-17 Boxplots showing mean and standard deviation values of the permeabilities (mD) of all studied deformation bands (single – red; clustered – yellow) and their parent rocks (blue). The boxes represent interquartile range of the data; bars indicate minimum and maximum values; circles show outliers; and orange lines indicate mean values of the datasets. Number of measured values: host (26); single deformation bands (62), and clustered deformation bands (17).

4.5 Discussion

4.5.1 Deformation band structure

Single deformation bands differ in all locations from one another by their thickness, with thinnest (<1 mm) occurring in the Isle of Thanet, and widest (<5 cm) in Favignana. Documented deformation bands from reservoir cores in Danian chalk show similar thickness values to the Isle of Thanet chalk: 0.05-0.5 mm (Wennberg et al., 2013). However, single bands documented from grainstones and packstones are thinner than those from this study: only a few mm in width (e.g., Agosta et al., 2010; Antonellini et al., 2014b; Tavani et al., 2017). Clustered band zones are much wider than single bands, with <70 cm measured in this study and typically up to 20 cm-wide zones were documented in the literature (e.g., Tondi, 2012; Rotevatn et al., 2016).

Anastomosing swarms may form the widest zones: up to a 1 m wide in the Isle of Thanet, and up to 5 m in Globigerina limestone in Malta (Rotevatn et al., 2016).

4.5.2. Force chain stress analysis

The force chain data are relatively scattered, however, angles of 270-345° normal to the strike of slip surfaces are the most common within the deformation bands, indicating that a substantial component of shear occurred during banding. A number of force chain trajectories for the single deformation bands in bioclastic grainstones (Favignana and Rhodes) is low because the grains are supported in the matrix and have few grain-to-grain contacts, indicating only negligible amount of pressure solution at grain contacts. However, the clustered deformation bands have more grain contact surfaces showing pressure solution as opposed to the undeformed rock or single deformation bands. Furthermore, their orientation represents the best-defined trend, which is oblique to the band. This suggests an increased amount of shear, as well as pressure solution at grain contacts for the clustered bands as compared to the single bands. The orientations of force chains within the dilation bands are more scattered than within their undeformed counterparts, indicating grain displacement in random orientations.

4.5.2 Deformation mechanisms

The results indicate that a range of deformation mechanisms contributed to the current microstructure of the studied deformation bands based on whether the bands are single or clustered, and in what lithofacies they occur.

Cumulative grain size curves show hardly changed values for undeformed and deformed rocks in San Vito lo Capo and Gargano, whereas their pore-throat sizes have been largely reduced. This indicates negligible cataclasis, whereas the pore space was occluded due to cementation. Microstructure analysis of the deformed and undeformed chalks show that the prominent deformation mechanism is the collapse of macropores that form the bodies of microfossils such as foraminifera. These macropores are not connected, which could explain the similarity of the MICP data for the undeformed chalk and the deformation bands. The other deformation bands studied experienced a significant decrease in grain-size indicating cataclastic deformation (e.g., Ballas et al., 2012). The single deformation bands in bioclastic grainstones show a lower percentage of cataclastic matrix than the clustered bands by a factor of c.5 (**Figure 4-15**), indicating that the clustered deformation bands evolved from single to clustered bands.

4.5.2.1 Single deformation bands in chalk

Strain within the Isle of Thanet chalk appears to have been accommodated by the fragmentation of the foraminifera shells, which form the largest pores (molds) in chalk (**Figure 4-11**). This supports observations done by Zhu et al. (2010), suggesting that pore collapse first initiates at the larger pores. Matrix within the band remains intact, showing no evidence of grain fracturing or enhanced post-deformation diagenesis, only slightly reduced interparticle microporosity due to compaction, and hence disaggregation of the micrite (**Figure 4-11**, middle). This is in agreement with the study done by Wennberg et al. (2013) on the deformation bands in Danian chalk, which showed closer packing and no fragmentation of the coccolith grains.

4.5.2.2 Single deformation bands in bioclastic grainstones

Single deformation bands show significantly reduced grain sizes compared to the undeformed parent rock. The peloids were smeared and crushed to fill the interparticle pore space to the extent that no intact peloids were preserved. Skeletal grains show slight reduction in size and increased angularity, indicating that some grain breakage has occurred. The micrite within single bands in Rhodes is loose and the microporosity of the matrix is high as opposed to the single deformation bands from Favignana. There is very little microporosity left within the matrix of single deformation bands from Favignana because loose micrite and some of the grain edges underwent aggrading neomorphism, with granular calcite replacing the fine micrite and margins of the grains (e.g., Flügel, 2013). Therefore, peloid disintegration and subsequent aggrading neomorphism play a significant role in the porosity destruction within these bands.

Single deformation bands in San Vito lo Capo studied by Tondi et al. (2006a), Tondi (2007) and Zambrano et al. (2017) display different textural zones across an individual band (the central Zone I is defined by cataclasis, the middle transition Zone II – by compaction, and the outer Zone III - by cementation). The bands analysed in this study are slightly different: Zone I is absent in all the bands, and Zone II shows partial cementation or compaction/cataclasis, which dissipates further away from the Zone III. The latter zone is defined by cementation for the single cemented bands and by compaction/cataclasis for the other bands (**Figure 4-12**). Single deformation bands in the studied grainstones are similar in their microstructures to the compactive shear bands in the Calcare Massiccio formation in the North of

Italy (Antonellini et al., 2014b). They all show soft plastic deformation at the grain boundaries, peloid smearing and little pressure solution.

4.5.2.3 Clustered deformation bands in bioclastic grainstones

Clustered deformation band zones are made of several mm-cm thick bands linking together and enclosing lenses of less deformed host rock (**Figure 4-8f,g**). The bands mostly contain micritic matrix and very few surviving intact skeletal grains (**Figure 4-10c,f**). This indicates that extensive grain fracturing has occurred during deformation (e.g., Ballas et al., 2012), because not only peloids have been disintegrated but also most of the skeletal grains. Grain sizes within these bands have been reduced by up to a factor of 8 compared to their parent rocks. Transition zones between these bands are slightly less deformed. They show higher percentage of surviving skeletal grains, less volume of cataclastic matrix, and a great amount of preserved interparticle porosity.

4.5.2.4 Single cemented bands

The grain size for the deformed and undeformed rock in Gargano and San Vito lo Capo shows very similar values, indicating only negligible cataclasis during deformation. The minus-cement porosity within the deformation bands is slightly higher (<2-3%) than that of the host rock but this may be within measurement error. However, the aforementioned observations and the fact that these bands show no visible shear displacement in the field and are parallel to fractures suggest that these bands may have formed in a dilational manner (e.g., Du Bernard et al., 2002; Exner et al., 2013; Lommatzsch et al., 2015). Sparry calcite cements in the San Vito lo Capo bands show an

irregular distribution, whereas the bands in Gargano are highly cemented. It is not entirely obvious why the deformation bands became so cemented given that they would have had similar porosity to the host carbonate after only a small amount of cementation had occurred. One possibility is that the cementation within the deformation bands was kinetically more favourable than in the host carbonate (e.g., Eichhubl et al., 2004; Ballas et al., 2012; Antonellini et al., 2014b; Lommatzsch et al., 2015). This could be the case for several reasons including: (i) deformation-related disaggregation of the grains could have removed organic matter from the surface of the grains within the band making them more susceptible for later calcite precipitation; (ii) small amounts of cement precipitating in the band during or immediately after deformation could have provided more favourable sites for later calcite precipitation than were present within the undeformed carbonate.

Even though dilation may lead to permeability drop due to the decrease in grain size and sorting, and hence, pore throat sizes (e.g., Ngwenya et al., 2003), dilation bands have been reported to act as a preferential path for fluid flow (e.g., Bense et al., 2003; Sample et al., 2006) and cementation (e.g., Wong et al., 1997). Porosity increase caused by dilation have been measured in several studies on dilation bands in sandstones, and the reported minus-cement porosity values vary between 4 and >7% (e.g., Du Bernard et al., 2002; Exner et al., 2013; Lommatzsch et al., 2015), which is higher than the ones measured in this study for carbonates: 2-3%. Porosity increase in the dilation bands in sandstones is typically followed by carbonate cementation (Exner et al., 2013; Lommatzsch et al., 2015), authigenic clay mineral growth (Du Bernard et al., 2002; Lommatzsch et al.,

2015), and dissolution of detrital grains (Exner et al., 2013). Cementation has been reported within the compactive shear bands in carbonates to accompany grain translation, rotation, granular flow, pore collapse or cataclasis (e.g., Rath et al., 2011; Zambrano et al., 2017; Cooke et al., 2018). However, no dilational bands have previously been observed in porous carbonate outcrops.

In most of the deformation bands throughout all the localities, some of the grains have been dissolved leaving moldic porosity behind, indicating rock-fluid interaction (e.g., Walter, 1985).

4.5.3 Geomechanics of deformation band formation

The deformational behaviour of porous sediments and soils is often represented using a non-linear yield surface, often referred to as a Cap-plasticity model, when plotted on a graph of differential stress, q , vs. mean effective stress, p (**Figure 4-18**). At low effective stress, the differential stress required for failure to occur increases with mean effective stress; here deformation occurs in a brittle dilatant manner. At higher effective stresses, the differential stress needed to achieve yield decreases with increasing effective stress; here deformation occurs in a ductile compactive manner (e.g., Wong and Baud, 2012). Therefore, dilatant shear bands in high-porosity rocks typically form at low confining pressures and high differential stress, whereas compactional shear bands form at higher confining pressures and low differential stress (Fossen et al., 2007; Cilona et al., 2012). An important parameter that is required to define the yield envelope is the stress required for yield under zero differential stress conditions; this is

often referred to as P^* or the apparent pre-consolidation pressure (**Figure 4-18**).

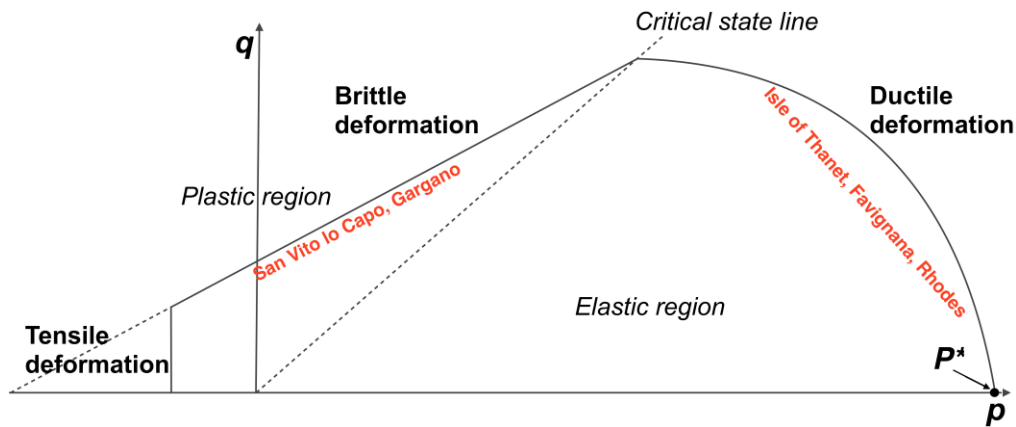


Figure 4-18 Yield surfaces in the p - q space, illustrating regimes, where studied deformation bands may have formed: brittle deformation regime (deformation bands in San Vito lo Capo and Gargano) and ductile deformation regime (deformation bands in Isle of Thanet, Favignana and Rhodes).

It is likely that the differences in the structures of the deformation bands described in the current work reflect differences in the position on the yield surface where deformation occurred. The deformation bands that experienced a significant porosity reduction (e.g., Isle of Thanet, Favignana, Rhodes) formed when the stresses in the subsurface intersected the ductile part of the yield surface. On the other hand, the cemented deformation features (e.g., San Vito lo Capo, Gargano) appear to have formed when the stresses in the subsurface intersected the brittle part of the yield surface.

4.5.4 Time-dependant evolution of deformation bands and its influence on their petrophysical properties

Deformation mechanisms occurring within the evolving deformation bands in porous carbonates are widely reported in the literature, and typically start from mechanical grain reorganisation and pore collapse (e.g., Tondi, 2007; Agosta et al., 2010; Rath et al., 2011; Rustichelli et al., 2012; Ciona et al.,

2012, 2014; Rotevatn et al., 2016). Secondly, they evolve to form intergranular pressure solution surfaces and pressure solution seams (e.g., Tondi et al., 2006a; 2016; Antonellini et al., 2008; Cilona et al., 2012, 2014). The latest stage of deformation band formation is accommodated by cataclasis (e.g., Tondi et al., 2006a; 2016; Rath et al., 2011; Cilona et al., 2012; Rotevatn et al., 2016; Tavani et al., 2016). Even though all deformation bands examined in this work can be categorised by one of these evolution stages, they also show how much deformation bands in carbonates may differ from one another. The differences between the bands identified in this study indicate that the two most important parameters controlling the formation of the deformation bands in carbonates are the composition of the host rock (in particular the texture and strength of the grains, and pore type) and the stress conditions that resulted in banding (**Figure 4-19**). Even though porosity of the host rock throughout localities varies between 38 and 52%, and average grain size spans on the range of 2 μm for chalk and 130-240 μm for bioclastic grainstones, these parameters do not seem to have a significant impact on the evolution of the deformation bands. When the host has high interparticle porosity, interparticle porosity within the bands is infilled by micrite from the breakdown of fossils due to the high-stress states at the fossil contact. Whereas when the dominant porosity type within the host is microporosity and moldic porosity, the latter porosity type is destroyed within the bands first due to the collapse of the fossils containing the molds. The studied carbonates were not deeply buried, thus peloids - the weakest grains - were still intact at the time of deformation. Therefore, they accommodated the strain during deformation, and hence were the first grains to

disaggregate and fill the pore space, as shown in the single bands in Favignana and Rhodes, whereas skeletal grains remain intact. Higher strains could not solely be accommodated by the deformation of soft peloids so cataclasis took over as the dominant deformation mechanism, as shown in the clustered bands in Favignana and Rhodes, where cataclastic matrix makes up for most of the rock's volume. Moreover, when the protolith did not contain peloids, deformation bands formed as a result of different deformation mechanisms. For example, the weakest grains in the Isle of Thanet chalk were thin foraminifera shells, and hence are implied to be the first fossils to collapse, as the moldic pore collapse is the only deformation mechanism observed within these bands. Whether compression or dilation resulted in banding, made a significant impact on deformation, because differences were noted between dilation and compactive-shear bands, where dilation-induced cementation and cataclasis were the dominant deformation mechanisms, respectively.

Cemented bands, such as the ones in San Vito lo Capo and Gargano show a slight increase in minus-cement porosity compared to their parent rock and only negligible grain-size reduction. Diagenesis may reduce the pore space due to aggrading neomorphism (e.g., of loose micrite within single bands in Favignana) or cementation (e.g., deformation bands in San Vito lo Capo and Gargano). Post-kinematic grain dissolution may increase porosity of the deformation bands significantly. However, dissolution may have occurred during uplift, in which case it might be absent if deeply buried.

At a macro-scale, deformation bands evolve from discontinuous thin single bands (from <1 mm to up to 5 cm in thickness) to continuous clustered

bands (up to 50 m in length), which form thick zones (up to 70 cm in width). They grow with increasing displacement (up to 5 cm offset for single bands, up to 20 cm for clustered bands).

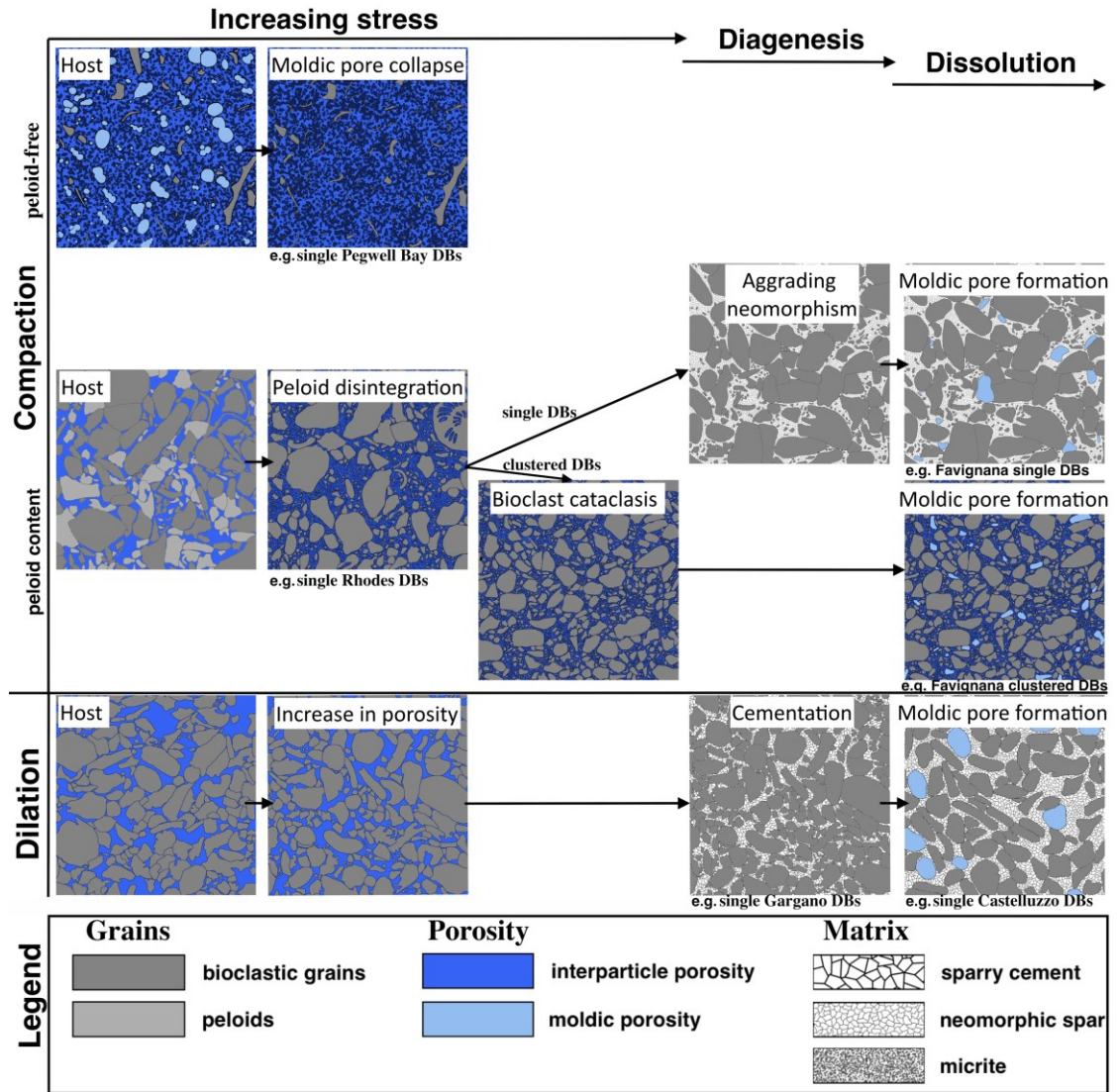


Figure 4-19 Schematic diagram illustrating evolution of the studied deformation bands, and their dependence on the sense of stress (dilation/compaction), peloid content and increasing magnitude of stress. Note how further diagenesis and grain dissolution might affect post-kinematic porosity.

Permeability values of single deformation bands and undeformed chalk in the Isle of Thanet are very similar. Microstructural analysis indicates that the porosity reduction occurred due to the collapse of moldic macroporosity.

Since this macroporosity was not connected its collapse did not significantly

impact permeability. The single deformation bands in San Vito lo Capo show a wide range of permeabilities because they were mostly affected by heterogeneous cementation. However, they all have a negative impact on permeability (up to 6 orders of magnitude of reduction compared to the parent rock) and reflects variation in cementation. Completely cemented single deformation bands in Gargano have the biggest impact on fluid flow by reducing the permeability by up to 6.5 orders of magnitude. The most significant effect on permeability across the deformation bands in porous carbonates was reported previously by Rath et al. (2011) in Leitha limestone, where the bands in addition to cataclasis have also experienced significant cementation. Single deformation bands in Favignana may reduce the permeability by 6 orders of magnitude, whereas single bands in Rhodes reduce the permeability only up to 2 orders of magnitude. The difference occurs because the disintegrated peloids filling the interparticle pore space within the latter bands have not undergone the aggrading neomorphism as within the bands in Favignana, what further reduces the porosity, and hence the permeability. Clustered deformation bands in Favignana and Rhodes have largely reduced grain sizes due to high-stress cataclasis, however, it has large amounts of well-connected microporosity within the matrix due to plastic deformation of soft micritic peloids. Depending on the volume of microporosity within the micrite and post-kinematic moldic porosity, permeability across the bands may be reduced between 1 to 5 orders of magnitude in Favignana, and up to 3 orders of magnitude in Rhodes. The permeabilities for the deformation bands in the San Vito lo Capo area measured by Antonellini et al. (2014a) are within the range of permeabilities

measured during this study; 10^1 - 10^3 mD. The values measured by Tondi et al. (2016) for the deformation bands (zone I) in Favignana; $3 \cdot 10^1$ to $1.3 \cdot 10^3$ mD are similar to those measured during the current study.

Despite the huge variations in permeabilities, it is likely that highly cemented bands in bioclastic grainstones will greatly reduce the effective permeability of the reservoirs, whereas irregularly cemented bands will have leakage points, and hence will not form barriers to fluid flow (**Figure 4-20**). Moreover, clustered bands in grainstones formed in high effective stress environment will always have a negative impact on the effective permeability of the reservoirs because they form continuous zones of greatly reduced interparticle porosity. Deformation bands in chalk will not have a significant impact on fluid flow.

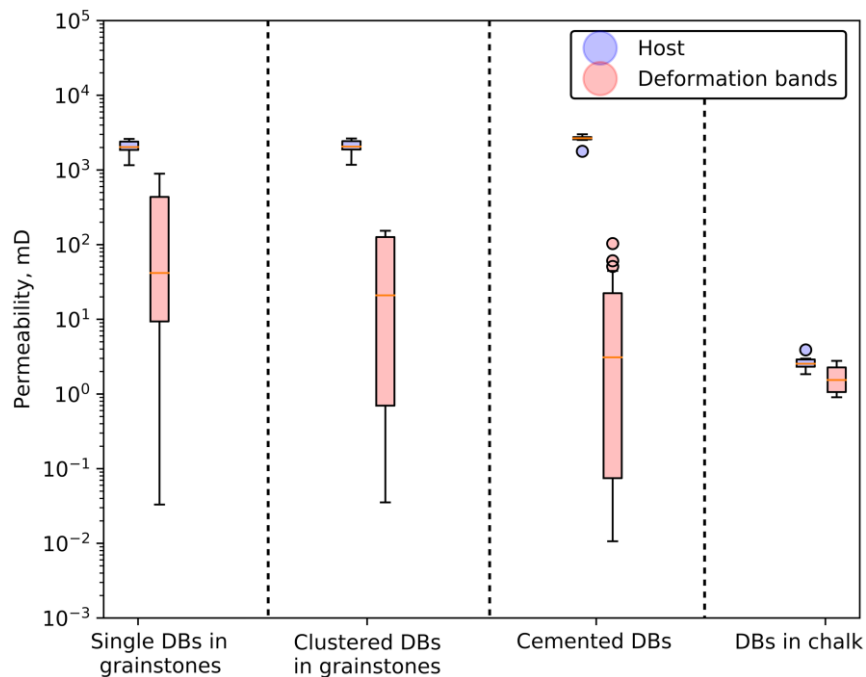


Figure 4-20 Boxplots showing mean and standard deviation values of the permeabilities (mD) of all studied deformation bands (red) and their parent rocks (blue). The boxes represent interquartile range of the data; bars indicate minimum and maximum values; circles show outliers; and orange lines indicate mean values of the datasets. DBs: deformation bands.

4.6 Conclusions

The two most important parameters responsible for deformation band evolution in high porosity carbonates are: composition/texture of the host rock, and the stress conditions during deformation. The composition of the host rock has a significant control on both deformation mechanisms and the processes that impact the petrophysical properties of the resulting deformation bands. For instance, bioclastic grainstones containing a significant proportion of soft peloids disaggregate and deform in a ductile manner during banding, filling the pore space between more competent components. The disintegrated peloids also act as a source of micrite for an aggrading neomorphism, which further reduces the porosity and permeability. Conversely, chalk experiences the collapse of macro-porosity within foraminifera, which does not have a significant impact on permeability. Dilation bands tend to experience enhanced cementation, which significantly reduces porosity and permeability. The precise reason for the enhanced cementation remains enigmatic but could reflect them acting as kinetically more favourable sites for calcite cementation. Selective grain dissolution may increase post-kinematic porosity. Most types of deformation bands have a negative impact on permeability, reducing it by up to 6.5 orders of magnitude as compared to the parent rock. However, the deformation bands are very heterogeneous, which causes a wide range of permeabilities between the samples, reflecting a degree of cementation (dilation bands), cataclasis (compactive shear bands), and/or diagenesis (all types of bands).

Chapter 5 Faulting in low-porosity carbonates: A case study from San Vito lo Capo, Sicily, Italy

5.1 Introduction

Faulted carbonates often contain wide zones of distributed strain due to pervasive fracturing and narrow zones of localized strain along the main slip surfaces showing more intense deformation by processes such as rock comminution, fragmentation and cataclasis (Aydin, 2000; Faulkner et al., 2010; Bense et al., 2013; Michie et al., 2014). Several models have been proposed to explain the structure of fault zones in carbonates. A popular model is that fault zones are composed of a core that accommodates most of the strain surrounded by a fractured damage zone (e.g., Agosta and Aydin, 2006). Increased displacement may create a more complicated structure containing numerous strands of fault rock and second-order slip surfaces (e.g., Billi et al., 2003; Agosta and Aydin, 2006; Billi, 2010). Recently, a number of studies have shown that mineralogy may have an important control on fault zone architecture in carbonates (e.g., Antonellini and Mollema, 2000; Cantrell et al., 2004; Frost et al., 2009; Bauer et al., 2016). Bauer et al. (2016) proposed a model for fault zones in low porosity carbonates, which takes into account both displacement and mineralogy. The authors suggest that low-displacement faults in limestones are composed of single-stranded discontinuous fault cores, the continuity of which increases with fault displacement. Faults in dolostones have far wider damage zones and contain widely distributed discontinuous multiple-

stranded cataclastic fault cores, which partially link up to form an anastomosing fault network. The model is supported by the observations made in other studies which suggest that fault rocks in tight dolomites are reminiscent of cataclastic shear bands (Antonellini and Mollema, 2000; Schröckenfuchs et al., 2015). Moreover, the fracture intensity is normally higher in dolomite than in limestone reservoirs (Stearns and Friedman, 1972; Safko and Hickey, 1992; Nelson and Serra, 1995; Hanks et al., 1997; Cantrell et al., 2004). Fault rocks are largely restricted to dolomites in mixed dolomite/limestone sequences (House and Gray, 1982; Frost et al., 2009; Bauer et al., 2016) possibly because limestone may accommodate strain more easily than dolomite, which remains susceptible to brittle deformation at depths sufficient to induce plastic deformation in limestone (e.g., Wu, 1993). Dolomite is not only more brittle than limestone, but also less soluble (e.g., Liu et al., 2005). Therefore, dolomite is not as susceptible to pressure solution and twinning as limestone and hence experiences lower pre-faulting strain (Donath, 1970).

Identifying the key controls on fault geometry from these observations is made difficult because the outcrops have often had significantly different tectonic histories. The impact of mineralogy on fault zone architecture was investigated by studying faults in tight limestones and dolomites in San Vito lo Capo peninsula, Sicily; a relatively small geographic area that have experienced very similar burial and tectonic histories. The results are presented on large scale fault architecture, microstructure and petrophysical properties of the different fault zone elements in these areas. The results are

then compared to other studies to identify key controls on fault zone architecture and the implications for subsurface fluid flow.

5.1.1 Tectonic setting of the study area

San Vito lo Capo is located in the westernmost sector of the Sicilian Orogenic Belt, which was active during the Cenozoic collision between the North-African continental margin and the Sardinia-Corsica block. The collision is mainly represented by a general southward convergence of folds and thrusts (e.g., Catalano et al., 1996). Giunta et al. (2000) documented three stages of the Neogene deformation in the area: i) E-W trending thrusting in the Early Miocene; ii) extensional faulting in the Late Miocene; iii) strike-slip faulting in the Plio-Pleistocene, which often reactivated pre-existing structures (e.g., Boccaletti et al. 1987; Tondi et al., 2006b). The lithofacies on which this study is based are Mid-to-Upper Cretaceous recrystallized bioclastic packstone (referred in the text as limestone) and Upper-Triassic secondary dolostone (**Figure 5-2**). Structural restoration suggests maximum burial depths of c.3 km and c.2 km for dolomite and limestone outcrops respectively (Stead, 2018). The studied faults include normal and strike-slip faults (**Figure 5-1**). Tondi et al. (2006b) described the NNE-striking Faro fault (**Figure 5-1**), located within the Mid-to-Upper Cretaceous packstones, but also cutting through marine deposits of Early Pleistocene age, as a left-lateral strike-slip fault that is continuous for c.3 km in length and forms a fault scarp up to 20 m high. The authors also documented the ESE-striking Castelluzzo fault (**Figure 5-1**), which is exposed for c.2 km in Early Pleistocene marine sediments along a 15 m high fault scarp. The small displacement deformation bands occurring within the Plio-Pleistocene bioclastic grainstones in the Castelluzzo plain

(**Figure 5-1**) indicate right-lateral strike-slip kinematics for the E-W and ESE-striking bands, left-lateral strike-slip kinematics for the NNW and N-S trending bands, whereas the NW-striking set is characterized by oblique normal kinematics (Tondi et al., 2006b). The authors concluded that the geometry of the stress field responsible for the overall deformation pattern observed in San Vito lo Capo had a maximum compression oriented roughly NW. Plio-Pleistocene strike-slip events are thought to have occurred at 290 m and 200 m depth in Pellegrino quarry and Faro fault, respectively (Stead, 2018).

Seven faults were studied within the Mid-to-Upper Cretaceous limestones: Torrazzo, Faro, Punta Negra 1,2,3, El Bahiro and Torre Isolidda (**Figure 5-1**); they strike between 000-037°, 165-189°, and rarely to around 123°. Two fault zones were studied in the Upper Triassic dolostone: Pellegrino quarry and Punta del Saraceno (**Figure 5-1**). Slip surfaces within these fault zones typically occur in three dominant orientations: 000-031°, 056-080° and 97-157°, although faults with other orientations are also common. Fault throws were difficult to determine for most of the faults as all, except those in the Pellegrino quarry, are exposed on a short flat beach platform. However, Punta Negra 3 and 2 faults are exposed next to a cliff, where the faults may be observed in a vertical section. There they show normal slip kinematics and a displacement of 3-5 meters. Strike-slip kinematic markers on the tectonic map suggest c.360-500 m throw for the Pellegrino quarry (**Figure 5-1**).

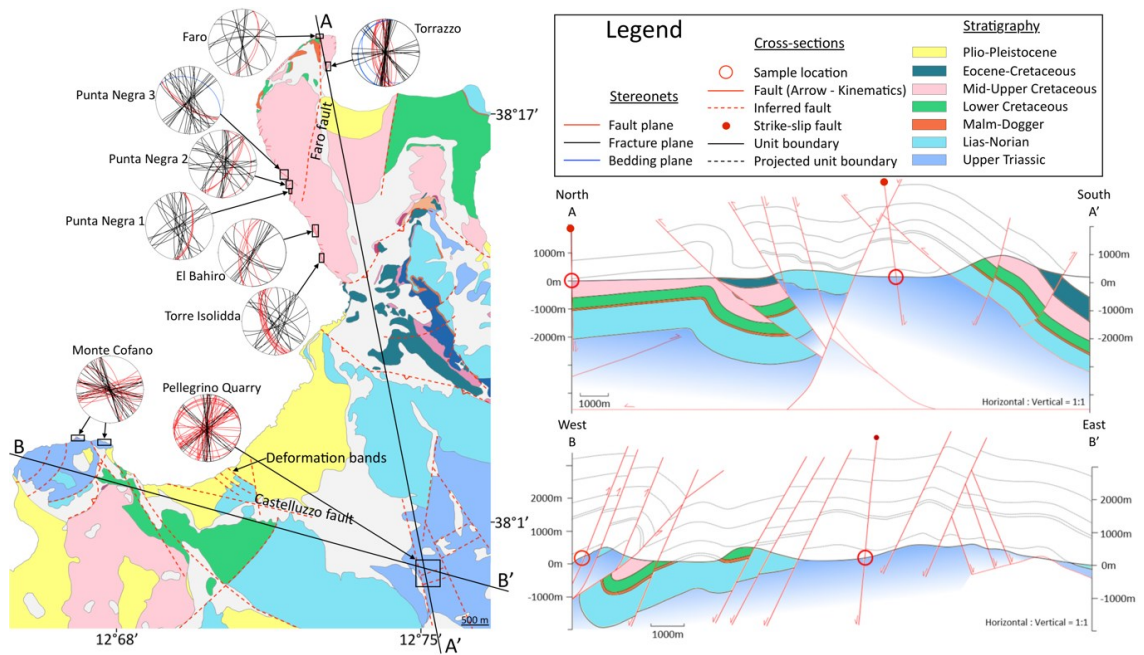


Figure 5-1 Left: geological map of San Vito lo Capo modified after Incandela et al. (1993). Studied fault outcrops are shown in black rectangles. Note that the inferred faults are indicated by red dashed lines, and observed faults are shown in red solid lines. Stereonets represent structural data for each study area. Right: interpreted cross-sections from North to South (top), and from West to East (bottom) of San Vito lo Capo peninsula (after Stead, 2018). Note that cross-section lines are marked on the geological map.

5.2 Samples and methods

5.2.1 Fault zone mapping

Detailed structural maps were produced for each fault zone as explained in **Section 3.2.2**. The maps were analysed in terms of width, internal architecture, heterogeneities of fault rocks, and aperture, spacing and crosscutting relationships of fractures. Samples were collected along fault strike at intervals of c. 1-3 m for each fault zone with accessible outcrop to represent any heterogeneity present within the fault zone while collecting protolith samples for comparison. A total of 192 oriented samples were collected and analysed.

5.2.2 Microstructural analysis

Blue-dyed epoxy-impregnated polished thin sections were examined using an optical microscope at magnifications of 4x-20x. Thin sections were stained with Alizarin Red-S and Potassium Ferricyanide to distinguish between calcite and dolomite (calcite stains in pink, whereas dolomite does not stain). Two types of scanning electron microscope, a FEI Quanta 650 FEG and a Tescan VEGA XM, were also used in back-scattered electron (BSE) mode for microstructural analysis. Carbon coated samples were analysed with CITL cold cathode luminescence 8200 mk3 microscope to examine fabrics, diagenetic phases, replacement, recrystallization and cement relationships.

5.2.3 Petrophysical analysis

Porosity and permeability values of the samples were determined as explained in **Section 3.5.1** and **Section 3.5.2**. Data were plotted using a visual analysis tool PETMiner, which allows to plot numerical (petrophysical measurements) and visual data (CT scans and micrographs) together (Harrison et al., 2017).

5.2.4 Mechanical properties of the protoliths

Hydrostatic and triaxial compression tests were performed on the two studied lithofacies to determine their bulk modulus and a yield point, respectively (**Figure 5-2**). The axial stress was applied at a strain rate of 10^{-5} s^{-1} . The maximum confining stress applied for the hydrostatic test was 70 MPa, and the confining stress used for the triaxial test was 5 MPa. The yield was identified from the triaxial test as an inflection point on the mean effective stress curve plotted against volumetric strain.

5.3 Results

5.3.1 Host rocks

Studied faults occur within Mid-to-Upper Cretaceous recrystallized bioclastic packstone and Upper-Triassic secondary dolostone (**Figure 5-2**). Their host rock porosity is <2%, and matrix permeability is in the range of 2×10^{-4} - 2×10^{-2} mD, with slightly lower values for the limestone. Dolostone is at least 2 times stronger than the limestone (**Figure 5-2**).

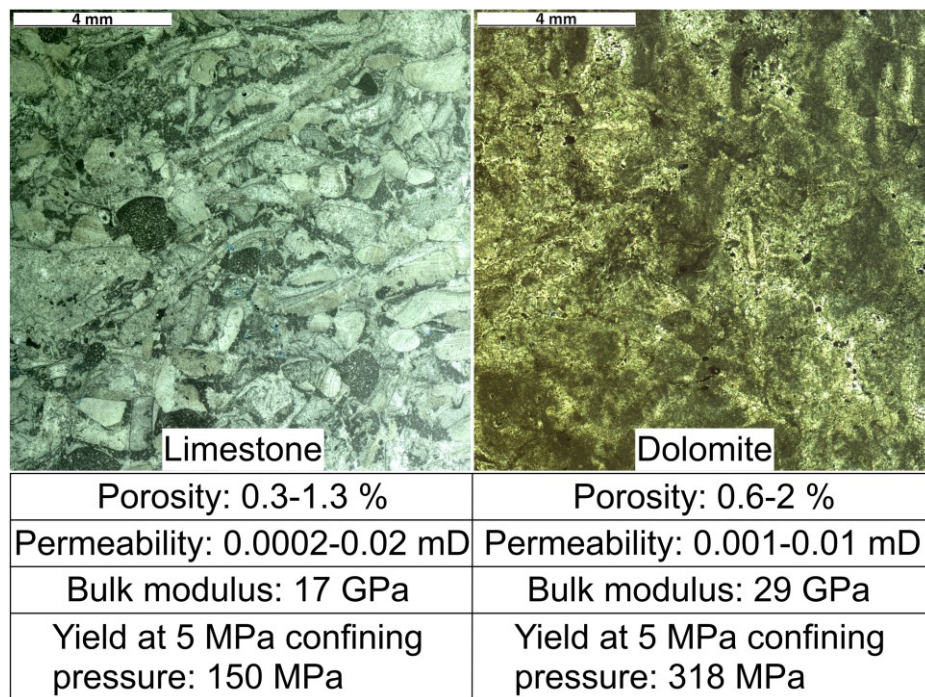


Figure 5-2 Micrographs of the two protolith rocks hosting the studied faults. Table displays main petrophysical and mechanical properties of the host rocks.

5.3.2 Fault zone architecture

5.3.2.1 Limestone

Faults in limestones are characterized by a thin cataclastic fault core (2-18 cm in width) surrounded by a fractured damage zone (**Figure 5-3a,b,d,e**).

The entire coastline within these limestones is fractured and contains numerous faults (**Figure 5-1**, red solid lines), therefore, it is difficult to

measure where damage zone of one fault ends and another starts. The faults dip between 52° and almost vertical. Fault scarps at Punta Negra 2,3, Torre Isolidda and El Bahiro are 1-2 metres high and their surfaces are weathered (**Figure 5-3**). The Faro fault zone consists of a fault core in the hanging-wall made up of a discontinuous thin cataclasite layer (<6 cm) along the slip surface, which is surrounded by continuous cohesive chaotic breccia up to 55 cm in width (**Figure 5-5a,d**). Crackle breccia bounds the chaotic breccia in the hanging-wall and the slip surface in the footwall, creating a fault core of up to 80 cm in width. The damage zone is at least 150 m wide and contains 20 cm-1 m thick layers of crackle breccia. Crackle breccia zones in the hanging wall are oriented parallel to the main fault and show spacing of c.5 metres. In the footwall, crackle breccia zones are mostly oriented perpendicular to the main fault forming concave-shape structures, and closer to the main fault they form irregularly shaped structures oriented parallel to the slip surface (**Figure 5-5a,b**). The Torrazzo fault is made up of a thicker fault core containing several splaying slip surfaces covered with thin cataclastic layers (1-7 cm in width) and cemented chaotic breccia in between the slip surfaces (up to 3.5 m in width) (**Figure 5-4**). The Punta Negra 1 fault contains an almost straight fault core containing cemented chaotic breccia of up to 65 cm in width (**Figure 5-3c**). Fault cores at Punta Negra 2,3, Torre Isolidda and El Bahiro are cut by fractures oriented perpendicular and orthogonal to the strike of the fault.

Cataclasite is cohesive and strong, and in most faults it is white-greyish in colour, except in Punta Negra 2, where it is pink. Only few clasts are sufficiently large to be visible to the eye; these are rounded to sub-rounded.

The cataclasite layer at Punta Negra 2,3, Torre Isolidda and El Bahiro is cut by fractures oriented perpendicular and orthogonal to the strike of the fault (**Figure 5-3a,b,d,e**). Chaotic breccia in Torrazzo and Punta Negra 1 is cohesive and very strong, containing sub-angular to sub-rounded clasts cemented by pink-creamy calcite micritic cement (**Figure 5-3h** and **Figure 5-4d**). Fractures blunt against the chaotic breccias (**Figure 5-3c** and **Figure 5-4b,c**). Chaotic breccia in Punta Negra 3, El Bahiro and Torre Isolidda is incohesive and made up of sub-angular to sub-rounded clasts embedded in a fine-grained matrix; it is cross-cut by fractures. Crackle breccia in Faro is cohesive and made up of angular clasts, the matrix is fine grained and black to reddish in colour. Fractures are not observed to cut the crackle breccia or the fault core in the Faro fault zone (**Figure 5-5b**).

Damage zones in all the aforementioned faults show three dominant sets of fractures: (1) parallel, (2) perpendicular, and (3) orthogonal to the principal slip surface. Set 2 is the dominant fracture set in most of the fault zones (except Faro fault, where Set 1 is the dominant orientation and usually cross-cuts the other fractures) and is pervasive throughout the whole damage zone. Set 2 fractures are the longest (reaching up to 15 m) and more open (up to 1.5 cm aperture) and narrowly spaced (typically 5-10 cm) than the other fracture sets. Set 1 fractures are also pervasive throughout the whole damage zone, however, they are usually short (c.1-2 m) and widely spaced (every 1 or more meters). Set 3 fractures are the shortest and usually abut against the other sets; their spacing is closest (1-10 cm) next to the fault core. The aperture of Fracture Set 3 is <2 mm, which is less than the other

fracture sets. An example of a typical damage zone in tight limestones in San Vito lo Capo is shown in **Figure 5-5c**.

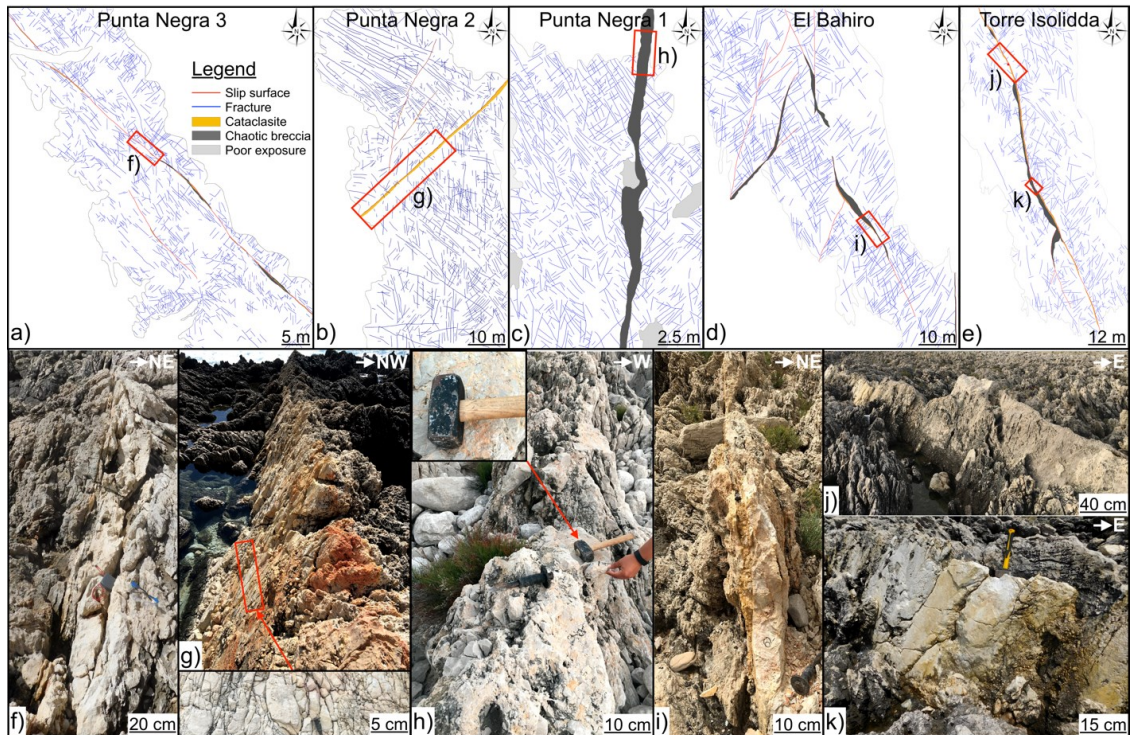


Figure 5-3 Structural maps (a-e) of faults in Mid-to-Upper Cretaceous limestone and representative outcrop photographs (f-k): their locations are marked on the maps in red rectangles. Note the fractured cataclasite walls (g, k) and weathered fault surfaces.

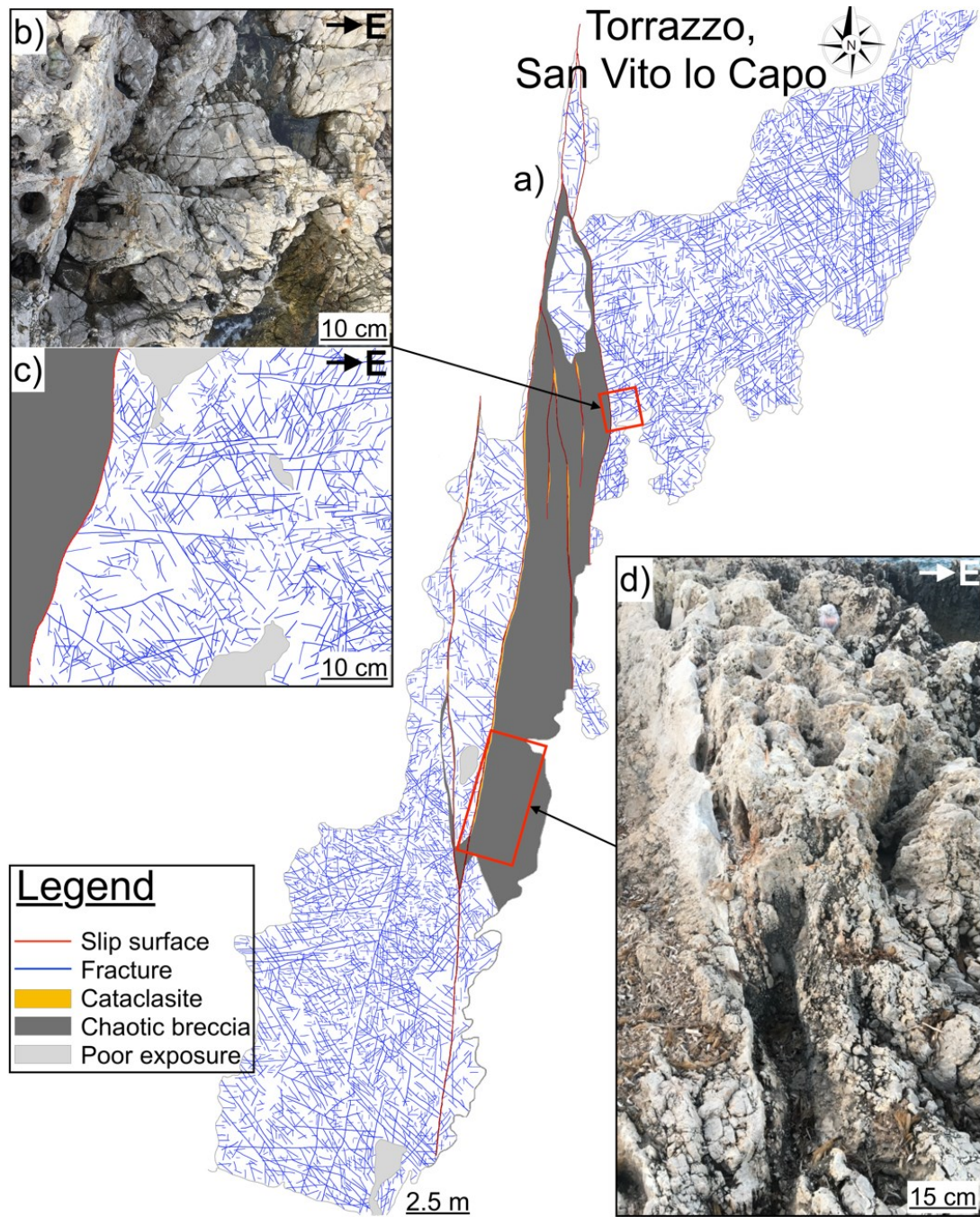


Figure 5-4 a) Structural map of the Torrazzo fault zone occurring within the Mid-to-Upper Cretaceous limestone. b) and c) show a close-up photograph and its structural interpretation of the fractures abutting against the fault core containing chaotic breccia, respectively. d) Photograph of the fault rocks: note white cataclastic layer on the left (west) that is adjacent to a cemented chaotic breccia (east).

Faro, San Vito lo Capo

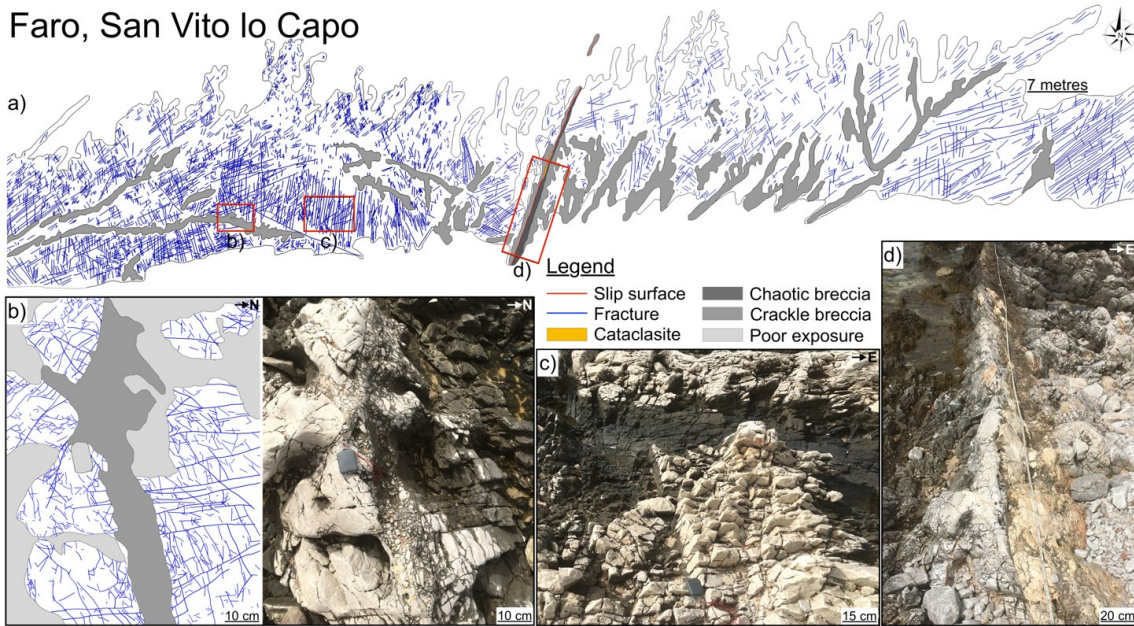


Figure 5-5 a) Structural map of the Faro fault zone occurring within the Mid-to-Upper Cretaceous limestone. b) shows a close-up photograph and its structural interpretation of the crackle breccia layer against which fractures terminate. c) is an outcrop photograph of the damage zone typical for the fault zones in the tight limestone of San Vito lo Capo. Note long fractures with spacing of c.5-10 cm perpendicular to which are shorter fractures. d) Photograph of the main fault core, note the chaotic breccia layer along the fault in a creamy colour.

5.3.2.2 Dolomite

Faults in dolostone are characterized by intensely fractured, wide damage zones and a complex array of anastomosing cataclasite bands that isolate lenses of fractured and crushed rock. Slip surfaces have polished and striated faces: the striations are consistent with vertical pure dip-slips (**Figure 5-6a**) and horizontal left-lateral slips (**Figure 5-6b**). However, they also may occur at any dip angle between horizontal and vertical (**Figure 5-6g,h**). The slip surfaces are covered from both sides with a cataclasite layer of a few cm in thickness (**Figure 5-6e,f**). These bands are tabular in shape and may form as single or clustered bands made up of several thinner individual bands that coalesced together. The cataclasites are reminiscent of deformation bands occurring in high-porosity granular rocks: planar structures, which do not

exhibit a well-defined plane of displacement discontinuity, often with small irregularities, such as eye and ramp structures (e.g., Antonellini et al., 1994; Fossen et al., 2007; Tondi et al., 2012). Single bands are 5 mm-5 cm thick, and clustered bands may reach up to 70 cm in width. No principal fault core has been observed within these fault zones, and cataclasite bands are spread throughout the entire available outcrop.

The damage zone comprises incohesive, pulverized rock. Fracture sets are similar to those observed within the damage zones in limestone – they show three dominant orientations: (1) parallel, (2) perpendicular, and (3) orthogonal to the slip surfaces. However, fractures are much more closely spaced than in the limestone and generate a rock fabric consisting of orthorhombic clasts 0.5–3 cm in size (**Figure 5-6e,f** and **Figure 5-7c,d**). The original dolostone structures (e.g., bedding) are significantly deformed. Fractures reach up to 15 m in length, but typically are a few cms to 2 meters long; their apertures are very thin (<2 mm), only the aperture of fractures perpendicular to the bands are wider: <1 cm. Larger scale fractures cross-cut the cataclasite bands in places where they have thinned to <3 cm. Other fractures do not cross the cataclasite bands (**Figure 5-6e,f,g,h** and **Figure 5-7c,d**). The damage zones continue throughout the outcrop, which is 820 m x 500 m in the Pellegrino quarry, and 280 m x 65 m at the coastline outcrop of Punta del Saraceno.

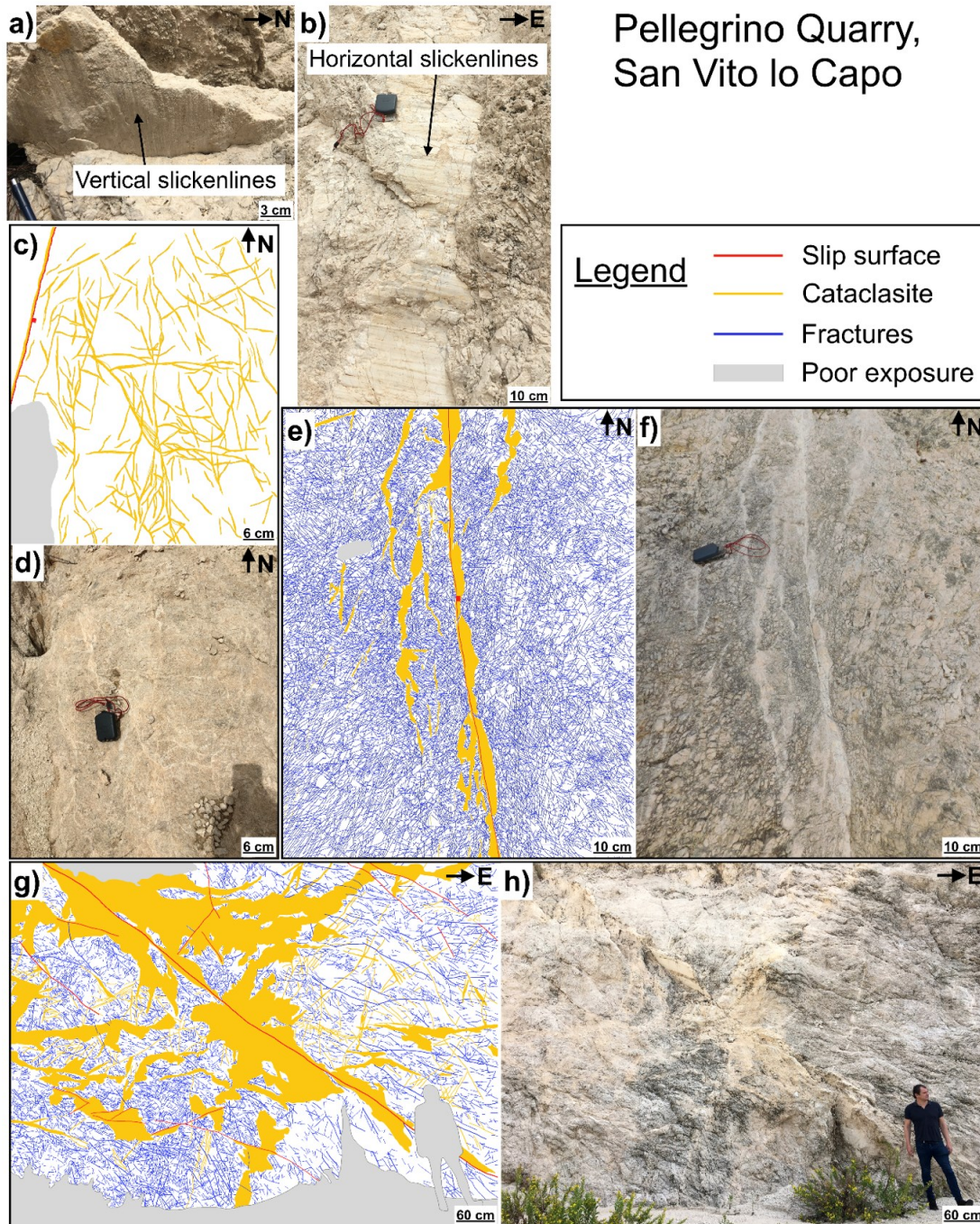


Figure 5-6 Representative maps and photographs of fault rocks and fracture patterns in dolomite of Pellegrino quarry. a) and b) show striated slip surfaces indicating vertical dip-slip and horizontal lateral slip, respectively. c) and d) show interpreted and photographed cataclasite band structures in the outcrop: note the anastomosing patterns and varying orientations forming a complex network of the bands. e) and f) structural map and original photograph of a representative close-up view of the slip surface and a cataclastic band network bounded by intensely fragmented rock within the Pellegrino fault zone. g) and h) show a vertical wider view of the Pellegrino quarry wall: note the complex network of cataclastic material and that only the dominant larger scale fractures are mapped.

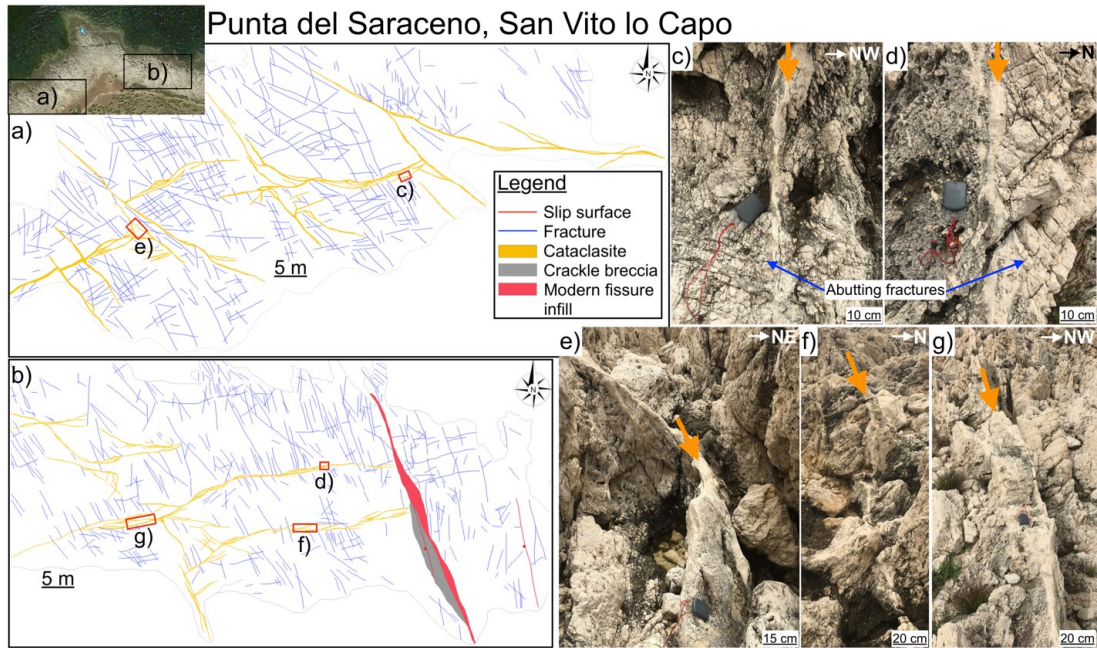


Figure 5-7 Structural maps of Punta del Saraceno study area (a-b). Note that only large scale dominant fractures are mapped. Small scale fractures are shown in field photographs (c-d), they terminate at the cataclasite bands. (e-g) show representative cataclasite bands, which are indicated by orange arrows. Photograph locations are marked on the structural maps.

5.3.3 Fault rock microstructure

Faults in tight limestone and dolomite were largely formed by brittle fragmentation and abrasion. The grain size decreased with evolving deformation: the clast diameter within the crackle breccias range between c.10-30 mm, mosaic breccias - c.5-15 mm, chaotic breccias - c.1-10 mm, and cataclasites - c.0.3-3 mm. The fault rocks in most of the faults in the limestone have a recrystallized fabric created by dolomitization (**Figure 5-8i-l**). The dolomitization is localized along the fault and does not appear to affect the limestone protolith or the damage zone. The fault rocks with the most intense brecciation seem to have the highest proportion of dolomite: rhomboid dolomite crystals replaced the fine cataclastic matrix as well as some of the clasts within the chaotic breccia (**Figure 5-8i**, **Figure 5-9**). The original limestone was completely replaced by a fine-grained dolomite when

the fault rock evolved to a cataclasite (**Figure 5-8j**). Some parts of the faults were reactivated allowing for re-brecciation, which formed crackle and chaotic breccias, the clasts of which are composed of dolomitized cataclasites (**Figure 5-8k,l**).

Fault rocks in Torrazzo and Punta Negra 1 fault zones did not experience dolomitization (**Figure 5-8a-f**). The crackle and chaotic breccia contain clasts floating in a very fine-grained calcite cement (**Figure 5-8b,c**). There are very few fine cataclastic fragments. Crackle breccia in Faro fault zone is made up of angular clasts the area between which is filled with a recent fine sedimentary material (**Figure 5-8h**). In dolomite-hosted fault zones, fractures between the clasts in crackle breccias are occasionally cemented by calcite (**Figure 5-8n**), usually they remain open (**Figure 5-8o,p**).

Cataclasites in all outcrops are made up of a few survivor clasts entirely surrounded by a finer cataclastic matrix (**Figure 5-8f,j,q,r**). Very few clasts are bigger than 2 mm in diameter, most are between 0.3-2 mm and make up <30% of the volume. Some cataclasites in dolostone comprise clasts that comprise only c.10% of the volume (**Figure 5-8r**). Particles within the matrix are rounded to sub-rounded. Pressure solution surfaces are also common (**Figure 5-8j**).

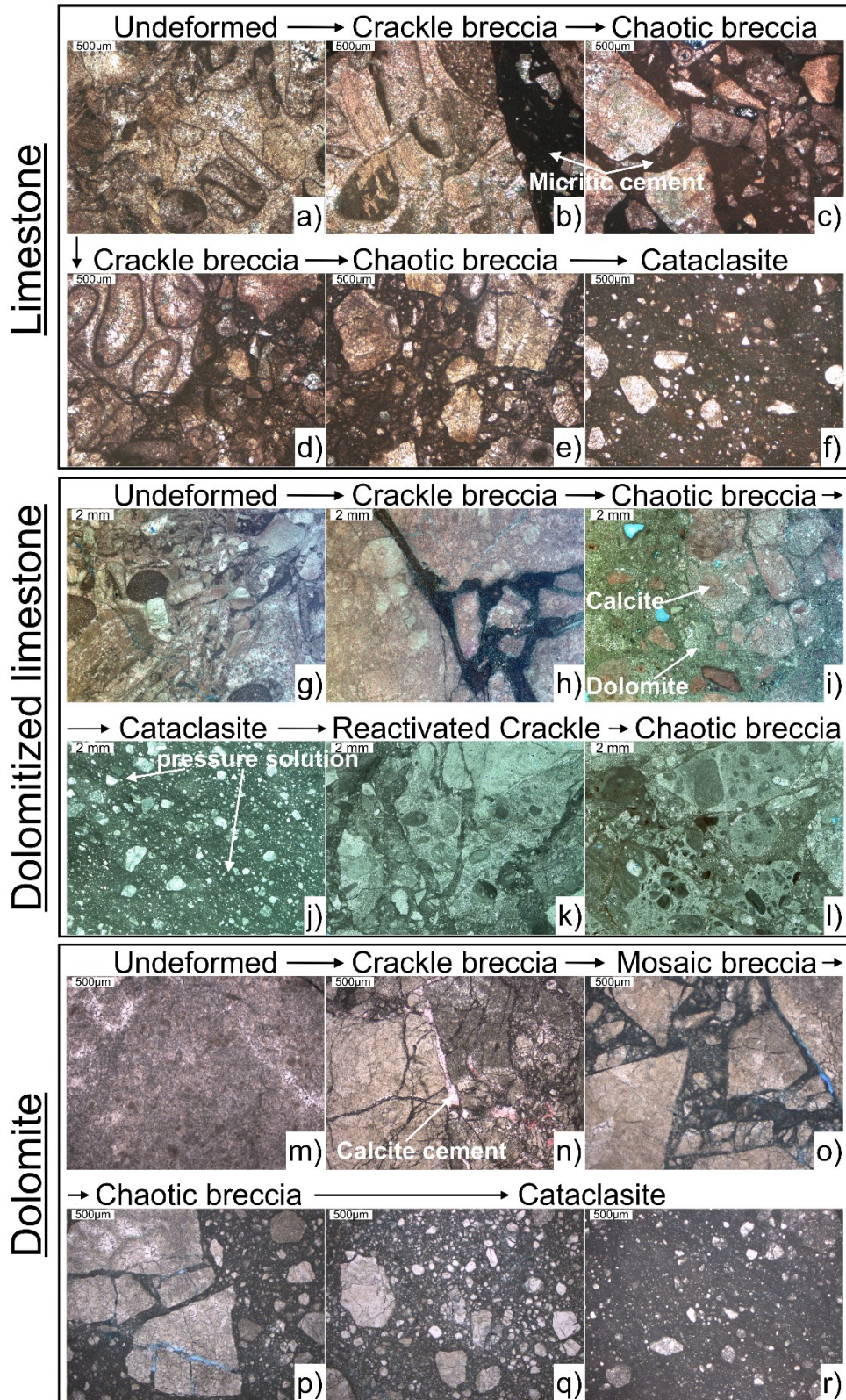


Figure 5-8 Micrographs showing fault rock evolution in tight limestones and dolomites in San Vito lo Capo. The stained (pink) minerals indicate calcite, and unstained – dolomite. Note the pore space along the clast boundaries (o), and calcite cement in the crackle breccia open voids (n). Matrix is typically made up of fine cataclastic material, only the crackle and mosaic breccia in limestone is filled with calcite micritic cement (b,c), and crackle breccia in limestone (Faro fault) is filled with modern sedimentary matrix (h). Porosity is in blue.

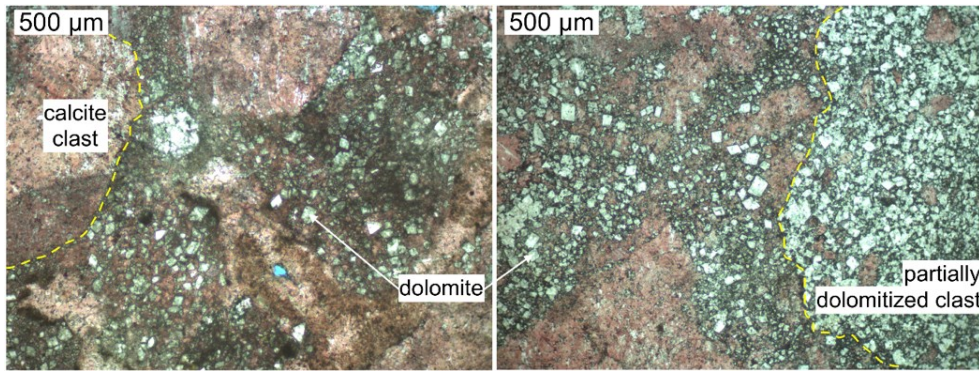


Figure 5-9 Micrographs showing the partially dolomitized chaotic breccia found in limestone-hosted fault zones. Note the rhomboid dolomite shapes within the matrix and large partially dolomitized clast. Most clasts remain calcite and show stained pink colour.

All fault rocks were investigated under CL microscope, and the results indicate that calcite typically shows dark luminescence in shades of brown and dark blue (**Figure 5-10a,b,d,e**). Limestone and dolomite within crackle and mosaic breccias show dark luminescence except for the edges of the clasts – they show orange lining (**Figure 5-10a-c**). Rare calcite cement filling the open voids or cracks in crackle or mosaic breccias shows bright orange luminescence with concentric growth zonation (**Figure 5-10a**).

Cathodoluminescence micrographs of partially dolomitized chaotic breccia clearly distinguishes calcite from dolomite: dolomite rhombs show bright orange luminescence and growth zonation. Both cataclasite fault rock occurring within dolomite-hosted outcrops and the completely dolomitized cataclasites within the limestone-hosted outcrops show light orange luminescence (**Figure 5-10c,f**). Calcitic cataclasite within the limestone-hosted outcrops shows dark luminescence (**Figure 5-10d**).

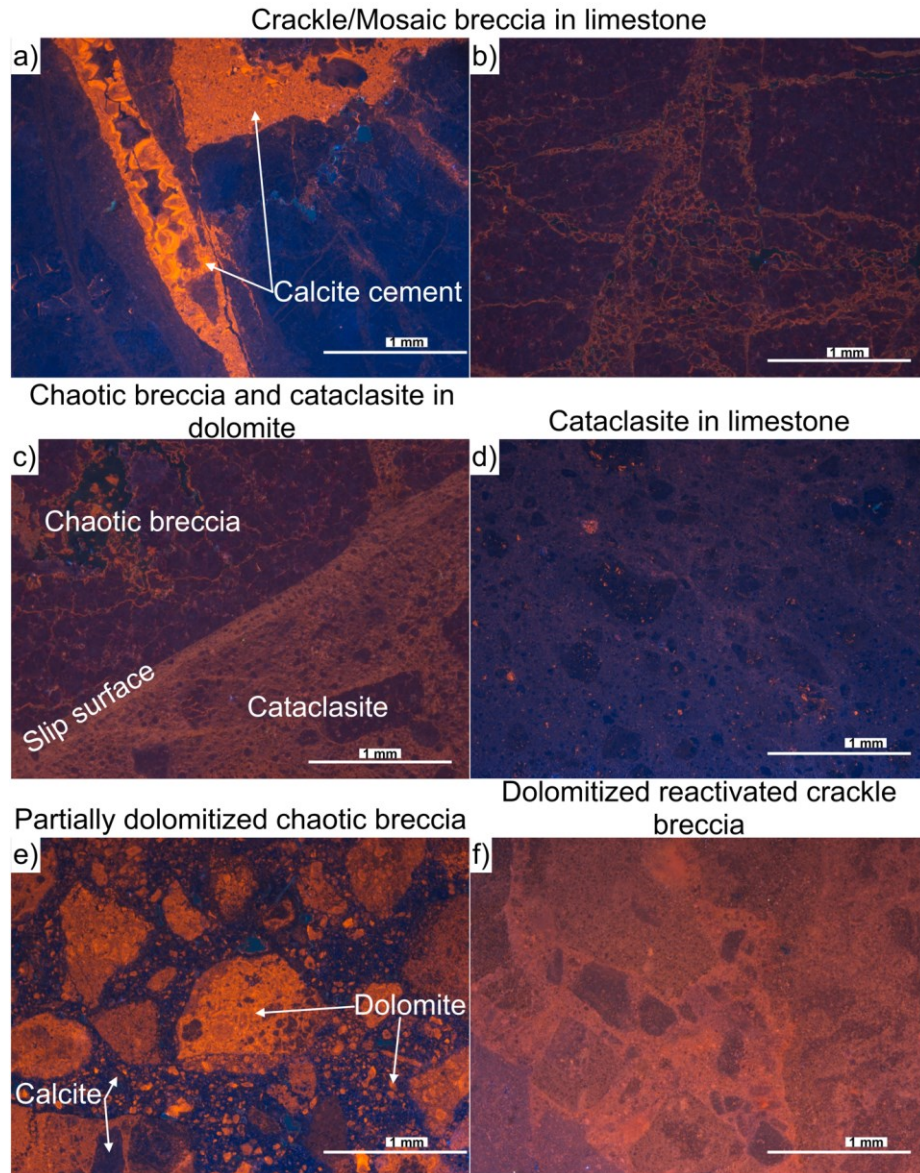


Figure 5-10 Representative CL images of the fault rocks in both tight limestones and dolomites in San Vito lo Capo. Note the typically dark luminescence of a calcite (a,b,d,e) and bright orange luminescence of the dolomitized grains (e,f) and a calcite cement (a).

5.3.4 Fault petrophysical properties

Porosity and permeability measurements of fault rocks and their protoliths show that faulting in tight carbonates almost always increases porosity (**Figure 5-11a**). However, faulting may result in either an increase or decrease in permeability (**Figure 5-11b**). The porosity and permeability for fault and host rocks are similar both for limestones and dolomites: porosity

and permeability of the fault rock range between c.0-15% and 10^{-6} - 10^2 mD, respectively. The results agree with fault rock data for tight limestone in Murge Plateau, Italy (Zambrano et al., 2016) and Northern Calcareous Alps, Austria (Bauer et al., 2016) (**Figure 5-11a,b**). Integration of petrophysical property measurements with CT scans and BSE images show that fault rock porosity and permeability decrease with increasing intensity of deformation. In particular, the crackle, mosaic and chaotic breccias have progressively decreasing porosity and permeability, with the lowest values observed for the cataclasite fault rocks (**Figure 5-11c-e**). Dolomitized cataclasite within the limestone-hosted outcrops has a porosity of 0.2% to 7% and permeabilities of 1×10^{-6} to 2×10^{-1} mD. Porosity and permeability of the cataclasite bands within dolomite-hosted outcrops are 2-5% and 8×10^{-4} - 2.5×10^{-1} mD, respectively. Cemented and cohesive breccias have similar porosity and permeability values to the cataclasites: 1.5-5% and 2×10^{-4} to 1.9×10^{-1} mD, respectively. Incohesive breccias show the highest porosity and permeability values: 3.8-7.2% and 0.2 to 140 mD, respectively (**Figure 5-11d**). Few core plugs have comparably low porosity but high permeability (0.8-2.2% and 3 to 500 mD, respectively), because they have fewer but longer cracks parallel to the length of the core (**Figure 5-11d**).

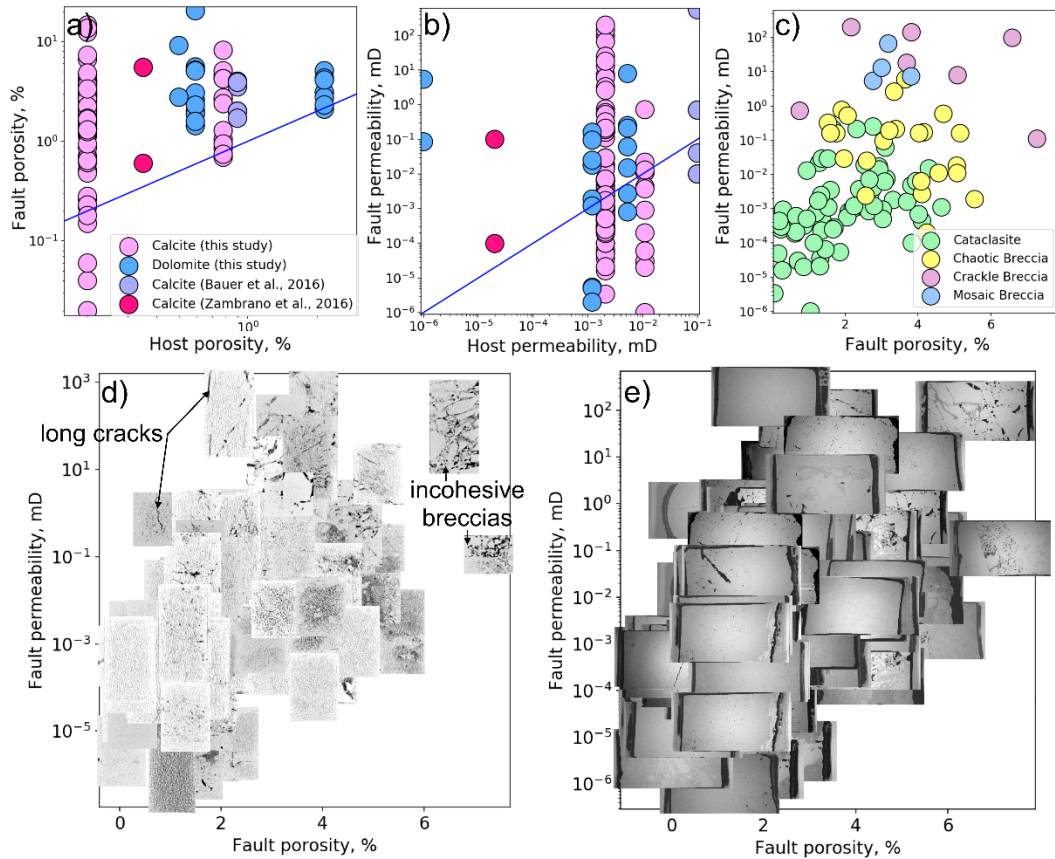


Figure 5-11 Porosity and permeability data for fault and host rock samples collected from tight carbonates in San Vito lo Capo combined with data from the literature. a-b) Porosity-permeability data is coloured in regard to mineralogy of the fault-hosted protolith rock, blue is the 1:1 line. c) Data is coloured in regard to the type of the fault rock. d) CT-scans of the fault rock core plugs. Note that porosity is in black and the higher the rock's density, the whiter the colour. All core plugs are 38 mm in diameter. e) Whole thin section BSEM scans of the fault rocks. Porosity is in black, and the width of the scan is 2.5 cm.

5.4 Discussion

5.4.1 Fault zone evolution

5.4.1.1 Faults in limestone

Based on fault zone internal architecture, abutting/cross-cutting relationships between fracture sets, fault rock width and fault rock microstructure, the faults in the Mid-to-Upper Cretaceous limestone may be separated into 3 groups:

1. Dolomitized faults that have been reactivated (Punta Negra 2,3, Torre Isolidda and El Bahiro faults);
2. Calcitic faults that have not been reactivated (Torrazzo and Punta Negra 3 faults);
3. Dolomitized faults that have not been reactivated (Faro fault).

Group 1 faults may be separated into 2 structural domains: a fault core consisting of a thin layer of cataclasite and incohesive chaotic breccia, and a fractured damage zone. Fracture density is the greatest close to the fault core. These fault rocks have been dolomitized and reactivated during the later faulting events forming polyphase breccias. The reactivation of the fault may be explained by the fault zone maintaining a lower shear resistance than that of the surrounding rock, or progressively decreasing strength as the zone experiences strain or displacement weakening (Sibson, 1977). Strain weakening processes may include; i) grain size reduction (Schmid et al., 1977) caused by cataclasis (Sibson, 1977); ii) water weakening (Carter et al., 1990); or iii) continual recrystallization during which a preferred crystallographic orientation develops (White et al., 1986). In terms of the latter, dolomitization is pervasive in several faults and is known to adversely affect the compressive strength of limestones (e.g., Williams and McNamara, 1992).

Group 2 faults have wider fault cores made up of a calcite cemented chaotic breccia. The fracture patterns associated with this group of faults are similar to others with sets oriented parallel, perpendicular and orthogonal to the principal slip surface, with the perpendicular fracture set being dominant.

Group 2 fault rocks have not been dolomitized possibly because the breccia

was resealed with a calcite microspar cement soon after the brecciation. It is also possible that the increased breccia strength resulting from cementation prevented these faults from being reactivated. All fractures abut against the fault cores of Group 2 faults possibly due to the contrast in mechanical properties between the fault core and damage zone caused by cementation.

Group 3 faults have a similar fault core as Group 1 faults: a thin layer of cataclasite and chaotic breccia, which was dolomitized. However, the breccia is cohesive compared to the incohesive Group 1 fault breccia. Moreover, the fault core was not reactivated as indicated by the monophase cataclasite and breccia. The damage zone is also more complex than that of the other faults: it contains crackle breccia layers parallel and perpendicular to the main fault, which are widely spread throughout the entire fault damage zone. This suggests that the later faulting may have been accommodated in the damage zone rather than the fault core possibly because the thick cohesive fault core was stronger than the surrounding damage zone (e.g., Woodcock et al., 2007). Crackle breccia forming layers within the damage zone of Group 3 fault contain angular clasts and a micritic dark matrix with a red colour. This suggests that the breccia acted as conduit to fluids that carried sediment, which filled the opened cracks and hardened with time. This created a contrast in mechanical properties between the breccia and the surrounding damage zone, which stopped fracture propagation. The fracture patterns associated with Group 3 faults are similar to those around other fault zones, however, the dominant fracture set is oriented parallel to the main fault and perpendicular to the crackle breccia layers. This fracture set cross-cuts the other fractures and abuts against the crackle breccia layers

suggesting that it was the last to form possibly soon after the crackle breccia. Therefore, the crackle breccia layers and the dominant fracture set oriented parallel to the principal slip surface may be the product of the last faulting event.

The aforementioned observations of faults in tight limestone suggest that fault rock does not re-fracture if it is resealed by cement or becomes cohesive and strong due to cataclasis making it stronger than the surrounding damage zone before the next faulting event occurs. Instead, further faulting is concentrated in weaker rocks. However, strain will concentrate around the fault core and allow polyphase fragmentation if the fault rock does not become cemented. In either case, fault zones in the studied limestones may be defined by the single fault core and localised damage zone model (e.g., Billi et al., 2003; Agosta and Aydin, 2006; Billi, 2010).

5.4.1.2 *Faults in dolomite*

Fault zones in San Vito lo Capo peninsula dolostones contain multiple branched cataclastic strands and intensely fragmented and pulverized host rock distributed over a very wide area. The rock appears to have been fragmented into decimetre-sized clasts during the first stages of faulting. Further faulting became localized within the damage zones reducing the clast size even further. Once their size was reduced to 0.5–3 cm, further evolution of the fault zone developed due to cataclastic deformation forming deformation bands reminiscent to those occurring within porous granular rocks. However, deformation bands in porous rocks form primarily by grain

scale cataclasis in contrast to fracture derived cataclasite bands studied in the low-porosity dolostones (Aydin and Johnson, 1978; Antonellini et al., 1994; Morgan and Boettcher, 1999; Fossen et al., 2007; Tondi et al., 2012). During the last stages of deformation, fractures propagated within the weaker pulverized rock but did not cross the harder cataclastic bands.

No principal slip plane and corresponding localised fault gouge was observed within the dolostone outcrops: cataclasites are distributed throughout the whole exposed fault zone. This may be because dolomite is very strong and once the strain is released, fractures propagate laterally rapidly, distributing the strain throughout a large area, instead of localizing the strain as in limestones. The cataclasite bands are not as laterally continuous as the fault rocks observed in limestones, where they can be tracked over the entire fault zone. Instead, they form anastomosing network throughout the fault zone. Therefore, fault zones in dolostones cannot be described in the sense of a single fault core and damage zone model but may better be defined by a multiple-stranded fault core model, similar to that proposed by Faulkner et al. (2003, 2010) for phyllosilicate-rich gouges in Carboneras fault zone or by Schröckenfuchs et al. (2015) and Bauer et al. (2016) for tight dolomites.

5.4.1.3 Fault zone evolution in the local tectonic context

The kinematic indicators identified on the studied faults suggest at least two faulting events. The first was extensional resulting in normal dip-slip displacements observed on the vertical cliff sections in limestones and vertical pure dip-slip striations in dolomites. The second was a strike-slip

event creating horizontal strike-slip striations in dolomites and recent fault scarps along the Faro fault showing left-lateral motion (Tondi et al., 2006b). The studied faults may be divided into 2 different fault sets: 1) NW-SE and NE-SW striking normal faults, dipping to SW and SE, respectively; 2) NNE-SSW and WSW-ENE trending strike-slip faults, showing left-lateral motion. Kinematics of these fault sets agree with the trends of the strike-slip deformation bands in the Castelluzzo plain analysed by Tondi et al. (2006b), and the local tectonic observations by Giunta et al. (2000) suggesting that extensional faulting occurred in the Late Miocene before the strike-slip faulting in the Plio-Pleistocene, which reactivated the previous normal fault structures. Despite experiencing similar deformation history, fault zones in the dolomite evolved in a very different manner to those in the limestone (**Figure 5-12**):

- 1) In the Late Miocene, during the first stages of normal fault initiation, displacement in limestone outcrops was localized along a narrow fault surface forming discontinuous fault rock on the slip plane and fractures concentrated around the main slip surface and oriented parallel and perpendicular to the strike of the fault (**Figure 5-12-1a**). Displacement in dolomite outcrops was distributed throughout a large area by intense fracturing and fragmentation, forming a large volume of pulverized rock (**Figure 5-12-1b**).
- 2) Fault rock in limestone evolved into a continuous fault core as displacement increased and was dolomitized (**Figure 5-12-2a**) or resealed by calcite cement (**Figure 5-12-2b**). In the

meantime, fault rock in dolomites was disintegrated into very small clasts and started acting as a porous rock, allowing single cataclasite bands to form in a NNW and W direction (**Figure 5-12-2c**). Therefore, faulting in dolomite switched from porosity-increasing processes (fracturing, fragmentation) to porosity-reducing processes (cataclasis).

- 3) In the Plio-Pleistocene, strike-slip events in limestone fault zones reactivated the uncemented fault cores forming polyphase breccias (**Figure 5-12-3a**). Strike-slip movements in dolomite fault zones developed a pervasive cataclasite band network throughout the entire fault zone (**Figure 5-12-3b**). Older cataclasite bands evolved to clustered zones and new cataclasite band sets formed in NW direction. Fractures formed in orthogonal direction to the strike of the slip surfaces and abutted against the previously inherited larger scale fractures. Evolving deformation then fractured the dolomitized fault rocks in limestone and pulverized rock between the cataclasite bands in dolomite cross-cutting only the thinnest bands.

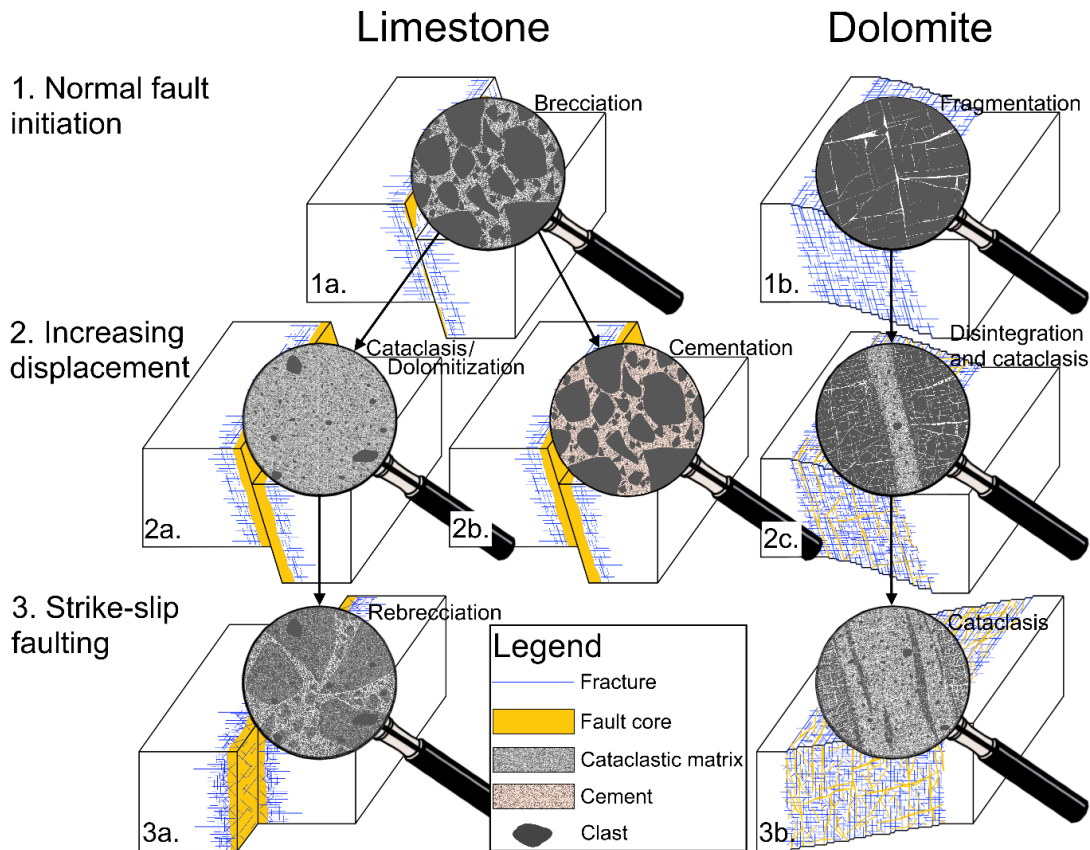


Figure 5-12 Conceptual models of the fault zone evolution in tight limestones and dolomites in San Vito lo Capo. Not to scale.

5.4.1.4 Mineralogy impact on fault zone architecture

Fault zone and fault core widths have been plotted against displacement using a revised compilation (**Table 5-1**) to Solum and Huisman (2017), and included the mineralogy of the protolith (**Figure 5-13**). Overall, fault zone thickness appears to scale linearly with displacement both for limestone and dolomite (**Figure 5-13a**). Several faults in dolomite show relatively thin fault cores for a given displacement compared to those in limestone, whereas several fault cores in limestones are thick compared to the general trend (**Figure 5-13b**). Accurate fault zone widths are more difficult to determine than the relatively thin cores due to limitation of size of many outcrops (**Figure 5-13a**). However, Bussolotto et al. (2007, 2015) argue that damage

zone thickness is not proportional to displacement and does not evolve any more after a threshold represented by the development of the main fault plane. Mayolle et al. (2019) show that fault damage zone thickness in carbonates scales linearly for displacements <100 m, above which opening-mode damage thickness tends to saturate rather than spread. Even though the widths of the studied fault zones were hard to determine, data from the available outcrops suggest that the fault zone in the Pellegrino quarry is wider than the one of the Faro fault proportionally to their displacements (**Figure 5-13a**).

The spread in the fault displacement-thickness relationships may be explained by the variation of fault zone architectures (e.g., single- and multiple-core fault zones). Mineralogy proved to have a significant impact on the fault zone architecture with the lower bounds of displacement-fault core thickness values representing calcitic limestones, and the upper bounds characterizing dolomites. Therefore, even though our triaxial tests showed that dolostone is at least 2 times stronger than the limestone (**Figure 5-2**), higher solubility and plasticity of calcite compared to dolomite allow limestone to accommodate more strain prior to faulting. On the other hand, faults and fractures propagate within the stronger dolomite where pre-failure strains are smaller (Ferrill and Morris, 2008) creating wide zones of deformation.

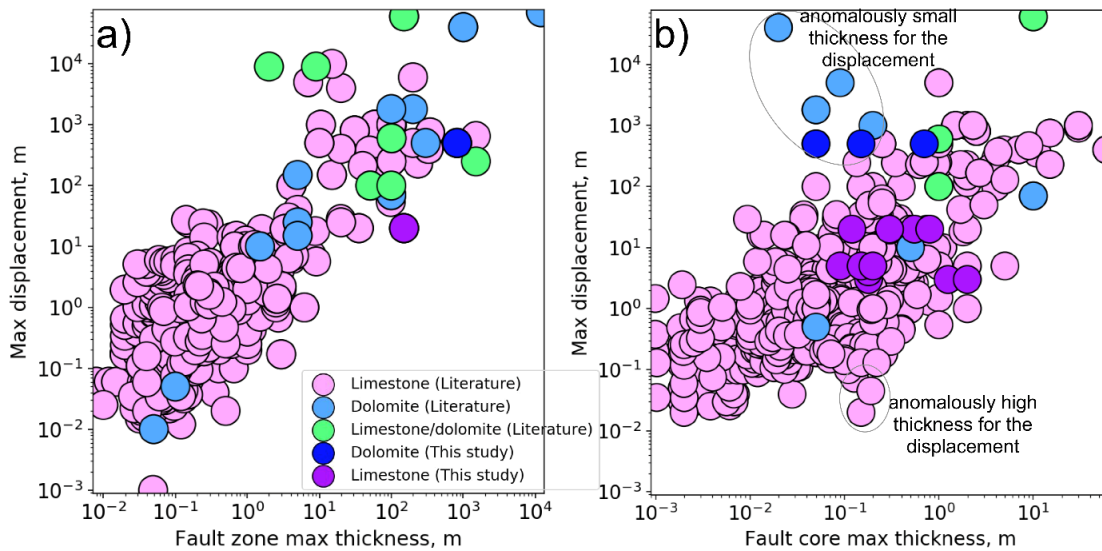


Figure 5-13 Logarithmic graphs showing relationships between maximum displacement and (a) fault zone and (b) fault core maximum thickness for carbonate rocks from a variety of areas compiled from literature (**Table 5-1**) and this study. Data is coloured based on mineralogy of the fault-hosting rock and the source data came from. a) Number of data points (n)=403; b) n =607.

Table 5-1 Reference list of the compiled displacement and fault zone thickness data for carbonate rocks (**Figure 5-13**). Studied location, fault kinematics and fault-hosted carbonate protolith mineralogy are listed for each reference. Limestone+dolomite indicate mixed limestone and dolomite sequences, whereas limestone, dolomite shows that faults in the studied area occurred both in limestone and dolomite outcrops.

Reference	Location	Fault kinematics	Carbonate rock type
Wojtal and Mitra (1986)	Southern Appalachian, USA	Thrust	Limestone+dolomite
Stewart and Hancock (1991)	Crete, Greece	Normal	Limestone
Roberts (1994)	Sub-Alpine Chains, France	Thrust	Limestone
Roberts and Stewart (1994)	Gulf of Corinth, Greece	Normal	Limestone
Childs et al. (1996)	Yorkshire, United Kingdom	Normal	Limestone

Ramsey and Onasch (1999)	USA	N/A	Limestone, dolomite
Salvini et al. (1999)	Southern Apennines, Italy	Strike-slip	Limestone
Antonellini and Mollema (2000)	The Southern Alps, Italy	Strike-slip	Dolomite
Grandinetti et al., (2000)	Northern Apennines, Italy	Thrust	Limestone
Teixell et al. (2000)	Pyrenees, France	Thrust	Limestone
Anders et al. (2001)	Utah, USA	Normal	Limestone+dolomite
Linzer et al. (2002)	Northern Alps, Austria	Strike-slip	Dolomite
Billi (2003)	Southern Apennines, Italy	Strike-slip	Limestone
Billi et al. (2003)	Southern and Central Apennines, Italy	Strike-slip, Transtensional, Normal	Limestone
Faulkner et al. (2003)	SE Spain	Strike-slip	Dolomite
Graham et al. (2003)	Central Apennines, Italy	Normal	Limestone
Micarelli et al. (2003)	Gulf of Corinth, Greece	Normal	Limestone
Sagy et al. (2003); Ran et al. (2014)	Dead Sea Rift, Israel	Normal	Limestone+dolomite
Young et al. (2003)	Suez rift, Egypt	Normal	Limestone
Konon (2004)	Holy Cross Mountains, Poland	Normal	Limestone+dolomite
Kostakioti et al. (2004)	Ionian Zone, Greece	Thrust	Limestone

Mazzoli et al. (2004)	Southern Apennines, Italy	Normal	Limestone
Mirabella et al., (2004)	Northern Apennines, Italy	Normal	Limestone
Agosta and Aydin (2006)	Central Apennines, Italy	Normal	N/A
Géraud et al. (2006)	Gulf of Corinth, Greece	Normal	Limestone
Graham Wall et al. (2006)	Letan, Albania	Strike-slip	Limestone
Micarelli et al. (2006)	Sicily, Italy	Normal	Limestone
Tondi et al. (2006a)	Central Apennines, Italy	N/A	Limestone
Bonson et al. (2007)	Malta	Normal	Limestone
Bussolotto et al. (2007)	Central Apennines, Italy	Normal	Limestone
Cappa et al. (2007)	Coaraze, France	Strike-slip	Limestone
Frost et al. (2009)	Eastern Alps, Austria	Strike-slip	Limestone+dolomite
Gaviglio et al. (2009)	Sussex, United Kingdom; Mons Basin, Belgium	Normal	Limestone
Wilson et al. (2009)	Suez Rift, Egypt	Normal	Limestone
Bastesen and Braathen (2010)	Suez Rift, Egypt; Oman; Svalbard, Norway	Normal	Limestone
Zahm et al. (2010)	Texas, USA	Normal	Limestone

Efstratios (2011)	West Macedonia, Greece	Normal	Limestone
Ferrill et al. (2011)	Texas, USA	Normal	Limestone
Elvik (2012)	Suez Rift, Egypt	Normal	Limestone
Healy et al. (2012)	Malta	Normal	Limestone
Matonti et al. (2012)	South Provence, France	Transtensional	Limestone
Reyer et al. (2012)	Lower Saxony, Germany	Normal	Limestone
Tondi et al. (2012)	Sicily, Italy	Strike-slip	Limestone
Bastesen et al. (2013)	Suez rift, Egypt	Normal	Limestone
Guglielmi et al. (2013)	SE France	Normal	Limestone
Tesei et al. (2013)	Northern Apennines, Italy	Thrust	Limestone
Bartel et al. (2014)	Southern Alps, Italy	Thrust	Dolomite
Collettini et al. (2014)	Northern Apennines, Italy	Normal	Limestone
Korneva et al. (2014)	Murge Plateau, Italy	Strike-slip, Normal	Limestone
Korneva et al. (2014)	Basilicata Region, Italy	Strike-slip, Transtensional	Limestone
Valoroso et al. (2014)	Central Apennines, Italy	Normal	Limestone
Woodcock et al. (2014)	South Wales, United Kingdom	Strike-slip, Thrust	Limestone

Brogi and Novellino (2015)	Northern Apennines, Italy	Normal	Limestone
Bussolotto et al. (2015)	Central Apennines, Italy	Normal	Limestone
Fondriest et al. (2015)	Italian Southern Alps, Italy	Transtensional	Dolomite
Lena et al. (2015)	Umbria-Marche Apennines, Italy	Thrust	Limestone
Novellino et al. (2015)	Southern Apennines, Italy	Normal	Limestone
Bauer et al. (2016)	Northern Alps, Austria	Strike-slip	Dolomite, limestone
Sagi et al. (2016)	Yorkshire, United Kingdom	Normal	Limestone
Tondi et al. (2016)	Sicily, Italy	N/A	Limestone
Zambrano et al. (2016)	Murge Plateau, Italy	Strike-slip	Limestone
Johannessen (2017)	Central Apennines, Italy	N/A	Limestone
This study	Sicily, Italy	Strike-slip, Normal	Dolomite, limestone

5.4.2 Impact of faulting on permeability

The thick fault cores in limestone containing cemented breccia or cataclasite surrounded by cohesive chaotic breccia act as a barrier to fracture propagation. Their permeability is in the range of 1×10^{-6} to 2×10^{-1} mD, which is similar or lower than the permeability of the protolith matrix (4×10^{-4} to 2×10^{-2} mD). Moreover, they are continuous, and hence could form baffles to cross-

fault fluid flow. Dolomitization of the fault rock comprising the other thin fault cores started at the stage of a chaotic breccia formation: rhombic dolomite crystals started replacing the fine calcite fragments produced by cataclastic deformation within the matrix and at the edges of the clasts. The entire fault rock became dolomitized with developing deformation. Similar observations of dolomitization related to tight limestone brecciation was observed by Tarasewicz et al. (2005). The authors suggested that fractures provided conduits for dolomitizing fluids, which diffused slowly into the limestone fragments. Likewise, it is likely that Group 1 and 3 fault cores in limestone-hosted outcrops acted as preferential flow pathways during the first-stages of faulting. Fault rock in Group 3 faults was affected by cross-cutting fractures as a result of later deformation, which would prevent them from acting as significant barriers to flow. Group 1 fault was not reactivated during the later stages of faulting perhaps because it underwent higher displacement than the other faults (20 m (Tondi et al., 2006b) compared to 3-5 m displacement for the Group 3 faults) producing a thicker and cohesive breccia layer which was stronger than the surrounding damage zone. Therefore, it is likely that faults in tight limestone always act as conduits to fluid flow unless they become cemented during or soon after the brecciation or experience high displacement and form continuous cohesive low permeability breccia layers.

The cataclasite bands in dolostones are pervasive throughout a very large area and are cross-cut by fractures only where they are thinner than c.3 cm. The cataclasite bands have a permeability of 8×10^{-4} to 2.5×10^{-1} mD, which is similar to the protolith matrix (1×10^{-3} to 1×10^{-2} mD). Therefore, since they are

not fractured, they are potential permeability baffles, and the size of the compartments is determined by the spacing between the band swarms.

The fracture density is higher within the dolomite-hosted fault zones compared to those within the limestone. However, fractures are wider and longer in the limestone damage zones than those hosted within the dolomite. Detailed modelling would be required to assess the implications of these differences on overall permeability, which is beyond the scope of this study.

5.4.3 Application to other dolomite reservoirs

Faults in tight dolomite-hosted outcrops have also been studied in several other locations: Sala Consilina quarry, Italy; Padul quarry in Granada basin, Spain; and Gaaden quarry, Austria (**Figure 5-14**). They all show striking similarities: wide fault zones consisting of distributed intensely fragmented rock and numerous 2nd order faults bounding compartments of the disintegrated rock (**Figure 5-14c**), and often form anastomosing cataclastic band networks (**Figure 5-14b**). Therefore, the proposed model (**Figure 5-12**) may be applied to other dolomite reservoirs or their analogues, despite having different tectonic histories.

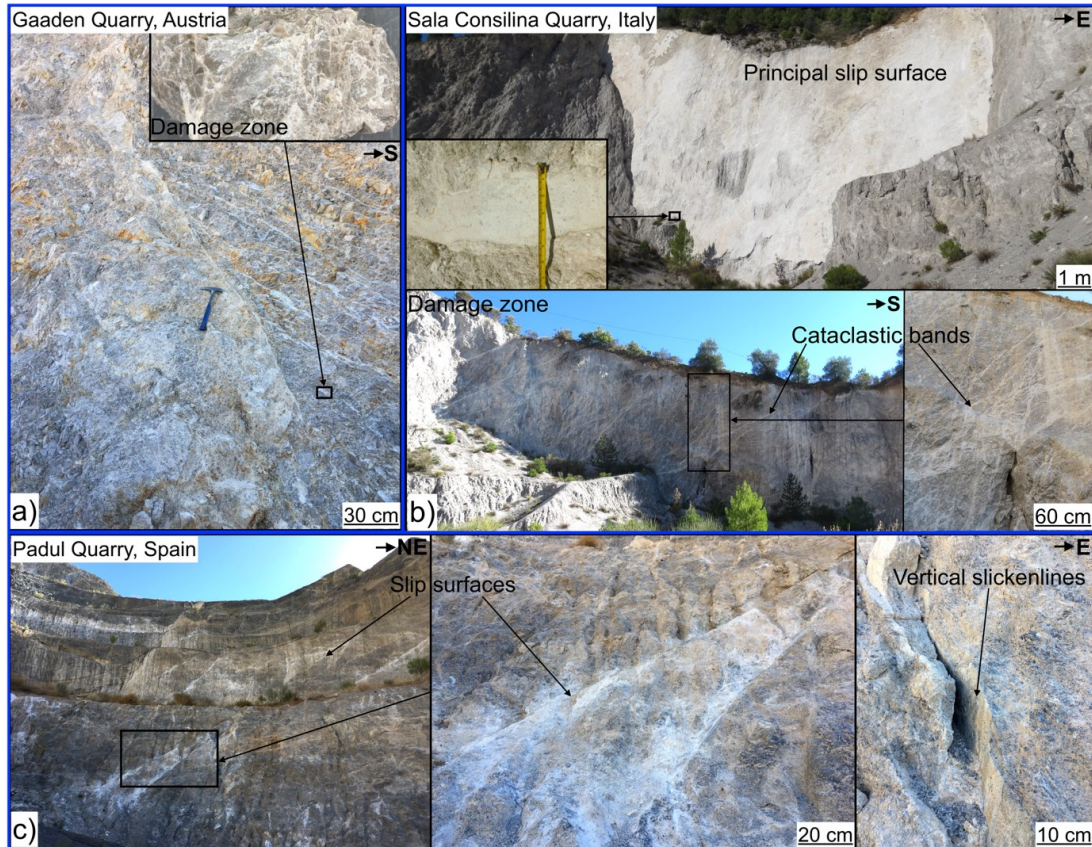


Figure 5-14 Photographs of fault zones observed in several dolomite outcrops in Europe: a) Gaaden Quarry, Austria; b) Sala Consilina Quarry, Italy; c) Padul Quarry, Spain. Note the intensely fragmented rock within the damage zone of all faults, and the white cataclasite rocks reminiscent to the ones in San Vito lo Capo.

5.5 Conclusions

Single fault core and damage zone models are often used for all faulted carbonate rocks. The compilation of documented fault core width and displacement data were compared in association with fault-hosted rock mineralogy, and the results show that fault core is generally thicker for limestones than for dolomites. A total of 9 fault zones were studied in limestones and dolomites in San Vito lo Capo peninsula, Sicily, Italy, with host rock porosity <2%. Proposed models for fault zone evolution suggest that unlike limestones, dolomites do not form a single fault core, but rather a complex network of anastomosing cataclasite bands spread throughout the fault zone length. The reason for this contrasting behaviour is possibly that

the dolomite is far more brittle than calcite resulting in intense fragmentation and disintegration of large volumes of rock during the first stages of faulting. These processes create a rock that is then prone to deform in a manner that is similar to that of porous granular rocks.

The differences between faults in limestones and dolomites may also have significant implications for fluid flow in the subsurface. In particular, the cataclasite bands create a connected network throughout the dolomite-hosted fault zone and only thinnest bands are cross-cut by fractures, therefore, making them potential baffles to fluid flow. The majority of the fault cores in limestone were dolomitized, later re-brecciated and then cross-cut by fractures suggesting that for most of the fault history they acted as conduits to fluid flow. Only the thick continuous chaotic breccia fault cores in limestone, which were resealed by calcite cement soon after the brecciation or became cohesive due to cataclasis, stop fracture propagation and were not reactivated during later stages of faulting and hence would likely form local baffles to cross-fault fluid flow.

Chapter 6 Mechanical properties of carbonates

6.1 Introduction

A number of studies have been conducted aiming to increase understanding of the deformational behaviour of carbonate rocks (e.g., Baud et al., 2000; Vajdova et al., 2004a; Baud et al., 2009). Analysed interactions between intrinsic and extrinsic properties and their effect on the rock strength indicate that deformation mechanisms are more complex in carbonates than in porous sandstones and the key controls on deformational behaviour remain poorly understood. In particular, hydrostatic and triaxial deformation experiments on sandstones indicate that most sands deform in a non-linear, inelastic manner at low (i.e. < 5 MPa) confining pressures (Zhang et al., 1990). At higher confining pressures, sands and sandstones compact elastically (linear compaction) until their yield point at which their compressibility increases. Sands placed under hydrostatic compression (i.e. $\sigma'_1 = \sigma'_3$) typically have yield points that lie between 2 and 70 MPa, while for cemented sandstones yield occurs from 40 to >1200 MPa (Wong et al., 1997). Wong et al. (1997) showed that hydrostatic and non-hydrostatic loadings are coupled in a triaxial compression experiment. In the compactive regime, they identified the yield stress as the onset of shear-enhanced compaction, C^* , at which the triaxial volumetric curve manifests an accelerated compaction with respect to a hydrostatic test.

All failure modes recognized for sandstones in the laboratory at the onset of inelastic deformation involve microcracking (e.g., Menéndez et al., 1996;

Baud et al., 2004). Two end-member modes of deformation based on the macroscopic structure of the sample following yield are localized and distributed deformation (e.g., Jamison and Stearns, 1982). Discrete slip planes form due to localised deformation whereas strain is accommodated throughout the sample during distributed deformation. The yield point at hydrostatic conditions, P^* , is inversely related to the grain-size and porosity, which is consistent with a Hertzian fracture model (Zhang et al., 1990).

In carbonates microcracking is not always the dominant deformation mechanism because even at room temperature additional deformation mechanisms such as mechanical twinning, dislocation slip and pressure solution may be active (e.g., Baud et al., 2000; Vajdova et al., 2004a). Baud et al. (2000) and Vajdova et al. (2004a) suggest that carbonates of intermediate porosity (3-18%) show dilatancy and shear localization in dry conditions and at low confining pressure, whereas shear-enhanced compaction is the most important deformation process at higher confining pressures and differential stresses. Even though hydrostatic loading always initiates compaction, whether porosity decreases or increases at yield depends on the interchange between pore collapse mechanisms and microcracking, which tends to dilate the sample (Wong et al., 2004). These authors suggest that large strain will cause compaction only if the increasing network of microcracks do not coalesce to produce shear localization. Higher porosity carbonates (>30%) generally display no macroscopic dilatancy but show shear-enhanced compaction even at low confining pressures (Baud et al., 2009). A micromechanical model involving plastic pore collapse (Curran and Carroll, 1979) was tested on the experimental data in the compactive

regime to explain the interplay of dilatancy and compaction of carbonate rocks (e.g., Baud et al. 2000; Vajdova et al., 2004a; Zhu et al., 2010). However, this had limited success indicating that a more appropriate model is needed to take into account the coupling between plasticity and microcracking. Previous works were limited by a few carbonate rock types and porosities (**Table 6-4**), such as very tight (<1.1%) Carrara and Yule marble (Hugman and Friedman, 1979; Walton et al., 2015), highly porous (>30%) Majella and Saint Maximin limestone (Baud et al., 2009; Zhu et al., 2010) and intermediate porosity (10-20%) Tavel, Indiana, Oolithe Blanche limestone (Vajdova et al., 2004a, 2010; Zhu et al., 2010; Regnet et al., 2015; Walton et al., 2015). In this study, the scope of previous studies was extended to include carbonates with a wider range of porosities and microstructures. In particular, the focus was placed on the intrinsic variables of the rocks that may have an impact on different failure mechanisms. Microstructural analysis was conducted to determine the initial grain sizes and dominant porosity types, and mercury injection capillary pressure (MICP) tests were conducted to determine the pore throat size distributions. Microstructural and macrostructural deformation was inspected using optical microscopy and CT-scanning, respectively. All samples were loaded up to a maximum confining pressure of 70 MPa under hydrostatic conditions. Those samples that did not fail under hydrostatic loading were then used for multistage-failure triaxial tests.

6.1.1 Microstructural controls on deformation

Deposition in varying environments coupled with later diagenetic alteration produces heterogeneous carbonates with complex microstructures. Often

these carbonates have a multimodal pore-size distribution (e.g., Anselmetti et al., 1998; Choquette and Pray, 1970; Pittman, 1971), which has a significant effect on the physical properties and mechanical behaviour of porous carbonates. Zhu et al. (2010) showed that the microporosity within the grains and cement is where microcrack damage initiates, leading to the collapse of macropores during deformation in the cataclastic flow regime. The heterogeneous microporosity distribution causes deformation to become partitioned between the constitutive elements of the rock: cement, micritic matrix and grains (e.g., Dautriat et al., 2011; Vajdova et al., 2012; Regnet et al., 2015). Baud et al. (2017) suggested that variations in the amount of cement may lead to large differences in mechanical strength and could promote or inhibit different localized failure modes during compaction. Samples in this study cover a number of lithofacies to include varying pore types, grain composition, porosity and cement volumes to investigate the impact of microstructures on mechanical behaviour.

6.1.2 Water weakening effect on deformation

The depletion events of the Ekofisk oil reservoir in the North Sea show how the presence of water can result in significant weakening of chalk (e.g., Teufel et al., 1991). In highly porous chalk, yield strength appears to negatively correlate with the saturation of water present in the rock (e.g., Risnes et al., 2005). A similar trend has been observed in moderate and low porosity limestones (e.g., Rutter, 1974; Lebedev et al., 2014). Nicolas et al. (2016) suggest that water has a weakening effect in the brittle regime: in their study stresses at the onset of dilatancy, C' , are lower for brine saturated samples than for those that were dry. The authors did not observe any

obvious effect of water on the stresses at the onset of inelastic compaction, C^* . In this study, tests have been performed on both dry and water saturated samples to account for any discrepancies occurring due to the water weakening effect.

6.2 Material and methods

6.2.1 Sample material

The samples used in the study come from numerous outcrops across six European countries (**Table 6-1**). Measurements were conducted on a wide range of rock types including: grainstones, packstones, boundstones, wackestones, mudstones and crystalline carbonates; their porosity ranges from <1 to 52%. All samples are essentially monomineralic consisting of at least 95% calcite or dolomite. Examples of the microstructure, pore throat size and grain size distributions of a range of the rock samples is provided in **Figure 6-1**.

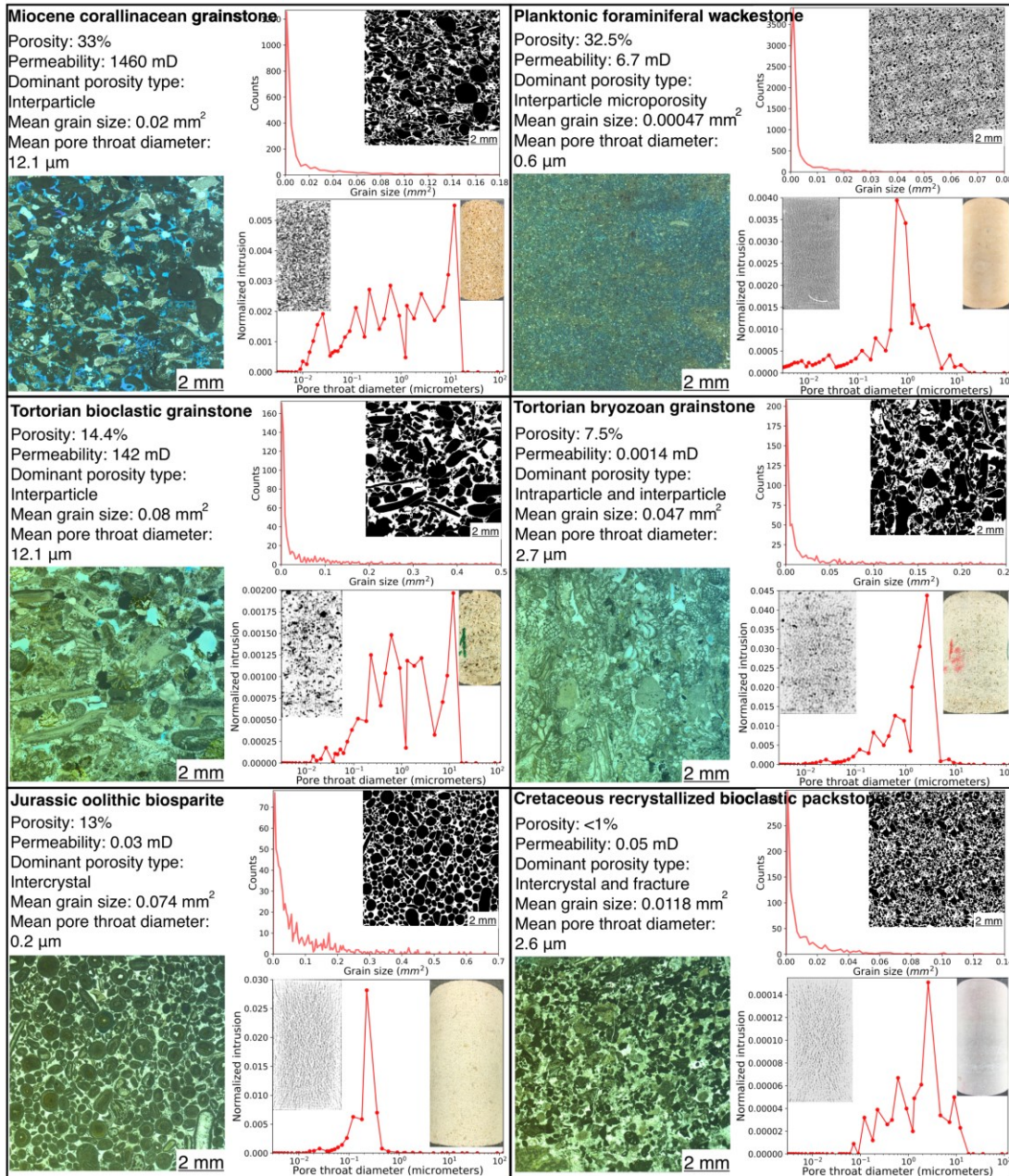


Figure 6-1 Examples of the studied rock samples with the data collected on them: grain size distribution with an interpreted grain map; optical micrograph; and MICP data displaying pore throat size distribution with photographs of the core plugs and their CT-scan transects. Note that porosity on the CT-scans is in black, whereas grains are shown in white – the whiter the colour, the denser the grains. CT-scans and core plug photographs are 38 mm in width.

Table 6-1 Summary of sample data used in this study. The carbonate rock and pore types were described as explained in **Section 2.1.1** and **Section 2.1.2.1**, respectively. PS refers to pressure solution.

Location	Formation	Rock classification	Age	Dominant pore type	Porosity (%)
United Kingdom:					
Flamborough Head	Chalk	Calcite cemented wackestone with veins	Upper Cretaceous	Interparticle microporosity and intercrystal	25.7
Isle of Thanet (Pegwell and Dumpton bays)	Chalk	Wackestone	Upper Cretaceous	Interparticle microporosity	39.6
North York Moors	Coralline Oolite	Calcite cemented oolitic grainstone	Oxfordian	Intercrystal	10
Cleeve Hill	Inferior Oolite Group	Calcite cemented oolitic grainstone	Middle Jurassic	Intercrystal	9.7
Italy:					
Gargano (Molinella)	Gravina calcarenite	Bioclastic grainstone	Lower Pleistocene	Interparticle	38
Gargano (Vignanotica)	Maiolica Formation	Radiolarian mudstone with veins	Tithonian–Aptian	Interparticle microporosity	8.8
San Vito lo Capo peninsula	1) Bioclastic grainstone	1) Bioclastic grainstone	1) Lower Pleistocene	1) Interparticle 2) Moldic	1) 43 2) 7.8 3) 2

	2) Cemented bioclastic grainstone	2) Calcite cemented bioclastic grainstone	2) Lower Pleistocene	3) Vugs 4) Fractures along	4) 5.6 5) <1 6) <1
	3) Dolomite 4) Marl 5) Cemented bioclastic packstone	3) Crystalline dolomite 4) Planktonic foraminiferal	Triassic 4) Middle Cretaceous 5) Lower Cretaceous-	stylolites and interparticle microporosity 5) Intercrystal	7) <1 8) <1 9) <1
	6) Bivalve packstone 7) Scaglia Formation 8) Crystalline limestone 9) Recrystallized bioclastic packstone	wackestone with stylolites 5) Cemented bioclastic packstone with veins 6) Bivalve packstone with veins and PS 7) Foraminiferal packstone with PS 8) Crystalline limestone with veins 9) Recrystallized bioclastic packstone	6) Dogger- Malm. 7) Eocene- Upper Cretaceous 8) Lias- Norian 9) Middle- Upper Cretaceous	6) Intercrystal 7) Fractures along PS 8) Fractures 9) Intercrystal	
Sicily (Favignana)	Bioclastic grainstone	Bioclastic grainstone	Lower Pleistocene	Interparticle	52
Greece (Rhodes island):					

Kallithea	Cape Arkhangelos calcarenite	Bioclastic grainstone	Lower Pleistocene	Interparticle	44.5
Kamiros	Profitis Ilias Unit	Pelagic radiolarian wackestone with veins	Upper Triassic- Upper Cretaceous	Intercrystal	<1
Spain (Granada basin):					
Cacín	Temperate- carbonate (TTC) sediments	1) Bryozoan grainstone 2) Bioclastic grainstone	Tortonian	1) Intraparticle and interparticle 2) Interparticle	1) 7.5 2) 14.4
Alfacar	Travertine	Boundstone	Pliocene- Quaternary	Vugs	23
Road-cut on highway N- 323, Bailén- Motril	Tuffa	Boundstone	Pliocene- Quaternary	Vugs	49
Malta:					
Malta island (Ghar Lapsi and Blue Grotto)	1) Globigerina Limestone Formation 2) Upper Coralline Limestone Formation	1) Planktonic foraminiferal wackestone 2) Bioclastic packstone 3) Bioclastic grainstone containing	Oligocene to Miocene	1) Interparticle microporosity 2) Interparticle 3) Interparticle	1) 32 2) 32.5 3) 9

	3) Lower Coralline Limestone Formation	benthic foram and red algae			
Gozo island (South of Gozo)	Attard Member	Rhodolitic algal packstone	Chattian	Interparticle	22
Austria:					
Gaaden	Dolomite	Crystalline dolomite with veins	Upper Triassic	Fracture	<1
St Margarethen	Leitha Limestone	1) Coralline grainstone 2) Coralline rudstone	Middle Miocene	1) Interparticle 2) Intraparticle	1) 33 2) 15

6.2.2 Sample preparation

The internal structure of the samples was investigated using a GE Bravo medical-style CT-scanner. These scans were used to identify the best position for drilling core plugs to avoid large vugs or fractures. Core plugs were drilled from the bulk sample blocks in a direction perpendicular to the apparent bedding plane. Depending on the size of the bulk sample, 2 or 4 core plugs were drilled from one block: half were used for dry and the other half for the water-saturated tests.

6.2.3 Experimental procedure

Each core plug was photographed and CT-scanned before and after the mechanical testing. If the sample remained intact during the testing, porosity and permeability were measured before and after the deformation. Thin sections for microstructural analysis were prepared from the undeformed and deformed samples.

6.2.3.1 Mechanical testing

The triaxial compression tests were conducted with the aim of determining the yield stress of the samples, as described in **Section 3.6.1.1** and **Section 3.6.1.2**. A total of 113 hydrostatic tests were conducted with loading-unloading cycles to constrain the evolution of irrecoverable strains, as well as 54 multiple and continuous failure state triaxial tests to produce the residual strength envelope.

6.2.4 Microstructural analysis

Blue-dyed epoxy-impregnated polished thin sections were prepared for the microstructural analysis from small blocks (2.5 x 4.5 cm) of undeformed

samples cut perpendicular to the bedding, and from deformed samples that were cut along a plane parallel to the axial direction of the core plug. The deformed core plugs were fragile so they were impregnated with epoxy before cutting to preserve their internal deformation.

Over a hundred images were taken for each thin section at a magnification of 4x using an optical microscope at a resolution of c.0.7 pixels per μm with a pixel size of 1.45 μm . The images were stitched together in Image Composite Editor (ICE) to produce a montage covering 9 × 9 mm area of each thin section. These optical images were used to make a microstructural map by manually outlining the grains, using the photo editor software GIMP. Processed images were imported into the image analysis software ImageJ to measure grain size.

6.2.5 Petrophysical properties

Porosity, permeability and pore throat sizes were measured as described in **Section 3.5**.

6.3 Results

6.3.1 Mechanical experiments

6.3.1.1 Hydrostatic tests

All samples were loaded and unloaded under hydrostatic conditions. The stress-strain curves during loading and unloading were not identical (**Figure 6-3 to Figure 6-6**) suggesting that all the samples experienced at least minor non-elastic deformation. The apparent irrecoverable strain may be explained by the presence of pre-existing cracks, which were closed during the initial loading and did not fully re-open during unloading, resulting in a stiffening of

the samples. Only the very porous samples (>30%) reached their yield point during the hydrostatic tests due to the 70 MPa maximum confining pressure available. At yield, these samples experienced an accelerated increase in volumetric strain. Three different behaviours were observed following yield:

- 1) Stress-strain curves showed strain hardening beyond the yield point punctuated by episodic stress drops (**Figure 6-2a**);
- 2) Stress-strain curves were flat beyond the yield point and then showed strain hardening behaviour (**Figure 6-2b**);
- 3) Stress-strain curves showed strain hardening beyond the yield point (**Figure 6-2c**).

Samples were deformed up to 6-16% of volumetric strain. Unloading paths of all the tests show that permanent compaction is significant in all the cases (**Figure 6-2**).

Water weakening is apparent for these samples, and differences in P^* for the dry samples may be as much as double those of the saturated samples.

However, slight differences in porosity and textural composition between the samples should be accounted for.

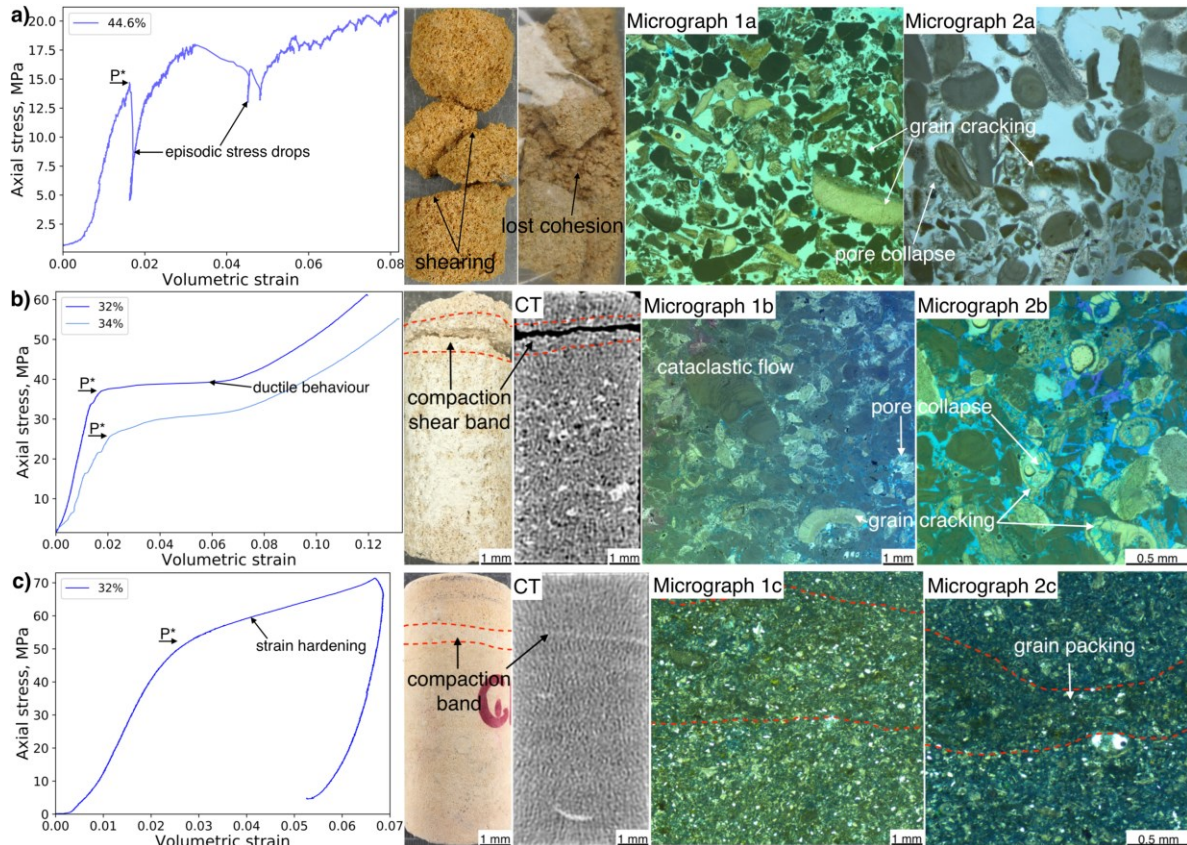


Figure 6-2 Examples of mechanical data for hydrostatic compression experiments on porous carbonates. These examples were chosen to show differences in failure mechanisms: a) Lower Pleistocene bioclastic grainstone was sheared or lost overall cohesion; b) Miocene coralline grainstone failed due to compactive shear banding; whereas c) Planktonic foraminiferal wackestone showed compaction banding during the failure. Critical pressure, P^* , is marked with arrows on the stress-strain curves.

6.3.1.2 Multiple and continuous failure state triaxial tests

Multistage-failure triaxial tests were performed on samples that did not fail under hydrostatic loading (samples with porosities <30%). Mechanical data for representative multistage-failure triaxial experiments and their results are shown in **Figure 6-3** to **Figure 6-6**. Two different behaviours were observed at yield: 1) sudden volumetric strain increase (**Figure 6-3** & **Figure 6-4**); and 2) sudden volumetric strain decrease (**Figure 6-5** & **Figure 6-6**). Volumetric strain increase was observed for samples with porosities >10%. Samples with porosities <6% experienced a strain decrease at yield, whereas samples

with porosities between c.6 and 10% indicated mixed behaviours. Typically, core plugs taken from the same bulk sample showed similar behaviour despite having slightly different porosities or being deformed under dry or wet conditions. Cemented samples showed complex mechanical behaviour. For example, partially cemented Plio-Pleistocene bioclastic grainstone with porosity c.7% indicated a switch in deformational behaviour. Volumetric strain abruptly decreased at initial yield at 5 MPa confining pressure, but at confining pressures above 15-20 MPa samples started showing sudden volumetric increase at each yield point. Volumetric strain decrease at yield is typically followed by ductile behaviour (**Figure 6-6**), except for the cemented dry samples, which show strain hardening beyond yield (**Figure 6-5**).

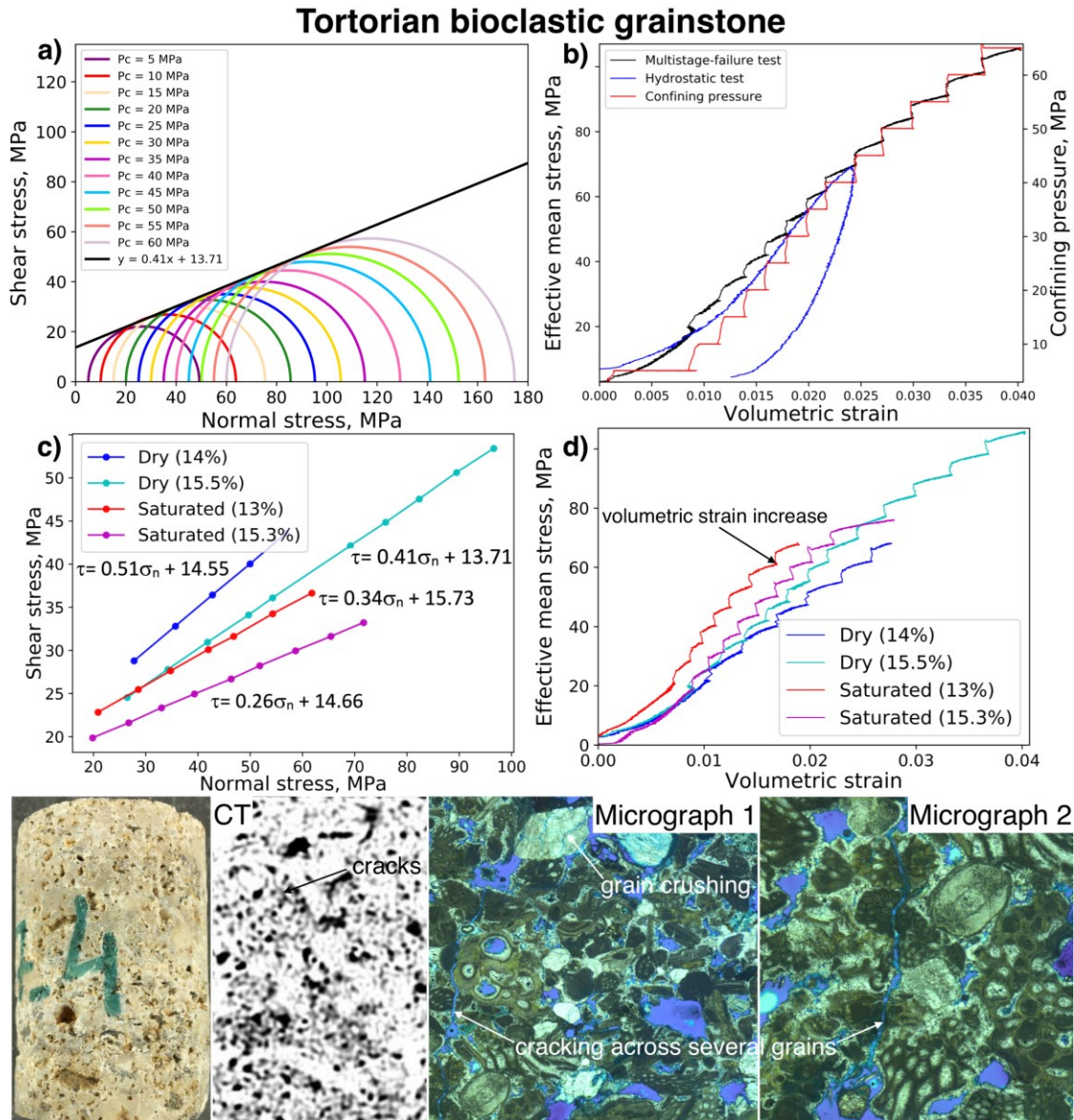


Figure 6-3 Examples of multistage-failure triaxial tests conducted on intermediate porosity limestone samples (c. 14.4%) beyond failure. a) Mohr circles for one of the b) multistage-failure tests. Note that inflection points on effective mean stress-volumetric strain graph show a sudden volumetric increase when confining pressure was increased to the next higher increment. c) Mohr diagrams with shear failure envelopes for all d) multistage-failure tests done on the Tortorian bioclastic grainstone samples. Numbers in the legend show porosity values (%). Photograph and CT-scan transect show macroscopical deformation of the samples. Micrographs illustrate dominant deformation mechanisms which caused the macroscopical failure of the samples: singular grain crushing and cracking across several grains. Both mechanisms are focused around the surfaces of the pores.

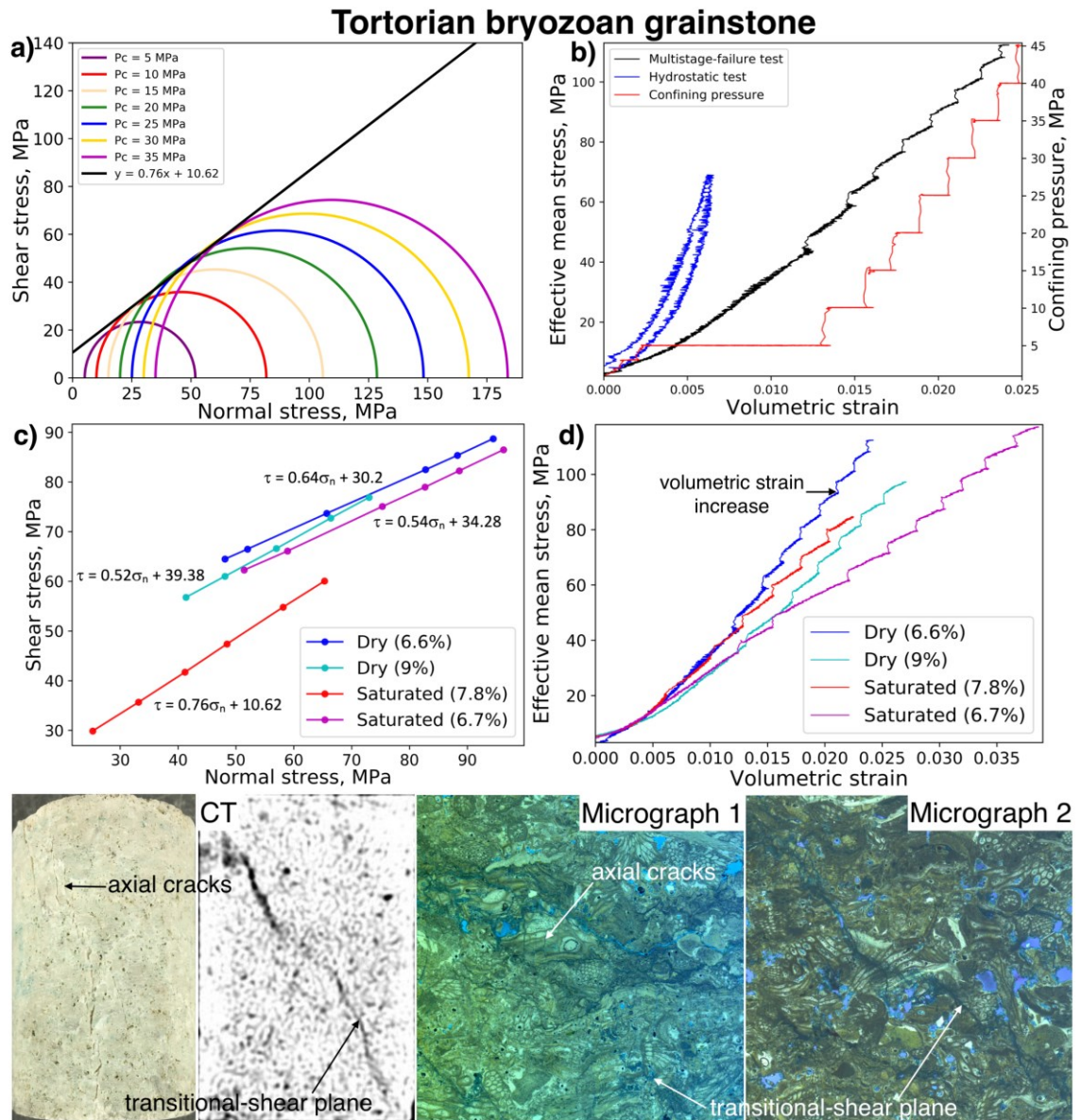


Figure 6-4 Examples of multistage-failure triaxial tests conducted on intermediate porosity limestone samples (c.7.5%) beyond failure. a) Mohr circles for one of the b) multistage-failure tests. Inflection points on effective mean stress-volumetric strain graph show a sudden volumetric increase when confining pressure was increased to the next higher increment. c) Mohr diagrams with shear failure envelopes for all d) multistage-failure tests done on the Tortorian bryozoan grainstone samples. Numbers in the legend show porosity values (%). Photograph and CT-scan transect show macroscopical deformation of the samples. Micrographs illustrate dominant deformation mechanisms which caused the macroscopical failure of the samples: brittle axial splitting with transformation to transitional-shear failure.

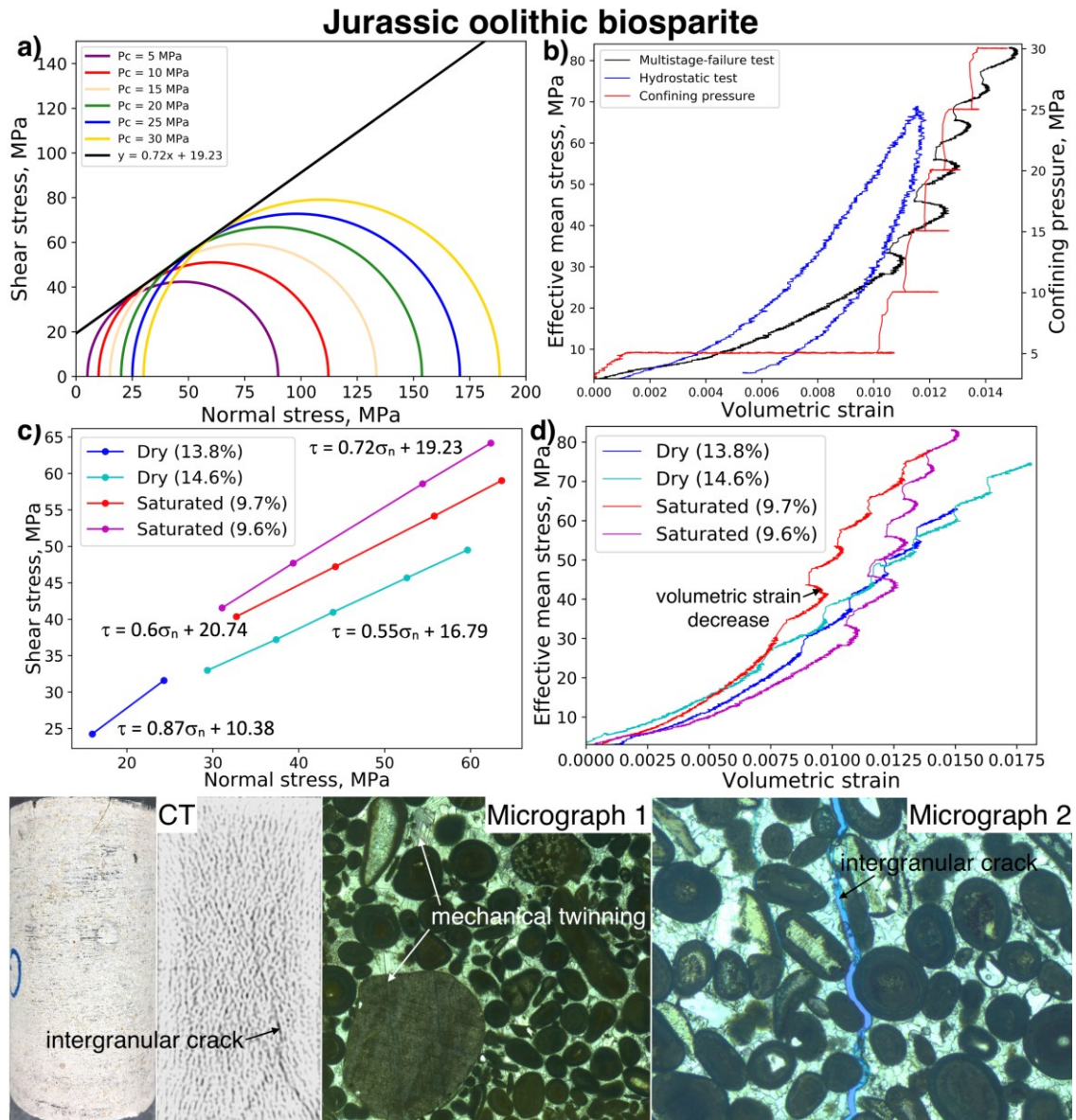


Figure 6-5 Examples of multistage-failure triaxial tests conducted on completely cemented limestone samples with porosity <13% beyond failure. a) Mohr circles for one of the b) multistage-failure tests. Inflection points on effective mean stress-volumetric strain graph show a sudden volumetric decrease and a strain hardening behaviour until the next increase in confining pressure. c) Mohr diagrams with shear failure envelopes for all d) multistage-failure tests done on the Jurassic oolitic biosparite samples. Numbers in the legend show porosity values (%). Photograph and CT-scan transect show macroscopical deformation of the samples. Micrographs illustrate dominant deformation mechanisms which caused the macroscopical failure of the samples: mechanical twinning of the cement and the grains, and intergranular cracks within the cement.

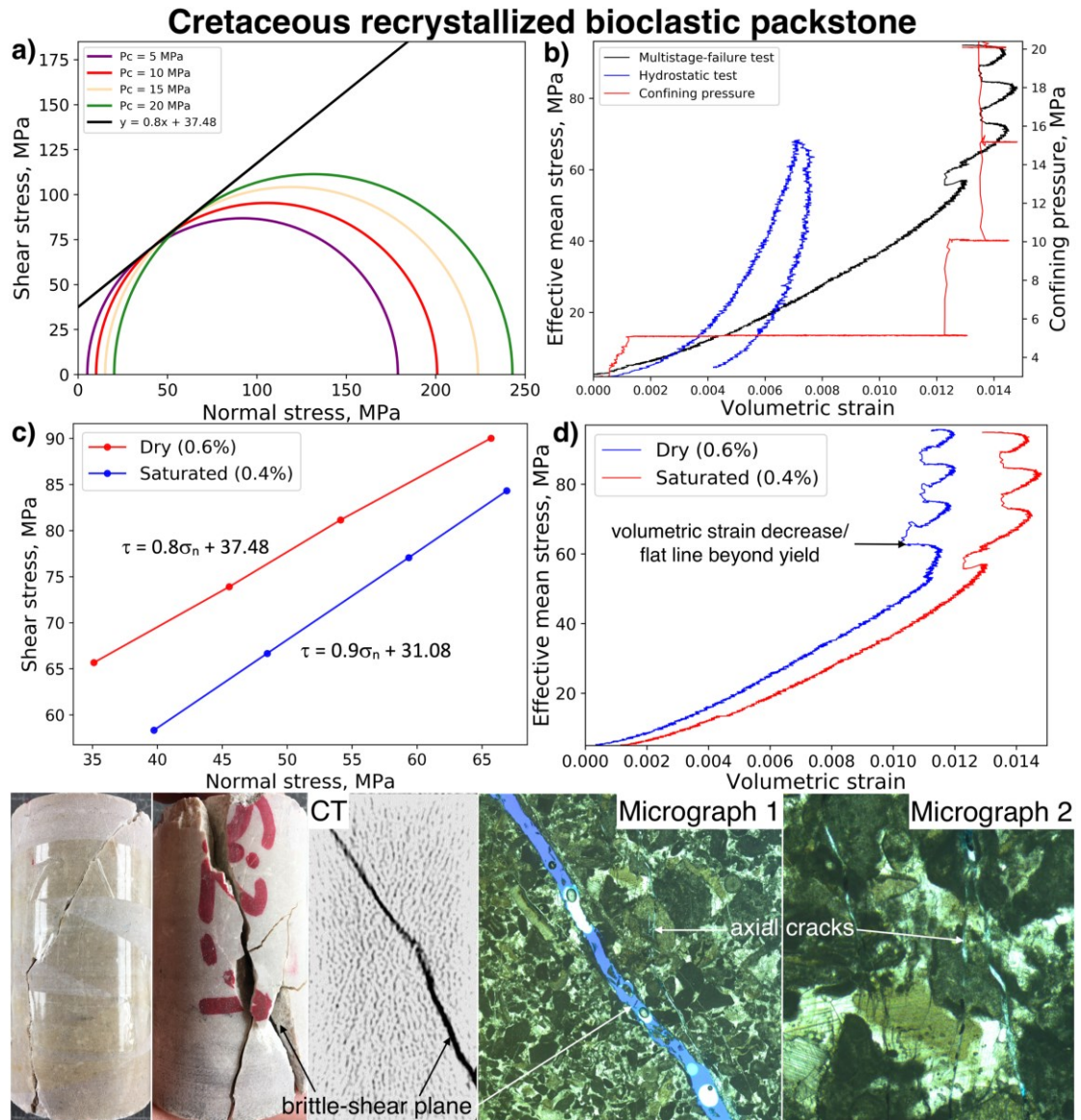


Figure 6-6 Examples of multistage-failure triaxial tests conducted on tight limestone samples (<1%) beyond failure. a) Mohr circles for one of the b) multistage-failure tests. Inflection points on effective mean stress-volumetric strain graph show a sudden volumetric decrease followed by a flat line until the next increase in confining pressure. c) Mohr diagrams with shear failure envelopes for all d) multistage-failure tests done on the Cretaceous recrystallized packstone samples. Numbers in the legend show porosity values (%). Photographs and CT-scan transect show macroscopical deformation of the samples. Micrographs illustrate dominant deformation mechanisms which caused the macroscopical failure of the samples: brittle-shear plane at an angle of c.57° and axial cracks that terminate at the main shear plane.

Friction coefficient and cohesion, determined from the Mohr circles, both increase within increasing yield stress but the data are very scattered (**Table 6-3** and **Figure 6-7**).

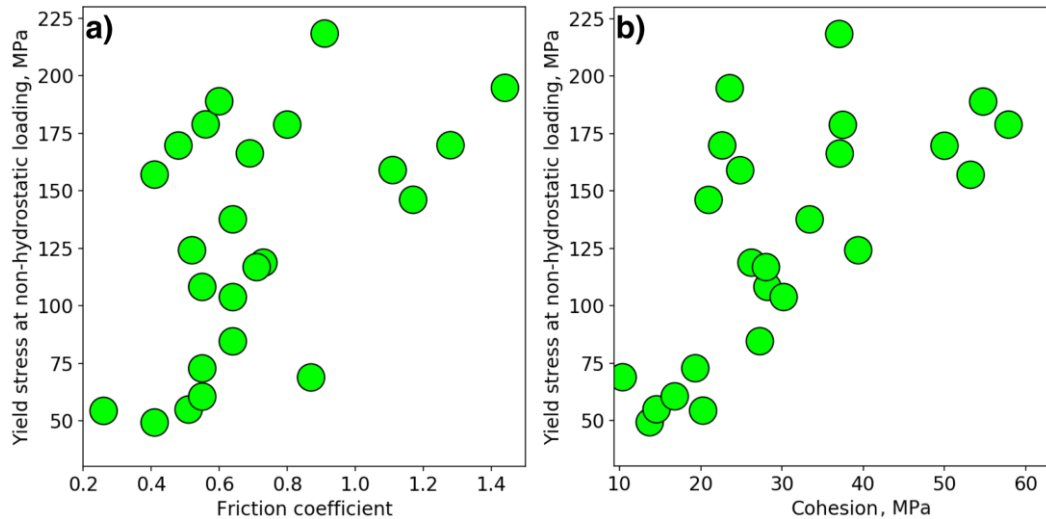


Figure 6-7 Yield stress measured during the multistage-failure tests plotted against a) friction coefficient, and b) cohesion (MPa).

6.3.2 Macroscopic deformation

Few highly porous (>40%) samples remained intact after deformation under hydrostatic loading. The bonds at the grain contacts were ruptured allowing for the rock to lose cohesion (**Figure 6-2a**), and hence macrostructural failure could not be inspected. Hydrostatically failed samples, which survived the deformation, typically show overall compaction – decrease in bulk volume. Visual inspection of the post-deformation samples revealed the presence of strain localization in the form of 1) compaction-shear bands (**Figure 6-2b**), and 2) compaction bands (**Figure 6-2c**). Compaction-shear bands contain macroscopic cracks indicating that the bands are not purely compactive (Baud et al., 2009).

After the multistage-failure loading, samples with porosity >25% show overall compaction: the diameter and axial length of the core plugs decreased by up to c.2 mm after the deformation. Samples with porosities between 10 and 20% show either minor compaction (<1 mm) or slight barrelling. Visual inspection of the samples after the tests indicates discontinuous cracking

throughout the sample (**Figure 6-3**). The recovered low porosity (<10%) samples were macroscopically sheared at angles between 45 and 80° (**Figure 6-4 & Figure 6-6**). Typically they show single shear planes or shear planes with multiple fractures splaying from the main shear surface (brecciation).

6.3.3 Microscopical deformation

Several dominant deformation mechanisms that caused the macroscopical failure of the samples were observed. The dominant failure mode under hydrostatic loading is cataclastic flow, which occurs by deformation mechanisms such as; i) grain crushing with cracks propagating at grain contacts; and ii) increase in the efficiency of grain packing. High-porosity fine-grained samples such as chalk and bioclastic packstone show increased grain packing compared to their undeformed rock (**Figure 6-8a**), and some samples show localized compaction resulting in the formation of compaction bands (**Figure 6-2c**). The larger grains indicate moldic pore collapse or singular grain cracking. High-porosity coarse-grained grainstones and packstones experience pore collapse as a result of grain crushing (**Figure 6-8b-d**). Grain crushing is manifested either by cracks propagating at grain contacts (**Figure 6-8d**), or by grains being abraded at their edges (**Figure 6-8b-c**). The original grains, thus, became surrounded by seams of fragments produced by cataclasis.

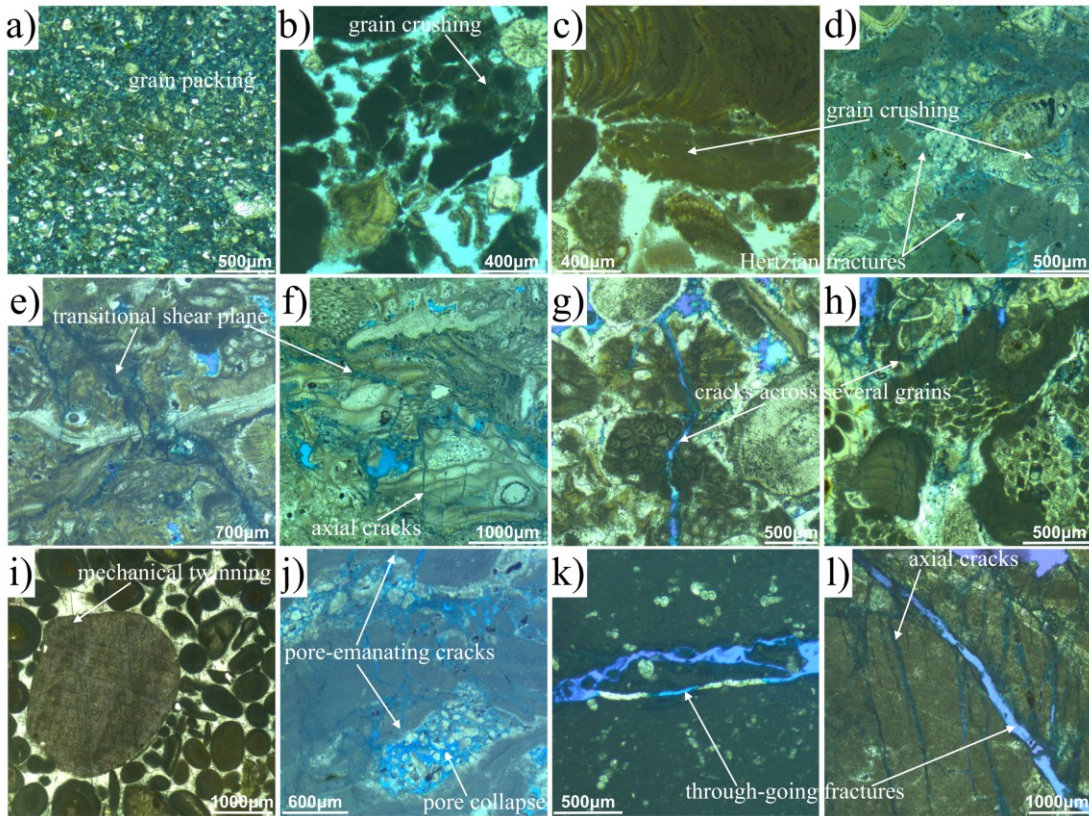


Figure 6-8 Micrographs showing examples of the dominant failure deformation mechanisms observed throughout the deformed carbonate rock samples. The pore space is highlighted by blue epoxy dye.

The dominant deformation mechanisms responsible for failure during multistage-failure loading were; i) mechanical twinning, and ii) microcracking. Microcracking occurs in the form of cracks propagating at grain contacts, pore-emanating cracks, intergranular and transgranular cracks. Transgranular cracks form brittle-shear planes or as axial cracks that coalesce to form a transitional shear-plane (**Table 6-3**). Transitional shear planes occur within samples with porosity between c.6 and 10% (**Figure 6-4**, **Figure 6-8e-f**). The tightest samples (<6%) show singular brittle-shear at which axial cracks terminate (**Figure 6-8l**). Cemented samples show pronounced mechanical twinning both within the spar and the grains compared to the undeformed specimens (**Figure 6-5**, **Figure 6-8i**). Some of these samples show discontinuous axial intergranular cracking (**Figure 6-5**).

Deformation within samples with large macropores and overall porosity between 10-20% is mostly pronounced around those pores. Stress concentrations near the irregular macroporosity resulted in focused damage in the periphery of the macropores and comminution that lead to pore collapse. Damage is manifested by pore-emanating cracks that propagated across a few grains and by grains being crushed around the surface of the pores (**Figure 6-3, Figure 6-8g**).

Core plugs from the same samples deformed to different strains show the same types of failure deformation mechanisms, only the extent and intensity of failure increased with increasing strain. Microstructural damage shows no difference between the samples deformed under dry or wet conditions, only for the slightly more intense deformation observed for the saturated samples.

Table 6-2 *Hydrostatic test results showing P^* values measured on dry and saturated samples on various carbonates. Samples were failed beyond the yield point, and deformation mechanisms which caused the macroscopical failure of the samples are indicated.*

Location	Rock classification	P^* (Dry, Saturated*)	Failure deformation mechanism
United Kingdom Flamborough Head	Calcite cemented wackestone with veins	56*	Distributed cataclastic flow
Isle of Thanet	Wackestone	17.1; 10.2*	Compaction band; Distributed cataclastic flow
Italy: Gargano (Molinella)	Bioclastic grainstone	27.2	Shear-compaction band

San Vito lo Capo peninsula	Bioclastic grainstone	14; 11.4*	Shear-compaction band; Distributed cataclastic flow
Sicily (Favignana)	Bioclastic grainstone	4.8; 2.7*	Distributed cataclastic flow
Greece (Rhodes island): Kallithea	Bioclastic grainstone	10.7	Shear-compaction band
Spain (Granada basin): Road-cut on highway N-323, Bailén-Motril	Boundstone	3.3	Distributed cataclastic flow
Malta: Malta island	1) Planktonic foraminiferal wackestone 2) Bioclastic packstone	1) 49.1; 23.1* 2) 28.3; 19.8*	1) Compaction band; Distributed cataclastic flow 2) Distributed cataclastic flow
Austria: St Margarethen	Corallinacean grainstone	30.7; 22.4*	Shear-compaction band

Table 6-3 Multistage-failure triaxial test results showing p - q values at yield point measured on dry and saturated samples on various carbonates at the confining pressure of 5 MPa. Samples were recovered after a few failure points, reaching confining pressures between 20 and 70 MPa. Friction coefficient and cohesion values determined from the Mohr circles are also indicated, as well as the deformation mechanisms which caused the macroscopical failure of the samples.

Location	Rock classification	Yield stress at 5 MPa confining pressure (Dry, Saturated*)		Friction coefficient	Cohesion	Failure deformation mechanism
		P	Q			
United Kingdom:						
North York Moors	Calcite cemented oolitic grainstone	42.7; 33.9*	112.7; 86.6*	0.72; 0.82*	27.1; 17.7*	Mechanical twinning; Intergranular cracking
Cleeve Hill	Calcite cemented oolitic grainstone	24.9; 31.9*	59.6; 80.2*	0.71; 0.66*	13.6; 20*	Mechanical twinning; Intergranular cracking
Italy:						
Gargano (Vignanotica)	Radiolarian mudstone with veins	59.9	164.7	0.48	50	Brittle-shear failure
San Vito lo Capo peninsula	1) Calcite cemented bioclastic grainstone	1) 44.36; 44.5*	1) 117.8; 118*	1) 0.6; 0.63*	1) 30.8; 30.2*	1) Pore-emanating cracks
	2) Planktonic foraminiferal	2) 68.3; 65.1*	2) 189.7; 180.2*	2) 1.44; 1*	2) 23.6; 32.5*	2) Fractures along stylolites

	wackestone					
	with stylolites					
	3) Cemented bioclastic packstone	3) 63;	3) 173.7;	3) 0.8;	3) 37.5;	3) Brittle-shear failure
		57*	155.6*	0.9*	31.1*	
	with veins					
	4) Bivalve packstone	4) 91.1;	4) 247.9;	4) 1.3;	4) 28.1;	4) Brittle-shear failure
	with veins	74.3*	207.6*	1.1*	34.93*	
	and PS					
	5) Foraminiferal packstone	5) 58.2;	5) 159.4;	5) 1.1;	5) 23.74;	5) Brittle-shear failure
		37.6*	90.1*	0.8*	33.1*	
	with PS					
	6) Crystalline limestone	6) 55.7	6) 152	6) 0.4	6) 53.2	6) Brittle-shear failure
	with veins					
	7) Recrystallized bioclastic packstone	7) 52.1	7) 141	7) 1.2	7) 21	7) Brittle-shear failure
Greece (Rhodes island):						
Kamiros	Pelagic radiolarian wackestone with veins	70.3;	188.2;	0.91;	37; 27.1*	Brittle-shear failure
		53*	143.6*	0.97*		
Spain (Granada basin):						
Cacín	1) Bryozoan grainstone	1) 41.3;	1) 109;	1) 0.58;	1) 34.8;	1) Transitional shear
		28*	68.7*	0.65*	22.5*	

						planes
	2) Bioclastic grainstone	2) 20.7; 19.8*	2) 47; 44.3*	2) 0.46; 0.3*	2) 14.3; 15.2*	2) Pore-emanating cracks
Alfacar	Boundstone	19.2	42.4			Pore-emanating cracks
Malta:						
Malta island (Ghar Lapsi and Blue Grotto)	Bioclastic grainstone containing benthic foram and red algae	31.5; 30.3*	79.5; 75.7*	0.64; 0.54*	27.3; 23.8*	Transitional shear planes
Gozo island (South of Gozo)	Rhodolitic algal packstone	21.5; 23.1*	49.3; 54.1*	0.26; 0.53*	20.3; 13.9*	Distributed cataclastic flow
Austria:						
Gaaden	Crystalline dolomite with veins	56.6	154.6			Brittle-shear failure
St Margarethen	Corallinean rudstone	27.7; 19.1*	67.7; 41.8*	0.55; 0.54*	19.3; 13*	Pore-emanating cracks

6.3.4 Microstructural texture impact on mechanical behaviour

All measured initial intrinsic sample properties are plotted against yield stress in **Figure 6-9**. Data show that yield stress at hydrostatic and non-hydrostatic loading is most strongly correlated with porosity (**Figure 6-9a,d**). The dominant deformation mechanisms that caused the macroscopical failure of the samples also correlate well with the porosity and may be divided into 3 porosity intervals: i) high porosity (25-53%); ii) intermediate porosity (6-25%); and iii) low porosity (<6%). High-porosity samples failed due to distributed cataclastic flow, compaction or compactive shear localization (**Table 6-2**). Deformation mechanisms for samples with intermediate-porosity include pore-emanating cracking, transitional-shear failure and mechanical twinning, whereas low-porosity samples failed due to brittle-shear failure (**Table 6-3**).

Pore size shows no correlation with the yield stress under hydrostatic loading (**Figure 6-9c**). Yield stress under non-hydrostatic loading and pore size follow a power law relationship (**Figure 6-9f**). The samples with the largest pore size have the lowest yield stress and is associated with pore-emanated cracking. The largest pore size corresponds to interparticle, moldic and vug porosity. The samples with the smallest pore size have the highest yield stress and indicates brittle and transitional-shear failures. The smallest pore size is associated with intercrystalline porosity and microporosity.

Grain size shows a poor correlation with yield stress both under hydrostatic and non-hydrostatic loading (**Figure 6-9b,e**). Even though highly porous (>25%) coarser-grained samples generally tend to have slightly lower yield stress compared to finer-grained carbonates, the values are widely spread and samples with similar porosity but different grain size may have similar

yield stresses (**Figure 6-9b**). However, grain size has an impact on the type of failure deformation mechanism for the very porous samples (>25%). In particular, fine-grained wackestones and packstones showed grain packing and distributed or localized cataclastic flow but no shearing, whereas coarse-grained grainstones were sheared or lost cohesion to become a cohesionless granular material. Moreover, the deformation mechanism that resulted in failure was the same for both hydrostatic and non-hydrostatic tests.

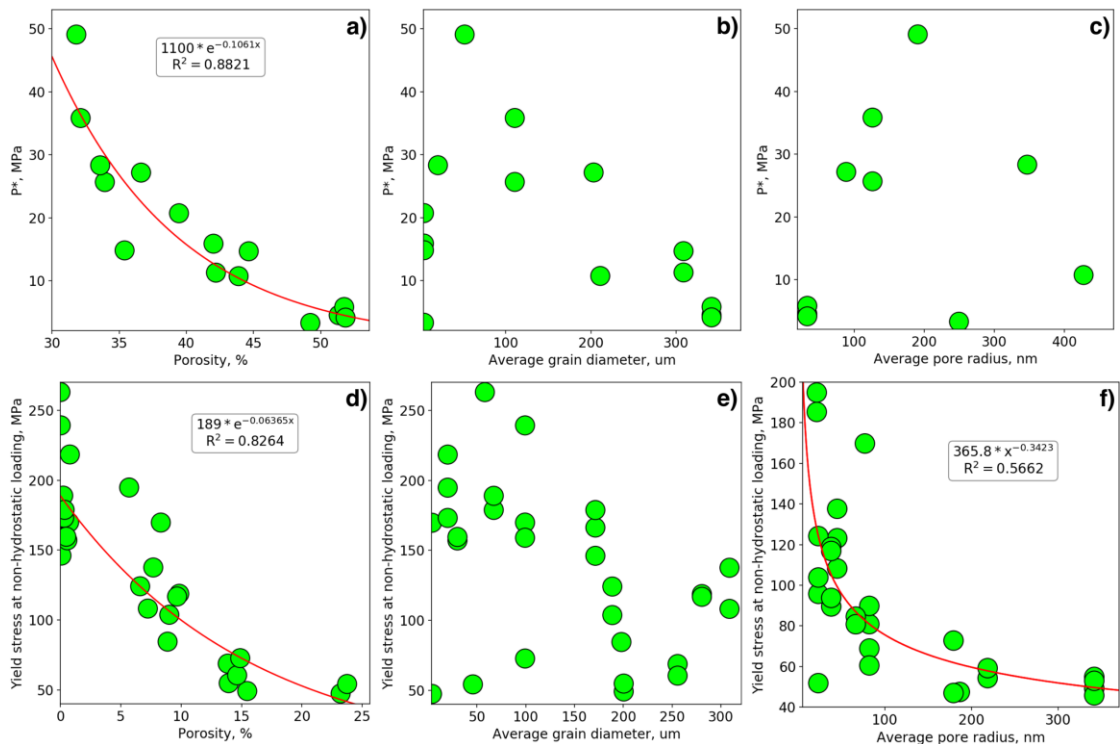


Figure 6-9 Yield stress at hydrostatic (a-c) and non-hydrostatic conditions (d-f) plotted against porosity (a,d), average grain diameter (b,e), and average pore radius (c,f) for all tested carbonate samples.

6.3.5 Permeability

Permeability was measured both before and after the triaxial experiments whenever the sample remained sufficiently intact. Measurements indicate an overall increase in permeability by up to five orders of magnitude for samples

with a porosity of <c.10% (**Figure 6-10**). Higher porosity samples (>c.10%) typically show reduced permeability after the deformation by as much as two orders of magnitude. However, some samples show little or no change in permeability due to deformation.

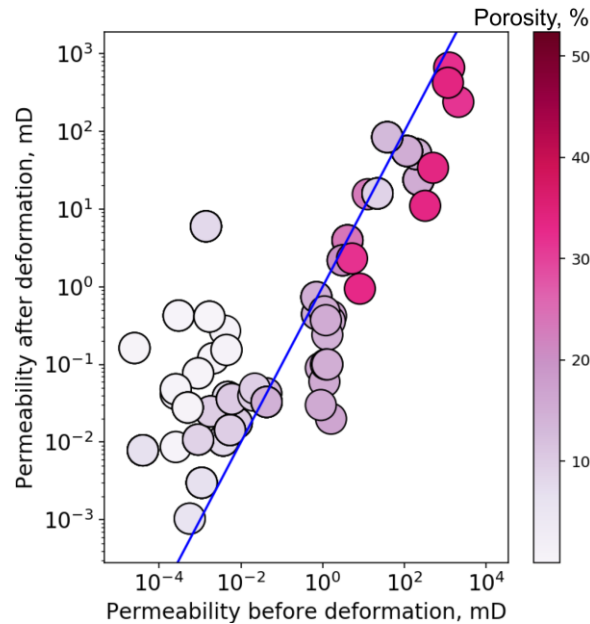


Figure 6-10 Permeability values (mD) before and after the triaxial loading coloured with respect to the initial porosity (%) of the samples. Blue line shows a relationship of 1:1.

6.4 Discussion

6.4.1 Mechanical response to failure

Elastoplastic behaviour of rocks is typically modelled in the p - q space using an elliptical model (e.g., Crawford and Yale, 2002; Wong et al., 2004; Schultz and Siddharthan, 2005). The yield envelope defines the transition between elastic and plastic regimes, where the critical state line of constant volume plastic deformation separates volumetric strain decrease and increase at failure. The brittle-ductile transition for carbonate rocks has been estimated at $\sigma_1/\sigma_3 = 5$ (Mogi et al., 1966), which has been supported by other studies (e.g., Walton et al., 2017). Dautriat et al. (2011) performed triaxial tests on

Estailades limestone while keeping the stress path coefficients, K , ($K = \Delta\sigma_3/\Delta\sigma_1$) constant. They found that for $K = 0$ and 0.125 , the mechanical response and the failure mode are typical of the brittle failure regime, whereas for $K \geq 0.25$, the mechanical responses are generally characteristic of the compactive cataclastic flow regime. A number of stress path coefficients were plotted, as well as the brittle-ductile transition proposed by Mogi et al. (1966) on data collected from the literature (**Table 6-4**) and that generated during the current study (**Figure 6-11c-f**). This brittle-ductile transition at non-hydrostatic loading separates the data at around 10% porosity, where samples with porosities $>10\%$ fall in the ductile failure regime at confining pressures >20 MPa, and samples with porosity $<10\%$ fall in the brittle failure regime at all confining pressures used (**Figure 6-11e-f**). This observation agrees with the study of Vajdova et al. (2004a), where triaxial loading of Tavel limestone indicated brittle failure at confining pressures of 10, 20 and 30 MPa. The partially cemented Plio-Pleistocene bioclastic grainstones also showed a switch in deformation behaviour at confining pressures >15 -20 MPa from abrupt volumetric strain decrease to volumetric strain increase at yield, indicating a transition from brittle to ductile behaviour. Therefore, the brittle-ductile transition also separates the dilational and compactional behaviour at yield. The yield stresses that fall in the dilational regime resulting in a sudden decrease in volumetric strain at yield, whereas yield stresses in the compactional regime resulting in a sudden increase in volumetric strain at yield. An exception are samples that undergo transitional-shear failure, which yield in the dilational regime but show a sudden increase in volumetric strain at yield. This may be caused by

the coalescence of microcracks resulting in localized shear-compaction (Wong et al., 2004). The difference in behaviours following yield under hydrostatic conditions indicate different deformation mechanisms that resulted in failure. For instance, flat stress-strain curves beyond the yield point in porous sandstones is typical of a transitional regime, where failure modes usually involve high-angle conjugate shear bands (e.g., Bésuelle, 2001; Baud et al., 2004, 2009). Visual inspection of the samples after the experiments showing this behaviour indeed indicated compaction-shear bands, however, at very shallow or horizontal angles. Strain hardening beyond the yield point was observed for fine-grained samples that developed compaction bands, whereas strain hardening punctuated by episodic stress drops was observed for coarse-grained samples, which were sheared or lost cohesion during the loading. This behaviour is comparable to the observations of Baud et al. (2004) on Bentheim sandstone, which showed similar stress drops and developed discrete compaction bands.

Even though the experiments in this study do not represent the full yield caps (**Figure 6-11e,f**), they do represent the stress conditions carbonates are likely to experience as a result of mechanical compaction at burial. In particular, the confining pressure of 70 MPa is around the maximum effective overburden stress that a rock would experience while being buried to around 6 km. Carbonates contain minerals that are prone to alteration and are more chemically reactive than siliciclastics. Therefore, they generally lose porosity due to cementation and pressure solution at shallow burial depths (<c.1 km) (e.g., Kupecz et al., 1997), thus c.50% of carbonate reservoirs have a porosity of <16% by the time they are buried to 0.75 km depth (Ehrenberg

and Nadeau, 2005). Therefore, carbonates are likely to show brittle-dilatant deformational behaviour even at shallow burial depth and therefore generally do not reach the compactional cap. However, some exceptions do exist. For instance, it seems likely that some chalk reservoirs that retain high porosity at depth due to overpressure or the presence of hydrocarbons may reach the compactive cap due to depletion.

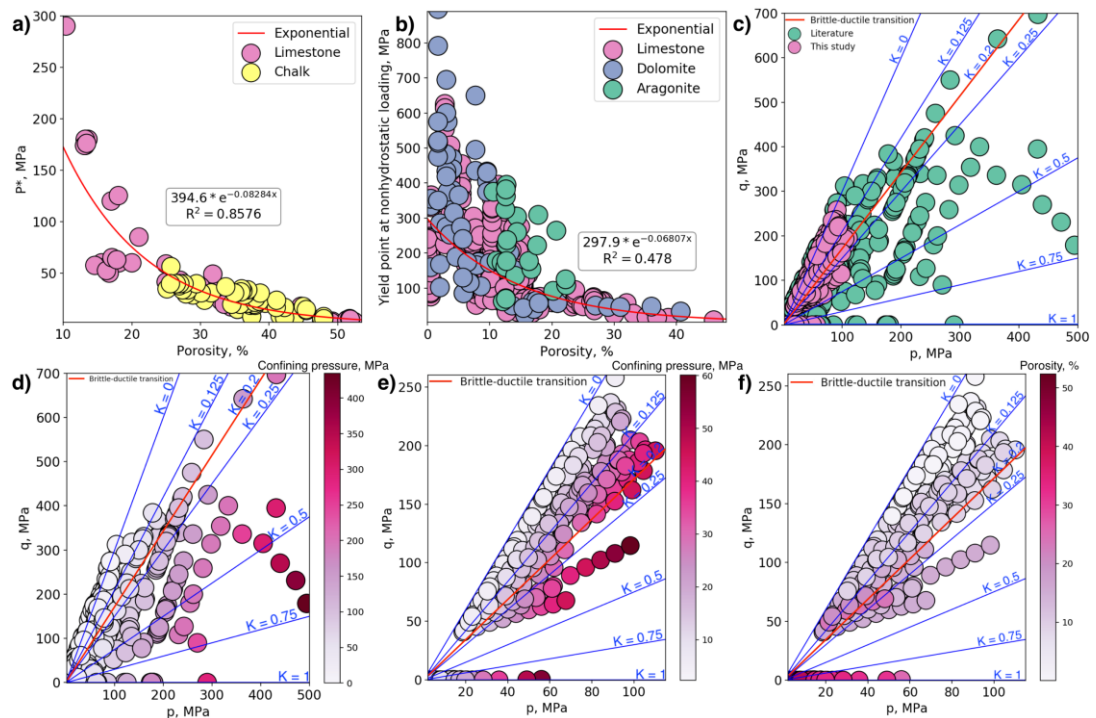


Figure 6-11 Yield (MPa) at a) hydrostatic, and b) non-hydrostatic conditions as a function of initial porosity (%) for various carbonate rocks. Data was collected from the literature (Table 6-4) and combined with the results of this study ($n=428$). Data is coloured with respect to mineralogy or distinctive carbonate rock type. c-d) Yield stress in p - q space for all collected data, and e-f) results of this study only. d-e) Data is coloured with respect to confining pressure (MPa), and f) porosity (%). Stress path coefficients, K , are marked in blue, brittle-ductile transition $\sigma_1/\sigma_3 = 5$ (Mogi et al., 1966) is in red.

6.4.2 Parameters controlling failure of carbonate rocks

Published data on the yield stress for various carbonate rocks were collected (Table 6-4) and combined with the results presented during this study (Figure 6-11). The yield stress clearly decreases with increasing porosity for

hydrostatic and non-hydrostatic loadings (**Figure 6-11a-b**). A gradual linear decrease is observed in the porosity range of 20 to 52%, and an abrupt increase of yield stress occurs for porosity values <20%, which is slightly higher than has been previously noted by Vajdova et al. (2004a). Grain size does not appear to exhibit any significant impact on yield stress, but affected the deformation mechanisms by which failure occurred for samples with porosity >25%. Chuhan et al. (2003) suggest that at low stresses (<5 MPa) the coarser carbonate sands have low yield stresses due to high angularity and low grain strength. Therefore, the sand experiences early grain crushing, which leads to early high-porosity loss. At 5-25 MPa stress, carbonate grains become finer due to a great initial grain crushing. That results in a more rapid reduction in compressibility, because finer grains are more difficult to crush and they provide an extra support for the remaining coarser grains. At these stresses grain crushing is concentrated mostly at the grain contacts, which increases the area of the grain contacts making them even less compressible. At stresses >25 MPa, the porosity reduction differences related to grain size and shape are significantly reduced and the greater compressibility of carbonate sands becomes less evident as the grain size increases. Hugman and Friedman (1979) and Přikryl (2001) noted that the coarser grained lithofacies are weaker than those that are finer-grained. However, Michie et al. (2014) show the opposite. The current study indicates that strength rarely depends on the grain size, as despite having very different grain sizes both wackestones and grainstones showed similar yield strengths for the same porosity. Moreover, differences in the dominant failure mechanism does not appear to impact yield stress. Pore size, however,

impacts the yield stress for samples with porosity <25%, where the yield stress decreases with increasing pore size. Samples with the largest vug, moldic or interparticle porosity showed the lowest yield stresses. Moreover, these pores are where the damage is focused. This observation agrees with the cataclastic pore collapse model (Zhu et al., 2010), where limestone with a bimodal pore size distribution, first yields at the large pores. The model predicts that uniaxial compressive strength, σ_u , is proportional to the inverse square root of the pore radius, r , and decreases with increasing porosity, ϕ , following a power law:

$$\sigma_u = \frac{1.325 K_{IC}}{\phi^{0.414} \sqrt{\pi r}}$$

K_{IC} is a critical stress intensity factor of a small crack on the circular pore surface, at which these extensile cracks initiate and propagate to a certain distance, then coalesce and lead to an instability of the rock, reaching σ_u .

There is a large amount of variability in the yield stress data for the same porosity values (**Figure 6-11a-b**). In sandstones, yield stresses for samples with similar porosities and grain sizes may deviate by as much as a factor of 2 from the trend predicted by Hertzian fracture model (Wong et al., 1997). It was suggested that other factors, such as mineralogy, the presence of water, cementation and clay content may exert control on the yield stress (e.g., Baud et al., 2000; Tembe et al., 2008). Despite the different extrinsic test variables, some of this scatter in carbonate yield stress may be explained based on variability in pore size (e.g., Zhu et al., 2010; Dautriat et al., 2011), as well as dolomite content (Crawford and Yale, 2002). The authors noted

that dolostones show significant increase in strength compared with limestones of similar porosity (**Figure 6-11b**).

Table 6-4 *Compilation of yield stress under various test conditions for carbonate rocks. C' denotes the onset of dilatancy, C^* denotes the onset of inelastic compaction, C is either C' or C^* (not defined in the literature), and P^* is the pre-consolidation pressure under hydrostatic conditions.*

Reference	Carbonate rock type	Average porosity, %	Test conditions	Yield stress type
<i>Baud et al. (2000)</i>	Solnhofen limestone	2.8	dry	C' , C^*
<i>Baud et al. (2009)</i>	Majella limestone	30	dry	P^*
	Chauvigny limestone	17	dry	P^*
<i>Baud et al. (2017)</i>	Leitha limestone	24.4	saturated with water	P^*
<i>Castagna et al. (2018)</i>	Comiso limestone	10.1	dry/saturated with water	C
<i>Cheung (2015)</i>	Indiana limestone	17.4	dry/saturated with water	C' , C^* , P^*
	Tavel limestone	13.4	dry/saturated with water	C' , C^* , P^*
<i>Cilona et al. (2014)</i>	Bolognano grainstone	27.6	dry	C^*
<i>Croizé et al. (2010)</i>	Dolostone	27	dry	C^*
	Marion Plateau limestone	30.5	dry/saturated with water	C^*
<i>Dautriat et al. (2011)</i>	Estailades limestone	28.1	saturated with water	P^*
<i>JCR database (DGI, 2000)</i>	Chalk	36.3	saturated with oil	P^*
<i>van Ditzhuijzen and de</i>	Sarawak limestone	33.4	saturated with water	C^*
<i>Waal (1984)</i>	Sarawak dolomite	35.9	saturated with water	C^*
<i>Hatzor et al. (1997)</i>	Aminadav Fm dolomite	8.8	dry	C
<i>Hugman and Friedman</i>	Yule Marble	0.59	dry	C

(1979)	Indiana limestone	8.4	dry	C
	Madison dolomite	4	dry	C
<i>Lisabeth and Zhu</i> (2015)	Indiana limestone	15.9	saturated with water	C',C*,P*
<i>Longuemare et al.</i> (1996)	Chalk	45	dry	P*
<i>Mowar et al. (1994)</i>	Cordoba Cream limestone	25	dry	P*
<i>Palchik and Hatzor</i> (2002)	Bina limestone	12.3	dry	C'
	Aminadav dolomite	10.8	dry	C'
	Yagur dolomite	11.2	dry	C'
	Sorek dolomite	15.6	dry	C'
	Beit-Meir dolomite	23	dry	C'
	Nekarot limestone	9	dry	C'
<i>Renner and Rummel</i> (1996)	Solnhofen limestone	4.6	dry	C',C*
	Cold-pressed aragonite	14.7	dry	C',C*
	Cold-pressed calcite	11	dry	C',C*
	Crushed Solnhofen limestone	12	dry	C',C*
<i>Vajdova et al. (2004a)</i>	Tavel limestone	10.4	dry	C',C*,P*
	Indiana limestone	15.6	dry	C',C*,P*
<i>Zhu et al. (2010)</i>	Tavel limestone	13.6	dry	P*

6.4.3 Failure deformation mechanisms

Microstructural observations indicate that microcracking was the dominant deformation mechanism in most of the samples under both hydrostatic and non-hydrostatic conditions. Cracks are known to nucleate from impinging grain contacts due to local tensile stress concentrations (Zhang et al., 1990) or from flaws on the surface of the pores or at stress concentrations within the solid part of the rock, such as micropores or small cracks (Sammis and Ashby, 1986). Microstructural analysis of the samples following deformation shows a general increase in crack length with decreasing porosity (**Figure 6-12**). For instance, cracks initiate due to stress concentrations at grain contacts and crack length is limited by the size of the grains in high-porosity rocks, where large pores are homogeneously distributed throughout the volume of the rock. Here the cracks do not propagate further than one grain but produce cataclastic flow. Lower porosity rocks, where macropores are irregularly distributed, fail due to stress concentrations at the flaws on the surface of those pores and damage is mostly focused around the macropores. Here the cracks propagate across a few grains and their length is limited by the distance between two adjacent pores. In the tightest samples, the transgranular cracks nucleate from micropores within the crystals or pre-existing cracks or the flaws within the solid part of the rock, such as cleavage or twin lamellae (e.g., Olsson and Peng, 1976; Fredrich et al., 1989). Here the crack length is limited by the size of the sample.

Even though microcracking dominates failure of most samples, plastic failure was observed for the completely cemented samples, where mechanical twinning was pervasive within the cement and the grains throughout the

volume of the sample. These samples also showed minor axial intergranular cracking. The cracks may have propagated from the defects at the edges of calcite spar through the dense cement leaving the more porous grains undeformed, as has been similarly observed by Dautriat et al. (2011) on porous limestone. These defects may have been created by the mechanical twinning during deformation.

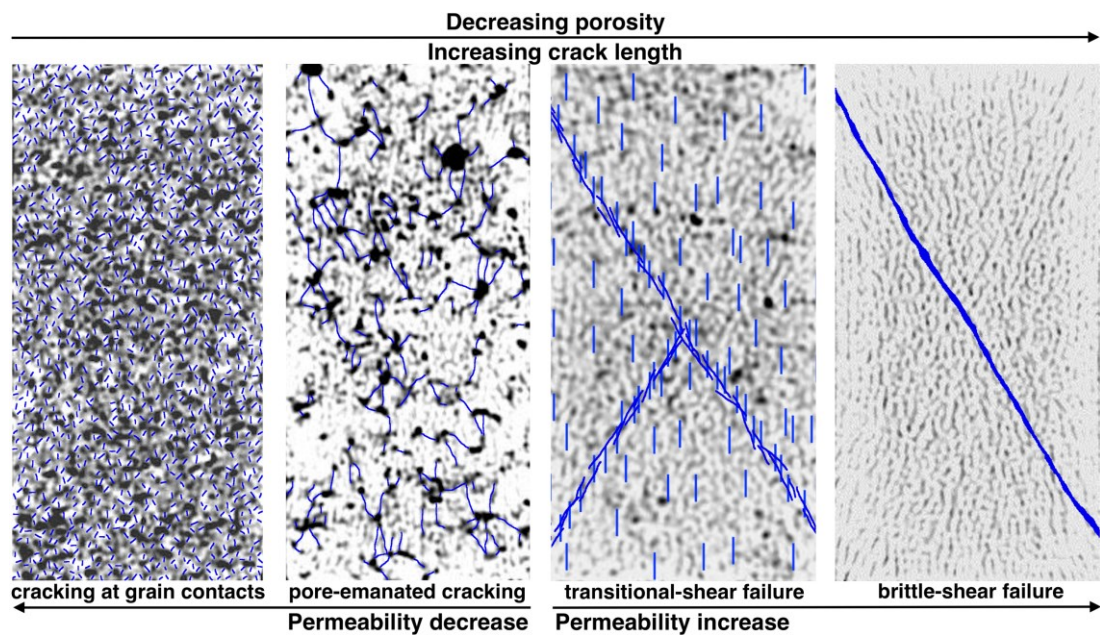


Figure 6-12 Schematic illustrating changes in failure deformation mechanisms in relation to initial porosity, as well as permeability changes induced by deformation. Note how different failure deformation mechanisms impact the permeability.

6.4.4 Water weakening effect on deformation

There is a general trend for yield stress to be higher for dry samples than those saturated with brine (**Figure 6-13**). Baud et al. (2000) studied the water weakening effect in conventional triaxial experiments on porous sandstone and quantified the observed water weakening parameter, λ , as $\lambda = (P^*_{wet}/P^*_{dry})^{2/3}$. In this study, water weakening parameter calculated for all samples is equal to 0.85, which seems consistent with other studies. For example, λ was found to be around 0.8 for a Majella bioclastic grainstone

(Baud et al., 2009), whereas lower values (c.0.6) were measured for the soft porous Lixhe chalk (Risnes et al., 2005). The impact of water on yield stress increases as porosity increases because high-porosity rocks can contain more water (**Figure 6-13a**).

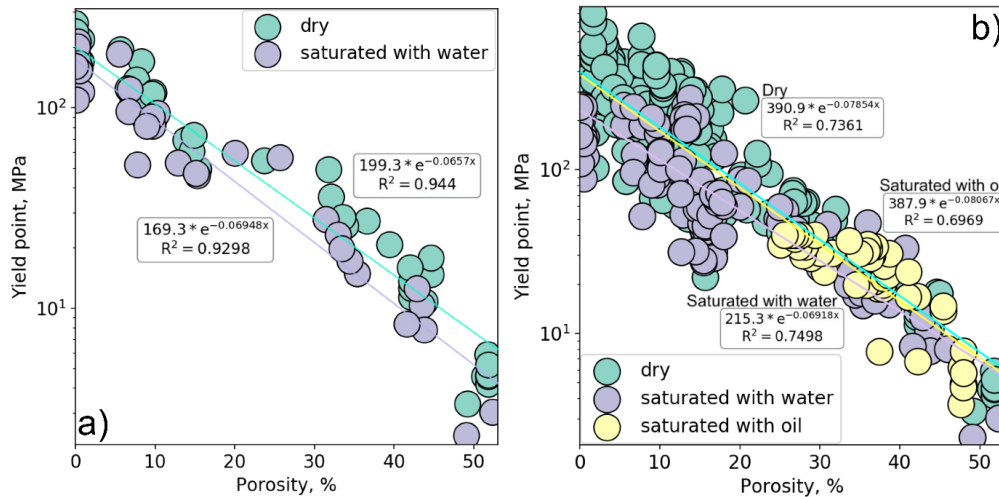


Figure 6-13 Yield point as a function of porosity illustrating impact of the test conditions on the failure for a) our data only; and b) our data combined with the documented data from the literature. Lines show best exponential fit through the data for dry and saturated samples with water/oil.

6.4.5 Impact of deformation on permeability

Deformation mechanisms that can cause drastic permeability changes in sandstones are quite well understood. The failure of highly porous sandstones typically creates microstructural baffles to fluid flow and reduces the permeability by several orders of magnitude (e.g., Zhu and Wong, 1997; Zhu et al., 1997; Boutéca et al., 2000; Vajdova et al., 2004b). Faulting of low-porosity sandstones tends to increase permeability due to dilation and increased crack connectivity (Zhu and Wong, 1997). Recently, Głowacki and Selvadurai (2016) observed a similar behaviour in Indiana limestone.

Permeability decreased in the ductile failure regime, where rock underwent irreversible textural changes and compaction of the pore space, similar to the

formation of compaction bands (e.g., Baud et al., 2009). Permeability increase was observed in the brittle failure regime due to the formation of a failure plane. Moreover, Lisabeth and Zhu (2015) observed permeability decrease in the Indiana limestone by up to a factor of 5 after the first few percent of strain in the cataclastic flow regime.

The deformation-induced permeability changes identified during the current study are consistent with those in the literature. In particular, porosity was increased by deformation of samples with porosity >10%, which failed in the ductile failure regime. Grain crushing in these samples occurred due to microcracking at grain contacts or in the periphery of macropores (**Figure 6-12**). Crack length was limited by grain size or distance between two adjacent macropores, thus microcracking lead to cataclastic flow and pore collapse rather than increased crack connectivity throughout the sample. Permeability was reduced by deformation of low-porosity samples (<10%), which failed in the brittle failure regime. Propagating transgranular and axial cracks in these samples coalesced to form through-going planes which increased the overall fracture connectivity (**Figure 6-12**).

For comparison, porosity-permeability data on naturally-faulted carbonates was collected from the literature and shown in **Figure 6-14**. Despite the much higher ranges of permeability values of the fault rock, data is consistent with the porosity-permeability measurements on samples deformed in the laboratory. In particular, permeability is most likely to be decreased due to faulting/deformation when the initial porosity is >c.10%. The much higher ranges of permeability values of the naturally-faulted rocks may be explained by solution/precipitation and other diagenetic processes

that alter the porosity/permeability in the ways which cannot be produced in the laboratory. For instance, the 6 orders of magnitude decrease in permeability for the very porous carbonates due to faulting may be caused by aggrading neomorphism/recrystallization (**Chapter 4**). The low permeabilities of the fault rocks in low-porosity carbonates may be explained by intense cataclasis and/or cementation (Cooke et al., 2019; **Chapter 5**). Cataclasis in these rocks forms fracture-derived cataclasites, which were impossible to develop in the laboratory at the present testing conditions, as the strains were not high enough.

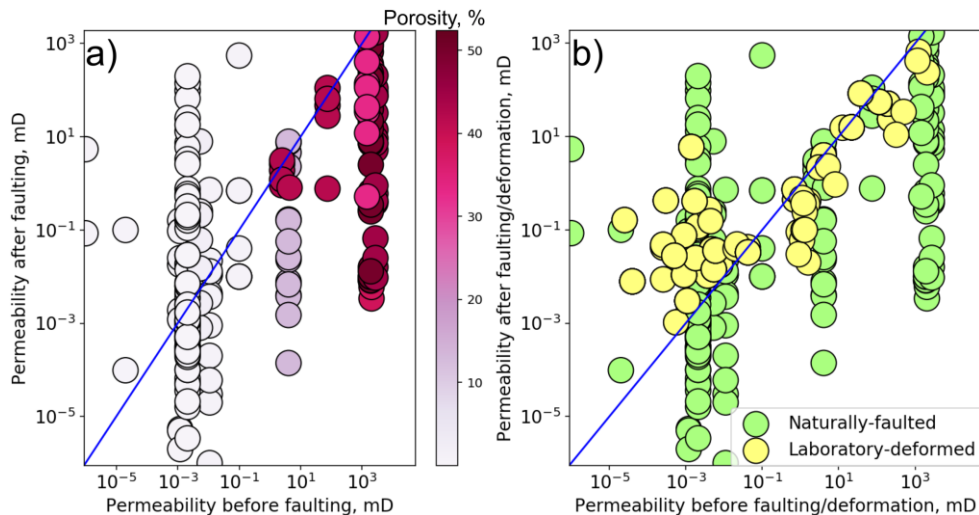


Figure 6-14 a) Permeability values of fault and host rocks collected from the literature on various carbonate rocks (Bauer et al., 2016; Zambrano et al., 2016; Cooke et al., 2019) and combined with the data from **Chapter 4** and **Chapter 5**, and coloured with respect to porosity of the host rock. b) Permeability values of naturally-faulted rocks and their protoliths (green) combined with the permeability data measured in this study before and after the laboratory-induced deformation (yellow). Blue is the 1:1 line.

6.5 Conclusions

Carbonates lose porosity at shallower depths than sandstones, which makes them more susceptible to brittle deformation even at shallow depths (<c. 1 km). The low range of confining pressures used in this study represent the mechanical deformation a carbonate rock would experience at shallow burial

depths (<c.6 km). However, deformation at deeper depths would still be similar to rock deformation at depths between c.1-6 km.

Test results show that despite the large scatter, yield stress corresponds well with porosity. Under non-hydrostatic loading, samples with porosities >10% deform in the ductile failure regime at confining pressures >20 MPa, and samples with porosity <10% deform in the brittle failure regime at all confining pressures used. Moreover, permeability change caused by deformation also correlates with porosity. Permeability decreases due to deformation for samples with porosity >10%, and vice versa. In general, brittle failure at non-hydrostatic loading was observed for samples with porosities <10%, and is associated with macroscopic transitional- or brittle-shear plane, which causes permeability increases of up to five orders of magnitude. Ductile behaviour with distributed or localized inelastic deformation is typical for samples with porosities >10%. This is caused by pore collapse associated with grain cracking evolving at grain contacts or focused damage in the periphery of macropores, which lead to a reduction in permeability by up to two orders of magnitude. Therefore, microcracking was the dominant failure deformation mechanism in most of the samples, and crack length was proportional to the initial porosity.

Even though yield stress does not depend on failure deformation mechanism, the type of failure mechanism depends on microstructural textures of the rock. In particular, grain size has an impact on the type of failure deformation mechanism for the very porous samples (>25%). For instance, fine-grained carbonates showed grain packing and distributed or localized cataclastic flow but no shearing, whereas coarse-grained samples

were sheared or lost overall cohesion. Pore size shows correlation with yield stress under non-hydrostatic loadings. The largest pore size associated with interparticle, moldic and vug porosity showed the lowest yield stress, whereas the smallest pore size corresponding to intercrystal porosity and microporosity indicated the highest yield stress.

Chapter 7 Discussion

7.1 Carbonate reservoirs

Carbonate reservoirs hold more than 60% of the world's oil and 40% of its gas reserves (e.g., Al-Anzi et al., 2003), and they have been proven to be one of the most prolific plays in the Middle East, USA Gulf Coast, offshore Brazil, North Sea, Central and Western Mediterranean region among others (**Figure 7-1**). Inherent features of deposited carbonate sediments, their depositional environment and early diagenetic processes are the key controls of the extent of prospective reservoir rocks. Sedimentary facies provide the initial porosity and size of a potential reservoir. Any subsequent alterations, such as those due to percolation of meteoric waters, exposure to hypersaline brines, compaction, tectonic or non-tectonic fracturing, depend on the initial sedimentological content and setting. Carbonate reservoirs have lower porosity values for a given burial depth compared to sandstones (**Figure 2-2**), which is due to a greater chemical reactivity of carbonate minerals relative to quartz leading to increased rates of chemical compaction and associated cementation. Many carbonate reservoir rocks still retain primary porosity, but most have undergone substantial enhancement or extensive occlusion of pore space due to environmental dynamics. Overall, carbonate reservoirs do not have lower permeability for a given porosity compared with sandstones but do have dramatically lower proportions of both high-porosity and high-permeability values (Ehrenberg and Nadeau, 2005). These authors suggest that relative scarcity of low-porosity (<8%) siliciclastic reservoirs at depths less than 6 km compared with carbonates

indicate that low-porosity reservoirs are simply more economically feasible in carbonates than in siliciclastics. The increased economic viability of low porosity carbonates reflects the more common occurrence of fractures in carbonates and the efficiency of these fractures to facilitate economic flow rates in low-porosity rock.

Carbonate reservoirs occur from peritidal and subaerially exposed lithofacies in Palaeozoic examples, through a long-term sequence of shallow-shelf sands and reefs, to relatively deep-marine lithofacies in the Cretaceous and Tertiary ranging from periplatform debris flows to deep-shelf pelagic chalks and deep-basinal mixed lithofacies that have been diagenetically modified, largely to dolomite (Roehl and Choquette, 2012). The authors note that many of the largest fields formed in Tertiary orogenic belts and other regions affected by Tertiary tectonics, primarily in carbonates of Cretaceous to Miocene in age.

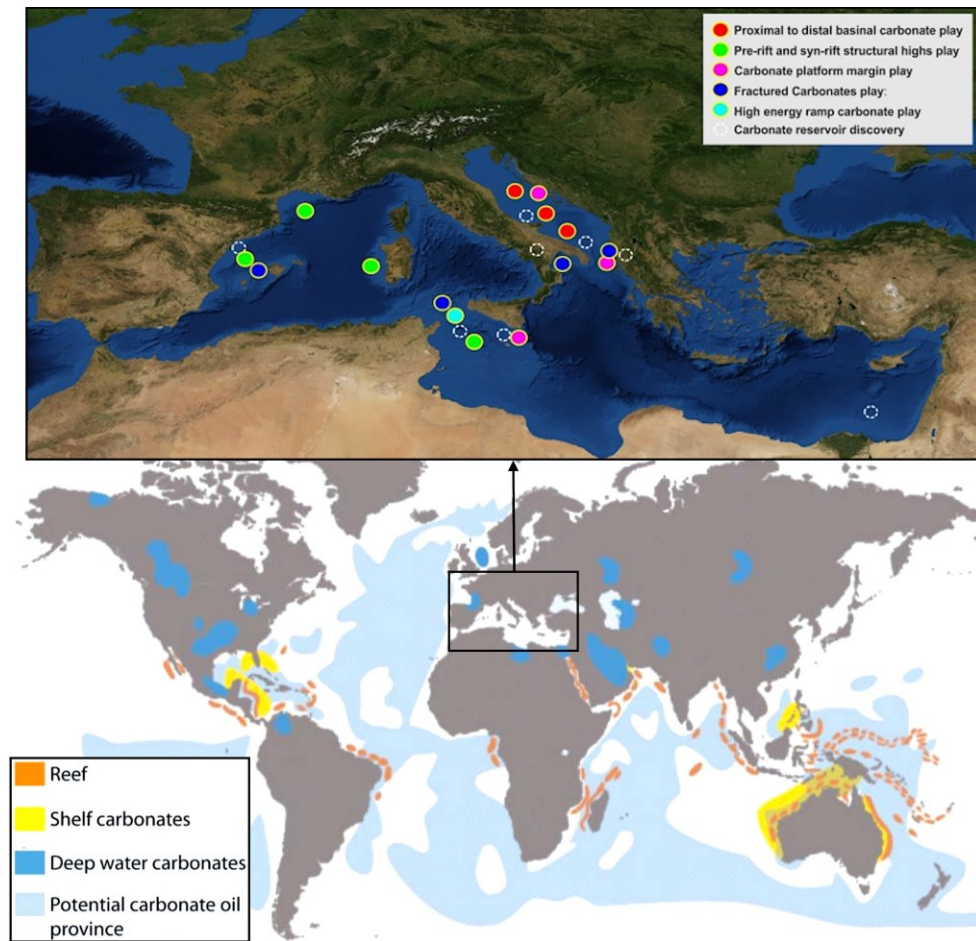


Figure 7-1 World distribution of carbonate reservoirs (modified from Schlumberger Market Analysis, 2007) and a zoom in of the Mediterranean Sea region with the main carbonate hydrocarbon discoveries in the Central and Western parts (modified from Di Cuia and Riva, 2016).

Conditions forming the highest reservoir rock porosities are: (1) type of lithofacies with high potential to preserve primary or early-formed porosity (mud-rich limestones; sucrosic to vuggy dolostones); (2) stratigraphic settings protected from near-surface porosity loss; and (3) conditions facilitating near-surface porosity creation (Ehrenberg and Nadeau, 2005).

Among carbonate rock types, grainstones generally have the highest permeability. Rock types with a higher mud content such as packstones and wackestones may have a higher porosity than grainstones but permeability is reduced by around 10 to 100 times due to the reduction on pore size (Akbar et al., 2000). However, pore systems of secondary origin are strongly

predominant in hydrocarbon-bearing carbonate reservoirs despite partial retention of primary porosity. In particular, the large majority of carbonate reservoirs acquired their favourable pore-system characteristics during diagenesis at or near the surface either by modifications of meteoric-water or more saline-waters in sabkha settings, or at burial (mesogenetic) by various carbonate mineral transformations and/or dissolution by aggressive fluids (Schmoker and Halley, 1982; Brown, 1997). Diagenetic alteration often leads to formation of extremely high-permeability layers, which are referred to as “super-k” layers (Akbar et al., 2000). For instance, the “super-k” layers in Neelam reservoir offshore Mumbai, India, were created by dissolution and leaching of the rock fabric by meteoric water during periods of low sea-level.

High-permeability may result either from high effective matrix-porosity (by hydraulically connected pores) or from secondary flow through fractures. Presence of fractures is extremely important because even a few fractures with small apertures control the fluid transport within the porous media (Nelson, 1985). Around half of carbonate reservoirs have a porosity of <16% by the time they are buried to 750 m depth (Ehrenberg and Nadeau, 2005). Therefore, fractured tight-carbonates form an important repository for subsurface geofluids (Agosta et al., 2007; Matonti et al., 2012; Korneva et al., 2015; Giuffrida et al., 2019), whereas reservoir rocks in carbonates with high matrix-porosity occur less often (**Figure 7-1**). The majority of high matrix-porosity reservoirs occur in pelagic chalk, which largely form in the North Sea and the Barents Sea; examples of such reservoirs include the Ekofisk, Hod and Valhall fields. Secondly, in rigid reefal carbonates with growth-framework and inter-/intraparticle porosity (Abu Dhabi, offshore

Australia and SE Asia), and algal rudstones (Italy, Austria), and rarely in grainstones such as Jurassic Smackover grainstone reservoir in the Mt. Vernon Field. Even when majority of carbonate fields owe their reservoir productivity to fracturing, other reservoirs involve fracturing at least to some extent (Roehl and Choquette, 2012). These reservoirs may be classified into four types as suggested by Nelson (2001). The reservoir types are illustrated in **Figure 7-2** with examples from this study. In **Type I** reservoirs, matrix porosity of the reservoir rock is close to 0%, and matrix permeability is similar to that of a sealing rock – on a scale of nanodarcies (e.g., Bramwell et al., 1999). Therefore, fractures provide essential reservoir porosity and permeability. Tight limestones and dolomites analysed in **Chapter 5** may represent this type of reservoir, as well as rocks with porosity <6% from **Chapter 6**, which showed brittle shearing and axial cracking whilst deformed beyond failure under triaxial loading. This type of rock is intensely fractured, and faulting typically creates high permeability pathways: the faults form open voids along a slip surface or continuous fault gauges with high-porosity breccias, or cataclasites, which are often cut by fractures (**Figure 7-6**). From the studied examples, faults in these reservoirs are unlikely to create effective barriers to fluid flow. At most, they will create conduit-barrier systems, due to intense fracturing within the damage zones. In **Type II** reservoirs, fractures provide permeability, but some of the hydrocarbons are stored within the matrix. This type of reservoir may be represented by samples with porosity between 6% and 10%, which failed due to brittle axial cracking, which coalesced at failure forming transitional shear-planes. This type of rock is prone to brittle deformation, and faulting may create similar

structures to the ones observed in the first type of reservoirs (**Figure 7-7c-g**).

Type III reservoirs have a high matrix-porosity but low matrix-permeability rock, where production comes from matrix, however, fractures provide the essential permeability. Fine-grained porous rocks such as chalk represent this type of reservoir. In this study, deformation bands were observed in high-porosity Upper Cretaceous chalk outcrops in SE England, which are analogues for chalk reservoirs in the North and Barents seas. The bands showed negligible impact on permeability because matrix permeability of the protolith rock is very low itself and further compaction mostly affects the macroporosity, which does not form a connected network. Higher displacement faults in these outcrops typically show brittle-dilational behaviour, and mostly formed as open faults (**Figure 7-7a-b**). **Type IV** reservoirs have high matrix porosity and permeability, which provides both hydrocarbon storage and flow pathways, and fractures may only enhance the permeability or create reservoir anisotropy. Rocks that may form this type of reservoir were studied in **Chapter 4**. Some lithofacies, such as Plio-Pleistocene bioclastic grainstone in Castelluzzo and Favignana island in Sicily, Italy, were only buried to as much as 50 m depth and have extremely high porosity and permeability. While similar rocks have never been observed in any hydrocarbon-bearing reservoirs, these and other less extreme examples suggest that faulting in high-porosity carbonates may form fault rocks with exceptionally low-permeabilities that may negatively affect hydrocarbon flow rates. However, these compactional low-permeability fault rocks may also have open voids along a slip surface, creating permeability anisotropy (**Figure 7-8**). In reservoirs with matrix porosity,

particularly in reservoir types II and III, early knowledge of fracture/matrix interaction is very important to determine whether the matrix porosity can be drained by the fracture network. Understanding the products of faulting are also crucial prior to reservoir exploitation in all types of reservoirs.

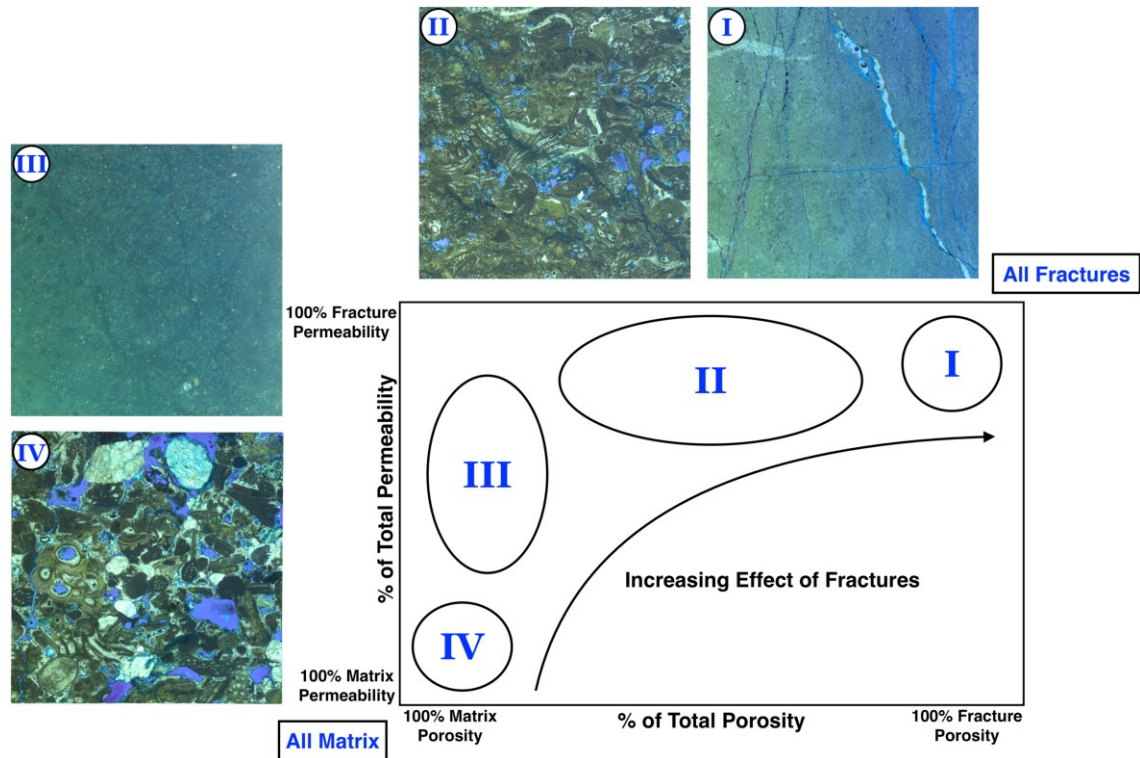


Figure 7-2 Fractured reservoir types based on matrix character (modified from Nelson, 2001). Examples are given for each reservoir type: I) Very tight reservoir, where fractures provide both storage and fluid pathways; II) Tight reservoir: fractures provide flow pathways, but there is some contribution from the matrix; III) High matrix-porosity and low matrix-permeability reservoir (e.g., chalk): fractures provide flow pathways, production comes from matrix, these reservoirs are suitable for secondary and tertiary recovery; and IV) High matrix-porosity and high matrix-permeability reservoir: matrix provides storage and flow, fractures may enhance the permeability.

7.2 Permeability changes induced by faulting and laboratory-deformation

7.2.1 High-porosity carbonates

Deformation structures formed due to faulting in high-porosity carbonates (38 and 52%) were studied within a variety of lithofacies: from micritic chalk to peloidal bioclastic grainstones and peloid-free bioclastic grainstones.

Different deformation mechanisms were identified depending on the initial properties of the host rock. For instance, chalk deformed by the collapse of macro-pores within foraminifera. The macroporosity collapse lead to the lowest porosity reduction compared to the other bands. Moreover, its effect on permeability was even less significant, as the macroporosity did not form a connected network. Single deformation bands formed within peloidal grainstones, which only underwent low-stress cataclasis, had a very high microporosity content within the loosened disintegrated peloids, thus their permeability was also only slightly reduced compared to the host rock. However, permeability was reduced by up to 6 orders of magnitude due to aggrading neomorphism replacing the fine micrite with neomorphic microspar. Clustered deformation bands have a much lower microporosity due to high-stress cataclasis, which filled most of the porosity with cataclastic matrix. Therefore, permeability reduction across clustered deformation bands is much more significant than after the low-stress cataclasis that formed the single deformation bands. However, the greatest porosity and permeability reduction was produced by dilation and cementation. The completely cemented parts of the bands reduced the permeability by up to 6.5 orders of magnitude. Therefore, even though permeability of deformation bands is always lower than that of their host rocks (**Figure 7-3a**), significant impact on fluid flow may only be produced by deformation bands, which underwent diagenetic processes such as cementation and recrystallization.

Under triaxial laboratory loading, samples with porosity >10% experienced either an overall decrease in bulk sample's volume or localization of

compaction/shear-compaction bands, were sheared or lost overall cohesion. At the microstructural scale, several deformation mechanisms were observed: cataclastic flow and pore-emanated cracking, resulting in focused damage around the macropores as well as their collapse. These samples typically showed slight reduction in permeability after the deformation, which may be decreased by up to a magnitude of 2 (**Figure 7-3d**).

7.2.2 Low-porosity carbonates

Fault zones in studied low-porosity limestones consist of laterally distinct, single-stranded fault cores made up of cataclasite or cemented chaotic breccias, and damage zones with fractures typically oriented parallel or perpendicular to the strike of the principal fault surface and strands of mosaic or crackle breccia. Fault zones in low-porosity dolomites consist of multiple stranded cataclastic fault cores and intensely fractured rock between the strands. Permeability measurements of the fault and host rocks show that cataclasites and cemented chaotic breccias typically reduce the permeability by up to a magnitude of 5 (**Figure 7-3b,c**), whereas crackle and mosaic breccias positively affect the fluid flow, increasing it by up to a magnitude of 6 (**Figure 7-3c**).

During the triaxial testing, carbonate samples with porosity <10% failed in a brittle-dilatant manner. The main deformation mechanisms, which resulted in the samples failing were transitional and brittle shearing, as well as mechanical twinning within the completely cemented samples. Permeabilities in these carbonates were always positively affected by the deformation, increasing it by up to five orders of magnitude (**Figure 7-3d**).

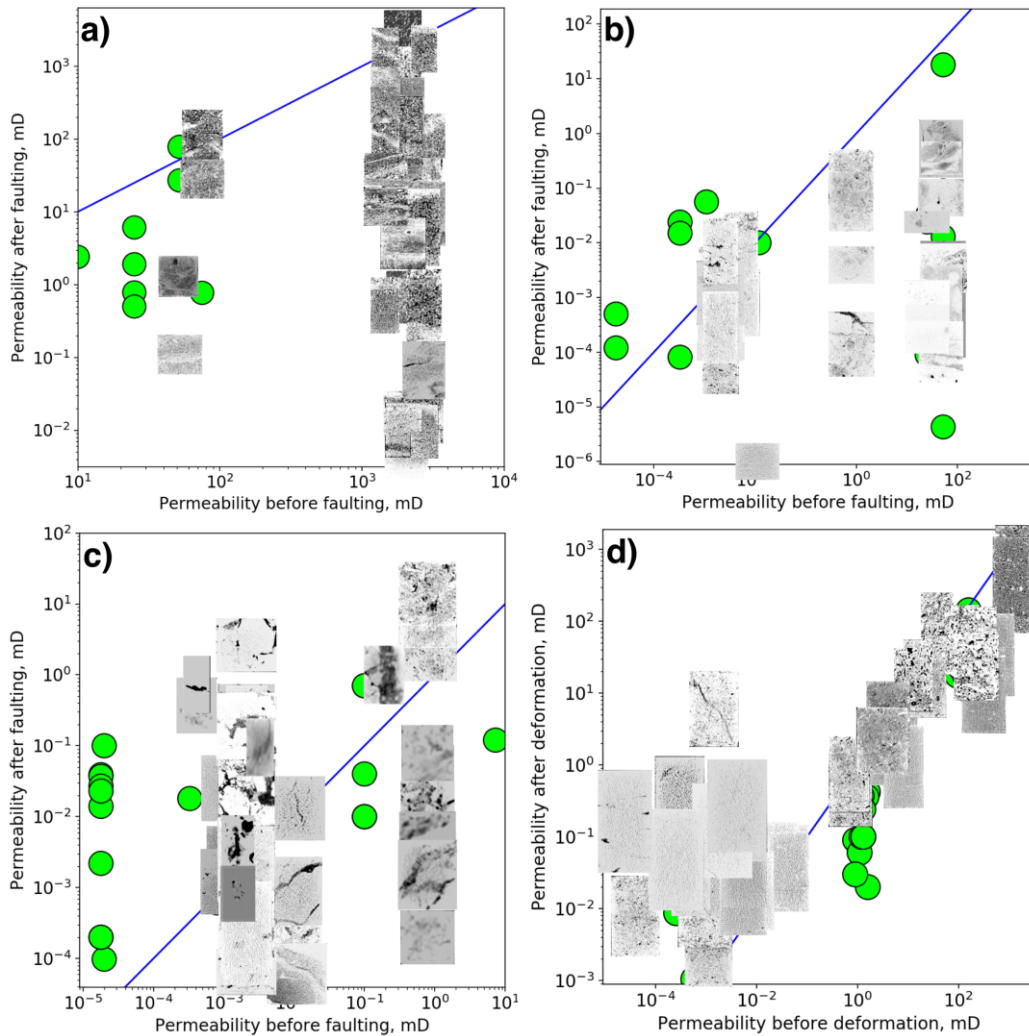


Figure 7-3 Permeability before and after (a-c) faulting and (d) lab-induced deformation. Note that CT-scans of core plugs are plotted instead of some data points, displaying internal views of the a) samples containing deformation bands; b) cataclasites; c) breccias; and d) samples after the triaxial deformation (whenever the samples remained sufficiently intact).

7.2.3 Sealing faults or conduits to flow?

A compilation of permeability values from **Chapter 4** on deformation bands in porous carbonate outcrops, from **Chapter 5** on fault rocks in tight limestones and dolomites, and from **Chapter 6** on laboratory-deformed samples, combined with the permeability values collected from the literature on naturally-faulted rocks is shown in **Figure 7-4a**. The data both for naturally-faulted and laboratory-deformed samples suggest that permeability decreases due to deformation/faulting for carbonate rocks with porosity

higher than around 10%, and may be either increased or decreased for lower porosity samples (**Figure 7-4b**). However, it is known, that natural faults in high-porosity carbonates may also form as open and/or dilational faults and would have higher permeability than that of their protolith. These faults typically have no fault rock or the fault rock is too fragile to collect (**Figure 7-7a,b & Figure 7-8**), which could explain why no permeability data have been reported in the literature for such faults. It has been considered that a fault will behave as a significant barrier if its permeability is four orders of magnitude lower than that of the protolith (e.g., Walsh et al., 1998; Fisher and Knipe, 2001). Therefore, four orders of magnitude difference between the permeability of the fault and the host rock is defined as a 'Sealing line'. Furthermore, 1:1 line for the fault and host rock permeability is defined as a 'Baffle-conduit line', above which the fault will be acting as a conduit to fluid flow, and below which it will be reducing the fluid flow (**Figure 7-4**).

Permeability analysis across naturally-faulted and laboratory-deformed carbonates suggests that faulting and deformation of high-porosity high-permeability carbonates will most likely restrain the fluid flow. These rocks are susceptible to grain-scale cataclasis and increased efficiency in grain packing, resulting in pore collapse. However, only a small percentage of faults in high-porosity carbonates will act as significant barriers to flow, and that is in naturally-occurring faults, where recrystallization and cementation are possible as opposed to the laboratory-induced deformation. Deformation of high-porosity low-permeability carbonates is likely to decrease the porosity but will have little impact on permeability. On another hand, faulting and laboratory-deformation of low-porosity and low-permeability rocks increases

permeability due to their tendency to fracture and brecciate. However, with time or with increasing deformation, in nature these same fault rocks may gain very low permeabilities due to high-strain cataclasis and/or cementation, making them potential barriers to fluid flow.

For these faults to act as significant barriers to fluid flow, they have to be continuous, vertically and laterally extensive, and act as barriers to fracture propagation. Fracture blunting was observed in the cemented fault cores in tight limestone-hosted outcrops as well as in the cataclasite bands in tight dolomite-hosted outcrops, and will be discussed in the following **Section 7.3**. However, the examination of continuity and extension of fault rocks in this work was only available on small portions of these faults, as they are bound by the sea and sandy patches or cliffs, and maximum length of the fault cores in limestone-hosted outcrops reach c.150 m, and fault zone outcrops in dolomite-hosted outcrops expose us much as 820 m x 500 m areas. The vertical extension of these faults is unclear.

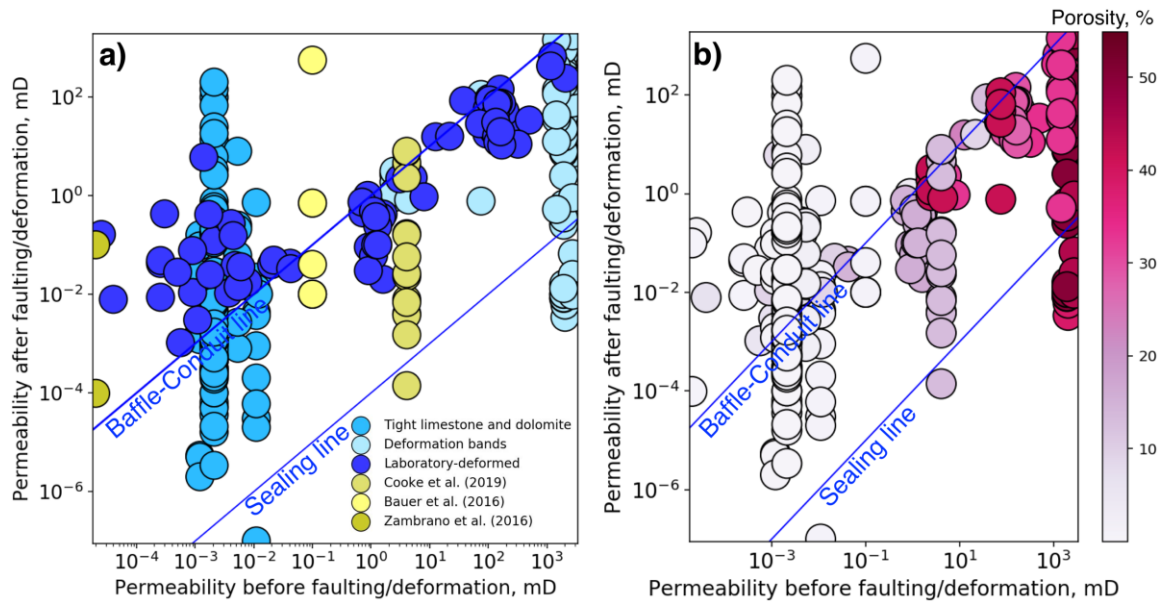


Figure 7-4 Collection of permeability values from **Chapter 4** on deformation bands in porous carbonate outcrops, from **Chapter 5** on fault rocks in tight limestones and dolomites, and from **Chapter 6** on lab-deformed samples, combined with the permeability values collected from the literature on naturally-faulted rocks. a) illustrates the references for the data; b) shows the same data coloured in respect to initial porosity (%) of the host rock samples.

7.3 Fault/Fracture interaction

The crux to how faults affect fluid flow depends on whether or not the fault cores are cut by open fractures. In this work, two types of fault rocks were observed, where fracture blunting was present: (i) cemented breccias in tight limestone-hosted outcrops, which formed thick fault cores laterally continuous by a maximum of 90 metres; and (ii) cataclasite bands in tight dolomite-hosted outcrops that formed complex anastomosing networks throughout the whole fault zone (**Figure 7-5**). However, most of the analysed fault rocks in carbonates showed polyphase deformation indicating reactivation, and were cut by later fractures (**Figure 7-6**). Even though fractures in the surface have bigger apertures compared to the ones in the subsurface (e.g., Lee and Farmer, 1993), faults in most carbonates would most likely form efficient permeability corridors in the subsurface even than

some of the fractures are abutting against the fault rock. Moreover, even when low-permeability fault rock is cut by a few fractures, which quickly equilibrate pressure differences across the fault, these low-permeability barriers may still affect sweep efficiency and cause production slow down.

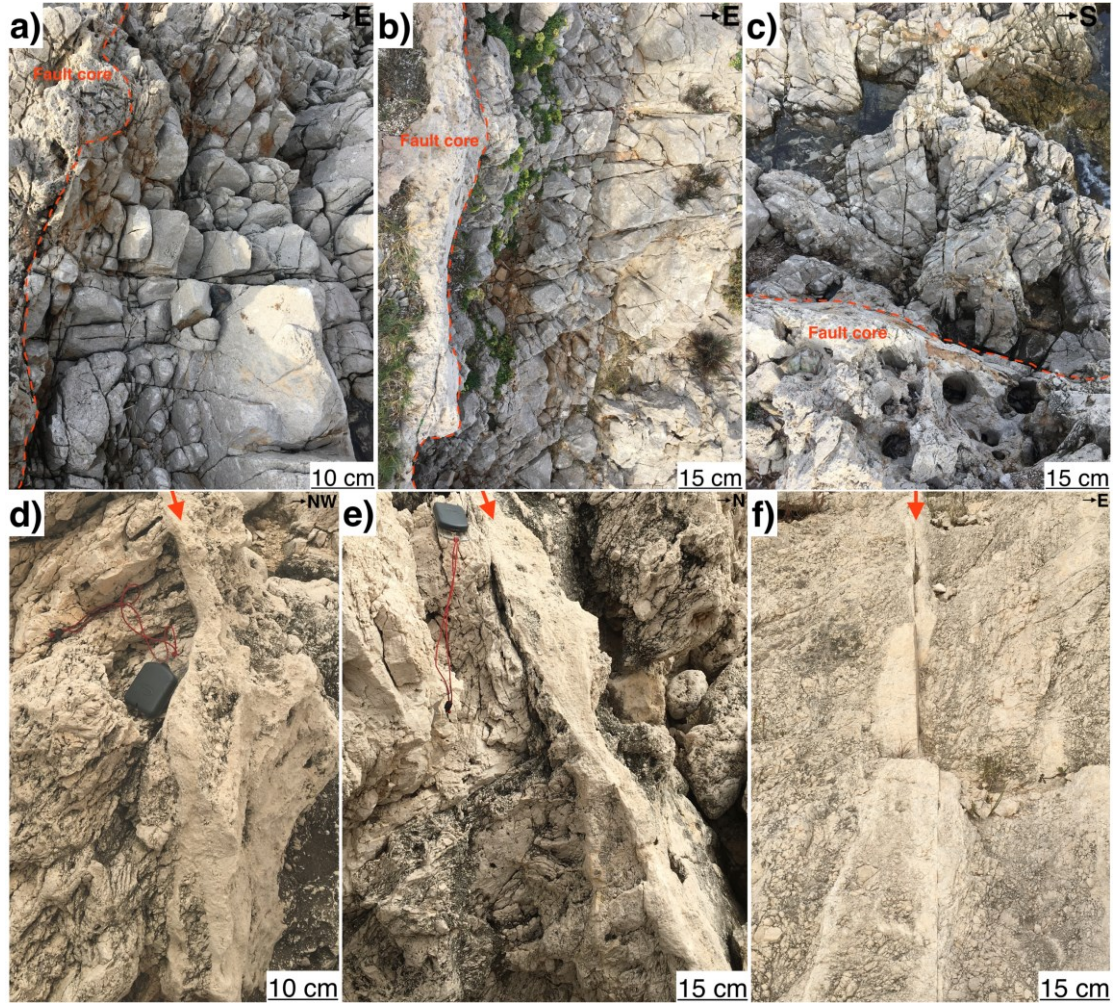


Figure 7-5 Outcrop photographs illustrating fault/fracture interaction along a cemented fault core in limestone-hosted rock (a-c), and cataclasite bands in dolomite-hosted rock (d-f) in San Vito lo Capo, Sicily, Italy. Note fracture blunting at the surface of the fault rock.

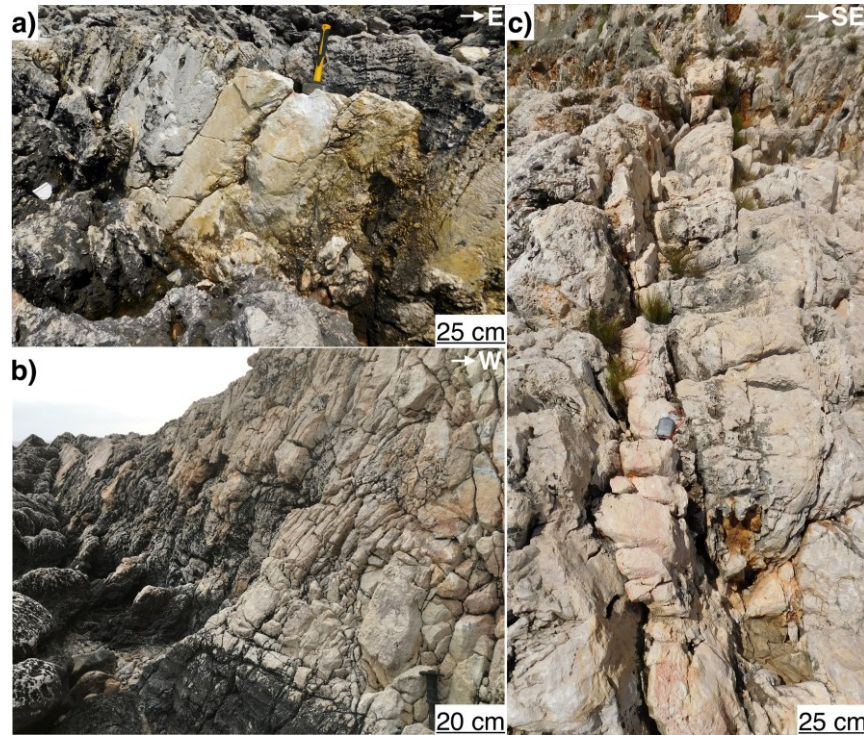


Figure 7-6 Outcrop photographs illustrating fault/fracture interaction along a dolomitized fault core in limestone-hosted rock in San Vito lo Capo, Sicily, Italy. Note how fractures cross-cut the fault rock, which shows yellow (a) and pink (b-c) colouration.

Most often, however, faulting in carbonates, especially at low displacements, produces no fault rock and forms dilational jogs along the strike of the fault (**Figure 7-7a-d**). In these cases, faults and fractures form one connected open network, and the fault zone acts as a permeability corridor. However, these faults are prone to cementation, where the open fault passageway may get filled with a continuous layer of cement (**Figure 7-7e-g**). If the fault is not reactivated by later faulting events, it may act as a barrier to propagating fractures.

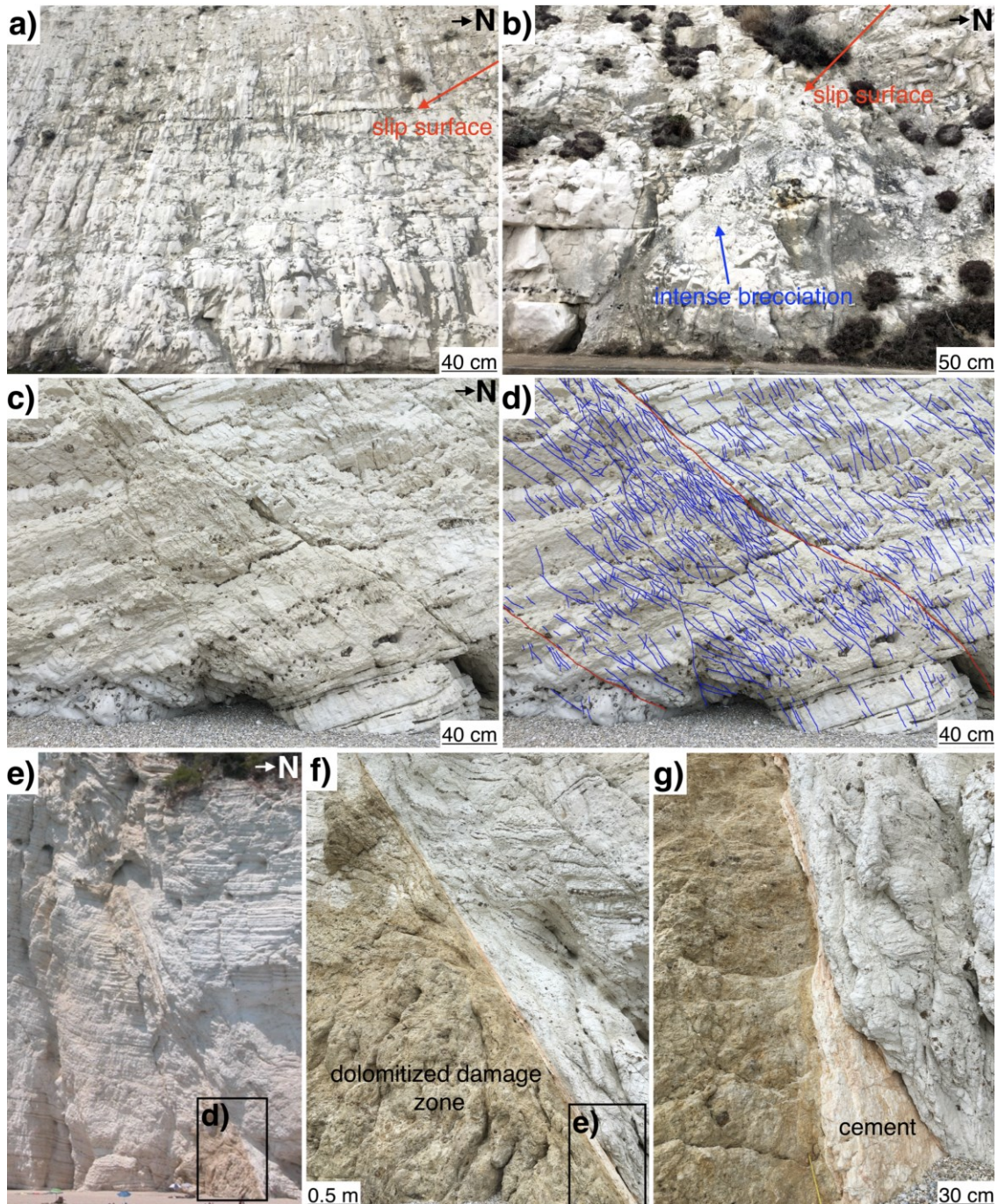


Figure 7-7 Photographs of a-b) Dumpton Bay (Isle of Thanet, SE England) and c-g) Vignagnotica (Gargano peninsula, Italy) cliffs, exposing a-d) open, and e-g) cemented faults. d) shows an interpretation of the slip surfaces (red) and fractures (blue) of an original image (c). f-g) are close-up photographs of a gravitational fault, a full image of which is showed in e). Note that the continuous layer of cement, formed along a slip surface, shows pink colouration, whereas the irregularly shaped brown patch in the footwall formed due to dolomitization. The host rock in Dumpton Bay (a-b) is Upper Cretaceous foraminiferal wackestone (chalk) with porosity of c.39.6%, and the host rock in Vignagnotica (c-g) is Tithonian–Aptian radiolarian mudstone with an average porosity of 8.8%.

Even in very high-porosity carbonates, more mature faulting stages produce slip surfaces along the previously deformed deformation bands or deformation band clusters, forming dilational zones (**Figure 7-8**). Moreover, faulting may produce very low-porosity fault rocks, which may then deform in a brittle-dilatant manner during the later faulting events and may be cut by open fractures (structure marked by no. 1 in **Figure 7-8b**). Although often the fractures bypass or stop at the surface of a deformation band (structures marked by no. 3 and 2, respectively, in **Figure 7-8b**). However, it is not known, if the observed fractures are related to an uplift, and if they would be forming in a similar manner in the subsurface.

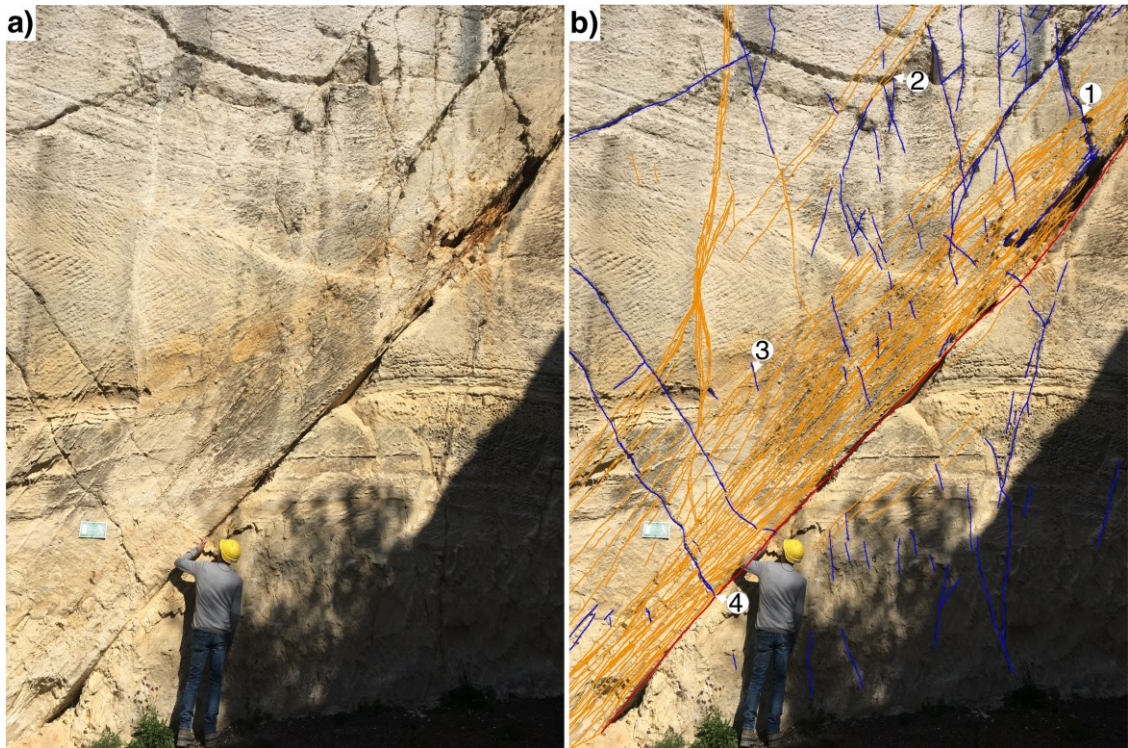


Figure 7-8 Photographs of a quarry wall at St Margarethen, Austria, exposing a fault within coralline grainstone of Middle Miocene in age, with a host rock porosity of c.33%. a) Original image, and b) interpretation of the deformational structures. Note a thick deformation band zone (orange) in the hanging wall, forming along a principal slip surface (red) and cut by fractures (blue). 1 indicates a fracture which cross-cuts the deformation bands; 2 shows a fracture blunting at the surface of the deformation band; 3 indicates a fracture which bypasses the deformation bands; and 4 shows a fracture which stops propagating at the slip surface.

7.4 Fault sealing prediction in carbonates

In siliciclastic reservoirs fault permeability (Manzocchi et al., 1999; Sperrevik et al. 2002; Jolley et al., 2007) and fault-dependent hydrocarbon column heights (Sperrevik et al., 2002; Bretan et al., 2003; Yielding et al., 2010) may be estimated by using empirical relationships of those parameters to the algorithms of Shale Gouge Ratio (Yielding et al., 1997); Clay Smear Potential (Lehner and Pilaar, 1997); Shale Smear Factor (Lindsay et al., 1993); Probabilistic Shale Smear Factor (Childs et al., 2007); or Effective Shale Gouge Ratio (Freeman et al., 2010), which are based on estimating clay concentration in the fault rocks. These algorithms are potentially valuable for predicting fault seal behaviour in clay-rich carbonate sequences such as those reported by Cornet et al. (2004). However, cataclasis and cementation are the most commonly found potential sealing mechanisms in carbonate fault zones, as documented in the literature (Solum and Huisman, 2017, and references therein) and observed in this work. Therefore, cataclasis and cementation, potentially together with other diagenetic processes such as dynamic recrystallization and pressure solution, will have to be predicted before static or dynamic fault-seal potential in carbonates can be examined successfully.

Up until now, it is unclear, how to derive similar parameters such as clay content for Shale Gouge Ratio estimation, to incorporate diagenetic processes in sealing predictions. This is likely to be difficult because even within the small geographic area, like in our studied case (**Chapter 5**), where rocks underwent the same faulting events and had the same host lithology, some faults became dolomitized and were reactivated (Punta Negra 2,3,

Torre Isolidda and El Bahiro faults), whereas other faults were resealed by cement and were not reactivated like the former faults (Torrazzo, Punta Negra 1). Therefore, these faults, despite undergoing the same faulting events, experienced different diagenetic processes, which had an impact on fracture propagation, and potentially, fluid flow. Moreover, cements that are externally derived to the fault zones are likely to be independent of displacement, thus, cementation may decrease the fault rock permeability at any displacement (e.g., Cooke et al., 2019). Therefore, considerably more research is needed to derive parameters for prediction of diagenetic processes in the fault zones.

Impact of mechanical deformation (i.e., cataclasis) on permeability, however, may be potentially predicted by deriving correlations between the fault displacement/thickness and mechanical properties of the host rock. The latter parameter is extremely important, because, as discussed in **Chapter 5**, lithofacies with different mechanical properties may respond differently to deformation. For instance, displacement may be localized in limestones, and distributed throughout a larger area in dolomites. It has been reported that carbonate fault rock heterogeneity (Michie and Haines, 2016; Michie et al., 2018) and cataclasite permeability variability (Cooke et al., 2019) increase with increasing displacement. Moreover, fault rock thickness (Solum and Huisman, 2017) and continuity (Michie et al., 2014; Bauer et al., 2016; Cooke et al., 2018) also tend to increase with increasing displacement. In porous sandstones, permeability has been shown to decrease as a function of cataclasis intensity: low-permeability reduction was observed in crush microbreccia of pure compaction bands and shear-enhanced compaction

bands, and high-permeability reduction was recorded in cataclasites/ultracataclasites of shear bands (band clusters, slipped bands and fault cores) (Ballas et al., 2015). In **Chapter 4**, similar observations were made in porous carbonates: permeability reduction was higher in clustered deformation bands compared to single deformation bands, which underwent grain-scale cataclasis, but no subsequent diagenesis. However, grain-scale and fracture-derived cataclasites are prone to cementation, because the formation of freshly broken surfaces act as loci for cement precipitation (Haines et al., 2016). Therefore, the greatest permeability reduction for the studied deformation bands (**Chapter 4**) was produced by the diagenetic processes, such as recrystallization and cementation. Although in some instances, fault rocks undergo a grain size reduction through cataclasis, yet they retain open intergranular pore space (e.g., Cooke et al., 2019, or **Figure 5-8o,p**). This may be caused due to differing intensities of cataclasis, pressure solution, or differential fault zone cementation (Agosta and Kirschner, 2003; Agosta, 2008). It has been suggested that differential fault zone cementation occurs when the rate of fracturing surpasses twice the rate of cement growth (Lander and Laubach, 2015; Ukar and Laubach, 2016). This may explain why pore space in some cataclasites or breccias are occluded by cement while in others it remains open. Therefore, even when it may be possible to predict permeability as a result of increasing cataclasis, diagenesis, once again, may greatly modify permeability of these fault rocks. Moreover, as learnt in **Chapter 5**, fault zone architecture should be taken into account while evaluating fault zone scaling relationships, because the derived relationships, and hence fault prediction parameters, may differ for

fault zones with single-stranded fault cores and fault zones forming multiple highly-strained cataclasite bands, as in the studied faulted tight dolomite outcrops.

Chapter 8 Conclusions

In this work, faults formed in natural settings were studied in two porosity end-members of carbonate rocks: highly-porous (>38%) and very tight (<2%). However, a wide range of carbonate rock types with porosities covering from as low as nearly 0% to as high as 52% were triaxially deformed beyond failure to study deformation mechanisms resulting in failure, and how they affect the permeability. These and the compilation of permeability values for naturally-faulted rocks from this study and the literature suggest that permeability decreases due to deformation/faulting for carbonates with porosity >c.10% and may be either increased or decreased for lower porosity rocks (**Figure 8-1**). Fracturing/brecciation produced both in the laboratory and in naturally-occurring fault zones, lead to permeability increase in low-porosity rocks. However, in natural settings, open and/or dilational faults may form even in high-porosity rocks, but typically they form no fault rock or the fault rock is too fragile to collect (**Figure 7-7a,b & Figure 7-8**). That could be the reason, why no permeability data are reported in the literature for such faults, although most likely they would be increasing the permeability. Cataclastic flow, which reduces the permeability, may be produced in the laboratory, but only the natural processes, such as recrystallization and cementation, as well as high-strain cataclasis, may have a significant impact on permeability reduction. Studied examples showed that faults in carbonates may form barriers to fluid flow in the following scenarios (**Figure 8-1**):

- 1) If carbonates were weak and highly porous at the time of faulting and were then not deformed in any way during subsequent burial. Sealing faults in these rocks may be formed by cataclasis, which produces micritic matrix for subsequent recrystallization, or by cementation. Therefore, cataclasis alone may reduce the permeability, but only the diagenetic processes may produce a fault rock with very low-permeabilities, which will have great impact on fluid flow.
- 2) If faults in low-porosity carbonates produce low permeability and high capillary entry pressure fault rocks, which are not cut by later open fractures. These fault rocks may be formed by high-strained cataclasis and/or cementation.

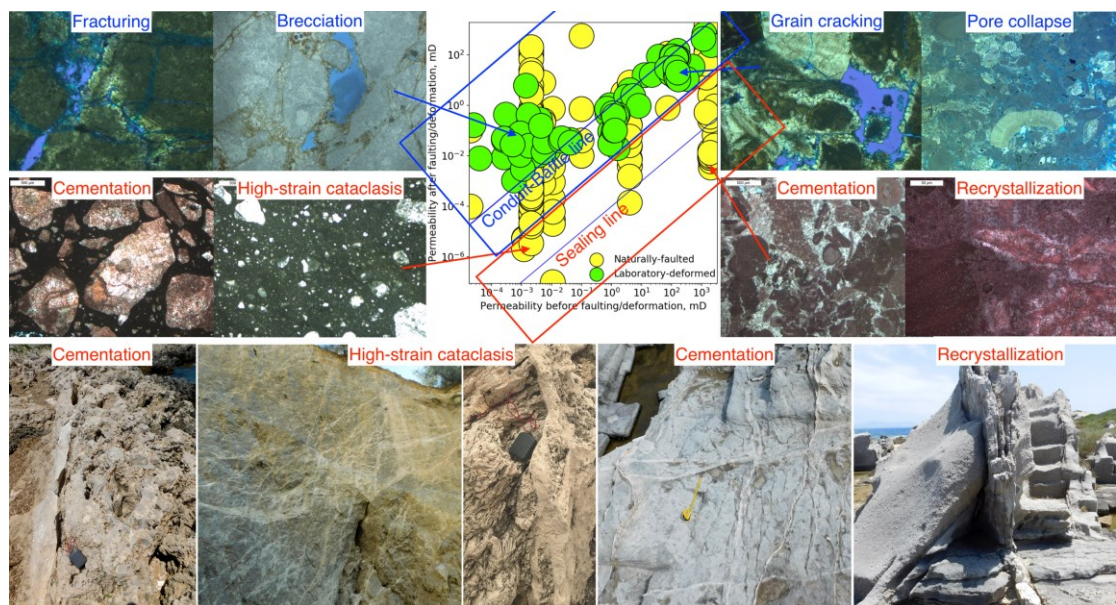


Figure 8-1 Summary of the results of this work: graph illustrates permeability before and after the laboratory-induced deformation (green) and natural faulting (yellow). Deformation mechanisms, observed at both deformation conditions, which result in increase or slight decrease in permeability are coloured in blue, and mechanisms, which lead to significant permeability reduction and may act as potential fault sealing mechanisms, are coloured in red.

In this study, only the outcrop analogues were studied, and documented examples from carbonate hydrocarbon reservoirs show that very few

examples exist providing good evidence of sealing faults. However, the reason may be that since most of the carbonate reservoirs lose porosity due to their susceptibility to early cementation and pressure solution, and hence, show brittle-dilatant deformational manner, the faults are likely to be cut by fractures. Therefore, it is hard to predict the presence of a sealing fault due to rapid pressure equilibration across the fault because of a presence of a few fractures, even though the fault rock may have an impact on sweep efficiency.

Other, less general findings of this work are the following:

- i. Faults in high-porosity carbonates: texture and composition of the host rock are key parameters controlling the deformation mechanisms occurring during the faulting. In particular, the presence of relatively weaker grains controls the way the fault is formed at a microstructural scale. For instance, strains in a host rock with a high percentage of peloids (micritic allochems with high microporosity) will be firstly accommodated by the disintegration of these peloids. The peloids are soft due to their high fraction of microporosity and lack of cementation; these get smeared into the pore space between the more competent skeletal grains, and may act as a source for recrystallization. The same strain in a similar rock without peloids would produce a fault rock with coarse cataclasite retaining high intergranular porosity (unless it becomes cemented). Similarly, in chalk, where the weakest grains are thin foraminifera shells, strain is firstly accommodated by the collapse of the macroporosity within these shells, resulting in a

dramatic decrease in porosity whilst hardly affecting the permeability, because this intraparticle porosity did not form a connected network.

- ii. Faults in low-porosity carbonates: the faults were studied in a relatively small geographic area, where tight carbonates have undergone the same faulting events, but a major difference was observed between the fault zone architectures in limestones and dolomites. The first faulting event formed localized faults with a single fault core surrounded by a damage zone within the limestone. The fault was either dolomitized as deformation proceeded or resealed by calcite cement soon after the brecciation. The dolomitized faults were reactivated during the second-stage of faulting forming polyphase breccias. Strain was distributed throughout a wider area in the dolomites during the first stage of faulting due to intense fragmentation and disintegration of large volumes of rock, forming a pulverized fault zone. The pulverized rock experienced cataclastic deformation during the second-stage of faulting forming an anastomosing network of deformation bands throughout the entire fault zone similar to those formed in high porosity rocks. The fracture spacing in the damage zone also varies significantly between the lithologies. In particular, damage zones in the limestone have a 5-10 cm fracture spacing whereas in the dolomite fracture spacing is 0.5–3 cm. Fractures are wider and longer in the limestone damage zones compared to those in the dolomite. It is likely that the differing mechanical and chemical properties of the dolomite and limestone

were responsible for them creating contrasting fault zone architectures.

- iii. Mechanical laboratory deformation of various types and porosity carbonates: under non-hydrostatic loading, samples with porosities >10% deformed in the ductile failure regime at confining pressures >20 MPa, and samples with porosity <10% deform in the brittle failure regime at all confining pressures used. Samples in the ductile failure regime failed due to distributed cataclastic flow, compaction or shear-compaction banding and focused damage around the macropores. In the brittle failure regime, samples showed transitional- and brittle-shear failure. Yield stress shows a good correlation with the initial porosity but grain size has negligible impact. Grain size did, however, impact the dominant mechanism that lead to failure of samples with porosity >25%. In particular, fine-grained carbonates showed an increase in grain packing and distributed or localized cataclastic flow but no shearing, whereas coarse-grained samples were sheared. Under non-hydrostatic loading, yield stress and pore size show a power-law relationship for samples with porosity <25%. Deformation resulted in a decreased permeability of samples with porosity >10%, whereas failure of samples with a lower porosity increased permeability.

8.1. Suggestions for further work

Even though the main and ultimate goal of this PhD's topic is to find similar algorithms for fault seal prediction as the ones available for clay rich rocks, such as Shale Gouge Ratio, achieving it still requires more research. There

are numerous knowledge gaps, that need to be filled before a robust algorithm for predicting an impact of faults on fluid flow can be developed. A few work suggestions, which were encountered during this study, but due to limited timeframes, could not be analysed, are presented below:

- i. The review on fault sealing in carbonates conducted by Solum and Huisman (2017) as well as the current study shows that cataclasis and cementation are the most commonly found potential fault sealing mechanisms in carbonates. However, it is not known, how thick cataclasite has to be for it to seal hydrocarbons on production/geological timescale. Moreover, outcrop studies report holes in fault rocks. The questions which should be asked then is how thin the fault rock is, and where the holes are, and how thick does it have to be to seal. More studies are also needed to be done on continuity of faults rocks.
- ii. The timing of faulting is not known in most of the documented outcrop studies, thus this should be assessed in the future work using fluid inclusion studies or isotope analysis (e.g., clustered C-O isotopes).
- iii. Fault/fracture relationships were only briefly touched during this study. Further work is needed on the interaction of fault and fracture systems in carbonates. Another very important and recently arising topic is hydraulic fracturing in carbonate reservoirs, especially for hydrothermal energy exploitation. Complex hydromechanical behaviour of fluid-induced fractures, including their geometry and interaction with pre-existing fractures, has not yet been completely

understood. Therefore, hydraulic fracturing requires further investigation, as well as understanding of the conditions, at which the faults are cut by fractures.

- iv. The overall trend of high-porosity carbonates deforming in a ductile compactive manner and low-porosity carbonates initially faulting in a dilatant, brittle manner is reminiscent of the ductile to brittle transition in sandstones (e.g., Fisher et al., 2003). The authors developed a model predicting possible deformation modes as a function of burial depth. In this case it was relatively easy to predict the evolution of P^* with burial depth because the main process responsible for porosity loss in sandstones is quartz cementation and there are simple models to predict the volume of quartz cement based on the time-temperature history, clay content and grain-size (e.g., Walderhaug, 1996). A preliminary database of the geomechanical properties of carbonates shows a correlation between critical stress and porosity (**Chapter 6**). However, development of a similar model for carbonates is more difficult as their diagenesis is not as predictable as that of sandstones, and a key aim will be to understand the controls on the scatter of stress-porosity relationship.
- v. Many sealing faults in siliciclastics have been reported to have a high clay content. Fault rocks in carbonates may also have very low permeabilities formed either due to clay smears formed along the fault planes, or due to juxtaposition of high permeability rocks against low permeability rocks, or due to enhanced pressure solution along the fault planes that would cause fault gouges similar to clay smears to

form. No outcrops like this have been encountered during this study, and there are only a small number of studies that have documented continuous clay smears in carbonates (e.g., Færseth, 2006; Elvik, 2012). Even though this may indicate that this process is not as efficient as within siliciclastic sequences, further work should assess the controls of clay smear continuity on carbonate-rich sequences.

- vi. The bulk permeability of fault zones in most carbonate reservoirs will be a product of matrix permeability, fracture permeability and fault core permeability. In this study, permeability measurements were based on core plugs and, therefore, they do not capture the effects of macroscopic fractures on permeability. The plug measurements from the fractured damage zones thus represent lower limits of permeability for that component of the fault zone and are insufficient to characterize the full permeability structure of fault zones in carbonates. Therefore, studies, measuring fracture permeability in carbonate damage zones, should be done at a larger scale.
- vii. A significant amount of research has been conducted on faults in carbonates in the last two decades, but mostly on outcrop analogues. There are no good examples of sealing faults in carbonate reservoirs. The evidence is not conclusive in most of the cases, as other processes, such as tilting contact, could be the reason of pressure differences (e.g., Al Dabbiya Rumaiha field - Noufal and Obaid, 2017). Therefore, examples from oil and gas companies should be shared with the public in order to test if results from the outcrops are comparable to the subsurface structures.

References

- Abate, B., Incandela, A., Renda, P., 1997. Carta Geologica delle Isole di Favignana e Levanzo. Dip. Di Geologia e Geodesia dell'Università degli Studi di Palermo, CoNISMa.
- Agosta, F., 2008. Fluid flow properties of basin-bounding normal faults in platform carbonates, Fucino Basin, central Italy. Geological Society, London, Special Publications, 299(1), pp.277-291.
- Agosta, F., Alessandroni, M., Tondi, E., Aydin, A., 2010. Oblique normal faulting along the northern edge of the Majella anticline, central Italy: Inferences on hydrocarbon migration and accumulation. Journal of Structural Geology, 32(9), 1317-1333.
- Agosta, F. and Aydin, A., 2006. Architecture and deformation mechanism of a basin-bounding normal fault in Mesozoic platform carbonates, central Italy. Journal of Structural Geology, 28(8), pp.1445-1467.
- Agosta, F. and Kirschner, D.L., 2003. Fluid conduits in carbonate-hosted seismogenic normal faults of central Italy. Journal of Geophysical Research: Solid Earth, 108(B4).
- Agosta, F., Prasad, M. and Aydin, A., 2007. Physical properties of carbonate fault rocks, fucino basin (Central Italy): implications for fault seal in platform carbonates. Geofluids, 7(1), pp.19-32.
- Akbar, M., Vissapragada, B., Alghamdi, A.H., Allen, D., Herron, M., Carnegie, A., Dutta, D., Olesen, J.R., Chourasiya, R.D., Logan, D. and Stief, D., 2000. A snapshot of carbonate reservoir evaluation. Oilfield Review, 12(4), pp.20-21.
- Al-Anzi, E., Al-Mutawa, M., Al-Habib, N., Al-Mumen, A., Nasr-El-Din, H., Alvarado, O., Brady, M., Davies, S., Fredd, C., Fu, D. and Lungwitz, B., 2003. Positive reactions in carbonate reservoir stimulation. Oilfield Review, 15(4), pp.28-45.

- Al-Obaid, R.H., Al-Thawad, F.M. and Gill, H., 2005. Identifying, Characterising and Locating Conductive Fault (s): Multi-Well Analysis Approach. In SPE Asia Pacific Oil and Gas Conference and Exhibition. Society of Petroleum Engineers.
- Alsharhan, A.S. and Sadd, J.L., 2000. Stylolites in Lower Cretaceous carbonate reservoirs, UAE.
- Anders, M.H., Christie-Blick, N., Wills, S. and Krueger, S.W., 2001. Rock deformation studies in the Mineral Mountains and Sevier Desert of west-central Utah: Implications for upper crustal low-angle normal faulting. *Geological Society of America Bulletin*, 113(7), pp.895-907.
- Anselmetti, F.S., Luthi, S. and Eberli, G.P., 1998. Quantitative characterization of carbonate pore systems by digital image analysis. *AAPG bulletin*, 82(10), pp.1815-1836.
- Antonellini, M.A., Aydin, A., Pollard, D.D., 1994. Microstructure of deformation bands in porous sandstones at Arches National Park, Utah. *Journal of structural geology*, 16(7), 941-959.
- Antonellini, M., Cilona, A., Tondi, E., Zambrano, M., Agosta, F., 2014a. Fluid flow numerical experiments of faulted porous carbonates, northwest Sicily (Italy). *Marine and Petroleum Geology*, 55, 186-201.
- Antonellini, M. and Mollema, P.N., 2000. A natural analog for a fractured and faulted reservoir in dolomite: Triassic Sella Group, northern Italy. *AAPG bulletin*, 84(3), pp.314-344.
- Antonellini, M., Tondi, E., Agosta, F., Aydin, A., Cello, G., 2008. Failure modes in deep-water carbonates and their impact for fault development: Majella Mountain, Central Apennines, Italy. *Marine and Petroleum Geology*, 25(10), 1074-1096.
- Antonellini, M., Petracchini, L., Billi, A., Scrocca, D., 2014b. First reported occurrence of deformation bands in a platform limestone, the Jurassic Calcare Massiccio Fm., northern Apennines, Italy. *Tectonophysics*, 628, 85-104.

Ameen, M. S., 1995. Fracture characterization in the Chalk and the evolution of the Thanet monocline, Kent, southern England. Geological Society, London, Special Publications 92, 149-174.

API (American Petroleum Institute), 1998, Recommended Practices for Core Analysis, 2nd Edition, Recommended Practice 40, second Edition, February.

Arroyo, M., Castellanza, R., Nova, R., 2005. Compaction bands and oedometric testing in cemented soils. *Soils and foundations*, 45(2), 181-194.

ASTM D4404-84(2004), Standard Test Method for Determination of Pore Volume and Pore Volume Distribution of Soil and Rock by Mercury Intrusion Porosimetry, ASTM International, West Conshohocken, PA, 2004.

Aydin, A., 2000. Fractures, faults, and hydrocarbon entrapment, migration and flow. *Marine and petroleum geology*, 17(7), pp.797-814.

Aydin, A., Borja, R.I., Eichhubl, P., 2006. Geological and mathematical framework for failure modes in granular rock. *Journal of Structural Geology*, 28(1), 83-98.

Aydin, A. and Eyal, Y., 2002. Anatomy of a normal fault with shale smear: Implications for fault seal. *AAPG bulletin*, 86(8), pp.1367-1381.

Aydin, A. and Johnson, A.M., 1978. Development of faults as zones of deformation bands and as slip surfaces in sandstone. *Pure and applied Geophysics*, 116(4-5), pp.931-942.

Banik, N., Singh, S.K., Al-Dohiem, A.A.A. and Al-Ajmi, N.H., 2007, January. Jurassic Fault framework and structural style in Bahra and its impact on fracture development. In International Petroleum Technology Conference. International Petroleum Technology Conference.

Ballas, G., Fossen, H. and Soliva, R., 2015. Factors controlling permeability of cataclastic deformation bands and faults in porous sandstone reservoirs. *Journal of Structural Geology*, 76, pp.1-21.

Ballas, G., Soliva, R., Sizun, J.P., Benedicto, A., Cavailhes, T., Raynaud, S., 2012. The importance of the degree of cataclasis in shear bands for fluid

flow in porous sandstone, Provence, France. AAPG bulletin, 96(11), 2167-2186.

Bartel, E.M., Neubauer, F., Heberer, B. and Genser, J., 2014. A low-temperature ductile shear zone: The gypsum-dominated western extension of the brittle Fella-Sava Fault, Southern Alps. *Journal of structural geology*, 69, pp.18-31.

Bastesen, E. and Braathen, A., 2010. Extensional faults in fine grained carbonates—analysis of fault core lithology and thickness—displacement relationships. *Journal of Structural Geology*, 32(11), pp.1609-1628.

Bastesen, E., Braathen, A. and Skar, T., 2013. Comparison of scaling relationships of extensional fault cores in tight carbonate and porous sandstone reservoirs. *Petroleum Geoscience*, 19(4), pp.385-398.

Baud, P., Exner, U., Lommatzsch, M., Reuschlé, T., Wong, T.F., 2017. Mechanical behavior, failure mode, and transport properties in a porous carbonate. *Journal of Geophysical Research: Solid Earth*, 122(9), 7363-7387.

Baud, P., Klein, E. and Wong, T.F., 2004. Compaction localization in porous sandstones: spatial evolution of damage and acoustic emission activity. *Journal of Structural Geology*, 26(4), pp.603-624.

Baud, P., Schubnel, A. and Wong, T.F., 2000. Dilatancy, compaction, and failure mode in Solnhofen limestone. *Journal of Geophysical Research: Solid Earth*, 105(B8), pp.19289-19303.

Baud, P., Vinciguerra, S., David, C., Cavallo, A., Walker, E., Reuschlé, T., 2009. Compaction and failure in high porosity carbonates: Mechanical data and microstructural observations. In *Rock Physics and Natural Hazards*, 869-898.

Bauer, H., Schröckenfuchs, T.C. and Decker, K., 2016. Hydrogeological properties of fault zones in a karstified carbonate aquifer (Northern Calcareous Alps, Austria). *Hydrogeology Journal*, 24(5), pp.1147-1170.

- Baxevanis, T., Papamichos, E., Flornes, O., Larsen, I., 2006. Compaction bands and induced permeability reduction in Tuffeau de Maastricht calcarenite. *Acta Geotechnica*, 1(2), 123-135.
- Bense, V.F., Gleeson, T., Loveless, S.E., Bour, O. and Scibek, J., 2013. Fault zone hydrogeology. *Earth-Science Reviews*, 127, pp.171-192.
- Berg, S.S. and Skar, T., 2005. Controls on damage zone asymmetry of a normal fault zone: outcrop analyses of a segment of the Moab fault, SE Utah. *Journal of Structural Geology*, 27(10), pp.1803-1822.
- Bergerat, F.T., Vandycke, S., 1994. Palaeostress analysis and geodynamical implications of Cretaceous-Tertiary faulting in Kent and the Boulonnais. *Journal of the Geological Society*, 151(3), 439-448.
- Bésuelle, P., 2001. Compacting and dilating shear bands in porous rock: Theoretical and experimental conditions. *Journal of Geophysical Research: Solid Earth*, 106(B7), 13435-13442.
- Bésuelle, P., Rudnicki, J.W., 2004. Localization: shear bands and compaction bands. *International Geophysics Series*, 89, 219-322.
- Billi, A., 2003. Solution slip and separations on strike-slip fault zones: theory and application to the Mattinata Fault, Italy. *Journal of Structural Geology*, 25(5), pp.703-715.
- Billi, A., 2007. On the extent of size range and power law scaling for particles of natural carbonate fault cores. *Journal of Structural Geology*, 29(9), pp.1512-1521.
- Billi, A., 2010. Microtectonics of low-P low-T carbonate fault rocks. *Journal of Structural Geology*, 32(9), pp.1392-1402.
- Billi, A. and Salvini, F., 2001. Fault-related solution cleavage in exposed carbonate reservoir rocks in the southern Apennines, Italy. *Journal of Petroleum Geology*, 24(2), pp.147-169.
- Billi, A., Salvini, F. and Storti, F., 2003. The damage zone-fault core transition in carbonate rocks: implications for fault growth, structure and permeability. *Journal of Structural geology*, 25(11), pp.1779-1794.

- Bjørkum, P. A., 1996. How important is pressure solution in causing dissolution of quartz in sandstones?. *Journal of Sedimentary Research*, 66, 147–154.
- Blenkinsop, T.G. and Rutter, E.H., 1986. Cataclastic deformation of quartzite in the Moine thrust zone. *Journal of Structural Geology*, 8(6), pp.669-681.
- Boccaletti, M., Cello, G. and Tortorici, L., 1987. Transtensional tectonics in the Sicily Channel. *Journal of Structural Geology*, 9(7), pp.869-876.
- Bockel-Rebelle, M.O., Hassall, J.K., Silva, F.P., Lozano, J.A., Al Deeb, M., Salem, S.E.A., Vesseron, M. and Al Mehsin, K., 2004, January. Faults, fracture corridors and diffuse fracturing: ranking the main structural heterogeneities within onshore Abu Dhabi fields. In Abu Dhabi International Conference and Exhibition. Society of Petroleum Engineers.
- Bonson, C.G., Childs, C., Walsh, J.J., Schöpfer, M.P. and Carboni, V., 2007. Geometric and kinematic controls on the internal structure of a large normal fault in massive limestones: the Maghlaq Fault, Malta. *Journal of Structural Geology*, 29(2), pp.336-354.
- Borja, R.I., Aydin, A., 2004. Computational modeling of deformation bands in granular media. I. Geological and mathematical framework. *Computer Methods in Applied Mechanics and Engineering*, 193(27-29), 2667-2698.
- Boutéca, M.J., Sarda, J.P. and Vincke, O., 2000, January. Constitutive law for permeability evolution of sandstones during depletion. In SPE International Symposium on Formation Damage Control. Society of Petroleum Engineers.
- Bouvier, J.D., Kaars-Sijpesteijn, C.H., Kluesner, D.F., Onyejekwe, C.C. and Van der Pal, R.C., 1989. Three-dimensional seismic interpretation and fault sealing investigations, Nun River Field, Nigeria. *AAPG bulletin*, 73(11), pp.1397-1414.
- Brace, W.F., Walsh, J.B. and Frangos, W.T., 1968. Permeability of granite under high pressure. *Journal of Geophysical research*, 73(6), pp.2225-2236.

- Bramwell, N.P., Caillet, G., Meciani, L., Judge, N., Green, M. and Adam, P., 1999, January. Chalk exploration, the search for a subtle trap. In Geological Society, London, Petroleum Geology Conference series (Vol. 5, No. 1, pp. 911-937). Geological Society of London.
- Brankman, C.M., Aydin, A., 2004. Uplift and contractional deformation along a segmented strike-slip fault system: the Gargano Promontory, southern Italy. *Journal of Structural Geology*, 26(5), 807-824.
- Brantut, N., Heap, M.J., Baud, P., Meredith, P.G., 2014. Mechanisms of time - dependent deformation in porous limestone. *Journal of Geophysical Research: Solid Earth*, 119(7), 5444-5463.
- Bretan, P., Yielding, G. and Jones, H., 2003. Using calibrated shale gouge ratio to estimate hydrocarbon column heights. *AAPG bulletin*, 87(3), pp.397-413.
- Brogi, A. and Novellino, R., 2015. Low Angle Normal Fault (LANF)-zone architecture and permeability features in bedded carbonate from inner Northern Apennines (Rapolano Terme, Central Italy). *Tectonophysics*, 638, pp.126-146.
- Buckley, J.S. and Liu, Y., 1998. Some mechanisms of crude oil/brine/solid interactions. *Journal of Petroleum Science and Engineering*, 20(3-4), pp.155-160.
- Burgess, C.J. and Peter, C.K., 1985, January. Formation, distribution, and prediction of stylolites as permeability barriers in the Thamama Group, Abu Dhabi. In Middle East Oil Technical Conference and Exhibition. Society of Petroleum Engineers.
- Bussolotto, M., Benedicto, A., Invernizzi, C., Micarelli, L., Plagnes, V. and Deiana, G., 2007. Deformation features within an active normal fault zone in carbonate rocks: The Gubbio fault (Central Apennines, Italy). *Journal of Structural Geology*, 29(12), pp.2017-2037.
- Bussolotto, M., Benedicto, A., Moen-Maurel, L. and Invernizzi, C., 2015. Fault deformation mechanisms and fault rocks in micritic limestones:

Examples from Corinth rift normal faults. *Journal of Structural Geology*, 77, pp.191-212.

Caine, J.S., Evans, J.P. and Forster, C.B., 1996. Fault zone architecture and permeability structure. *Geology*, 24(11), pp.1025-1028.

Cantrell, D., Swart, P. and Hagerty, R., 2004. Genesis and characterization of dolomite, Arab-D reservoir, Ghawar field, Saudi Arabia. *GeoArabia*, 9(2), pp.11-36

Cappa, F., Guglielmi, Y. and Virieux, J., 2007. Stress and fluid transfer in a fault zone due to overpressures in the seismogenic crust. *Geophysical Research Letters*, 34(5).

Carter, N.L., Kronenberg, A.K., Ross, J.V. and Wiltschko, D.V., 1990. Control of fluids on deformation of rocks. Geological Society, London, Special Publications, 54(1), pp.1-13.

Casolari, E., Negri, A., Picotti, V., Bertotti, G., 2000. Neogene stratigraphy and sedimentology of the Gargano Promontory (southern Italy). *Eclogae Geologicae Helveticae*, 93(1), 7-24.

Castagna, A., Ougier-Simonin, A., Benson, P.M., Browning, J., Walker, R.J., Fazio, M. and Vinciguerra, S., 2018. Thermal Damage and Pore Pressure Effects of the Brittle-Ductile Transition in Comiso Limestone. *Journal of Geophysical Research: Solid Earth*, 123(9), pp.7644-7660.

Castiglioni, B., Sauro, U., 2016. Large collapse dolines in Puglia (southern Italy): the cases of "Dolina Pozzatina" in the Gargano plateau and of "Puli" in the Murge. *Acta Carsologica*, 29(2).

Catalano, R., D'argenio, B., Montanari, L., Morlotti, E., Torelli, L., 1985. Marine geology of the NW Sicily offshore (Sardinia Channel) and its relationships with mainland structures. *Bollettino della Societa Geologica Italiana*, 104(2), 207-215.

Catalano, R., Di Stefano, P., Sulli, A. and Vitale, F.P., 1996. Paleogeography and structure of the central Mediterranean: Sicily and its offshore area. *Tectonophysics*, 260(4), pp.291-323.

Celico, F., Petrella, E. and Celico, P., 2006. Hydrogeological behaviour of some fault zones in a carbonate aquifer of Southern Italy: an experimentally based model. *Terra Nova*, 18(5), pp.308-313.

Cello, G., Invernizzi, C., Mazzoli, S.T. and Tondi, E., 2001. Fault properties and fluid flow patterns from Quaternary faults in the Apennines, Italy. *Tectonophysics*, 336(1-4), pp.63-78.

Channell, J.E.T., d'Argenio, B., Horvath, F., 1979. Adria, the African promontory, in *Mesozoic Mediterranean palaeogeography*. *Earth-Science Reviews*, 15(3), 213-292.

Chambon, G., Schmittbuhl, J., Corfdir, A., Orellana, N., Diraison, M. and Géraud, Y., 2006. The thickness of faults: From laboratory experiments to field scale observations. *Tectonophysics*, 426(1-2), pp.77-94.

Chester, F.M., Chester, J.S., Kirschner, D.L., Schulz, S.E. and Evans, J.P., 2004. Structure of large-displacement, strike-slip fault zones in the brittle continental crust. *Rheology and deformation in the lithosphere at continental margins*, 1, pp.223-260.

Chester, F.M., Evans, J.P. and Biegel, R.L., 1993. Internal structure and weakening mechanisms of the San Andreas fault. *Journal of Geophysical Research: Solid Earth*, 98(B1), pp.771-786.

Chester, F.M. and Logan, J.M., 1986. Implications for mechanical properties of brittle faults from observations of the Punchbowl fault zone, California. *Pure and Applied Geophysics*, 124(1-2), pp.79-106.

Cheung, C.S.N., 2015. Experimental deformation in sandstone, carbonates and quartz aggregate (No. BNL-113352-2016-TH). Brookhaven National Laboratory (BNL), Upton, NY (United States).

Childs, C., Nicol, A., Walsh, J.J. and Watterson, J., 1996. Growth of vertically segmented normal faults. *Journal of Structural Geology*, 18(12), pp.1389-1397.

Childs, C., Walsh, J.J., Manzocchi, T., Strand, J., Nicol, A., Tomasso, M., Schöpfer, M.P. and Aplin, A.C., 2007. Definition of a fault permeability

predictor from outcrop studies of a faulted turbidite sequence, Taranaki, New Zealand. Geological Society, London, Special Publications, 292(1), pp.235-258.

Childs, C., Walsh, J.J. and Watterson, J., 1997. Complexity in fault zone structure and implications for fault seal prediction. In Norwegian Petroleum Society Special Publications (Vol. 7, pp. 61-72). Elsevier.

Chilingar, G.V., 1960. Notes on classification of carbonate rocks on basis of chemical composition. Journal of Sedimentary Research, 30(1), pp.157-158.

Chilovi, C., de Feyter, A.J., Pompucci, A., 2000. Wrench zone reactivation in the Adriatic Block; the example of the Mattinata fault system (SE Italy). Bollettino della Società Geologica Italiana, 119(1), 3-8.

Chinnery, M., 1966. Secondary faulting: I. Theoretical aspects. Canadian Journal of Earth Sciences, 3(2), pp.163-174.

Choquette, P.W., Pray, L.C., 1970. Geologic nomenclature and classification of porosity in sedimentary carbonates. AAPG bulletin, 54(2), 207-250.

Chuhan, F.A., Kjeldstad, A., Bjørlykke, K. and Høeg, K., 2003. Experimental compression of loose sands: relevance to porosity reduction during burial in sedimentary basins. Canadian Geotechnical Journal, 40(5), pp.995-1011.

Churcher, P.L., French, P.R., Shaw, J.C. and Schramm, L.L., 1991, February. Rock properties of Berea sandstone, Baker dolomite, and Indiana limestone. In SPE International Symposium on Oilfield Chemistry (Vol. 20, p. 22). Anaheim, CA: Society of Petroleum Engineers.

Cilona, A., Baud, P., Tondi, E., Agosta, F., Vinciguerra, S., Rustichelli, A., Spiers, C.J., 2012. Deformation bands in porous carbonate grainstones: field and laboratory observations. Journal of Structural Geology, 45, 137-157.

Cilona, A., Faulkner, D.R., Tondi, E., Agosta, F., Mancini, L., Rustichelli, A., Baud, P., Vinciguerra, S., 2014. The effects of rock heterogeneity on compaction localization in porous carbonates. Journal of Structural Geology, 67, 75-93.

- Collettini, C., Carpenter, B.M., Viti, C., Cruciani, F., Mollo, S., Tesei, T., Trippetta, F., Valoroso, L., Chiaraluce, L., 2014. Fault structure and slip localization in carbonate-bearing normal faults: An example from the Northern Apennines of Italy. *Journal of Structural Geology*, 67, pp.154-166.
- Coney, D., Fyfe, T.B., Retail, P. and Smith, P.J., 1993, January. Clair appraisal: the benefits of a co-operative approach. In Geological Society, London, Petroleum Geology Conference series (Vol. 4, No. 1, pp. 1409-1420). Geological Society of London.
- Cooke, A.P., Fisher, Q.J., Michie, E.A., Yielding, G., 2018. Investigating the controls on fault rock distribution in normal faulted shallow burial limestones, Malta, and the implications for fluid flow. *Journal of Structural Geology*.
- Cooke, A.P., Fisher, Q.J., Michie, E.A., Yielding, G., 2019. Permeability of carbonate fault rocks: a case study from Malta. *Petroleum Geoscience*, pp.petgeo2019-055.
- Cornet, F.H., Doan, M.L., Moretti, I. and Borm, G., 2004. Drilling through the active Aigion Fault: the AIG10 well observatory. *Comptes Rendus Geoscience*, 336(4-5), pp.395-406.
- Cornée, J.J., Moissette, P., Joannin, S., Suc, J.P., Quillévéré, F., Krijgsman, W., Hilgen, F., Koskeridou, E., Münch, P., Lécuyer, C., Desvignes, P., 2006. Tectonic and climatic controls on coastal sedimentation: the Late Pliocene–Middle Pleistocene of northeastern Rhodes, Greece. *Sedimentary Geology*, 187(3-4), 159-181.
- Cowie, P.A. and Scholz, C.H., 1992. Physical explanation for the displacement-length relationship of faults using a post-yield fracture mechanics model. *Journal of Structural Geology*, 14(10), pp.1133-1148.
- Crawford, B.R. and Yale, D.P., 2002, January. Constitutive modeling of deformation and permeability: relationships between critical state and micromechanics. In SPE/ISRM Rock Mechanics Conference. Society of Petroleum Engineers.

- Croizé, D., Bjørlykke, K., Jahren, J., Renard, F., 2010a. Experimental mechanical and chemical compaction of carbonate sand. *Journal of Geophysical Research: Solid Earth*, 115(B11).
- Croizé, D., Ehrenberg, S.N., Bjørlykke, K., Renard, F. and Jahren, J., 2010b. Petrophysical properties of bioclastic platform carbonates: implications for porosity controls during burial. *Marine and Petroleum Geology*, 27(8), pp.1765-1774.
- Croizé, D., Renard, F. and Gratier, J.P., 2013. Compaction and porosity reduction in carbonates: A review of observations, theory, and experiments. In *Advances in Geophysics* (Vol. 54, pp. 181-238). Elsevier.
- Curran, J.H. and Carroll, M.M., 1979. Shear stress enhancement of void compaction. *Journal of Geophysical Research: Solid Earth*, 84(B3), pp.1105-1112.
- Cuss, R.J., Rutter, E.H. and Holloway, R.F., 2003. The application of critical state soil mechanics to the mechanical behaviour of porous sandstones. *International Journal of Rock Mechanics and Mining Sciences*, 40(6), pp.847-862.
- Davidson, D.A. and Snowdon, D.M., 1978. Beaver River Middle Devonian Carbonate: Performance review of a high-relief, fractured gas reservoir with water influx. *Journal of Petroleum Technology*, 30(12), pp.1-672.
- Davis, L.A., Moss, R.M. and Pepin, G.P., 1992. Direct measurement of the constituent porosities in a dual-porosity matrix. *The Log Analyst*, 33(02).
- Dautriat, J., Bornert, M., Gland, N., Dimanov, A. and Raphanel, J., 2011. Localized deformation induced by heterogeneities in porous carbonate analysed by multi-scale digital image correlation. *Tectonophysics*, 503(1-2), pp.100-116.
- Dercourt, J.E.A., Zonenshain, L.P., Ricou, L.E., Kazmin, V.G., Le Pichon, X., Knipper, A.L., Grandjacquet, C., Sbertshikov, I.M., Geyssant, J., Lepvrier, C., Pechersky, D.H., 1986. Geological evolution of the Tethys belt from the Atlantic to the Pamirs since the Lias. *Tectonophysics*, 123(1-4), 241-315.

Di Cuia, R. and Riva, A., 2016. Mediterranean Carbonate Potential: Lessons from Existing Discoveries.

Donath, F.A., 1970. Some information squeezed out of a rock. *American Scientist*, 58, pp.54-72.

Downey, M.W., 1984. Evaluating seals for hydrocarbon accumulations. *AAPG bulletin*, 68(11), pp.1752-1763.

Downey, M.W., 1994. Hydrocarbon Seal Rocks: Chapter 8: Part II. Essential Elements.

Duermeijer, C.E., Nyst, M., Meijer, P.T., Langereis, C.G., Spakman, W., 2000. Neogene evolution of the Aegean arc: paleomagnetic and geodetic evidence for a rapid and young rotation phase. *Earth and Planetary Science Letters*, 176(3), 509-525.

Du Bernard, X., Eichhubl, P., Aydin, A., 2002. Dilation bands: A new form of localized failure in granular media. *Geophysical Research Letters*, 29(24), 29-1.

Dunham, R.J., 1962. Classification of carbonate rocks according to depositional texture. In: W.E. Ham (Editor), *Classification of Carbonate Rocks*. Am. Assoc. Pet. Geol., Mem.,1, pp.108-121.

Dunham, K.C., 1988. Pennine mineralisation in depth. *Proceedings of the Yorkshire Geological Society*, 47(1), pp.1-12.

Dunnington, H.V., 1967, January. Aspects of diagenesis and shape change in stylolitic limestone reservoirs. In 7th World Petroleum Congress. World Petroleum Congress.

Dutton, S.P. and Willis, B.J., 1998. Comparison of outcrop and subsurface sandstone permeability distribution, lower cretaceous fall river formation, South Dakota and Wyoming. *Journal of Sedimentary Research*, 68(5), pp.890-900.

Efstratios, D. 2011. Quantitative analysis of geometric evolution of fault zones of Mavropigis' lignite field in Ptolemais Basin (W. Macedonia, Greece). MSc Thesis, Aristotle University of Thessaloniki.

- Ehrenberg, S.N. and Nadeau, P.H., 2005. Sandstone vs. carbonate petroleum reservoirs: A global perspective on porosity-depth and porosity-permeability relationships. *AAPG bulletin*, 89(4), pp.435-445.
- Eichhubl, P., Davatz, N.C. and Becker, S.P., 2009. Structural and diagenetic control of fluid migration and cementation along the Moab fault, Utah. *AAPG bulletin*, 93(5), pp.653-681.
- Eichhubl, P., Hooker, J.N. and Laubach, S.E., 2010. Pure and shear-enhanced compaction bands in Aztec Sandstone. *Journal of Structural Geology*, 32(12), pp.1873-1886.
- Eichhubl, P., Taylor, W.L., Pollard, D.D., Aydin, A., 2004. Paleo-fluid flow and deformation in the Aztec Sandstone at the Valley of Fire, Nevada—Evidence for the coupling of hydrogeologic, diagenetic, and tectonic processes. *Geological Society of America Bulletin*, 116(9-10), 1120-1136.
- El Ghar, M.A. and Hussein, A.W., 2005, November. Post-depositional changes of the lower-middle eocene limestones of the area between Assiut and Minia, West of the Nile Valley, Egypt. In *Proceedings of the first international conference on the geology of the Tethys* (pp. 224-248). Cairo University Press.
- Elvik, L., 2012. Characterisation of extensional faults in carbonate rocks (Suez Rift, Egypt); with particular focus on the role of shale smear. MSc thesis, The University of Bergen.
- Engelder, J.T., 1974. Cataclasis and the generation of fault gouge. *Geological Society of America Bulletin*, 85(10), pp.1515-1522.
- Engelhardt V., W., 1960. *Der Porenraum der Sedimente*.
- Evans, J.P., Forster, C.B. and Goddard, J.V., 1997. Permeability of fault-related rocks, and implications for hydraulic structure of fault zones. *Journal of structural Geology*, 19(11), pp.1393-1404.
- Exner, U., Kaiser, J., Gier, S., 2013. Deformation bands evolving from dilation to cementation bands in a hydrocarbon reservoir (Vienna Basin, Austria). *Marine and petroleum geology*, 43, 504-515.

- Fabre, D. and Gustkiewicz, J., 1997. Poroelastic properties of limestones and sandstones under hydrostatic conditions. *International Journal of Rock Mechanics and Mining Sciences*, 34(1), pp.127-134.
- Fabricius, I.L. and Rana, M.A., 2010, January. Tilting oil-water contact in the chalk of Tyra Field as interpreted from capillary pressure data. In Geological Society, London, Petroleum Geology Conference series (Vol. 7, No. 1, pp. 463-472). Geological Society of London.
- Faulkner, D.R., Jackson, C.A.L., Lunn, R.J., Schlische, R.W., Shipton, Z.K., Wibberley, C.A.J. and Withjack, M.O., 2010. A review of recent developments concerning the structure, mechanics and fluid flow properties of fault zones. *Journal of Structural Geology*, 32(11), pp.1557-1575.
- Faulkner, D.R., Lewis, A.C. and Rutter, E.H., 2003. On the internal structure and mechanics of large strike-slip fault zones: field observations of the Carboneras fault in southeastern Spain. *Tectonophysics*, 367(3-4), pp.235-251.
- Ferrill, D.A. and Morris, A.P., 2003. Dilational normal faults. *Journal of Structural Geology*, 25(2), pp.183-196.
- Ferrill, D.A. and Morris, A.P., 2008. Fault zone deformation controlled by carbonate mechanical stratigraphy, Balcones fault system, Texas. *AAPG bulletin*, 92(3), pp.359-380.
- Ferrill, D.A., Morris, A.P., McGinnis, R.N., Smart, K.J. and Ward, W.C., 2011. Fault zone deformation and displacement partitioning in mechanically layered carbonates: The Hidden Valley fault, central Texas. *AAPG bulletin*, 95(8), pp.1383-1397.
- Færseth, R.B., 2006. Shale smear along large faults: continuity of smear and the fault seal capacity. *Journal of the Geological Society*, 163(5), pp.741-751.
- Finkel, E.A. and Wilkinson, B.H., 1990. Stylolitization as Source of Cement in Mississippian Salem Limestone, West-Central Indiana (1). *AAPG Bulletin*, 74(2), pp.174-186.

- Fisher, Q.J., Casey, M., Harris, S.D. and Knipe, R.J., 2003. Fluid-flow properties of faults in sandstone: The importance of temperature history. *Geology*, 31(11), pp.965-968.
- Fisher, Q.J. and Jolley, S.J., 2007. Treatment of faults in production simulation models. Geological Society, London, Special Publications, 292(1), pp.219-233.
- Fisher, Q.J., Knipe, R., 1998. Fault sealing processes in siliciclastic sediments. Geological Society, London, Special Publications, 147(1), 117-134.
- Fisher, Q.J., Knipe, R.J., 2001. The permeability of faults within siliciclastic petroleum reservoirs of the North Sea and Norwegian Continental Shelf. *Marine and Petroleum Geology*, 18(10), 1063-1081.
- Flügel, E., 2013. *Microfacies of carbonate rocks: analysis, interpretation and application*. Springer Science & Business Media.
- Folk, R.L., 1962. Spectral subdivision of limestone types. In: *Classification of Carbonate Rocks* (Ed. by W. E. Ham). Mem. Am. Ass. Petrol. Geol. Telsa, 1, pp.62-84.
- Folk, R.L., 1974. The natural history of crystalline calcium carbonate; effect of magnesium content and salinity. *Journal of Sedimentary Research*, 44(1), pp.40-53.
- Fondriest, M., Aretusini, S., Di Toro, G. and Smith, S.A., 2015. Fracturing and rock pulverization along an exhumed seismogenic fault zone in dolostones: The Foiana Fault Zone (Southern Alps, Italy). *Tectonophysics*, 654, pp.56-74.
- Fossen, H., Hesthammer, J., 1997. Geometric analysis and scaling relations of deformation bands in porous sandstone. *Journal of Structural Geology*, 19(12), 1479-1493.
- Fossen, H., Schultz, R.A., Shipton, Z.K., Mair, K., 2007. Deformation bands in sandstone: a review. *Journal of the Geological Society*, 164(4), 755-769.

- Fossen, H., Soliva, R., Ballas, G., Trzaskos, B., Cavalcante, C., Schultz, R.A., 2017. A review of deformation bands in reservoir sandstones: geometries, mechanisms and distribution. Geological Society, London, Special Publications, 459, SP459-4.
- Fredrich, J.T., Evans, B. and Wong, T.F., 1989. Micromechanics of the brittle to plastic transition in Carrara marble. *Journal of Geophysical Research: Solid Earth*, 94(B4), pp.4129-4145.
- Freeman, S.R., Harris, S.D. and Knipe, R.J., 2010. Cross-fault sealing, baffling and fluid flow in 3D geological models: tools for analysis, visualization and interpretation. Geological Society, London, Special Publications, 347(1), pp.257-282.
- Frost, E., Dolan, J., Sammis, C., Hacker, B., Cole, J. and Ratschbacher, L., 2009. Progressive strain localization in a major strike-slip fault exhumed from midseismogenic depths: Structural observations from the Salzach-Ennstal-Mariazell-Puchberg fault system, Austria. *Journal of Geophysical Research: Solid Earth*, 114(B4).
- Füchtbauer, H., 1959. Zur Nomenklatur der Sedimentgesteine. *Erdöl und Kohle*, 12(8), pp.605-613.
- Gallagher, J.J., Friedman, M., Handin, J. and Sowers, G.M., 1974. Experimental studies relating to microfracture in sandstone. *Tectonophysics*, 21(3), pp.203-247.
- Garrison, R.E., 1981. Diagenesis of oceanic carbonate sediments: a review of the DSDP perspective.
- Gaviglio, P., Bekri, S., Vandycke, S., Adler, P.M., Schroeder, C., Bergerat, F., Darquennes, A. and Coulon, M., 2009. Faulting and deformation in chalk. *Journal of structural geology*, 31(2), pp.194-207.
- van Gent, H.W., Holland, M., Urai, J.L. and Loosveld, R., 2010. Evolution of fault zones in carbonates with mechanical stratigraphy—Insights from scale models using layered cohesive powder. *Journal of Structural Geology*, 32(9), pp.1375-1391.

Géraud, Y., Diraison, M. and Orellana, N., 2006. Fault zone geometry of a mature active normal fault: a potential high permeability channel (Pirgaki fault, Corinth rift, Greece). *Tectonophysics*, 426(1-2), pp.61-76.

Giorgioni, M., Korneva, I., Tondi, E., Agosta, F. and Cilona, A., 2013, March. Permeability Structures of Fault Zones Crosscutting Tight Cretaceous Platform Carbonates (Val D'agri, Southern Italy). In *Offshore Mediterranean Conference and Exhibition*. Offshore Mediterranean Conference.

Giuffrida, A., La Bruna, V., Castelluccio, P., Panza, E., Rustichelli, A., Tondi, E., Giorgioni, M. and Agosta, F., 2019. Fracture simulation parameters of fractured reservoirs: Analogy with outcropping carbonates of the Inner Apulian Platform, southern Italy. *Journal of Structural Geology*, 123, pp.18-41.

Giunta, G., Nigro, F. and Renda, P., 2000. Extensional tectonics during Maghrebides chain building since late Miocene: examples from Northern Sicily. In *Annales Societatis Geologorum Poloniae* (Vol. 70, No. 1, pp. 81-98).

Giunta, G., Luzio, D., Tondi, E., De Luca, L., Giorgianni, A., D'Anna, G., Renda, P., Cello, G., Nigro, F., Vitale, M., 2004. The Palermo (Sicily) seismic cluster of September 2002, in the seismotectonic framework of the Tyrrhenian Sea-Sicily border area. *Annals of Geophysics*.

Głowacki, A. and Selvadurai, A.P.S., 2016. Stress-induced permeability changes in Indiana limestone. *Engineering geology*, 215, pp.122-130.

Goult, N.R., 2003. Reservoir stress path during depletion of Norwegian chalk oilfields. *Petroleum Geoscience*, 9(3), pp.233-241.

Graham, B., Antonellini, M. and Aydin, A., 2003. Formation and growth of normal faults in carbonates within a compressive environment. *Geology*, 31(1), pp.11-14.

Graham Wall, B.R., Girbacea, R., Mesonjesi, A. and Aydin, A., 2006. Evolution of fracture and fault-controlled fluid pathways in carbonates of the Albanides fold-thrust belt. *AAPG bulletin*, 90(8), pp.1227-1249.

- Grandinetti, F., Marcelli, C., Ferrara, E. and Barchi, M.R., 2000. Modelli di evoluzione cinematica per un'anticlinale umbro-marchigiana. *Bollettino-Societa Geologica Italiana*, 119(3), pp.541-552.
- Groshong Jr, R.H., 1988. Low-temperature deformation mechanisms and their interpretation. *Geological Society of America Bulletin*, 100(9), pp.1329-1360.
- Grove, C., Jerram, D.A., 2011. jPOR: An ImageJ macro to quantify total optical porosity from blue-stained thin sections. *Computers & Geosciences*, 37(11), 1850-1859.
- Guerriero, V., Mazzoli, S., Iannace, A., Vitale, S., Carravetta, A. and Strauss, C., 2013. A permeability model for naturally fractured carbonate reservoirs. *Marine and Petroleum Geology*, 40, pp.115-134.
- Guéguen, Y. and Sarout, J., 2009. Crack-induced anisotropy in crustal rocks: predicted dry and fluid-saturated Thomsen's parameters. *Physics of the Earth and Planetary Interiors*, 172(1-2), pp.116-124.
- Guglielmi, Y., Henry, P., Cappa, F. and Derode, B., 2013, January. Relationships between slow slip, seismicity and fluids leakage during a pressurized fault zone rupture in situ experiment: Importance for reservoir/caprock stimulation monitoring and efficiency assessment. In 47th US Rock Mechanics/Geomechanics Symposium. American Rock Mechanics Association.
- Hadizadeh, J.A.F.A.R. and Rutter, E.H., 1982, January. Experimental study of cataclastic deformation of a quartzite. In The 23rd US Symposium on Rock Mechanics (USRMS). American Rock Mechanics Association.
- Haines, T.J., Michie, E.A., Neilson, J.E. and Healy, D., 2016. Permeability evolution across carbonate hosted normal fault zones. *Marine and Petroleum Geology*, 72, pp.62-82.
- Haines, T.J., Neilson, J.E., Healy, D., Michie, E.A., Aplin, A.C., 2015. The impact of carbonate texture on the quantification of total porosity by image analysis. *Computers & Geosciences*, 85, 112-125.

- Hamaker, S. and Harris, R., 2007. Fault-related ground-water compartmentalization in the East Tintic Mining District, Utah.
- Hancock, P.L., 1985. Brittle microtectonics: principles and practice. *Journal of structural geology*, 7(3-4), pp.437-457.
- Hancock, P.L., 1994. From joints to paleostress. *Peri-Tethyan platforms*. Editions Technip, Paris, pp.145-158.
- Hanken, N., Bromley, R.G., Miller, J., 1996. Plio - Pleistocene sedimentation in coastal grabens, north - east Rhodes, Greece. *Geological Journal*, 31(3), 271-296.
- Hanks, C.L., Lorenz, J., Teufel, L. and Krumhardt, A.P., 1997. Lithologic and structural controls on natural fracture distribution and behavior within the Lisburne Group, northeastern Brooks Range and North Slope subsurface, Alaska. *AAPG bulletin*, 81(10), pp.1700-1720.
- Harding, T.P. and Tuminas, A.C., 1988. Interpretation of footwall (lowside) fault traps sealed by reverse faults and convergent wrench faults. *AAPG Bulletin*, 72(6), pp.738-757.
- Hardman, R.F.P. and Booth, J.E., 1991. The significance of normal faults in the exploration and production of North Sea hydrocarbons. *Geological Society, London, Special Publications*, 56(1), pp.1-13.
- Harris, P.M., Kendall, C.G.S.C. and Lerche, I., 1985. Carbonate cementation—a brief review.
- Harrison, D.G., Efford, N.D., Fisher, Q.J. and Ruddle, R.A., 2017. PETMiner—A Visual Analysis Tool for Petrophysical Properties of Core Sample Data. *IEEE transactions on visualization and computer graphics*, 24(5), pp.1728-1741.
- Hassan, K.M., 2007. Stratigraphy of Karbala–Najaf area, Central IRAQ. *Iraqi Bulletin of Geology and Mining*, 3(2), pp.53-62.

- Hatzor, Y.H., Zur, A. and Mimran, Y., 1997. Microstructure effects on microcracking and brittle failure of dolomites. *Tectonophysics*, 281(3-4), pp.141-161.
- Healy, D., 2009. Anisotropy, pore fluid pressure and low angle normal faults. *Journal of Structural Geology*, 31(6), pp.561-574.
- Healy, D., Michie, E., Haines, T., Neilson, J., Alsop, I., Timms, N. and Wilson, M. 2012. Outcrop-scale variations in petrophysical properties of faulted carbonates: exploring the relative influence of lithology, displacement and juxtaposition. Search and Discovery Article #120061, presented at the AAPG Hedberg Conference, 'Fundamental Controls on Flow in Carbonates'.
- Heap, M.J., Baud, P., Reuschlé, T. and Meredith, P.G., 2014. Stylolites in limestones: Barriers to fluid flow?. *Geology*, 42(1), pp.51-54.
- Hendry, J.P., Gregg, J.M., Shelton, K.L., Somerville, I.D. and Crowley, S.F., 2015. Origin, characteristics and distribution of fault-related and fracture-related dolomitization: Insights from Mississippian carbonates, Isle of Man. *Sedimentology*, 62(3), pp.717-752.
- Hermanrud, C., Teige, G.M.G., Lien, T. and Osnes, M.O., 2019, September. Depth-Dependent Fault Sealing in the Greater Oseberg Area. In Fifth International Conference on Fault and Top Seals.
- Hettema, M.H.H., Schutjens, P.M.T.M., Verboom, B.J.M. and Gussinklo, H.J., 2000. Production-induced compaction of a sandstone reservoir: the strong influence of stress path. *SPE Reservoir Evaluation & Engineering*, 3(04), pp.342-347.
- Heydari, E., 2000. Porosity loss, fluid flow, and mass transfer in limestone reservoirs: application to the Upper Jurassic Smackover Formation, Mississippi. *AAPG bulletin*, 84(1), pp.100-118.
- Hickman, R. J. 2004. Formulation and implementation of a constitutive model for soft rock.
- Higgins, M. W. 1971. Cataclastic Rocks. Professional Paper, United States Geological Survey, no. 687, 97 pp.

- Hollis, C., Bastesen, E., Boyce, A., Corlett, H., Gawthorpe, R., Hirani, J., Rotevatn, A. and Whitaker, F., 2017. Fault-controlled dolomitization in a rift basin. *Geology*, 45(3), pp.219-222.
- Honda, N., Kamel, M., Abouelenein, M., Loader, C. and Akbar, M., 1996, January. Fault interpretation and fracture morphology: A case study of Jurassic carbonate reservoir in El-Bunduq oil field, offshore Abu Dhabi and Qatar. In Abu Dhabi International Petroleum Exhibition and Conference. Society of Petroleum Engineers.
- House, W.M. and Gray, D.R., 1982. Cataclasites along the Saltville thrust, USA and their implications for thrust-sheet emplacement. *Journal of Structural Geology*, 4(3), pp.257-269.
- Høgnesen, E.J., Standnes, D.C. and Austad, T., 2004. Scaling spontaneous imbibition of aqueous surfactant solution into preferential oil-wet carbonates. *Energy & fuels*, 18(6), pp.1665-1675.
- Hugman III, R.H.H. and Friedman, M., 1979. Effects of texture and composition on mechanical behavior of experimentally deformed carbonate rocks. *AAPG Bulletin*, 63(9), pp.1478-1489.
- Hurley, N.F. and Budros, R., 1990. Albion-scipio and stoney point fields-USA, Michigan Basin.
- Incandela, A., Di Maggio, C., Abate, B., P. Renda, 1993. Carta geologica dei Monti Di Capo San Vito, Scale: 1:25,000; Code: null258.
- Issen, K.A., 2002. The influence of constitutive models on localization conditions for porous rock. *Engineering Fracture Mechanics*, 69(17), 1891-1906.
- Issen, K.A., Rudnicki, J.W., 2000. Conditions for compaction bands in porous rock. *Journal of Geophysical Research: Solid Earth*, 105(B9), 21529-21536.
- Jamison, W.R. and Stearns, D.W., 1982. Tectonic deformation of Wingate Sandstone, Colorado National Monument. *AAPG Bulletin*, 66(12), pp.2584-2608.

Jeanne, P., Guglielmi, Y. and Cappa, F., 2012. Multiscale seismic signature of a small fault zone in a carbonate reservoir: Relationships between VP imaging, fault zone architecture and cohesion. *Tectonophysics*, 554, pp.185-201.

Ji, Y., Baud, P., Vajdova, V., Wong, T.F., 2012. Characterization of pore geometry of Indiana limestone in relation to mechanical compaction. *Oil & Gas Science and Technology—Revue d'IFP Energies nouvelles*, 67(5), 753-775.

Ji, Y., Hall, S.A., Baud, P., Wong, T.F., 2014. Characterization of pore structure and strain localization in Majella limestone by X-ray computed tomography and digital image correlation. *Geophysical Journal International*, 200(2), 701-719.

Johannessen, M.U., 2017. Fault core and its geostatistical analysis: Insight into the fault core thickness and fault displacement. MSc, The University of Bergen.

Johansen, T.E.S. and Fossen, H., 2008. Internal geometry of fault damage zones in interbedded siliciclastic sediments. Geological Society, London, Special Publications, 299(1), pp.35-56.

Johnson, C.A., Sattar, M.A., Rosell, R., Al-Shekaili, F., Al-Zaabi, N. and Gombos, A., 2002, January. Structure and regional context of onshore fields in Abu Dhabi, UAE. In Abu Dhabi International Petroleum Exhibition and Conference. Society of Petroleum Engineers.

Jolley, S.J., Dijk, H., Lamens, J.H., Fisher, Q.J., Manzocchi, T., Eikmans, H. and Huang, Y., 2007. Faulting and fault sealing in production simulation models: Brent Province, northern North Sea. *Petroleum Geoscience*, 13(4), pp.321-340.

Jolley, S.J., Fisher, Q.J. and Ainsworth, R.B., 2010. Reservoir compartmentalization: an introduction. Geological Society, London, Special Publications, 347(1), pp.1-8.

Karcz, Z., Aharonov, E., Ertas, D., Polizzotti, R., Scholz, C.H., 2006, Stability of a sodium chloride indenter contact undergoing pressure solution, *Geology*, 34(1), 61–63.

Kennedy, W. J., R. E. Garrison (1975). "Morphology and genesis of nodular chalks and hardgrounds in the Upper Cretaceous of southern England." *Sedimentology* 22(3), 311-386.

Keszthelyi, D., Dysthe, D.K. and Jamtveit, B., 2016. Compaction of North-sea chalk by pore-failure and pressure solution in a producing reservoir. *Frontiers in Physics*, 4, p.4.

Khan, M. and Teufel, L.W., 2000. The effect of geological and geomechanical parameters on reservoir stress path and its importance in studying permeability anisotropy. *SPE Reservoir Evaluation & Engineering*, 3(05), pp.394-400.

Kim, J.C., Lee, Y.I. and Hisada, K.I., 2007. Depositional and compositional controls on sandstone diagenesis, the Tetori Group (Middle Jurassic–Early Cretaceous), central Japan. *Sedimentary Geology*, 195(3-4), pp.183-202.

Kim, Y.S., Peacock, D.C. and Sanderson, D.J., 2004. Fault damage zones. *Journal of structural geology*, 26(3), pp.503-517.

Kirschner, D.L. and Kennedy, L.A., 2001. Limited syntectonic fluid flow in carbonate-hosted thrust faults of the Front Ranges, Canadian Rockies, inferred from stable isotope data and structures. *Journal of Geophysical Research: Solid Earth*, 106(B5), pp.8827-8840.

Klinkenberg, L.J., 1941. The permeability of porous media to liquids and gases. In *Drilling and production practice*. American Petroleum Institute.

Knipe, R.J., 1992. Faulting processes and fault seal. In *Structural and tectonic modelling and its application to petroleum geology* (pp. 325-342). Elsevier.

Knott, S.D., 1993. Fault seal analysis in the North Sea. *AAPG Bulletin*, 77(5), pp.778-792.

- Koepnick, R.B., 1987. Distribution and permeability of stylolite-bearing horizons within a Lower Cretaceous carbonate reservoir in the Middle East. *SPE Formation Evaluation*, 2(02), pp.137-142.
- Konon, A., 2004. Successive episodes of normal faulting and fracturing resulting from progressive extension during the uplift of the Holy Cross Mountains, Poland. *Journal of Structural Geology*, 26(3), pp.419-433.
- Korneva, I., Bastesen, E., Corlett, H., Eker, A., Hirani, J., Hollis, C., Gawthorpe, R.L., Rotevatn, A. and Taylor, R., 2018. The effects of dolomitization on petrophysical properties and fracture distribution within rift-related carbonates (Hammam Faraun Fault Block, Suez Rift, Egypt). *Journal of Structural Geology*, 108, pp.108-120.
- Korneva, I., Tondi, E., Agosta, F., Rustichelli, A., Spina, V., Bitonte, R. and Di Cuia, R., 2014. Structural properties of fractured and faulted Cretaceous platform carbonates, Murge Plateau (southern Italy). *Marine and Petroleum Geology*, 57, pp.312-326.
- Kostakioti, A., Xypolias, P., Kokkalas, S. and Doutsos, T., 2004. Quantitative analysis of deformation along the fault damage zone of the Klimatia thrust (NW Greece, Ionian Zone). *Bulletin of The Geological Society of Greece*, 36(4), pp.1643-1651.
- Kupecz, J.A., Gluyas, J. and Bloch, S., 1997. Reservoir quality prediction in sandstones and carbonates: An overview.
- Lander, R.H. and Laubach, S.E., 2015. Insights into rates of fracture growth and sealing from a model for quartz cementation in fractured sandstones. *Bulletin*, 127(3-4), pp.516-538.
- Lapponi, F., Casini, G., Sharp, I., Blendinger, W., Fernández, N. and Hunt, D., 2011. From outcrop to 3D modelling: a case study of a dolomitized carbonate reservoir, Zagros Mountains, Iran. *Petroleum Geoscience*, 17(3), pp.283-307.

- Lebedev, M., Wilson, M.E. and Mikhaltsevitch, V., 2014. An experimental study of solid matrix weakening in water-saturated Savonnières limestone. *Geophysical Prospecting*, 62(6), pp.1253-1265.
- Lee, C.H. and Farmer, I.W., 1993. *Fluid flow in discontinuous rocks*. Chapman & Hall.
- Lehner, F.K. and Pilaar, W.F., 1997. The emplacement of clay smears in synsedimentary normal faults: inferences from field observations near Frechen, Germany. In *Norwegian Petroleum Society Special Publications* (Vol. 7, pp. 39-50). Elsevier.
- Lena, G., Barchi, M.R., Alvarez, W., Felici, F. and Minelli, G., 2015. Mesostructural analysis of SC fabrics in a shallow shear zone of the Umbria–Marche Apennines (Central Italy). *Geological Society, London, Special Publications*, 409(1), pp.149-166.
- Lezin, C., Odonne, F., Massonnat, G.J. and Escadeillas, G., 2009. Dependence of joint spacing on rock properties in carbonate strata. *AAPG bulletin*, 93(2), pp.271-290.
- Li, Y.G., Vidale, J.E., Day, S.M., Oglesby, D.D. and Cochran, E., 2003. Postseismic fault healing on the rupture zone of the 1999 M 7.1 Hector Mine, California, earthquake. *Bulletin of the Seismological Society of America*, 93(2), pp.854-869.
- Lind, I., Nykjaer, O., Priisholm, S. and Springer, N., 1994. Permeability of stylolite-bearing chalk. *Journal of Petroleum Technology*, 46(11), pp.986-993.
- Lindsay, N.G., Murphy, F.C., Walsh, J.J., Watterson, J., Flint, S. and Bryant, I., 1993. Outcrop studies of shale smears on fault surfaces. *The geological modelling of hydrocarbon reservoirs and outcrop analogues*, 15, pp.113-123.
- Linzer, H.G., Decker, K., Peresson, H., Dell'Mour, R. and Frisch, W., 2002. Balancing lateral orogenic float of the Eastern Alps. *Tectonophysics*, 354(3-4), pp.211-237.

Lisabeth, H.P. and Zhu, W., 2015. Effect of temperature and pore fluid on the strength of porous limestone. *Journal of Geophysical Research: Solid Earth*, 120(9), pp.6191-6208.

Litsey, L.R., MacBride Jr, W.L., Al-Hinai, K.M. and Dismukes, N.B., 1986. Shuaiba reservoir geological study, Yibal field, Oman. *Journal of Petroleum Technology*, 38(06), pp.651-661.

Liu, Z., Yuan, D. and Dreybrodt, W., 2005. Comparative study of dissolution rate-determining mechanisms of limestone and dolomite. *Environmental Geology*, 49(2), pp.274-279.

Longuemare, P., Schneider, F., Onaisi, A. and Shahrour, I., 1996, January. Study of the Behaviour of a Petroleum Reservoir During Depletion Using an Elasto-plastic Constitutive Model. In *ISRM International Symposium- EUROCK 96. International Society for Rock Mechanics and Rock Engineering*.

Lommatzsch, M., Exner, U., Gier, S., Grasemann, B., 2015. Dilatant shear band formation and diagenesis in calcareous, arkosic sandstones, Vienna Basin (Austria). *Marine and petroleum geology*, 62, 144-160.

López-Horgue, M.A., Iriarte, E., Schröder, S., Fernández-Mendiola, P.A., Caline, B., Corneyllie, H., Frémont, J., Sudrie, M. and Zerti, S., 2010. Structurally controlled hydrothermal dolomites in Albian carbonates of the Asón valley, Basque Cantabrian Basin, Northern Spain. *Marine and Petroleum Geology*, 27(5), pp.1069-1092.

Lønøy, A., 2006. Making sense of carbonate pore systems. *AAPG bulletin*, 90(9), 1381-1405.

Lucia, F.J., 1995. Rock-fabric/petrophysical classification of carbonate pore space for reservoir characterization. *AAPG bulletin*, 79(9), 1275-1300.

Lucia, F.J., 2004. Origin and petrophysics of dolostone pore space. *Geological Society, London, Special Publications*, 235(1), pp.141-155.

- Lucia, F.J. and Major, R.P., 1994. Porosity evolution through hypersaline reflux dolomitization. *Dolomites: A Volume in Honour of Dolomieu*, pp.325-341.
- Machel, H.G., 1997. Recrystallization versus neomorphism, and the concept of 'significant recrystallization' in dolomite research. *Sedimentary Geology*, 113(3-4), pp.161-168.
- Mallon, A.J., Swarbrick, R.E., 2002. A compaction trend for non-reservoir North Sea Chalk. *Marine and Petroleum Geology*, 19(5), 527-539.
- Manzocchi, T., Walsh, J.J., Nell, P. and Yielding, G., 1999. Fault transmissibility multipliers for flow simulation models. *Petroleum Geoscience*, 5(1), pp.53-63.
- Marchegiani, L., Van Dijk, J.P., Gillespie, P.A., Tondi, E., Cello, G., 2006. Scaling properties of the dimensional and spatial characteristics of fault and fracture systems in the Majella Mountain, central Italy. *Geological Society, London, Special Publications*, 261(1), 113-131.
- Matonti, C., Lamarche, J., Guglielmi, Y. and Marié, L., 2012. Structural and petrophysical characterization of mixed conduit/seal fault zones in carbonates: example from the Castellans fault (SE France). *Journal of Structural Geology*, 39, pp.103-121.
- Mayolle, S., Soliva, R., Caniven, Y., Wibberley, C., Ballas, G., Milesi, G. and Dominguez, S., 2019. Scaling of fault damage zones in carbonate rocks. *Journal of Structural Geology*, 124, pp.35-50.
- Mazzoli, S., Ascione, A., Buscher, J.T., Pignatosa, A., Valente, E. and Zattin, M., 2014. Low-angle normal faulting and focused exhumation associated with late Pliocene change in tectonic style in the southern Apennines (Italy). *Tectonics*, 33(9), pp.1802-1818.
- McCaig, A.M., Wayne, D.M., Marshall, J.D., Banks, D. and Henderson, I., 1995. Isotopic and fluid inclusion studies of fluid movement along the Gavarnie Thrust, central Pyrenees; reaction fronts in carbonate mylonites. *American Journal of Science*, 295(3), pp.309-343.

Mehmood, M., Yaseen, M., Khan, E.U. and Khan, J.M., 2018. Dolomite and dolomitization model—A short review. *International Journal of Hydrology*, 2(5), pp.549-553.

Menéndez, B., Zhu, W. and Wong, T.F., 1996. Micromechanics of brittle faulting and cataclastic flow in Berea sandstone. *Journal of structural geology*, 18(1), pp.1-16.

Micarelli, L., Benedicto, A., Invernizzi, C., Saint-Bezar, B., Michelot, J.L. and Vergely, P., 2005. Influence of P/T conditions on the style of normal fault initiation and growth in limestones from the SE-Basin, France. *Journal of Structural geology*, 27(9), pp.1577-1598.

Micarelli, L., Benedicto, A., Wibberley, C.A.J., 2006a. Structural evolution and permeability of normal fault zones in highly porous carbonate rocks. *Journal of Structural Geology*, 28(7), 1214-1227.

Micarelli, L., Moretti, I. and Daniel, J.M., 2003. Structural properties of rift-related normal faults: the case study of the Gulf of Corinth, Greece. *Journal of Geodynamics*, 36(1-2), pp.275-303.

Micarelli, L., Moretti, I., Jaubert, M. and Moulouel, H., 2006b. Fracture analysis in the south-western Corinth rift (Greece) and implications on fault hydraulic behavior. *Tectonophysics*, 426(1-2), pp.31-59.

Michie, E.A.H., 2015. Influence of host lithofacies on fault rock variation in carbonate fault zones: A case study from the Island of Malta. *Journal of Structural Geology*, 76, 61-79.

Michie, E.A.H. and Haines, T.J., 2016. Variability and heterogeneity of the petrophysical properties of extensional carbonate fault rocks, Malta. *Petroleum Geoscience*, 22(2), pp.136-152.

Michie, E.A.H., Haines, T.J., Healy, D., Neilson, J.E., Timms, N.E. and Wibberley, C.A.J., 2014. Influence of carbonate facies on fault zone architecture. *Journal of Structural Geology*, 65, pp.82-99.

- Michie, E.A.H., Yielding, G. and Fisher, Q.J., 2018. Predicting transmissibilities of carbonate-hosted fault zones. Geological Society, London, Special Publications, 459(1), pp.121-137.
- Mirabella, F., Ciaccio, M.G., Barchi, M.R. and Merlini, S., 2004. The Gubbio normal fault (Central Italy): geometry, displacement distribution and tectonic evolution. *Journal of Structural Geology*, 26(12), pp.2233-2249.
- Mitchell, T.M. and Faulkner, D.R., 2009. The nature and origin of off-fault damage surrounding strike-slip fault zones with a wide range of displacements: A field study from the Atacama fault system, northern Chile. *Journal of Structural Geology*, 31(8), pp.802-816.
- Mogi, K., 1966. Pressure dependence of rock strength and transition from brittle fracture to ductile flow. *Bulletin Earthquake Research Institute*, 44, pp.215-232.
- Morawietz, F.H., 1958. Die Anlösungserscheinungen in der Juranagelfluh und ihre Bedeutung für die Diagenese. PhD Thesis, Tübingen, Germany.
- Morgan, J.K. and Boettcher, M.S., 1999. Numerical simulations of granular shear zones using the distinct element method: 1. Shear zone kinematics and the micromechanics of localization. *Journal of Geophysical Research: Solid Earth*, 104(B2), pp.2703-2719.
- Mowar, S., Zaman, M., Stearns, D.W. and Roegiers, J.C., 1994, January. Pore collapse mechanisms in Cordoba Cream limestone. In 1st North American Rock Mechanics Symposium. American Rock Mechanics Association.
- Mozley, P.S. and Goodwin, L.B., 1995. Patterns of cementation along a Cenozoic normal fault: A record of paleoflow orientations. *Geology*, 23(6), pp.539-542.
- Nelson, R.A., 1981. Significance of fracture sets associated with stylolite zones: geologic notes. *AAPG Bulletin*, 65(11), pp.2417-2425.
- Nelson, R.A., 1985. Contributions in Petroleum Geology and Engineering. No. 1, Gulf, Houston, pp.320.

- Nelson, R., 2001. Geologic analysis of naturally fractured reservoirs. Elsevier.
- Nelson, R.A. and Serra, S., 1995. Vertical and lateral variations in fracture spacing in folded carbonate sections and its relation to locating horizontal wells. *Journal of Canadian Petroleum Technology*, 34(06).
- Ngwenya, B.T., Kwon, O., Elphick, S.C. and Main, I.G., 2003. Permeability evolution during progressive development of deformation bands in porous sandstones. *Journal of Geophysical Research: Solid Earth*, 108(B7).
- Nicolas, A., Fortin, J., Regnet, J.B., Dimanov, A. and Guéguen, Y., 2016. Brittle and semi-brittle behaviours of a carbonate rock: influence of water and temperature. *Geophysical Journal International*, 206(1), pp.438-456.
- Noufal, A. and Obaid, K., 2017, November. Sealing Faults: A Bamboozling Problem in Abu Dhabi Fields. In Abu Dhabi International Petroleum Exhibition & Conference. Society of Petroleum Engineers.
- Novellino, R., Prosser, G., Spiess, R., Viti, C., Agosta, F., Tavarnelli, E. and Bucci, F., 2015. Dynamic weakening along incipient low-angle normal faults in pelagic limestones (Southern Apennines, Italy). *Journal of the Geological Society*, 172(3), pp.283-286.
- Ogilvie, S.R. and Glover, P.W., 2001. The petrophysical properties of deformation bands in relation to their microstructure. *Earth and Planetary Science Letters*, 193(1-2), pp.129-142.
- Olsson, W.A. and Peng, S.S., 1976, February. Microcrack nucleation in marble. In *International Journal of Rock Mechanics and Mining Sciences & Geomechanics Abstracts* (Vol. 13, No. 2, pp. 53-59). Pergamon.
- O'Neill, N., 1988. Fahud field review: a switch from water to gas injection. *Journal of petroleum technology*, 40(05), pp.609-618.
- Otsu, N., 1979. A threshold selection method from gray-level histograms. *IEEE transactions on systems, man, and cybernetics*, 9(1), 62-66.

Ozkaya, S.I. and Minton, K.R., 2007. Flow potential of fracture corridors and large conductive fractures in a clastic reservoir, Oman. Geological Society, London, Special Publications, 270(1), pp.245-263.

Palchik, V. and Hatzor, Y.H., 2002. Crack damage stress as a composite function of porosity and elastic matrix stiffness in dolomites and limestones. Engineering Geology, 63(3-4), pp.233-245.

Peacock, D.C.P., 2001. The temporal relationship between joints and faults. Journal of Structural Geology, 23(2-3), pp.329-341.

Peacock, D.C.P., 2002. Propagation, interaction and linkage in normal fault systems. Earth-Science Reviews, 58(1-2), pp.121-142.

Peacock, D.C.P., Fisher, Q.J., Willemse, E.J.M. and Aydin, A., 1998. The relationship between faults and pressure solution seams in carbonate rocks and the implications for fluid flow. Geological Society, London, Special Publications, 147(1), pp.105-115.

Peacock, D.C.P. and Sanderson, D.J., 1991. Displacements, segment linkage and relay ramps in normal fault zones. Journal of Structural Geology, 13(6), pp.721-733.

Perez, R.J. and Boles, J.R., 2004. Mineralization, fluid flow, and sealing properties associated with an active thrust fault: San Joaquin basin, California. AAPG bulletin, 88(9), pp.1295-1314.

Pettijohn, F.J., 1975. Sedimentary rocks (Vol. 3). New York: Harper & Row.

Pittman, E.D., 1971. Microporosity in carbonate rocks. AAPG Bulletin, 55(10), pp.1873-1878.

Pollard, D.D. and Aydin, A., 1988. Progress in understanding jointing over the past century. Geological Society of America Bulletin, 100(8), pp.1181-1204.

Přikryl, R., 2001. Some microstructural aspects of strength variation in rocks. International Journal of Rock Mechanics and Mining Sciences, 38(5), pp.671-682.

Purser, B.H., Tucker, M.E. and Zenger, D.H., 1994. Problems, progress and future research concerning dolomites and dolomitization. *Dolomites: A volume in honour of Dolomieu*, 21, pp.3-20.

Qu, D. and Tveranger, J., 2016. Incorporation of deformation band fault damage zones in reservoir models. *AAPG Bulletin*, 100(3), pp.423-443.

Rahman, M.H., Pierson, B.J., Yusoff, W. and Ismail, W., 2011, January. Classification of microporosity in carbonates: examples from Miocene carbonate reservoirs of central Luconia, offshore Sarawak, Malaysia. In *International petroleum technology conference*. International Petroleum Technology Conference.

Ramsey, D.W. and Onasch, C.M., 1999. Fluid migration in a cratonic setting: the fluid histories of two fault zones in the eastern midcontinent. *Tectonophysics*, 305(1-3), pp.307-323.

Ran, G., Eyal, S., Yoseph, Y., Amir, S. and Noam, W., 2014. The permeability of fault zones: a case study of the Dead Sea rift (Middle East). *Hydrogeology Journal*, 22(2), pp.425-440.

Rath, A., Exner, U., Tschegg, C., Grasemann, B., Laner, R., Draganits, E., 2011. Diagenetic control of deformation mechanisms in deformation bands in a carbonate grainstone. *AAPG bulletin*, 95(8), 1369-1381.

Rawling, G.C., Goodwin, L.B. and Wilson, J.L., 2001. Internal architecture, permeability structure, and hydrologic significance of contrasting fault-zone types. *Geology*, 29(1), pp.43-46.

Rawnsley, K. and Wei, L., 2001. Evaluation of a new method to build geological models of fractured reservoirs calibrated to production data. *Petroleum Geoscience*, 7(1), pp.23-33.

Regnet, J.B., David, C., Fortin, J., Robion, P., Makhloufi, Y. and Collin, P.Y., 2015. Influence of microporosity distribution on the mechanical behavior of oolitic carbonate rocks. *Geomechanics for Energy and the Environment*, 3, pp.11-23.

- Renner, J. and Rummel, F., 1996. The effect of experimental and microstructural parameters on the transition from brittle failure to cataclastic flow of carbonate rocks. *Tectonophysics*, 258(1-4), pp.151-169.
- Reyer, D., Bauer, J.F. and Philipp, S.L., 2012. Fracture systems in normal fault zones crosscutting sedimentary rocks, Northwest German Basin. *Journal of Structural Geology*, 45, pp.38-51.
- Riley, P.R., Goodwin, L.B. and Lewis, C.J., 2010. Controls on fault damage zone width, structure, and symmetry in the Bandelier Tuff, New Mexico. *Journal of Structural Geology*, 32(6), pp.766-780.
- Robert, R., Robion, P., Souloumiac, P., David, C. and Sallet, E., 2018. Deformation bands, early markers of tectonic activity in front of a fold-and-thrust belt: Example from the Tremp-Graus basin, southern Pyrenees, Spain. *Journal of Structural Geology*, 110, pp.65-85.
- Robert, R., Souloumiac, P., Robion, P. and David, C., 2019. Numerical Simulation of Deformation Band Occurrence and the Associated Stress Field during the Growth of a Fault-Propagation Fold. *Geosciences*, 9(6), p.257.
- Roberts, G.P., 1994. Displacement localization and palaeo-seismicity of the Rencurel thrust zone, French sub-alpine chains. *Journal of Structural Geology*, 16(5), pp.633-646.
- Roberts, G. and Stewart, I., 1994. Uplift, deformation and fluid involvement within an active normal fault zone in the Gulf of Corinth, Greece. *Journal of the Geological Society*, 151(3), pp.531-541.
- Roehl, P.O. and Choquette, P.W. eds., 2012. Carbonate petroleum reservoirs. Springer Science & Business Media.
- Rosenfeld, M.A., 1949. Some aspects of porosity and cementation. *Producers Monthly*, 13(7), 39-42.
- Rotevatn, A., Thorsheim, E., Bastesen, E., Fossmark, H.S., Torabi, A., Sælen, G., 2016. Sequential growth of deformation bands in carbonate grainstones in the hangingwall of an active growth fault: Implications for

deformation mechanisms in different tectonic regimes. *Journal of Structural Geology*, 90, 27-47.

Ruddy, I., Andersen, M.A., Pattillo, P.D., Bishlawi, M. and Foged, N., 1989. Rock compressibility, compaction, and subsidence in a high-porosity chalk reservoir: A case study of Valhall field. *Journal of Petroleum Technology*, 41(07), pp.741-746.

Rudnicki, J.W., 2004. Shear and compaction band formation on an elliptic yield cap. *Journal of Geophysical Research: Solid Earth*, 109(B3).

Rustichelli, A., 2010. Mechanical stratigraphy of carbonate rocks: examples from the Maiella Mountain (central Italy) and the Granada Basin (southern Spain). Ph. D Thesis, p.185.

Rustichelli, A., Tondi, E., Agosta, F., Cilona, A., Giorgioni, M., 2012. Development and distribution of bed-parallel compaction bands and pressure solution seams in carbonates (Bolognana Formation, Majella Mountain, Italy). *Journal of Structural Geology*, 37, 181-199.

Ruddy, I., Andersen, M.A., Pattillo, P.D., Bishlawi, M. and Foged, N., 1989. Rock compressibility, compaction, and subsidence in a high-porosity chalk reservoir: A case study of Valhall field. *Journal of Petroleum Technology*, 41(07), pp.741-746.

Rutter, E.H., 1974. The influence of temperature, strain rate and interstitial water in the experimental deformation of calcite rocks. *Tectonophysics*, 22(3-4), pp.311-334.

Safko, P.S. and Hickey, J.J., 1992. A preliminary approach to the use of borehole data, including television surveys, for characterizing secondary porosity of carbonate rocks in the Floridan aquifer system. *Water-Resources Investigations Report*, 91, p.416

Sagi, D.A., Arnhild, M. and Karlo, J.F., 2014. Quantifying fracture density and connectivity of fractured chalk reservoirs from core samples: implications for fluid flow. *Geological Society, London, Special Publications*, 374(1), pp.97-111.

- Sagi, D.A., De Paola, N., McCaffrey, K.J.W. and Holdsworth, R.E., 2016. Fault and fracture patterns in low porosity chalk and their potential influence on sub-surface fluid flow—A case study from Flamborough Head, UK. *Tectonophysics*, 690, pp.35-51.
- Sagy, A., Reches, Z.E. and Agnon, A., 2003. Hierarchic three-dimensional structure and slip partitioning in the western Dead Sea pull-apart. *Tectonics*, 22(1).8.
- Salvini, F., Billi, A. and Wise, D.U., 1999. Strike-slip fault-propagation cleavage in carbonate rocks: the Mattinata Fault Zone, Southern Apennines, Italy. *Journal of Structural Geology*, 21(12), pp.1731-1749.
- Sammis, C.G. and Ashby, M.F., 1986. The failure of brittle porous solids under compressive stress states. *Acta metallurgica*, 34(3), pp.511-526.
- Schmid, S.M., Boland, J.N. and Paterson, M.S., 1977. Superplastic flow in fine grained limestone. *Tectonophysics*, 43(3-4), pp.257-291.
- Schmoker, J.W. and Halley, R.B., 1982. Carbonate porosity versus depth: a predictable relation for south Florida. *AAPG bulletin*, 66(12), pp.2561-2570.
- Schöpfer, M.P., Childs, C. and Walsh, J.J., 2006. Localisation of normal faults in multilayer sequences. *Journal of Structural Geology*, 28(5), pp.816-833.
- Schröckenfuchs, T., Bauer, H., Grasemann, B. and Decker, K., 2015. Rock pulverization and localization of a strike-slip fault zone in dolomite rocks (Salzach–Ennstal–Mariazell–Puchberg fault, Austria). *Journal of Structural Geology*, 78, pp.67-85.
- Schueller, S., Braathen, A., Fossen, H. and Tveranger, J., 2013. Spatial distribution of deformation bands in damage zones of extensional faults in porous sandstones: Statistical analysis of field data. *Journal of Structural Geology*, 52, pp.148-162.
- Schultz, R.A. and Siddharthan, R., 2005. A general framework for the occurrence and faulting of deformation bands in porous granular rocks. *Tectonophysics*, 411(1-4), pp.1-18.

Schutjens, P.M.T.M. and De Ruig, H., 1997. The influence of stress path on compressibility and permeability of an overpressurised reservoir sandstone: some experimental data. *Physics and Chemistry of the Earth*, 22(1-2), pp.97-103.

Seif, E.S.S.A., Bahabri, A.A. and Abd, A.E.H.E.S., 2018. Geotechnical properties of Precambrian carbonate, Saudi Arabia. *Arabian Journal of Geosciences*, 11(17), p.500.

Sharp, I., Gillespie, P., Morsalnezhad, D., Taberner, C., Karpuz, R., Vergés, J., Horbury, A., Pickard, N., Garland, J. and Hunt, D., 2010. Stratigraphic architecture and fracture-controlled dolomitization of the Cretaceous Khami and Bangestan groups: an outcrop case study, Zagros Mountains, Iran. Geological Society, London, Special Publications, 329(1), pp.343-396.

Shipton, Z.K. and Cowie, P.A., 2001. Damage zone and slip-surface evolution over μm to km scales in high-porosity Navajo sandstone, Utah. *Journal of Structural Geology*, 23(12), pp.1825-1844.

Shipton, Z.K. and Cowie, P.A., 2003. A conceptual model for the origin of fault damage zone structures in high-porosity sandstone. *Journal of Structural Geology*, 25(3), pp.333-344.

Shipton, Z.K., Evans, J.P. and Thompson, L.B., 2005. The geometry and thickness of deformation-band fault core and its influence on sealing characteristics of deformation-band fault zones.

Sibson, R.H., 1977. Fault rocks and fault mechanisms. *Journal of the Geological Society*, 133(3), pp.191-213.

Sibson, R.H., 1994. Crustal stress, faulting and fluid flow. Geological Society, London, Special Publications, 78(1), pp.69-84.

Smalley, C., England, W.A., Muggeridge, A., Abacioglu, Y. and Cawley, S., 2004. Rates of reservoir fluid mixing: implications for interpretation of fluid data. Geological Society, London, Special Publications, 237(1), pp.99-113.

- Soliva, R., Ballas, G., Fossen, H., Philit, S., 2016. Tectonic regime controls clustering of deformation bands in porous sandstone. *Geology*, 44(6), 423-426.
- Solum, J.G., 2015, September. Static and dynamic fault seal potential in carbonates. In *Fourth International Conference on Fault and Top Seals*.
- Solum, J.G. and Huisman, B.A.H., 2017. Toward the creation of models to predict static and dynamic fault-seal potential in carbonates. *Petroleum Geoscience*, 23(1), pp.70-91.
- Sperrevik, S., Færseth, R.B. and Gabrielsen, R.H., 2000. Experiments on clay smear formation along faults. *Petroleum Geoscience*, 6(2), pp.113-123.
- Sperrevik, S., Gillespie, P.A., Fisher, Q.J., Halvorsen, T. and Knipe, R.J., 2002. Empirical estimation of fault rock properties. In *Norwegian Petroleum Society Special Publications (Vol. 11, pp. 109-125)*. Elsevier.
- Stead, J., 2018. The Impact of Burial History on the Permeability of Carbonate-Hosted Faults. MSc thesis, University of Leeds.
- Stearns, D.W. and Friedman, M., 1972. Reservoirs in fractured rock: Geologic exploration methods.
- Stenger, B.A., Pham, T.R., Al-Sahhaf, A.A. and Al-Muhaish, A.S., 2001, January. Assessing the oil water contact in Haradh Arab-D. In *SPE Annual Technical Conference and Exhibition*. Society of Petroleum Engineers.
- Stewart, I.S. and Hancock, P.L., 1991. Scales of structural heterogeneity within neotectonic normal fault zones in the Aegean region. *Journal of Structural Geology*, 13(2), pp.191-204.
- Storti, F., Billi, A. and Salvini, F., 2003. Particle size distributions in natural carbonate fault rocks: insights for non-self-similar cataclasis. *Earth and Planetary Science Letters*, 206(1-2), pp.173-186.
- Swennen, R., Dewit, J., Fierens, E., Muchez, P., Shah, M., Nader, F. and Hunt, D., 2012. Multiple dolomitization events along the Pozalagua Fault (Pozalagua Quarry, Basque–Cantabrian Basin, Northern Spain). *Sedimentology*, 59(4), pp.1345-1374.

- Tada, R., Siever, R., 1986, Experimental knife-edge pressure solution of halite, *Geochimica et Cosmochimica Acta*, 50(1), 29–36.
- Tada, R., Siever, R., 1989. Pressure solution during diagenesis. *Annual Review of Earth and Planetary Sciences*, 17(1), 89-118.
- Tarasewicz, J.P., Woodcock, N.H. and Dickson, J.A.D., 2005. Carbonate dilation breccias: examples from the damage zone to the Dent Fault, northwest England. *Geological Society of America Bulletin*, 117(5-6), pp.736-745.
- Tarokh, A., Li, Y., Labuz, J.F., 2017. Hardening in porous chalk from precompaction. *Acta Geotechnica*, 12(4), 949-953.
- Tavani, S., Granado, P., Balsamo, F., Pizzati, M., Cantarero, I., Corradetti, A., Muñoz, J.A., 2017. Shear-enhanced compaction-solution bands in quartz-rich calcarenites of the Cotiella Massif (Spanish Pyrenees). *Journal of Structural Geology*.
- Tavani, S., Vitale, S., Grifa, C., Iannace, A., Parente, M., Mazzoli, S., 2016. Introducing dolomite seams: hybrid compaction–solution bands in dolomitic limestones. *Terra Nova*, 28(3), 195-201.
- Teixell, A., Durney, D.W. and Arboleya, M.L., 2000. Stress and fluid control on decollement within competent limestone. *Journal of Structural Geology*, 22(3), pp.349-371.
- Tembe, S., Baud, P. and Wong, T.F., 2008. Stress conditions for the propagation of discrete compaction bands in porous sandstone. *Journal of Geophysical Research: Solid Earth*, 113(B9).
- Tesei, T., Collettini, C., Viti, C. and Barchi, M.R., 2013. Fault architecture and deformation mechanisms in exhumed analogues of seismogenic carbonate-bearing thrusts. *Journal of Structural Geology*, 55, pp.167-181.
- Teufel, L.W., Rhett, D.W. and Farrell, H.E., 1991, January. Effect of reservoir depletion and pore pressure drawdown on in situ stress and deformation in the Ekofisk field, North Sea. In: *The 32nd US Symposium on Rock Mechanics (USRMS)*. American Rock Mechanics Association.

Thomas, D. C., and Pugh, V. J., "A Statistical Analysis of the Accuracy and Reproducibility of Standard Core Analysis," *The Log Analyst*, March-April 1989.

Todaro, S., Zarcone, G., Mindszenty, A., Di Stefano, P., 2012. Karstic overprint of Upper Triassic peritidal cycles: the example of the Panormide Carbonate Platform at San Vito lo Capo (Sicily). In 86° Congresso della Società Geologica Italiana, Cosenza, Italia. Vol. 21, 1020-1022.

Tondi, E., 2007. Nucleation, development and petrophysical properties of faults in carbonate grainstones: evidence from the San Vito Lo Capo peninsula (Sicily, Italy). *Journal of Structural Geology*, 29(4), 614-628.

Tondi, E., Antonellini, M., Aydin, A., Marchegiani, L., Cello, G., 2006a. The role of deformation bands, stylolites and sheared stylolites in fault development in carbonate grainstones of Majella Mountain, Italy. *Journal of structural geology*, 28(3), 376-391.

Tondi, E., Cilona, A., Agosta, F., Aydin, A., Rustichelli, A., Renda, P., Giunta, G., 2012. Growth processes, dimensional parameters and scaling relationships of two conjugate sets of compactive shear bands in porous carbonate grainstones, Favignana Island, Italy. *Journal of Structural Geology*, 37, 53-64.

Tondi, E., Piccardi, L., Cacon, S., Kontny, B., Cello, G., 2005. Structural and time constraints for dextral shear along the seismogenic Mattinata Fault (Gargano, southern Italy). *Journal of Geodynamics*, 40(2), 134-152.

Tondi, E., Rustichelli, A., Cilona, A., Balsamo, F., Storti, F., Napoli, G., Agosta, F., Renda, P., Giorgioni, M., 2016. Hydraulic properties of fault zones in porous carbonates, examples from central and southern Italy. *Italian Journal of Geosciences*, 135(1), 68-79.

Tondi, E., Zampieri, D., Giunta, G., Renda, P., Alessandrini, M., Unti, M., Giorgianni, A., Cello, G., 2006b. Active faults and inferred seismic sources in the San Vito lo Capo peninsula, northwestern Sicily, Italy. *Geological Society, London, Special Publications*, 262(1), 365-377.

- Tropeano, M., Sabato, L., 2000. Response of Plio-Pleistocene mixed bioclastic-lithoclastic temperate-water carbonate systems to forced regressions: the Calcarenite di Gravina Formation, Puglia, SE Italy. Geological Society, London, Special Publications, 172(1), 217-243.
- Tucker, M.E., Wright, V.P., 2009. Carbonate sedimentology. John Wiley & Sons.
- Ukar, E. and Laubach, S.E., 2016. Syn-and postkinematic cement textures in fractured carbonate rocks: Insights from advanced cathodoluminescence imaging. *Tectonophysics*, 690, pp.190-205.
- Vajdova, V., Baud, P. and Wong, T.F., 2004a. Compaction, dilatancy, and failure in porous carbonate rocks. *Journal of Geophysical Research: Solid Earth*, 109(B5).
- Vajdova, V., Baud, P. and Wong, T.F., 2004b. Permeability evolution during localized deformation in Bentheim sandstone. *Journal of Geophysical Research: Solid Earth*, 109(B10).
- Vajdova, V., Baud, P., Wu, L., Wong, T.F., 2012. Micromechanics of inelastic compaction in two allochemical limestones. *Journal of Structural Geology*, 43, 100-117.
- Vajdova, V., Zhu, W., Chen, T.M.N., Wong, T.F., 2010. Micromechanics of brittle faulting and cataclastic flow in Tavel limestone. *Journal of Structural Geology*, 32(8), 1158-1169.
- Valoroso, L., Chiaraluce, L. and Collettini, C., 2014. Earthquakes and fault zone structure. *Geology*, 42(4), pp.343-346.
- Vandycke, S., 2002. Palaeostress records in Cretaceous formations in NW Europe: extensional and strike-slip events in relationships with Cretaceous-Tertiary inversion tectonics. *Tectonophysics* 357(1-4), 119-136.
- ten Veen, J.H., Kleinspehn, K.L., 2002. Geodynamics along an increasingly curved convergent plate margin: Late Miocene-Pleistocene Rhodes, Greece. *Tectonics*, 21(3).

Vermilye, J.M. and Scholz, C.H., 1998. The process zone: A microstructural view of fault growth. *Journal of Geophysical Research: Solid Earth*, 103(B6), pp.12223-12237.

Vidale, J.E. and Li, Y.G., 2003. Damage to the shallow Landers fault from the nearby Hector Mine earthquake. *Nature*, 421(6922), p.524.

Walderhaug, O., 1996. Kinetic modeling of quartz cementation and porosity loss in deeply buried sandstone reservoirs. *AAPG bulletin*, 80(5), 731-745.

Walsh, J.J., Watterson, J., Heath, A.E. and Childs, C., 1998. Representation and scaling of faults in fluid flow models. *Petroleum Geoscience*, 4(3), pp.241-251.

Walter, L.M., 1985. Relative reactivity of skeletal carbonates during dissolution: implications for diagenesis.

Walton, G., Arzua, J., Alejano, L.R. and Diederichs, M.S., 2015. A laboratory-testing-based study on the strength, deformability, and dilatancy of carbonate rocks at low confinement. *Rock Mechanics and Rock Engineering*, 48(3), pp.941-958.

Walton, G., Hedayat, A., Kim, E. and Labrie, D., 2017. Post-yield strength and dilatancy evolution across the brittle–ductile transition in Indiana limestone. *Rock Mechanics and Rock Engineering*, 50(7), pp.1691-1710.

Wardlaw, N.C., Li, Y. and Forbes, D., 1987. Pore-throat size correlation from capillary pressure curves. *Transport in porous media*, 2(6), pp.597-614.

Wardlaw, N.C., McKellar, M. and Yu, L., 1988. Pore and throat size distributions determined by mercury porosimetry and by direct observation. *Carbonates and Evaporites*, 3(1), p.1.

Welch, M.J., Souque, C., Davies, R.K., Knipe, R.J., 2015. Using mechanical models to investigate the controls on fracture geometry and distribution in chalk. *Geological Society, London, Special Publications*, 406(1), 281-309.

Wennberg, O.P., Casini, G., Jahanpanah, A., Lapponi, F., Ineson, J., Wall, B.G., Gillespie, P., 2013. Deformation bands in chalk, examples from the

Shetland Group of the Oseberg Field, North Sea, Norway. *Journal of Structural Geology*, 56, 103-117.

Wennberg, O.P., Rennan, L., 2018. A brief introduction to the use of X-ray computed tomography (CT) for analysis of natural deformation structures in reservoir rocks. *Geological Society, London, Special Publications*, 459(1), 101-120.

Whitaker, F.F., Xiao, Y. and Haynes, C., 2007, April. Geothermal Convection: A Viable Mechanism for Early Burial Dolomitisation of Platform Carbonates. In 2007 AAPG Annual Convention and Exhibition.

White, S.H., Bretan, P.G. and Rutter, E.H., 1986. Fault-zone reactivation: kinematics and mechanisms. *Philosophical Transactions of the Royal Society of London. Series A, Mathematical and Physical Sciences*, 317(1539), pp.81-97.

Wibberley, C.A., Yielding, G. and Di Toro, G., 2008. Recent advances in the understanding of fault zone internal structure: a review. *Geological Society, London, Special Publications*, 299(1), pp.5-33.

Wilkins, S.J. and Naruk, S.J., 2007. Quantitative analysis of slip-induced dilation with application to fault seal. *AAPG bulletin*, 91(1), pp.97-113.

Williams, D.M. and McNamara, K., 1992. Limestone to dolomite to dedolomite conversion and its effect on rock strength: a case study. *Quarterly Journal of Engineering Geology and Hydrogeology*, 25(2), pp.131-135.

Wilson, J.E., Chester, J.S. and Chester, F.M., 2003. Microfracture analysis of fault growth and wear processes, Punchbowl Fault, San Andreas system, California. *Journal of Structural Geology*, 25(11), pp.1855-1873.

Wilson, P., Gawthorpe, R.L., Hodgetts, D., Rarity, F. and Sharp, I.R., 2009. Geometry and architecture of faults in a syn-rift normal fault array: the Nukhul half-graben, Suez rift, Egypt. *Journal of Structural Geology*, 31(8), pp.759-775.

- Wojtal, S. and Mitra, G., 1986. Strain hardening and strain softening in fault zones from foreland thrusts. *Geological Society of America Bulletin*, 97(6), pp.674-687.
- Woodcock, N.H., Dickson, J.A.D. and Tarasewicz, J.P.T., 2007. Transient permeability and reseat hardening in fault zones: evidence from dilation breccia textures. *Geological Society, London, Special Publications*, 270(1), pp.43-53.
- Woodcock, N.H., Miller, A.V.M. and Woodhouse, C.D., 2014. Chaotic breccia zones on the Pembroke Peninsula, south Wales: Evidence for collapse into voids along dilational faults. *Journal of Structural Geology*, 69, pp.91-107.
- Woodcock, N.H. and Mort, K., 2008. Classification of fault breccias and related fault rocks. *Geological Magazine*, 145(3), pp.435-440.
- Woodcock, N.H., Omma, J.E. and Dickson, J.A.D., 2006. Chaotic breccia along the Dent Fault, NW England: implosion or collapse of a fault void?. *Journal of the Geological Society*, 163(3), pp.431-446.
- Wong, T. F., Baud, P., 2012. The brittle-ductile transition in porous rock: A review. *Journal of Structural Geology*, 44, 25-53.
- Wong, T.F., David, C. and Menendez, B., 2004. Mechanical compaction. *International Geophysics Series*, 89, pp.55-114.
- Wong, T.F., David, C. and Zhu, W., 1997. The transition from brittle faulting to cataclastic flow in porous sandstones: Mechanical deformation. *Journal of Geophysical Research: Solid Earth*, 102(B2), pp.3009-3025.
- Wu, S., 1993. Microstructures, deformation mechanisms and strain patterns in a vertical profile, inner Appalachian fold-thrust belt, Alabama. *Journal of structural geology*, 15(2), pp.129-144.
- Yielding, G., Bretan, P. and Freeman, B., 2010. Fault seal calibration: a brief review. *Geological Society, London, Special Publications*, 347(1), pp.243-255.
- Yielding, G., Freeman, B. and Needham, D.T., 1997. Quantitative fault seal prediction. *AAPG bulletin*, 81(6), pp.897-917.

Young, M.J., Gawthorpe, R.L. and Sharp, I.R., 2003. Normal fault growth and early syn-rift sedimentology and sequence stratigraphy: Thal Fault, Suez Rift, Egypt. *Basin Research*, 15(4), pp.479-502.

Zahm, C.K., Zahm, L.C. and Bellian, J.A., 2010. Integrated fracture prediction using sequence stratigraphy within a carbonate fault damage zone, Texas, USA. *Journal of Structural Geology*, 32(9), pp.1363-1374.

Zambrano, M., Tondi, E., Korneva, I., Panza, E., Agosta, F., Janiseck, J.M., Giorgioni, M., 2016. Fracture properties analysis and discrete fracture network modelling of faulted tight limestones, Murge Plateau, Italy. *Italian Journal of Geosciences*, 135(1), pp.55-67.

Zambrano, M., Tondi, E., Mancini, L., Arzilli, F., Lanzafame, G., Materazzi, M., Torrieri, S., 2017. 3D Pore-network quantitative analysis in deformed carbonate grainstones. *Marine and Petroleum Geology*, 82, 251-264.

Zambrano, M., Tondi, E., Mancini, L., Lanzafame, G., Trias, F.X., Arzilli, F., Materazzi, M., Torrieri, S., 2018. Fluid flow simulation and permeability computation in deformed porous carbonate grainstones. *Advances in Water Resources*, 115, 95-111.

Zawisza, L., 2004, January. Hydrodynamic conditions of hydrocarbon accumulation exemplified by the Pomorsko and Czerwiensk oil fields in the Polish Lowland. In *SPE Annual Technical Conference and Exhibition*. Society of Petroleum Engineers.

Zhang, X. and Sanderson, D.J., 1996. Numerical modelling of the effects of fault slip on fluid flow around extensional faults. *Journal of Structural Geology*, 18(1), pp.109-119.

Zhang, X. and Spiers, C.J., 2005. Compaction of granular calcite by pressure solution at room temperature and effects of pore fluid chemistry. *International Journal of Rock Mechanics and Mining Sciences*, 42(7-8), pp.950-960.

Zhang, J., Wong, T.F. and Davis, D.M., 1990. Micromechanics of pressure-induced grain crushing in porous rocks. *Journal of Geophysical Research: Solid Earth*, 95(B1), pp.341-352.

Zhu, W. and Wong, T.F., 1997. The transition from brittle faulting to cataclastic flow: Permeability evolution. *Journal of Geophysical Research: Solid Earth*, 102(B2), pp.3027-3041.

Zhu, W., Baud, P. and Wong, T.F., 2010. Micromechanics of cataclastic pore collapse in limestone. *Journal of Geophysical Research: Solid Earth*, 115(B4).

Zhu, W., Montesi, L.G. and Wong, T.F., 1997. Shear-enhanced compaction and permeability reduction: Triaxial extension tests on porous sandstone. *Mechanics of Materials*, 25(3), pp.199-214.

Zeybek, M., Kuchuk, F.J. and Hafez, H., 2002, January. Fault and fracture characterization using 3D interval pressure transient tests. In Abu Dhabi International Petroleum Exhibition and Conference. Society of Petroleum Engineers.

Zubtsov, S., Renard, F., Gratier, J.P., Dysthe, D.K., Traskine, V., 2005. Single-contact pressure solution creep on calcite monocrystals. *Geological Society, London, Special Publications*, 243(1), 81-95.

Appendices

Appendix 1. Porosity-permeability data for all studied fault rocks, including the data collected from the literature. Other known fault data, such as fault throw and fault rock thickness, are also included.

sample_id	Throw, m	Density	Host porosity, %	Fault porosity, %	Deformation type	Min fault thickness, m	Max fault thickness, m	Host permeability, mD	Fault permeability, mD	Burial depth, m
si001_x	3	2.63	0.59	5.56	Breccia	7	8	0.0012	0.0019	2910
si001_y	3	2.69	0.59	5.16	Breccia	7	8	0.0012	0.16	2910
si001_z	3	2.7	0.59	5.07	Breccia	7	8	0.0012	0.018	2910
si002_y	3	2.76	0.59	2.59	Cataclasite	6	12	0.0012	0.025	2910
si002_z	3	2.75	0.59	3.05	Cataclasite	6	12	0.0012	0.095	2910
si003	5		0.59		Cataclasite	2	4	0.0012		2910
si004_z		2.24	0.59	20.32	Breccia	15	19	0.0012		2910
si005_y		2.6	0.59	1.43	Breccia	30	40	0.0012		2910
si005_z		2.68	0.59	2.02	Breccia	30	40	0.0012	0.0012	2910
si006_x		2.66	0.59	1.88	Breccia	10	23	0.0012	5.4E-06	2910
si006_y		2.65	0.59	2.3	Breccia	10	23	0.0012	0.000005	2910
si006_z		2.64	0.59	1.58	Breccia	10	23	0.0012	0.000002	2910
si015_x	5	2.62	0.78	4.57		7	20	0.011	0.011	1969
si015_y	5	2.63	0.78	5.08	Breccia	7	20	0.011	0.011	1969
si015_z	5	2.64	0.78	4.24	Breccia	7	20	0.011	0.0002	1969
si016_x	5	2.76	0.78	0.69	Cataclasite	8		0.011	0.00003	1969
si016_y	5	2.76	0.78	1.04	Cataclasite	8		0.011	0.000001	1969
si016_z	5	2.76	0.78	0.85	Cataclasite	8		0.011	0.00002	1969
si017a_z	5	2.57	0.78	4.23	Breccia	30		0.011		1969
si018b_x	5	2.62	0.78	2.66	Breccia	30		0.011	0.0009	1969
si018b_y	5	2.63	0.78	2.72	Breccia	30		0.011	0.0043	1969
si018b_z	5	2.63	0.78	2.38	Breccia	30		0.011	0.0037	1969

si019a_x	5	2.67	0.78	1.28	Breccia	100	0.011	0.022	1969
si019a_y	5	2.67	0.78	0.94	Breccia	100	0.011	0.013	1969
si019a_z	5	2.67	0.78	0.74	Breccia	100	0.011	0.72	1969
si024	5		0.02		Cataclasite	4			2530
si025			0.02		Breccia	8			2530
si026			0.02		Breccia	4			2530
sc02_z	5000	2.58	0.5	9.12	Cataclasite	2	0.000001	0.085	970
sc04	5000	2.78	0.5	2.76	Breccia		0.000001	5.4	970
si031_z	20	2.48	0.78	8.17	Cataclasite		0.011	0.00006	950
si033_x	20	2.61	0.2	1.9	Cataclasite	18	0.0021	0.76	1180
si033_y	20	2.61	0.2	2.53	Cataclasite	18	0.0021	0.019	1180
si033_z	20	2.62	0.2	1.85	Cataclasite	18	0.0021	0.000054	1180
si034_x	20	2.68	0.2	3.13	Chaotic breccia	12	0.0021	0.0075	1180
si034_y	20	2.64	0.2	2.92	Chaotic breccia	12	0.0021	0.017	1180
si034_z	20	2.71	0.2	1.37	Chaotic breccia	12	0.0021	0.00045	1180
si035_x	20	2.47	0.2	6.6	Chaotic breccia	125	0.0021	97	1180
si035_y	20	2.52	0.2	4.7	Chaotic breccia	125	0.0021	0.59	1180
si035_z	20	2.53	0.2	4.16	Chaotic breccia	125	0.0021	0.17	1180
si036_x	20	2.72	0.2	3.81	Cataclasite	8	0.0021	7.3	1180
si036_y	20	2.75	0.2	2.28	Cataclasite	8	0.0021	0.0011	1180
si036_z	20	2.78	0.2	1.31	Cataclasite	8	0.0021	0.000036	1180
si037_x_1	20	2.77	0.2	1.34	Mosaic breccia	18	0.0021	0.00023	1180
si037_x_2	20	2.56	0.2	3.82	Mosaic breccia	18	0.0021	141	1180
si037_y	20	2.57	0.2	3.18	Mosaic breccia	18	0.0021	66	1180

si037_z_1	20	2.57	0.2	1.45	Mosaic breccia	18	0.0021	0.000065	1180
si037_z_2	20	2.52	0.2	3	Mosaic breccia	18	0.0021	13	1180
si038_z	20	2.66	0.2	2.64	Cataclasite	7	0.0021	0.00085	1180
si039_x	20	2.72	0.2	2.93	Cataclasite	11	0.0021	0.014	1180
si039_y	20	2.72	0.2	3.31	Cataclasite	11	0.0021	0.0018	1180
si039_z	20	2.71	0.2	2.68	Cataclasite	11	0.0021	0.0026	1180
si040_x	20	2.62	0.2	1.75	Chaotic breccia	200	0.0021	0.16	1180
si040_y	20	2.62	0.2	2.06	Chaotic breccia	200	0.0021	0.52	1180
si040_z	20	2.59	0.2	2.56	Chaotic breccia	200	0.0021	0.0024	1180
si041_x	20	2.59	0.2	4.03	Chaotic breccia	130	0.0021	0.16	1180
si041_y	20	2.65	0.2	2.77	Chaotic breccia	130	0.0021	0.0042	1180
si041_z	20	2.63	0.2	4.11	Chaotic breccia	130	0.0021	0.00044	1180
si042_z	20	2.64	0.2	4.02	breccia	5	0.0021	0.00069	1180
si044_x	5	2.75	2.15	3.1	Cataclasite	8	0.0053	0.061	2530
si044_y	5	2.7	2.15	5.09	Cataclasite	8	0.0053	7.9	2530
si044_z	5	2.78	2.15	2.09	Cataclasite	8	0.0053	0.0008	2530
si045	5		2.15		Cataclasite	5	0.0053		2530
si046_x	5	2.77	2.15	2.76	Cataclasite	30	0.0053	0.25	2530
si046_y	5	2.77	2.15	2.31	Cataclasite	30	0.0053	0.21	2530
si046_z_1	5	2.73	2.15	4.3	Cataclasite	30	0.0053	0.015	2530
si046_z_2	5	2.73	2.15	4.11	Cataclasite	30	0.0053	0.0027	2530
si058_x	5	2.75	0.2	0.71	Breccia	8	0.0021	0.00028	1180
si058_y	5	2.72	0.2	0.51	Breccia	8	0.0021	0.00052	1180
si058_z	5	2.75	0.2	0.04	Breccia	8	0.0021	3.4E-06	1180
si059_x	5				Breccia	36			1180
si059_y	5				Breccia	36			1180

si059_z	5				Breccia	36			1180
si060_x	5	2.72	0.2	0.15	Breccia	58	0.0021	0.000049	1180
si060_y	5	2.7	0.2	0.48	Breccia	58	0.0021	0.00032	1180
si060_z	5		0.2	0.26	Breccia	58	0.0021	0.000016	1180
si061_x	5	2.71	0.2	3.03	Breccia	16	0.0021	0.00094	1180
si061_y	5	2.71	0.2	3.03	Breccia	16	0.0021	0.0005	1180
si061_z	5	2.7	0.2	2.99	Breccia	16	0.0021		1180
si062_x	5				Breccia	13			1180
si062_y	5				Breccia	13			1180
si062_z	5				Breccia	13			1180
si063_x	5	2.65	0.2	3.39	Breccia	18	0.0021	0.21	1180
si063_y	5	2.62	0.2	3.65	Breccia	18	0.0021	6	1180
si063_z	5				Breccia	18			1180
si065_x	5	2.78	0.2	1.52	Cataclasite	8	0.0021	0.32	1180
si065_y	5	2.78	0.2	1.59	Cataclasite	8	0.0021	0.0035	1180
si065_z_1	5	2.64	0.2	4.09	Cataclasite	8	0.0021	0.0063	1180
si065_z_2	5	2.79	0.2	1.13	Cataclasite	8	0.0021	0.0001	1180
si066_x	5	2.7	0.2	2.2	Cemented fracture		0.0021	0.001	1180
si066_y	5	2.71	0.2	0.86	Cemented fracture		0.0021	0.00032	1180
si066_z	5	2.72	0.2	0.22	Cemented fracture		0.0021	0.00025	1180
si067_x	5	2.74	0.2	4.65	Cataclasite	5	0.0021	0.0011	1180
si067_y	5	2.74	0.2	3.7	Cataclasite	5	0.0021	0.0016	1180
si067_z	5	2.73	0.2	3.83	Cataclasite	5	0.0021	0.0001	1180
si068_x	5	2.77	0.2	2.05	Cataclasite	16	0.0021	0.00056	1180
si068_y	5	2.76	0.2	2.16	Cataclasite	16	0.0021	198	1180
si068_z	5	2.82	0.2	0.06	Cataclasite	16	0.0021	0.00052	1180
si069_x	5	2.72	0.2	0.28	Cataclasite	14	0.0021	0.00094	1180
si069_y	5	2.71	0.2	0.64	Cataclasite	14	0.0021	0.00061	1180
si069_z	5	2.69	0.2	1.19	Cataclasite	14	0.0021	0.00076	1180
si070_x	5	2.61	0.2	3.82	Cataclasite	1.5	0.0021	0.0048	
si070_y	5	2.69	0.2	0.68	Cataclasite	1.5	0.0021		
si070_z	5	2.63	0.2	2.79	Cataclasite	1.5	0.0021	0.0012	

si071_z	5	2.5	0.2	7.28	Cataclasite	2		0.0021	0.11	
si072_z_1	5	2.61	0.2	3.08	Cataclasite	8		0.0021	0.0062	
si072_z_2	5	2.6	0.2	3.95	Cataclasite	8		0.0021	0.0064	
si073_z_1	5	2.66	0.2	1.59	Breccia	55		0.0021	0.16	
si073_z_2	5	2.32	0.2	14.64	Breccia	55		0.0021	25	
si073_x	5	2.65	0.2	1.96	Breccia	55		0.0021	0.029	
si073_y	5	2.6	0.2	3.69	Breccia	55		0.0021	18	
si074_x	5	2.4	0.2	12.36	Breccia	3.5		0.0021	3.3	
si074_z	5	2.37	0.2	13.58	Breccia	3.5		0.0021	0.19	
si077_x	1000				Cataclasite	2	9			3100
si077_y	1000				Cataclasite	2	9			3100
si077_z	1000				Cataclasite	2	9			3100
si078_x	1000				Cataclasite	2	9			3100
si078_y	1000				Cataclasite	2	9			3100
si078_z	1000				Cataclasite	2	9			3100
si079_z	1000	2.7		3.21	Cataclasite	2	9		0.19	3100
si080_x	1000				Cataclasite	2	9			3100
si080_y	1000				Cataclasite	2	9			3100
si080_z	1000				Cataclasite	2	9			3100
si081_x	1000				Cataclasite	2	9			3100
si081_y	1000				Cataclasite	2	9			3100
si081_z	1000				Cataclasite	2	9			3100
si082_x	1000				Cataclasite	2	9			3100
si082_y	1000				Cataclasite	2	9			3100
si082_z	1000				Cataclasite	2	9			3100
si083_x	1000				Cataclasite	2	9			3100
si083_y	1000				Cataclasite	2	9			3100
si083_z	1000				Cataclasite	2	9			3100
si053_x_1	5	2.75	0.2	2.66	Cataclasite			0.0021	0.0071	1180
si053_x_2	5	2.7	0.2	4.82	Cataclasite			0.0021		1180
si053_y	5	2.77	0.2	1.35	Cataclasite			0.0021	0.029	1180
si053_z	5	2.75	0.2	1.52	Cataclasite			0.0021	0.029	1180

si054_x	5	2.79	0.2	0.61	Cataclasite		0.0021	0.00019	1180
si054_y	5	2.78	0.2	1.53	Cataclasite		0.0021	0.0011	1180
si054_z	5	2.8	0.2	0.64	Cataclasite		0.0021	0.00021	1180
si085_x	5	2.82	0.2	0.02	Cataclasite		0.0021		1180
si085_y	5	2.81	0.2	0.23	Cataclasite		0.0021	0.0003	1180
si085_z	5	2.82	0.2	0.18	Cataclasite		0.0021	0.00044	1180
si086_y	5		0.2		Cataclasite		0.0021		1180
si086_x	5	2.72	0.2	2.24	Cataclasite		0.0021	0.0012	1180
si086_z	5	2.76	0.2	1.7	Cataclasite		0.0021	0.00028	1180
si087_y	5	2.76	0.2	1.66	Cataclasite		0.0021	0.00025	1180
si087_z	5	2.78	0.2	1.33	Cataclasite		0.0021	0.0025	1180
si088_x_1	5	2.78	0.2	1.66	Cataclasite		0.0021	0.21	1180
si088_x_2	5	2.77	0.2	0.94	Cataclasite		0.0021	0.00051	1180
si088_y	5	2.76	0.2	1.25	Cataclasite		0.0021	0.0017	1180
si088_z	5	2.76	0.2	1.3	Cataclasite		0.0021	0.000021	1180
si091		2.61	0.2	3.341579	Breccia	60	0.0021	2.6	
si016b_1			50.27	24.49	Deformation band		1935	660	
si018_3			50.27	38.57	Deformation band		1935	1670	
si018_1			50.27	38.98	Deformation band		1935	1580	
si020_2			50.27	46.56	Deformation band		1935	1310	
si020_1			50.27	46.05	Deformation band		1935	1200	
si018_2			50.27	38.66	Deformation band		1935	1620	
si022b_f			50.27	20.62	Deformation band		1935	0.016	
si016b_2			50.27	23.68	Deformation band		1935	365	
si016b_3			50.27	21.94	Deformation band		1935	270	
si021b			50.27	27.04	Deformation band		1935	18	
si022a_1_i			50.27	43.43	Deformation band		1935	1020	
si022b_2_i			50.27	36.12	Deformation band		1935	0.67	
si022a_2_i			50.27	42.39	Deformation band		1935	1700	
si014b_2			44.65	24.47	Deformation band		2725	0.38	
si009			44.65	26.17	Deformation band		2725	89	
si014b_1			44.65	18.82	Deformation band		2725	0.016	

si012_1	44.65	24	Deformation band	2725	14
si013_2	44.65	22.2	Deformation band	2725	32
si013_1	44.65	20.74	Deformation band	2725	75
si011	44.65	13.16	Deformation band	2725	0.066
si021a	50.27	28.39	Deformation band	1935	56
si008_3	44.65	26.83	Deformation band	2725	110
si019b	50.27	22.98	Deformation band	1935	895
si010	44.65	15.82	Deformation band	2725	
si012_2	44.65	23.63	Deformation band	2725	5.2
si008_1	44.65	18.29	Deformation band	2725	9.2
si008_2	44.65	27.08	Deformation band	2725	0.6
si022a_f	50.27	42.05	Deformation band	1935	
si012_3	44.65	31.34	Deformation band	2725	
si014_1	44.65	29.22	Deformation band	2725	7.2
si014_2	44.65	32.17	Deformation band	2725	1710
si014_3	44.65	31.32	Deformation band	2725	0.42
gr5_f_z	38.71	36.63	Deformation band	2039	300
gr4_z_1	38.71	19.99	Deformation band	2039	0.0034
gr4_z_2	38.71	17.78	Deformation band	2039	0.006
gr4_y	38.71	11.84	Deformation band	2039	65
gr4_x	38.71	17.08	Deformation band	2039	289
si050_x_1	50.27	19.11	Deformation band	1935	39
si050_x_2	50.27	18.06	Deformation band	1935	105
si050_z_1	50.27	26.33	Deformation band	1935	7.2
si050_z_2	50.27	19.56	Deformation band	1935	0.27
si050_y_1	50.27	18.95	Deformation band	1935	7.2
si050_y_2	50.27	18.53	Deformation band	1935	8.6
si049_x_1	50.27	11.23	Deformation band	1935	0.25
si049_x_2	50.27	17.88	Deformation band	1935	7.8
si049_y_1	50.27	19.92	Deformation band	1935	2.5
si049_y_2	50.27	21.35	Deformation band	1935	15
si049_z_2	50.27	18.96	Deformation band	1935	0.0082

si049_z_1	50.27	18.15	Deformation band	1935	0.0084
si052_z_1	50.27	22.11	Deformation band	1935	0.0099
si052_z_2	50.27	23.66	Deformation band	1935	0.01
si052_y	50.27	22.52	Deformation band	1935	0.35
si052_x	50.27	21.69	Deformation band	1935	22
si055_y_1	44.65	18.97	Deformation band	2725	74
si055_y_2	44.65	17.99	Deformation band	2725	207
si055_z_1	44.65	19.16	Deformation band	2725	0.9
si055_z_2	44.65	21.29	Deformation band	2725	0.025
si055_x	44.65	18.07	Deformation band	2725	0.0095
si048_z_1	50.27	31.39	Deformation band	1935	229
si048_z_2	50.27	31.73	Deformation band	1935	191
si048_y	50.27	34.08	Deformation band	1935	181
si051_z	50.27	21.94	Deformation band	1935	0.013
rh1_1	42.01	16.79	Deformation band	75	111
rh1_2	42.01	23.8	Deformation band	75	47
rh2			Deformation band		
rh3_1	42.01	10.05	Deformation band	75	28
rh4			Deformation band	75	
rh9	42.01	38.77	Deformation band	75	65
rh10_1	42.01	35.5	Deformation band	75	0.77
pb1_af	42.4	43.8	Deformation band	2.5	2.6
pb1_bf	42.4	42	Deformation band	2.5	1.9
pb1_cf	42.4	35.4	Deformation band	2.5	0.91
pb2_af	42.4	42.4	Deformation band	2.5	3.1
pb2_bf	42.4	40.7	Deformation band	2.5	
pb3	42.4	39.5	Deformation band	2.5	1.2
db_f	41.98	37.84	Deformation band	4.4	0.81
db_h	41.98		Deformation band	4.4	
au4_1	33		Deformation band	1460	137
au4_2	33		Deformation band	1460	1408
au4_3	33		Deformation band	1460	114

au5_1		33		Deformation band		1460	0.52
au5_2		33		Deformation band		1460	405
au6		33		Deformation band		1460	35
au7_1		33		Deformation band		1460	12
au7_2		33		Deformation band		1460	43
Bauer_2016	100	0.9	2	Cataclasite	0.2	0.1	0.01
Bauer_2016	100	0.9	3.5	Cataclasite	0.4	0.1	0.7
Bauer_2016	100	0.9	2	Cataclasite	0.05	0.1	0.01
Bauer_2016	100	0.9	4	Cataclasite	0.2	0.1	0.7
Bauer_2016	100	0.9	3.9	Breccia		0.1	551
Bauer_2016	100	0.9	2	Cataclasite	4	0.1	0.01
Bauer_2016	100	0.9	1.7	Breccia	0.1	0.1	0.04
Zambrano_2016	20	0.35	0.6			0.00002	0.000098
Zambrano_2016	20	0.35	5.5			0.00002	0.1
Cooke_2019		13.19286	7.32			4.058571	4.6
Cooke_2019		13.19286	9.37			4.058571	7.52
Cooke_2019		13.19286	4.01			4.058571	0.0078
Cooke_2019		13.19286	1.23			4.058571	0.004
Cooke_2019		13.19286	1.52			4.058571	0.168
Cooke_2019		13.19286	2.33			4.058571	0.0038
Cooke_2019		13.19286	1.52			4.058571	0.023
Cooke_2019		13.19286	1.52			4.058571	0.0068
Cooke_2019		13.19286	1.52			4.058571	0.026
Cooke_2019		13.19286	1.52			4.058571	0.0015
Cooke_2019		13.19286	6.75			4.058571	2.3
Cooke_2019		13.19286	6.82			4.058571	7.84
Cooke_2019		13.19286	5.24			4.058571	0.00014
Cooke_2019		13.19286	13.87			4.058571	0.16
Cooke_2019		13.19286	13.98			4.058571	0.057

Appendix 2. Results from the mechanical tests.

sample_id	Density g/cm ³	Porosity, %	Dry/Saturate d	Yield point, MPa	Confinin g pressure , MPa	Test at which failed	Median grain diameter , um	p, MPa	q, MPa	Friction coefficien t	Cohesio n	Pore Radius , nm
gr5_f_z	1.728509 7	36.6279 3	dry	27.17	27.17	Hydrostati c	163.724	27.17	0			88.8
si056_i1_3	2.487819 1	7.69707 2	dry	179.84 1	15.0212	Multistage -failure triaxial	275.605	69.9611 3	164.819 8	0.64	33.4	45.2
si056_i1_4	2.487819 1	7.69707 2	dry	196.27 9	20.4745	Multistage -failure triaxial	275.605	79.076	175.804 5	0.64	33.4	45.2
si056_i1_5	2.487819 1	7.69707 2	dry	210.20 8	25.0418	Multistage -failure triaxial	275.605	86.7638 7	185.166 2	0.64	33.4	45.2
si056_i1_6	2.487819 1	7.69707 2	dry	223.00 4	30.0423	Multistage -failure triaxial	275.605	94.3628 7	192.961 7	0.64	33.4	45.2
si056_i1_7	2.487819 1	7.69707 2	dry	238.18 8	35.0231	Multistage -failure triaxial	275.605	102.744 7	203.164 9	0.64	33.4	45.2
si056_i2_1	2.487010 2	6.86751 9	saturated with water	123.14	5.11003	Multistage -failure triaxial	275.605	44.4533 5	118.03	0.63	30.2	45.2
si056_i2_2	2.487010 2	6.86751 9	saturated with water	144.25 5	10.0921	Multistage -failure triaxial	275.605	54.8130 7	134.162 9	0.63	30.2	45.2
si056_i2_3	2.487010 2	6.86751 9	saturated with water	164.98 1	15.0544	Multistage -failure triaxial	275.605	65.0299 3	149.926 6	0.63	30.2	45.2

si056_i2_4	2.487010 2	6.86751 9	saturated with water	178.07 6	20.7256	Multistage -failure triaxial	275.605	73.1757 3	157.350 4	0.63	30.2	45.2
si056_i2_5	2.487010 2	6.86751 9	saturated with water	189.12 8	25.0382	Multistage -failure triaxial	275.605	79.7348 8	164.089 8	0.63	30.2	45.2
si056_y_3	2.509189 2	7.25	dry	143.77 3	15.062	Multistage -failure triaxial	275.605	57.9656 7	128.711	0.55	28.2	45.2
si056_y_4	2.509189 2	7.25	dry	158.41	20.0241	Multistage -failure triaxial	275.605	66.1527 3	138.385 9	0.55	28.2	45.2
si056_y_5	2.509189 2	7.25	dry	173.25 9	25.0403	Multistage -failure triaxial	275.605	74.4465 3	148.218 7	0.55	28.2	45.2
si056_y_6	2.509189 2	7.25	dry	185.00 7	30.0604	Multistage -failure triaxial	275.605	81.7092 7	154.946 6	0.55	28.2	45.2
si056_y_7	2.509189 2	7.25	dry	199.37 2	35.5137	Multistage -failure triaxial	275.605	90.1331 3	163.858 3	0.55	28.2	45.2
si056_y_8	2.509189 2	7.25	dry	210.73 9	40.0417	Multistage -failure triaxial	275.605	96.9408	170.697 3	0.55	28.2	45.2
si056_y_9	2.509189 2	7.25	dry	223.60 6	45.0422	Multistage -failure triaxial	275.605	104.563 5	178.563 8	0.55	28.2	45.2
si064y_i1_1	2.560086 6	5.69817 4	dry	194.79	5.07064	Multistage -failure triaxial	20	68.3104 3	189.719 4	1.44	23.56	21.6
si064y_i1_2	2.560086 6	5.69817 4	dry	246.70 2	10.0921	Multistage -failure triaxial	20	88.9620 7	236.609 9	1.44	23.56	21.6
rh7_1	1.548134 5	43.8891 8	dry	10.746 3	10.74	Hydrostati c	143.046	10.7421	0.0063			427.3

gra07_4_1	2.285029 8	15.4733 9	dry	49.25	5.08024	Multistage -failure triaxial	91.4555	19.8034 9	44.1697 6	0.41	13.71	341.5
gra07_4_2	2.285029 8	15.4733 9	dry	63.773 8	10.0226	Multistage -failure triaxial	91.4555	27.9396 7	53.7512	0.41	13.71	341.5
gra07_4_3	2.285029 8	15.4733 9	dry	75.416	15.0635	Multistage -failure triaxial	91.4555	35.181	60.3525	0.41	13.71	341.5
gra07_4_4	2.285029 8	15.4733 9	dry	85.532 1	20.0453	Multistage -failure triaxial	91.4555	41.8742 3	65.4868	0.41	13.71	341.5
gra07_4_5	2.285029 8	15.4733 9	dry	95.180 7	25.0861	Multistage -failure triaxial	91.4555	48.4509 7	70.0946	0.41	13.71	341.5
gra07_4_6	2.285029 8	15.4733 9	dry	105.49	30.0536	Multistage -failure triaxial	91.4555	55.1990 7	75.4364	0.41	13.71	341.5
gra07_4_7	2.285029 8	15.4733 9	dry	115.06 4	35.0544	Multistage -failure triaxial	91.4555	61.7242 7	80.0096	0.41	13.71	341.5
gra07_4_8	2.285029 8	15.4733 9	dry	129.11 6	40.0748	Multistage -failure triaxial	91.4555	69.7552	89.0412	0.41	13.71	341.5
gra07_4_9	2.285029 8	15.4733 9	dry	141.10 1	45.0559	Multistage -failure triaxial	91.4555	77.0709 3	96.0451	0.41	13.71	341.5
gra07_4_10	2.285029 8	15.4733 9	dry	152.37 2	50.0763	Multistage -failure triaxial	91.4555	84.1748 7	102.295 7	0.41	13.71	341.5
gra07_4_11	2.285029 8	15.4733 9	dry	162.93	55.0377	Multistage -failure triaxial	91.4555	91.0018	107.892 3	0.41	13.71	341.5

gra07_4_12	2.285029 8	15.4733 9	dry	174.64 9	60.0541	Multistage -failure triaxial	91.4555	98.2524	114.594 9	0.41	13.71	341.5
gra07_3_1	2.326980 8	13.9405 8	dry	54.9	5.0512	Multistage -failure triaxial	91.4555	21.6674 7	49.8488	0.51	14.55	341.5
gra07_3_2	2.326980 8	13.9405 8	dry	73.884 9	10.0532	Multistage -failure triaxial	91.4555	31.3304 3	63.8317	0.51	14.55	341.5
gra07_3_3	2.326980 8	13.9405 8	dry	89.762 2	15.0945	Multistage -failure triaxial	91.4555	39.9837 3	74.6677	0.51	14.55	341.5
gra07_3_4	2.326980 8	13.9405 8	dry	101.89 8	19.998	Multistage -failure triaxial	91.4555	47.298 81.9		0.51	14.55	341.5
gra07_3_5	2.326980 8	13.9405 8	dry	114.90 9	25.1034	Multistage -failure triaxial	91.4555	55.0386	89.8056	0.51	14.55	341.5
gra07_3_6	2.326980 8	13.9405 8	dry	125.93 5	30.0847	Multistage -failure triaxial	91.4555	62.0348	95.8503	0.51	14.55	341.5
gra08_2	2.099354 6	23.2069 2	dry	47.5	5.0603	Multistage -failure triaxial	3.9	19.2068 7	42.4397			186.5
gra06_1_2	2.505549 6	6.61176 4	dry	155.95 6	10.0714	Multistage -failure triaxial	95.8445	58.6996	145.884 6	0.52	39.38	23.4
gra06_1_3	2.505549 6	6.61176 4	dry	173.62 8	15.0529	Multistage -failure triaxial	95.8445	67.9112 7	158.575 1	0.52	39.38	23.4
gra06_1_4	2.505549 6	6.61176 4	dry	189.84 7	20.0541	Multistage -failure triaxial	95.8445	76.6517 3	169.792 9	0.52	39.38	23.4

gra06_1_5	2.505549 6	6.61176 4	dry	207.79 6	30.0611	Multistage -failure triaxial	95.8445	89.3060 7	177.734 9	0.52	39.38	23.4
gra06_1_6	2.505549 6	6.61176 4	dry	222.83 6	35.0236	Multistage -failure triaxial	95.8445	97.6277 3	187.812 4	0.52	39.38	23.4
gra06_1_7	2.505549 6	6.61176 4	dry	236.35	40.0059	Multistage -failure triaxial	95.8445	105.453 9	196.344 1	0.52	39.38	23.4
gra06_2_2	2.491084 5	7.81844 2	saturated with water	81.819 5	10.0625	Multistage -failure triaxial	95.8445	33.9815	71.757	0.76	10.62	23.4
gra06_2_3	2.491084 5	7.81844 2	saturated with water	105.72	15.0839	Multistage -failure triaxial	95.8445	45.2959 3	90.6361	0.76	10.62	23.4
gra06_2_4	2.491084 5	7.81844 2	saturated with water	128.54 4	20.0433	Multistage -failure triaxial	95.8445	56.2102	108.500 7	0.76	10.62	23.4
gra06_2_5	2.491084 5	7.81844 2	saturated with water	148.23 3	25.0443	Multistage -failure triaxial	95.8445	66.1072	123.188 7	0.76	10.62	23.4
gra06_2_6	2.491084 5	7.81844 2	saturated with water	167.35 6	30.0453	Multistage -failure triaxial	95.8445	75.8155 3	137.310 7	0.76	10.62	23.4
gra06_2_7	2.491084 5	7.81844 2	saturated with water	183.77 1	35.0069	Multistage -failure triaxial	95.8445	84.5949 3	148.764 1	0.76	10.62	23.4
gra06_3_1	2.504541 1	6.71765 3	saturated with water	95.76	5.08074	Multistage -failure triaxial	95.8445	35.3071 6	90.6792 6	0.54	34.28	23.4
gra06_3_2	2.504541 1	6.71765 3	saturated with water	113.75	10.0433	Multistage -failure triaxial	95.8445	44.6122	103.706 7	0.54	34.28	23.4

gra06_3_3	2.504541 1	6.71765 3	saturated with water	154.00 2	15.0741	Multistage -failure triaxial	95.8445	61.3834	138.927 9	0.54	34.28	23.4
gra06_3_4	2.504541 1	6.71765 3	saturated with water	174.80 2	20.0758	Multistage -failure triaxial	95.8445	71.6512	154.726 2	0.54	34.28	23.4
gra06_3_5	2.504541 1	6.71765 3	saturated with water	187.97 1	25.0578	Multistage -failure triaxial	95.8445	79.3622	162.913 2	0.54	34.28	23.4
gra06_3_6	2.504541 1	6.71765 3	saturated with water	202.27 2	30.0399	Multistage -failure triaxial	95.8445	87.4506	172.232 1	0.54	34.28	23.4
gra06_3_7	2.504541 1	6.71765 3	saturated with water	212.48 7	35.0416	Multistage -failure triaxial	95.8445	94.1900 7	177.445 4	0.54	34.28	23.4
gra06_3_8	2.504541 1	6.71765 3	saturated with water	225.79 5	40.0571	Multistage -failure triaxial	95.8445	101.969 7	185.737 9	0.54	34.28	23.4
gra06_3_9	2.504541 1	6.71765 3	saturated with water	240.56 2	45.0187	Multistage -failure triaxial	95.8445	110.199 8	195.543 3	0.54	34.28	23.4
gra06_4_1	2.469078 7	9.02343 4	dry	103.8	5.04136	Multistage -failure triaxial	95.8445	37.9609 1	98.7586 4	0.64	30.2	23.4
gra06_4_2	2.469078 7	9.02343 4	dry	141.27 1	10.0433	Multistage -failure triaxial	95.8445	53.7858 7	131.227 7	0.64	30.2	23.4
gra06_4_3	2.469078 7	9.02343 4	dry	162.88 4	15.1044	Multistage -failure triaxial	95.8445	64.3642 7	147.779 6	0.64	30.2	23.4
gra06_4_4	2.469078 7	9.02343 4	dry	179.82 3	20.0758	Multistage -failure triaxial	95.8445	73.3248 7	159.747 2	0.64	30.2	23.4

gra06_4_5	2.469078 7	9.02343 4	dry	194.12 4	25.8455	Multistage -failure triaxial	95.8445	81.9383 3	168.278 5	0.64	30.2	23.4
gra06_4_6	2.469078 7	9.02343 4	dry	207.66 3	30.0793	Multistage -failure triaxial	95.8445	89.2738 7	177.583 7	0.64	30.2	23.4
gra07_2_1	2.304777 1	15.3325 3	saturated with water	45.81	5.08074	Multistage -failure triaxial	91.4555	18.6571 6	40.7292 6	0.26	14.66	341.5
gra07_2_2	2.304777 1	15.3325 3	saturated with water	55.607 5	10.2206	Multistage -failure triaxial	91.4555	25.3495 7	45.3869	0.26	14.66	341.5
gra07_2_3	2.304777 1	15.3325 3	saturated with water	64.1	15.0059	Multistage -failure triaxial	91.4555	31.3706	49.0941	0.26	14.66	341.5
gra07_2_4	2.304777 1	15.3325 3	saturated with water	72.346 4	20.1851	Multistage -failure triaxial	91.4555	37.5722	52.1613	0.26	14.66	341.5
gra07_2_5	2.304777 1	15.3325 3	saturated with water	81.626 6	25.0492	Multistage -failure triaxial	91.4555	43.9083 3	56.5774	0.26	14.66	341.5
gra07_2_6	2.304777 1	15.3325 3	saturated with water	89.774 5	30.0906	Multistage -failure triaxial	91.4555	49.9852 3	59.6839	0.26	14.66	341.5
gra07_2_7	2.304777 1	15.3325 3	saturated with water	97.700 9	35.0729	Multistage -failure triaxial	91.4555	55.9489	62.628	0.26	14.66	341.5
gra07_2_8	2.304777 1	15.3325 3	saturated with water	104.61 8	40.0551	Multistage -failure triaxial	91.4555	61.5760 7	64.5629	0.26	14.66	341.5
gra07_2_9	2.304777 1	15.3325 3	saturated with water	112.72 5	45.0701	Multistage -failure triaxial	91.4555	67.6217 3	67.6549	0.26	14.66	341.5

gra07_1_1	2.358241 5	12.9257	saturated with water	52.98	5.0507	Multistage -failure triaxial	91.4555	21.0271 3	47.9293	0.34	15.73	341.5
gra07_1_2	2.358241 5	12.9257	saturated with water	64.992 1	10.3279	Multistage -failure triaxial	91.4555	28.5493	54.6642	0.34	15.73	341.5
gra07_1_3	2.358241 5	12.9257	saturated with water	72.499 3	15.0733	Multistage -failure triaxial	91.4555	34.2153	57.426	0.34	15.73	341.5
gra07_1_4	2.358241 5	12.9257	saturated with water	80.227 9	20.0551	Multistage -failure triaxial	91.4555	40.1127	60.1728	0.34	15.73	341.5
gra07_1_5	2.358241 5	12.9257	saturated with water	88.695	25.0172	Multistage -failure triaxial	91.4555	46.2431 3	63.6778	0.34	15.73	341.5
gra07_1_6	2.358241 5	12.9257	saturated with water	100.29 8	30.0611	Multistage -failure triaxial	91.4555	53.4734	70.2369	0.34	15.73	341.5
gra07_1_7	2.358241 5	12.9257	saturated with water	113.12 3	35.063	Multistage -failure triaxial	91.4555	61.083	78.06	0.34	15.73	341.5
gra10_4	1.372085 4	49.2296 7	dry	3.3220 8	3.26868	Hydrostati c	3.9	3.28648	0.0534			249.6
ch3_1_1	2.349765 6	13.8607 5	dry	68.86	5.07999	Multistage -failure triaxial	206.608 5	26.3399 9	63.7800 1	0.87	10.38	82.2
ch3_1_2	2.349765 6	13.8607 5	dry	92.222 5	10.0615	Multistage -failure triaxial	206.608 5	37.4485	82.161	0.87	10.38	82.2
ch3_2_4	2.403445 2	9.74217 8	saturated with water	148.14 4	25.2154	Multistage -failure triaxial	206.608 5	66.1916	122.928 6	0.6	20.74	82.2
ch3_2_5	2.403445 2	9.74217 8	saturated with water	164.93 1	30.0202	Multistage -failure triaxial	206.608 5	74.9904 7	134.910 8	0.6	20.74	82.2

ch3_4_1	2.331136 1	14.6395 6	dry	60.53	5.02191	Multistage -failure triaxial	206.608 5	23.5246 1	55.5080 9	0.55	16.79	82.2
ch3_4_2	2.331136 1	14.6395 6	dry	84.194 9	10.0527	Multistage -failure triaxial	206.608 5	34.7667 7	74.1422	0.55	16.79	82.2
ch3_4_3	2.331136 1	14.6395 6	dry	101.22 8	15.7436	Multistage -failure triaxial	206.608 5	44.2384	85.4844	0.55	16.79	82.2
ch3_4_4	2.331136 1	14.6395 6	dry	115.77 6	20.1546	Multistage -failure triaxial	206.608 5	52.0284	95.6214	0.55	16.79	82.2
ch3_4_5	2.331136 1	14.6395 6	dry	130.74 1	25.1563	Multistage -failure triaxial	206.608 5	60.3512	105.584 7	0.55	16.79	82.2
ch3_4_6	2.331136 1	14.6395 6	dry	141.10 4	30.099	Multistage -failure triaxial	206.608 5	67.1006 7	111.005	0.55	16.79	82.2
si057_z_2		43.5268 42.2015	saturated with water	10.3	10.2082	Hydrostati c	275.605	10.2388	0.0918			
si057_y_2_1		42.2015 3	dry	11.3	11.2818	Hydrostati c	275.605	11.2878 7	0.0182			
si057_y_2_2		42.2015 3	dry	12.535 8	12.3838	Hydrostati c	275.605	12.4344 7	0.152			
si057_y_2_3		42.2015 3	dry	13.557 2	13.3205	Hydrostati c	275.605	13.3994	0.2367			
si057_x_1_1		44.6435 5	dry	14.69	14.2785	Hydrostati c	275.605	14.4156 7	0.4115			
si057_x_1_2		44.6435 5	dry	17.757 5	17.4736	Hydrostati c	275.605	17.5682 3	0.2839			
si057_z_1		42.8952 6	saturated with water	12.5	12.3126	Hydrostati c	275.605	12.3750 7	0.1874			
si17c_1		49.09	saturated with water	2.31	2.30193	Hydrostati c	266.249 5	2.30462	0.00807			33.3

si17c_2		51.34	dry	4.56	4.52028	Hydrostati	266.249					
			saturated			c	5	4.53352	0.03972			33.3
si17c		52.38	with water	3.02	2.98071	Hydrostati	266.249	2.99380				33.3
						c	5	7	0.03929			
si028		51.75	dry	5.85	5.78854	Hydrostati	266.249	5.80902				33.3
						c	5	7	0.06146			
si028a_1		51.85	dry	4.17	4.11477	Hydrostati	266.249					33.3
				4.5518		c	5	4.13318	0.05523			
si028a_2		51.85	dry	4	4.50673	Hydrostati	266.249	4.52176				33.3
				4.6238		c	5	7	0.04511			
si028a_3		51.85	dry	8	4.58387	Hydrostati	266.249	4.59720				33.3
				5.2001		c	5	7	0.04001			
si028a_4		51.85	dry	7	5.02469	Hydrostati	266.249	5.08318				33.3
			saturated			c	5	3	0.17548			
pb1_a_f		43.81	with water	7.78	7.66154	Hydrostati		7.70102				
			saturated		8.28549	c	3.9	7	0.11846			
pb1_a_h		41.62	with water	8.31	8	Hydrostati		8.29366	0.02450			
					15.7559	c	3.9	5	2			
pb1_b_f		42.02	dry	15.89	1	Hydrostati		15.8006				
					20.7152	c	3.9	1	0.13409			
pb3_f		39.45	dry	20.72	8	Hydrostati		20.7168	0.00472			
						c	3.9	5	4			
pb1_c_f		35.4	dry	14.83	14.823	Hydrostati		14.8253	0.00699			
			saturated		14.8161	c	3.9	4	6			
pb1_c_h		35.397	with water	14.84	8	Hydrostati		14.8241				
			saturated			c	3.9	2	0.02382			
fh3		25.7	with water	56.3	55.8334	Hydrostati		55.9889				
		32.1275				c	3.9	3	0.4666			
au1_1	1.822179	6	dry	35.82	35.8096	Hydrostati		35.8130				
		31.4697	saturated			c	49.768	7	0.0104			126.3
au1_2	1.840521	4	with water	27.67	27.5828	Hydrostati		27.6118				
	1.768756	33.9290				c	49.768	7	0.0872			126.3
au2_1	8	1	dry	25.67	25.4626	Hydrostati		25.5317				
						c	49.768	3	0.2074			126.3

au2_2	1.754783	34.4625 8	saturated with water	17.17	17.1375	Hydrostati c	49.768	17.1483 3	0.0325				126.3
au3_1_1	2.272270 1	15.1707	saturated with water	46.98	5.13805	Multistage -failure triaxial	62.8365	19.0853 7	41.8419 5	0.54	12.96		179.3
au3_1_2	2.272270 1	15.1707	saturated with water	71.411	10.0989	Multistage -failure triaxial	62.8365	30.5362 7	61.3121	0.54	12.96		179.3
au3_1_3	2.272270 1	15.1707	saturated with water	85.683 3	15.0992	Multistage -failure triaxial	62.8365	38.6272 3	70.5841	0.54	12.96		179.3
au3_2_1	2.285162 6	14.8956 8	dry	72.78	5.08908	Multistage -failure triaxial	62.8365	27.6527 2	67.6909 2	0.55	19.32		179.3
au3_2_2	2.285162 6	14.8956 8	dry	93.968 4	10.0502	Multistage -failure triaxial	62.8365	38.0229 3	83.9182	0.55	19.32		179.3
au3_2_3	2.285162 6	14.8956 8	dry	109.86 6	15.0704	Multistage -failure triaxial	62.8365	46.6689 3	94.7956	0.55	19.32		179.3
au3_2_4	2.285162 6	14.8956 8	dry	122.34 2	20.0709	Multistage -failure triaxial	62.8365	54.1612 7	102.271 1	0.55	19.32		179.3
ma15_1_1	2.049736 1	23.7420 7	dry	54.32	5.03002	Multistage -failure triaxial	17.9185	21.4600 1	49.2899 8	0.26	20.28		218.6
ma15_1_2	2.049736 1	23.7420 7	dry	69.187 4	10.0699	Multistage -failure triaxial	17.9185	29.7757 3	59.1175	0.26	20.28		218.6
ma15_1_3	2.049736 1	23.7420 7	dry	78.637 2	15.0901	Multistage -failure triaxial	17.9185	36.2724 7	63.5471	0.26	20.28		218.6
ma15_1_4	2.049736 1	23.7420 7	dry	86.881 1	20.0709	Multistage -failure triaxial	17.9185	42.3409 7	66.8102	0.26	20.28		218.6

ma15_1_5	2.049736 1	23.7420 7	dry	94.116 1	25.032	Multistage -failure triaxial	17.9185	48.0600 3	69.0841	0.26	20.28	218.6
ma15_2_1	2.136722 4	20.0653 6	saturated with water	59.23	5.09009	Multistage -failure triaxial	17.9185	23.1367 3	54.1399 1	0.53	13.86	218.6
ma15_2_2	2.136722 4	20.0653 6	saturated with water	73.779 2	10.0719	Multistage -failure triaxial	17.9185	31.3076 7	63.7073	0.53	13.86	218.6
ma15_2_3	2.136722 4	20.0653 6	saturated with water	86.647 3	15.0409	Multistage -failure triaxial	17.9185	38.9097 7	71.6064	0.53	13.86	218.6
gl1_1	1.838385 5	31.8055 6	dry	49.066 1	48.9933	Hydrostati c	28.3845	49.0175 7	0.0728			190.8
gl1_2	1.807063 3	32.9981 8	saturated with water	23.134 9	23.1171	Hydrostati c	28.3845	23.1230 3	0.0178			190.8
gl2_1	1.790442 3	33.5810 7	dry	28.323 3	28.2902	Hydrostati c	13.319	28.3012 3	0.0331			346.9
gl2_2	1.796279 6	33.4549 3	saturated with water	19.775 5	20	Hydrostati c	13.319	19.9251 7	0			346.9
gr3_x_1	2.474673 7	8.32404 8	dry	169.71	5.02092	Multistage -failure triaxial	3.9	59.9172 8	164.689 1	0.48	50	77.1
gr3_x_2	2.474673 7	8.32404 8	dry	194.56 6	15.0037	Multistage -failure triaxial	3.9	74.8578 3	179.562	0.48	50	77.1
gr3_x_3	2.474673 7	8.32404 8	dry	220.48 3	20.1427	Multistage -failure triaxial	3.9	86.9228 3	200.340	0.48	50	77.1
gr3_x_4	2.474673 7	8.32404 8	dry	234.85 3	30.0271	Multistage -failure triaxial	3.9	98.3024 9	204.825	0.48	50	77.1
si056_i1_1	2.487819 1	7.69707 2	dry	137.61	5.1383	Multistage -failure triaxial	275.605	49.2955 3	132.471 7	0.64	33.4	45.2

si056_i1_2	2.487819 1	7.69707 2	dry	161.38 4	10.0404	Multistage -failure triaxial	275.605	60.4882 7	151.343 6	0.64	33.4	45.2
si056_y_1	2.509189 2	7.25	dry	108.23	5.01962	Multistage -failure triaxial	275.605	39.4230 8	103.210 4	0.55	28.2	45.2
si056_y_2	2.509189 2	7.25	dry	128.62 1	10.0605	Multistage -failure triaxial	275.605	49.5806 7	118.560 5	0.55	28.2	45.2
si029_z_1	2.694325 6	0.21935 2	dry	166.3	5.0512	Multistage -failure triaxial	91.461	58.8008	161.248 8	0.69	37.1	
si029_z_2	2.694325 6	0.21935 2	dry	173.50 6	10.0335	Multistage -failure triaxial	91.461	64.5243 3	163.472 5	0.69	37.1	
si029_z_3	2.694325 6	0.21935 2	dry	196.47 3	15.0945	Multistage -failure triaxial	91.461	75.554	181.378 5	0.69	37.1	
si029_z_4	2.694325 6	0.21935 2	dry	219.21 8	20.451	Multistage -failure triaxial	91.461	86.7066 7	198.767	0.69	37.1	
si043_z_1	2.708029 7	0.09616 4	dry	146.12	5.09009	Multistage -failure triaxial	91.461	52.1000 6	141.029 9	1.17	20.96	
si043_z_2	2.708029 7	0.09616 4	dry	183.64 8	10.1122	Multistage -failure triaxial	91.461	67.9574 7	173.535 8	1.17	20.96	
si043_z_3	2.708029 7	0.09616 4	dry	225.71 6	15.0748	Multistage -failure triaxial	91.461	85.2885 3	210.641 2	1.17	20.96	
si064_z_1_1	2.560802 1	5.53597 4	saturated with water	185.25	5.07974	Multistage -failure triaxial	20	65.1364 9	180.170 3	1.02	32.5	21.6

si064_z_1_2	2.560802 1	5.53597 4	saturated with water	214.35 6	10.0433	Multistage -failure triaxial	20	78.1475 3	204.312 7	1.02	32.5	21.6
si064_z_1_3	2.560802 1	5.53597 4	saturated with water	246.03 7	15.0059	Multistage -failure triaxial	20	92.0162 7	231.031 1	1.02	32.5	21.6
si075_y_1	2.693680 4	0.72847 5	dry	169.85	5.07039	Multistage -failure triaxial	73.718	59.9969 3	164.779 6	1.28	22.63	
si075_y_2	2.693680 4	0.70197 4	dry	212.98	10.0921	Multistage -failure triaxial	73.718	77.7214	202.887 9	1.28	22.63	
si075_y_i1_1	2.694386 8	0.13288 6	dry	159.03	5.03151	Multistage -failure triaxial	73.718	56.3643 4	153.998 5	1.11	24.85	
si075_y_i1_2	2.694386 8	0.13288 6	dry	196.13 8	10.034	Multistage -failure triaxial	73.718	72.0686 7	186.104	1.11	24.85	
si075_y_i1_3	2.694386 8	0.13288 6	dry	227.69 7	15.0953	Multistage -failure triaxial	73.718	85.9625 3	212.601 7	1.11	24.85	
si075_y_i2_1	2.687745	0.52492	saturated with water	75.82	10.0994	Multistage -failure triaxial	73.718	32.0062 7	65.7206			
si075_y_i2_2	2.687745	0.52492	saturated with water	84.878 5	15.0605	Multistage -failure triaxial	73.718	38.3331 7	69.818			
si075_y_i2_3	2.687745	0.52492	saturated with water	88.025 4	20.0413	Multistage -failure triaxial	73.718	42.7026 7	67.9841			
si075_z_1	2.689267 9	0.79890 2	saturated with water	119.56	5.07591	Multistage -failure triaxial	73.718	43.2372 7	114.484 1	0.49	37.1	

si075_z_2	2.689267 9	0.79890 2	saturated with water	157.00 4	20.0515	Multistage -failure triaxial	73.718	65.7023 3	136.952 5	0.49	37.1
si076_y	2.705356 6	0.01187 4	dry	262.99	5.13378	Multistage -failure triaxial	28.5405	91.0858 5	257.856 2		
si076_z_2_1	2.697184 3	0.37358 1	saturated with water	212.75	5.13906	Multistage -failure triaxial	28.5405	74.3427 1	207.610 9	1.108	34.93
si076_z_2_2	2.697184 3	0.37358 1	saturated with water	246.69	10.0418	Multistage -failure triaxial	28.5405	88.9245 3	236.648 2	1.108	34.93
si084_y_1_1	2.697923	0.18637 7	dry	178.91 3	5.07064	Multistage -failure triaxial	44.873	63.0180 9	173.842 4	0.56	57.89
si084_y_1_2	2.697923	0.18637 7	dry	226.32	10.0724	Multistage -failure triaxial	44.873	82.1549 3	216.247 6	0.56	57.89
si084_y_1_3	2.697923	0.18637 7	dry	241.31 1	15.0741	Multistage -failure triaxial	44.873	90.4864	226.236 9	0.56	57.89
si084_y_2_1	2.700613 5	0.16077 9	saturated with water	109.16 1	5.04086	Multistage -failure triaxial	44.873	39.7475 7	104.120 1	0.88	34.97
si084_y_2_2	2.700613 5	0.16077 9	saturated with water	202.87 7	10.1506	Multistage -failure triaxial	44.873	74.3927 3	192.726 4	0.88	34.97
si084_y_2_3	2.700613 5	0.16077 9	saturated with water	230.39 5	15.0733	Multistage -failure triaxial	44.873	86.8472	215.321 7	0.88	34.97
si084_y_i1_1	2.689961	0.28783 5	saturated with water	201.19	5.05095	Multistage -failure triaxial	44.873	70.4306 3	196.139 1	0.92	38.35

si084_y_i1_2	2.689961	0.287835	saturated with water	231.391	10.7419	Multistage -failure triaxial	44.873	84.2916	220.6491	0.92	38.35	
si084_y_i2_1	2.689961	0.418457	saturated with water	165.97	5.05095	Multistage -failure triaxial	44.873	58.69063	160.9191	1.45	18.64	
si084_y_i2_2	2.689961	0.418457	saturated with water	222.013	10.0527	Multistage -failure triaxial	44.873	80.70613	211.9603	1.45	18.64	
si084_z_1	2.7040423	0.24283	dry	188.96	5.07792	Multistage -failure triaxial	44.873	66.37195	183.8821	0.6	54.76	
si084_z_2	2.7040423	0.24283	dry	224.269	10.1138	Multistage -failure triaxial	44.873	81.49887	214.1552	0.6	54.76	
si084_z_3	2.7040423	0.24283	dry	242.362	15.3309	Multistage -failure triaxial	44.873	91.00793	227.0311	0.6	54.76	
tr4_y_1_1	2.6935348	0.58378	dry	157.06	5.07089	Multistage -failure triaxial	30	55.73393	151.9891	0.41	53.22	
tr4_y_1_2	2.6935348	0.58378	dry	181.719	10.1511	Multistage -failure triaxial	30	67.3404	171.5679	0.41	53.22	
tr4_y_1_3	2.6935348	0.58378	dry	192.992	15.0741	Multistage -failure triaxial	30	74.38007	177.9179	0.41	53.22	
gra06_1_1	2.5055496	6.611764	dry	124.18	5.01108	Multistage -failure triaxial	95.8445	44.73405	119.1689	0.52	39.38	23.4
gra06_2_1	2.4910845	7.818442	saturated with water	51.84	5.10018	Multistage -failure triaxial	95.8445	20.68012	46.73982	0.76	10.62	23.4

nym_1_1	2.460871 2	9.84593 9	dry	118.78	5.09034	Multistage -failure triaxial	264.796 5	42.9868 9	113.689 7	0.73	26.24	38.3
nym_1_2	2.460871 2	9.84593 9	dry	145.04 1	10.0812	Multistage -failure triaxial	264.796 5	55.0678	134.959 8	0.73	26.24	38.3
nym_1_3	2.460871 2	9.84593 9	dry	163.94 3	15.0825	Multistage -failure triaxial	264.796 5	64.7026 7	148.860 5	0.73	26.24	38.3
nym_1_4	2.460871 2	9.84593 9	dry	183.63 3	20.0443	Multistage -failure triaxial	264.796 5	74.5738 7	163.588 7	0.73	26.24	38.3
nym_1_5	2.460871 2	9.84593 9	dry	202.43 7	25.0258	Multistage -failure triaxial	264.796 5	84.1628 7	177.411 2	0.73	26.24	38.3
nym_1_6	2.460871 2	9.84593 9	dry	217.22 9	30.0468	Multistage -failure triaxial	264.796 5	92.4408 7	187.182 2	0.73	26.24	38.3
nym_2_1	2.455440 9	9.99105 9	saturated with water	89.55	5.08984	Multistage -failure triaxial	264.796 5	33.2432 3	84.4601 6	0.83	17.21	38.3
nym_2_2	2.455440 9	9.99105 9	saturated with water	120.56 4	10.4455	Multistage -failure triaxial	264.796 5	47.1516 7	110.118 5	0.83	17.21	38.3
nym_2_3	2.455440 9	9.99105 9	saturated with water	144.04 4	15.0726	Multistage -failure triaxial	264.796 5	58.0630 7	128.971 4	0.83	17.21	38.3
nym_2_4	2.455440 9	9.99105 9	saturated with water	162.25 6	20.0177	Multistage -failure triaxial	264.796 5	67.4304 7	142.238 3	0.83	17.21	38.3
nym_3_1	2.466831 6	9.66774 1	dry	116.84	5.0512	Multistage -failure triaxial	264.796 5	42.3141 3	111.788 8	0.71	28.02	38.3

nym_3_2	2.466831 6	9.66774 1	dry	144.04	10.0335	Multistage -failure triaxial	264.796 5	54.7023 3	134.006 5	0.71	28.02	38.3
nym_3_3	2.466831 6	9.66774 1	dry	166.19 5	15.0158	Multistage -failure triaxial	264.796 5	65.4088 7	151.179 2	0.71	28.02	38.3
nym_3_4	2.466831 6	9.66774 1	dry	186.33 4	20.1644	Multistage -failure triaxial	264.796 5	75.5542 7	166.169 6	0.71	28.02	38.3
nym_3_5	2.466831 6	9.66774 1	dry	202.92 4	25.0283	Multistage -failure triaxial	264.796 5	84.3268 7	177.895 7	0.71	28.02	38.3
nym_3_6	2.466831 6	9.66774 1	dry	217.81 6	30.0497	Multistage -failure triaxial	264.796 5	92.6384 7	187.766 3	0.71	28.02	38.3
nym_4_1	2.448920 7	10.2995 6	saturated with water	93.77	5.07039	Multistage -failure triaxial	264.796 5	34.6369 3	88.6996 1	0.8	18.2	38.3
nym_4_2	2.448920 7	10.2995 6	saturated with water	120.69 3	10.1004	Multistage -failure triaxial	264.796 5	46.9646	110.592 6	0.8	18.2	38.3
nym_4_3	2.448920 7	10.2995 6	saturated with water	141.66 2	15.1014	Multistage -failure triaxial	264.796 5	57.2882 7	126.560 6	0.8	18.2	38.3
nym_4_4	2.448920 7	10.2995 6	saturated with water	160.95 7	20.063	Multistage -failure triaxial	264.796 5	67.0276 7	140.894	0.8	18.2	38.3
nym_4_5	2.448920 7	10.2995 6	saturated with water	181.40 8	25.0394	Multistage -failure triaxial	264.796 5	77.1622 7	156.368 6	0.8	18.2	38.3
ch3_2_1	2.403445 2	9.74217 8	saturated with water	80.86	5.15926	Multistage -failure triaxial	206.608 5	30.3928 4	75.7007 4	0.6	20.74	82.2

ch3_2_2	2.403445 2	9.74217 8	saturated with water	104.04 7	10.0822	Multistage -failure triaxial	206.608 5	41.4038	93.9648	0.6	20.74	82.2
ch3_2_3	2.403445 2	9.74217 8	saturated with water	128.00 9	15.0938	Multistage -failure triaxial	206.608 5	52.7322	112.915 2	0.6	20.74	82.2
ch3_3_1	2.412294	9.65603	saturated with water	89.83	5.09034	Multistage -failure triaxial	206.608 5	33.3368 9	84.7396 6	0.72	19.23	82.2
ch3_3_2	2.412294	9.65603	saturated with water	112.18 2	10.0527	Multistage -failure triaxial	206.608 5	44.0958	102.129 3	0.72	19.23	82.2
ch3_3_3	2.412294	9.65603	saturated with water	133.54 7	15.0741	Multistage -failure triaxial	206.608 5	54.5650 7	118.472 9	0.72	19.23	82.2
ch3_3_4	2.412294	9.65603	saturated with water	153.77 8	20.0837	Multistage -failure triaxial	206.608 5	64.6484 7	133.694 3	0.72	19.23	82.2
ch3_3_5	2.412294	9.65603	saturated with water	170.63 7	25.0455	Multistage -failure triaxial	206.608 5	73.576	145.591 5	0.72	19.23	82.2
ch3_3_6	2.412294	9.65603	saturated with water	188.30 9	30.0468	Multistage -failure triaxial	206.608 5	82.8008 7	158.262 2	0.72	19.23	82.2
rh11_1_1	2.700011 4	0.55411 4	saturated with water	152.95	5.09993	Multistage -failure triaxial		54.3832 9	147.850 1	0.97	27.14	
rh11_1_2	2.700011 4	0.55411 4	saturated with water	184.13 4	10.1605	Multistage -failure triaxial		68.1516 7	173.973 5	0.97	27.14	
rh11_1_3	2.700011 4	0.55411 4	saturated with water	211.55 4	15.1029	Multistage -failure triaxial			196.451 1	0.97	27.14	

rh11_1_4	2.700011 4	0.55411 4	saturated with water	240.32 7	20.0453	Multistage -failure triaxial	20	93.4725 3	220.281 7	0.97	27.14
rh11_2_1	2.698868	0.79189	dry	218.4	10.0438	Multistage -failure triaxial	20	79.4958 7	208.356 2	0.91	37.04
rh11_2_2	2.698868	0.79189	dry	243.48 9	15.0263	Multistage -failure triaxial	20	91.1805 3	228.462 7	0.91	37.04
rh11_3	2.707448 1	0.32109 7	dry	173.15	5.13906	Multistage -failure triaxial	20	61.1427 1	168.010 9		
rh11_4	2.70094	0.52251 1	saturated with water	144.4	5.12871	Multistage -failure triaxial	20	51.5524 7	139.271 3		
au8_1	2.697543 2	0.49635 7	dry	159.59	5.03126	Multistage -failure triaxial	30	56.5508 4	154.558 7		
gl6_1_1	2.455719 5	8.88305	dry	84.563 9	5.04036	Multistage -failure triaxial	70.7425	31.5482 1	79.5235 4	0.64	27.27 66.6
gl6_1_2	2.455719 5	8.88305	dry	112.81 7	10.061	Multistage -failure triaxial	70.7425	44.313	102.756	0.64	27.27 66.6
gl6_1_3	2.455719 5	8.88305	dry	148.20 8	15.0817	Multistage -failure triaxial	70.7425	59.4571 3	133.126 3	0.64	27.27 66.6
gl6_1_4	2.455719 5	8.88305	dry	167.61 8	20.0453	Multistage -failure triaxial	70.7425	69.2362	147.572 7	0.64	27.27 66.6
gl6_1_5	2.455719 5	8.88305	dry	184.62 6	25.0074	Multistage -failure triaxial	70.7425	78.2136	159.618 6	0.64	27.27 66.6

gl6_1_6	2.455719 5	8.88305	dry	201.21 6	30.0089	Multistage -failure triaxial	70.7425	87.0779 3	171.207 1	0.64	27.27	66.6
gl6_1_7	2.455719 5	8.88305	dry	217.60 9	35.0497	Multistage -failure triaxial	70.7425	95.9028	182.559 3	0.64	27.27	66.6
gl6_1_8	2.455719 5	8.88305	dry	233.41 1	40.0591	Multistage -failure triaxial	70.7425	104.509 7	193.351 9	0.64	27.27	66.6
gl6_2_1	2.455615 3	8.99145 1	saturated with water	80.806 7	5.08933	Multistage -failure triaxial	70.7425	30.3284 5	75.7173 7	0.54	23.78	66.6
gl6_2_2	2.455615 3	8.99145 1	saturated with water	97.689 1	10.0704	Multistage -failure triaxial	70.7425	39.2766 3	87.6187	0.54	23.78	66.6
gl6_2_3	2.455615 3	8.99145 1	saturated with water	119.47 4	15.0438	Multistage -failure triaxial	70.7425	49.8538 7	104.430 2	0.54	23.78	66.6
gl6_2_4	2.455615 3	8.99145 1	saturated with water	136.75 3	20.0453	Multistage -failure triaxial	70.7425	58.9478 7	116.707 7	0.54	23.78	66.6
gl6_2_5	2.455615 3	8.99145 1	saturated with water	149.50 3	25.0468	Multistage -failure triaxial	70.7425	66.5322	124.456 2	0.54	23.78	66.6
gl6_2_6	2.455615 3	8.99145 1	saturated with water	164.24 6	30.1073	Multistage -failure triaxial	70.7425	74.8202	134.138 7	0.54	23.78	66.6
gl6_2_7	2.455615 3	8.99145 1	saturated with water	176.68 5	35.0908	Multistage -failure triaxial	70.7425	82.2888 7	141.594 2	0.54	23.78	66.6
gl6_2_8	2.455615 3	8.99145 1	saturated with water	192.53 7	40.0335	Multistage -failure triaxial	70.7425	90.868	152.503 5	0.54	23.78	66.6

gl6_2_9	2.455615 3	8.99145 1	saturated with water	207.10 9	45.0549	Multistage -failure triaxial	70.7425	99.0729 3	162.054 1	0.54	23.78	66.6
si18_2_1	2.699654 8	0.03767 8	dry	239.23 2	5.07039	Multistage -failure triaxial	73.718	83.1242 6	234.161 6			
si18_2_2	2.689372 7	0.02126 7	saturated with water	194.80 1	10.1216	Multistage -failure triaxial	73.718	71.6814	184.679 4			
si18_1_1_1	2.689883 4	0.35825 2	dry	178.81 8	5.11962	Multistage -failure triaxial	91.461	63.0190 8	173.698 4	0.8	37.48	
si18_1_1_2	2.689883 4	0.35825 2	dry	200.79 7	10.0817	Multistage -failure triaxial	91.461	73.6534 7	190.715 3	0.8	37.48	
si18_1_1_3	2.689883 4	0.35825 2	dry	223.61 4	15.1226	Multistage -failure triaxial	91.461	84.6197 3	208.491 4	0.8	37.48	
si18_1_1_4	2.689883 4	0.35825 2	dry	242.88 7	20.1526	Multistage -failure triaxial	91.461	94.3974	222.734 4	0.8	37.48	
si18_1_2_1	2.699809 2	0.03264 6	saturated with water	160.77 3	5.14789	Multistage -failure triaxial	91.461	57.0229 3	155.625 1	0.9	31.08	
si18_1_2_2	2.699809 2	0.03264 6	saturated with water	193.16 7	10.062	Multistage -failure triaxial	91.461	71.097	183.105	0.9	31.08	
si18_1_2_3	2.699809 2	0.03264 6	saturated with water	217.87 9	15.162	Multistage -failure triaxial	91.461	82.7343 3	202.717	0.9	31.08	
si18_1_2_4	2.699809 2	0.03264 6	saturated with water	240.49 9	20.065	Multistage -failure triaxial	91.461	93.543 16.6666	220.434	0.9	31.08	
Croizé et al. (2010)		27	dry	50				7	50			

Croizé et al. (2010)	26.4	dry	50		16.6666	
		saturated			7	50
Croizé et al. (2010)	24.7	with water	50		16.6666	
		saturated			7	50
Croizé et al. (2010)	25	with water	48		16	48
		saturated			2.66666	
Croizé et al. (2010)	46	with water	8		7	8
Renner and Rummel (1996)	5.5	dry	370	100	190	270
Renner and Rummel (1996)	5.5	dry	425	150	241.666	
					7	275
Renner and Rummel (1996)	5.5	dry	454	195	281.333	
					3	259
Renner and Rummel (1996)	3.7	dry	459	119	232.333	
					3	340
Renner and Rummel (1996)	3.7	dry	484.8	148.8	260.8	336
Renner and Rummel (1996)	3.7	dry	507.5	193.5	298.166	
					7	314
Renner and Rummel (1996)	14.4	dry	304	195	231.333	
					3	109
Renner and Rummel (1996)	14.4	dry	260	150	186.666	
					7	110
Renner and Rummel (1996)	12.7	dry	225	80	128.333	
					3	145
Renner and Rummel (1996)	12.5	dry	325	150	208.333	
					3	175
Renner and Rummel (1996)	20.2	dry	92	50	64	42
Renner and Rummel (1996)	10.6	dry	375	195	255	180
Renner and Rummel (1996)	14.1	dry	135	50	78.3333	
					3	85

Renner and Rummel (1996)	12.6	dry	362	150	220.666 7	212
Renner and Rummel (1996)	12.7	dry	395	195	261.666 7	200
Renner and Rummel (1996)	22.3	dry	108	50	69.3333 3	58
Renner and Rummel (1996)	12.6	dry	382	150	227.333 3	232
Renner and Rummel (1996)	22.2	dry	125	50	75	75
Renner and Rummel (1996)	17.8	dry	309	150	203	159
Renner and Rummel (1996)	20.7	dry	264	150	188	114
Renner and Rummel (1996)	8.5	dry	216	80	125.333 3	136
Renner and Rummel (1996)	12	dry	100	50	66.6666 7	50
Renner and Rummel (1996)	11.8	dry	155	80	105	75
Renner and Rummel (1996)	11.9	dry	270	150	190	120
Renner and Rummel (1996)	14.7	dry	275	150	191.666 7	125
Renner and Rummel (1996)	10.3	dry	357	150	219	207
Renner and Rummel (1996)	11.4	dry	395	150	231.666 7	245
Renner and Rummel (1996)	15.8	dry	133	80	97.6666 7	53
Renner and Rummel (1996)	12.5	dry	275	150	191.666 7	125
Renner and Rummel (1996)	12.8	dry	218	80	126	138

Renner and Rummel (1996)	11.9	dry	222	80	127.333	3	142
Renner and Rummel (1996)	15.1	dry	230	80	130		150
Renner and Rummel (1996)	14.9	dry	275	150	191.666	7	125
Palchik and Hatzor (2002)	29	dry	46	0	15.3333	3	46
Cilona et al. (2014)	27	dry	49.7	5	19.9		44.7
Cilona et al. (2014)	27	dry	49.42	5	19.8066	7	44.42
Cilona et al. (2014)	26.3	dry	61.65	12.5	28.8833	3	49.15
Cilona et al. (2014)	28.3	dry	63.175	15	31.0583	3	48.175
Cilona et al. (2014)	28	dry	62.24	20	34.08		42.24
Cilona et al. (2014)	27.3	dry	65	25	38.3333	3	40
Cilona et al. (2014)	26.7	dry	74.07	25	41.3566	7	49.07
Cilona et al. (2014)	26.6	dry	71.17	25	40.39		46.17
Cilona et al. (2014)	26.8	dry	63.1	35	44.3666	7	28.1
Cilona et al. (2014)	32	dry	57	54		55	3
Vajdova et al. (2004a)	10.4	dry	257	50	119		207
Vajdova et al. (2004a)	10.4	dry	289	100	163		189
Vajdova et al. (2004a)	10.4	dry	315	150	205		165
Vajdova et al. (2004a)	10.4	dry	327	200	242.333	3	127
Vajdova et al. (2004a)	10.4	dry	330	240	270		90
Vajdova et al. (2004a)	15.6	dry	61	20	33.6666	7	41
Vajdova et al. (2004a)	15.6	dry	68	30	42.6666	7	38

Vajdova et al. (2004a)	15.6	dry	69	40	49.6666	7	29
					56.3333	3	19
Vajdova et al. (2004a)	15.6	dry	69	50			
Mowar et al. (1994)	25	dry	41.4	41.4	41.4		0
Longuemare et al. (1996)	45	dry	17.5	17.5	17.5		0
Zhu et al. (2010)	13.6	dry	180	180	180		0
Baud et al. (2009)	30	dry	37	37	37		0
Baud et al. (2009)	17	dry	120	120	120		0
van Ditzhuijzen and de Waal (1984)	36	saturated with water	47		15.6666	7	47
van Ditzhuijzen and de Waal (1984)	30	saturated with water	25		8.33333	3	25
van Ditzhuijzen and de Waal (1984)	31	saturated with water	46		15.3333	3	46
van Ditzhuijzen and de Waal (1984)	38.7	saturated with water	15		5		15
van Ditzhuijzen and de Waal (1984)	33.1	saturated with water	26.5		8.83333	3	26.5
van Ditzhuijzen and de Waal (1984)	35.2	saturated with water	17.6		5.86666	7	17.6
van Ditzhuijzen and de Waal (1984)	40.7	saturated with water	33		11		33
van Ditzhuijzen and de Waal (1984)	26.8	saturated with water	36.4		12.1333	3	36.4
van Ditzhuijzen and de Waal (1984)	36.9	saturated with water	15.8		5.26666	7	15.8
JCR_2000_1	47.6633	saturated with oil	3.6832	3.68329	3.68329		0
JCR_2000_2	47.9586	saturated with oil	4.8734	4.87345	4.87345		0
JCR_2000_3	47.9586	saturated with oil	4.6750	4.67501	4.67501		0

JCR_2000_4	47.6836	saturated with oil	6.1637 7	6.16377	6.16377	0
JCR_2000_5	47.9791	saturated with oil	7.7508 1	7.75081	7.75081	0
JCR_2000_6	47.9785	saturated with oil	5.7167 9	5.71679	5.71679	0
JCR_2000_7	42.2739	saturated with oil	6.7184 3	6.71843	6.71843	0
JCR_2000_8	45.4626	saturated with oil	13.658 6	13.6586	13.6586	0
JCR_2000_9	45.4431	saturated with oil	14.601 2	14.6012	14.6012	0
JCR_2000_10	42.2568	saturated with oil	16.690 1	16.6901	16.6901	0
JCR_2000_11	41.0568	saturated with oil	16.642 5	16.6425	16.6425	0
JCR_2000_12	37.4741	saturated with oil	7.7185 7	7.71857	7.71857	0
JCR_2000_13	37.2803	saturated with oil	18.732 4	18.7324	18.7324	0
JCR_2000_14	37.9688	saturated with oil	18.681 6	18.6816	18.6816	0
JCR_2000_15	37.8707	saturated with oil	19.723 6	19.7236	19.7236	0
JCR_2000_16	36.8677	saturated with oil	20.717 4	20.7174	20.7174	0
JCR_2000_17	35.8051	saturated with oil	19.677 4	19.6774	19.6774	0
JCR_2000_18	34.5658	saturated with oil	19.729 1	19.7291	19.7291	0
JCR_2000_19	37.9696	saturated with oil	21.658 2	21.6582	21.6582	0
JCR_2000_20	38.5797	saturated with oil	22.649 4	22.6494	22.6494	0

JCR_2000_21	38.069	saturated with oil	25.775 7	25.7757	25.7757	0
JCR_2000_22	41.0979	saturated with oil	23.637 5	23.6375	23.6375	0
JCR_2000_23	38.7194	saturated with oil	30.586 8	30.5868	30.5868	0
JCR_2000_24	36.5749	saturated with oil	29.747 29.747	29.747	29.747	0
JCR_2000_25	36.2995	saturated with oil	28.705 4	29.7474	29.7474	0
JCR_2000_26	36.378	saturated with oil	33.715 5	28.7055	28.7055	0
JCR_2000_27	36.9104	saturated with oil	32.724 3	33.7153	33.7153	0
JCR_2000_28	36.202	saturated with oil	31.732 2	32.7242	32.7242	0
JCR_2000_29	36.0057	saturated with oil	30.692 34.709	34.709	34.709	0
JCR_2000_30	35.8869	saturated with oil	23.654 5	31.7325	31.7325	0
JCR_2000_31	34.9818	saturated with oil	30.797 2	30.6922	30.6922	0
JCR_2000_32	30.593	saturated with oil	36.647 8	23.6548	23.6548	0
JCR_2000_33	31.5785	saturated with oil	28.717 1	30.7971	30.7971	0
JCR_2000_34	33.6849	saturated with oil	30.849 6	36.6476	36.6476	0
JCR_2000_35	28.9025	saturated with oil	29.761 9	28.7179	28.7179	0
JCR_2000_36	30.1031	saturated with oil	29.761 1	30.8491	30.8491	0
JCR_2000_37	27.8995	saturated with oil	29.761 3	29.7613	29.7613	0

JCR_2000_38	28.176	saturated with oil	33.729 7	33.7297	33.7297	0
JCR_2000_39	27.3891	saturated with oil	33.731	33.731	33.731	0
JCR_2000_40	25.1271	saturated with oil	34.726 9	34.7269	34.7269	0
JCR_2000_41	26.918	saturated with oil	37.750 2	37.7502	37.7502	0
JCR_2000_42	29.4169	saturated with oil	39.680 9	39.6809	39.6809	0
JCR_2000_43	27.607	saturated with oil	39.683 9	39.6839	39.6839	0
JCR_2000_44	26.9972	saturated with oil	39.734 5	39.7345	39.7345	0
JCR_2000_45	26.4857	saturated with oil	39.735 3	39.7353	39.7353	0
JCR_2000_46	25.6202	saturated with oil	39.736 8	39.7368	39.7368	0
Lisabeth and Zhu (2015)	16.3	saturated with water	56.2	56.2	56.2	0
Lisabeth and Zhu (2015)	15.9	saturated with water	40.1	30	33.3666 7	10.1
Lisabeth and Zhu (2015)	16.7	saturated with water	33.6	20	24.5333 3	13.6
Lisabeth and Zhu (2015)	16.8	saturated with water	31.4	20	23.8 16.2666	11.4
Lisabeth and Zhu (2015)	16.8	saturated with water	28.8	10	7 51.7333	18.8
Lisabeth and Zhu (2015)	16.7	saturated with water	55.2	50	3	5.2
Lisabeth and Zhu (2015)	15.5	saturated with water	27.1	10	15.7	17.1
Lisabeth and Zhu (2015)	15.8	saturated with water	42	30	34	12

Lisabeth and Zhu (2015)	15.8	saturated with water	52.8	50	50.9333 3	2.8
Lisabeth and Zhu (2015)	16.7	saturated with water	50	50	50	0
Lisabeth and Zhu (2015)	15.5	saturated with water	27.9	10	15.9666 7	17.9
Lisabeth and Zhu (2015)	14.5	saturated with water	31.6	10	17.2	21.6
Lisabeth and Zhu (2015)	14.6	saturated with water	57.5	57.5	57.5	0
Lisabeth and Zhu (2015)	15.9	saturated with water	44.6	30	34.8666 7	14.6
Lisabeth and Zhu (2015)	15.7	saturated with water	45.4	20	28.4666 7	25.4
Lisabeth and Zhu (2015)	15	saturated with water	58.6	50	52.8666 7	8.6
Lisabeth and Zhu (2015)	16.3	saturated with water	52.5	52.5	52.5	0
Baud et al. (2017)	30.9941	saturated with water	28.011 8	28.0118	28.0118	0
Baud et al. (2017)	27.0349	saturated with water	43.013 1	43.0131	43.0131	0
Baud et al. (2017)	24.9849	saturated with water	58.884 2	58.8842	58.8842	0
Baud et al. (2017)	21.0298	saturated with water	85.045 5	85.0455	85.0455	0
Baud et al. (2017)	18.0343	saturated with water	125.29 8	125.298	125.298	0
Castagna et al. (2018)	10.1	dry	108.88	7	40.96	101.88
Castagna et al. (2018)	10.1	saturated with water	105.09	12	43.03	93.09
Castagna et al. (2018)	10.1	dry	160.59	15	63.53	145.59
Castagna et al. (2018)	10.1	saturated with water	120.97	25	56.99	95.97
Castagna et al. (2018)	10.1	dry	161.73	15	63.91	146.73

Castagna et al. (2018)	10.1	saturated with water	127.66	25	59.22	102.66
Castagna et al. (2018)	10.1	dry	160.74	15	63.58	145.74
Castagna et al. (2018)	10.1	saturated with water	122.07	25	57.3566 7	97.07
Castagna et al. (2018)	10.1	dry	159.44	15	63.1466 7	144.44
Castagna et al. (2018)	10.1	saturated with water	128.81	25	59.6033 3	103.81
Castagna et al. (2018)	10.1	dry	133.31	15	54.4366 7	118.31
Castagna et al. (2018)	10.1	saturated with water	100.96	25	50.32 80.3133	75.96
Castagna et al. (2018)	10.1	dry	180.94	30	3	150.94
Castagna et al. (2018)	10.1	saturated with water	127.25	50	75.75 35.2333	77.25
Cheung (2015)	17	dry	65.7	20	3	45.7
Cheung (2015)	17.6	dry	73.3	30	44.4333 3	43.3
Cheung (2015)	17.1	dry	72.8	40	50.9333 3	32.8
Cheung (2015)	18.1	dry	75	50	58.3333 3	25
Cheung (2015)	17.1	dry	65	65	65	0
Cheung (2015)	17.2	saturated with water	62.7	20	34.2333 3	42.7
Cheung (2015)	16.8	saturated with water	68.2	30	42.7333 3	38.2
Cheung (2015)	16.6	saturated with water	70.6	40	50.2 57.1333	30.6
Cheung (2015)	17.4	saturated with water	71.4	50	3	21.4

Cheung (2015)	17.8	saturated with water	63	63	63	0
Cheung (2015)	12.6	dry	220.8	130	160.266	90.8
Cheung (2015)	13.2	dry	180	180	180	0
Cheung (2015)	13.1	saturated with water	215.5	90	131.833	125.5
Cheung (2015)	14.6	saturated with water	209.2	90	129.733	119.2
Cheung (2015)	12.9	saturated with water	204.1	100	134.7	104.1
Cheung (2015)	13.5	saturated with water	207.6	130	155.866	77.6
Cheung (2015)	13.2	saturated with water	174	174	174	0
Cheung (2015)	13.1	saturated with water	174	174	174	0
Cheung (2015)	13.4	saturated with water	176	176	176	0
Baud et al. (2000)	2.8	dry	225	25	91.6666	200
Baud et al. (2000)	2.8	dry	260.5	35	110.166	225.5
Baud et al. (2000)	2.8	dry	295	50	131.666	245
Renner and Rummel (1996)	5.5	dry	258	0	86	258
Renner and Rummel (1996)	5.5	dry	260	0	86.6666	260
Renner and Rummel (1996)	5.5	dry	298	10	106	288
Renner and Rummel (1996)	3.7	dry	312	0	104	312
Renner and Rummel (1996)	11.8	dry	81	10	33.6666	71

Renner and Rummel (1996)	8.5	dry	250	50	116.666 7	200
Renner and Rummel (1996)	12.5	dry	318	150	206	168
Palchik and Hatzor (2002)	6.1	dry	170	0	56.6666 7	170
Palchik and Hatzor (2002)	15.7	dry	77	0	25.6666 7	77
Palchik and Hatzor (2002)	13.6	dry	80	0	26.6666 7	80
Palchik and Hatzor (2002)	10.4	dry	65	0	21.6666 7	65
Palchik and Hatzor (2002)	14.3	dry	64	0	21.3333 3	64
Palchik and Hatzor (2002)	13.6	dry	78	0	26	78
Palchik and Hatzor (2002)	5.4	dry	274	0	91.3333 3	274
Palchik and Hatzor (2002)	5.8	dry	85	0	28.3333 3	85
Palchik and Hatzor (2002)	20.9	dry	57	0	19	57
Palchik and Hatzor (2002)	6.4	dry	174	0	58	174
Palchik and Hatzor (2002)	15.4	dry	43	0	14.3333 3	43
Palchik and Hatzor (2002)	8.2	dry	174	0	58	174
Palchik and Hatzor (2002)	8.6	dry	105	0	35	105
Palchik and Hatzor (2002)	16.8	dry	60	0	20	60
Palchik and Hatzor (2002)	17.5	dry	64	0	21.3333 3	64

Palchik and Hatzor (2002)	13.6	dry	50	0	16.6666	7	50
Palchik and Hatzor (2002)	15.7	dry	22	0	7.33333	3	22
Palchik and Hatzor (2002)	17.1	dry	40	0	13.3333	3	40
Palchik and Hatzor (2002)	8.3	dry	177	0	59		177
Palchik and Hatzor (2002)	10.1	dry	141	0	47		141
Palchik and Hatzor (2002)	7.6	dry	162	0	54		162
Palchik and Hatzor (2002)	9.3	dry	150	0	50		150
Palchik and Hatzor (2002)	10.4	dry	163	0	54.3333	3	163
Palchik and Hatzor (2002)	8.4	dry	175	0	58.3333	3	175
					74.6666		
Vajdova et al. (2004a)	10.4	dry	204	10	7		194
Vajdova et al. (2004a)	10.4	dry	224	20	88		204
					101.666		
Vajdova et al. (2004a)	10.4	dry	245	30	7		215
					16.3333		
Vajdova et al. (2004a)	15.6	dry	39	5	3		34
					23.3333		
Vajdova et al. (2004a)	15.6	dry	50	10	3		40
Cheung (2015)	18	dry	52.7	5	20.9		47.7
					28.1333		
Cheung (2015)	17.5	dry	64.4	10	3		54.4
					16.3666		
Cheung (2015)	18	saturated with water	39.1	5	7		34.1
					26.6333		
Cheung (2015)	18	saturated with water	59.9	10	3		49.9

Cheung (2015)	14.8	dry	121.9	5	43.9666 7	116.9
Cheung (2015)	12.3	dry	178.7	10	66.2333 3	168.7
Cheung (2015)	14.9	dry	170.1	30	76.7 104.333	140.1
Cheung (2015)	13.2	dry	213	50	3 161.633	163
Cheung (2015)	14.1	dry	304.9	90	3 36.8666	214.9
Cheung (2015)	12.4	with water saturated	100.6	5	7 30.3	95.6
Cheung (2015)	12.6	with water saturated	70.9	10	23.7666 7	60.9
Cheung (2015)	12.7	with water saturated	31.3	20	7 78.7333	11.3
Cheung (2015)	13.6	with water saturated	176.2	30	3 114.866	146.2
Cheung (2015)	13.2	with water saturated	244.6	50	7 130.733	194.6
Cheung (2015)	13.8	with water	272.2	60	3 225	212.2
Baud et al. (2000)	2.8	dry	475	100	318 354	375
Baud et al. (2000)	2.8	dry	554	200	362 336	354
Baud et al. (2000)	2.8	dry	586	250	405 315	336
Baud et al. (2000)	2.8	dry	615	300	440 270	315
Baud et al. (2000)	2.8	dry	620	350	472 231	270
Baud et al. (2000)	2.8	dry	626	395	494.666 7	231
Baud et al. (2000)	2.8	dry	614	435	133.333 3	179
Renner and Rummel (1996)	5.5	dry	300	50	191.333 3	250
Renner and Rummel (1996)	5.5	dry	414	80	3 334	334

Renner and Rummel (1996)	5.5	dry	389	100	196.333 3	289
Renner and Rummel (1996)	5.5	dry	355	50	151.666 7	305
Renner and Rummel (1996)	3.7	dry	361.7	49.7	153.7	312
Renner and Rummel (1996)	3.7	dry	414.2	99.2	204.2	315
Renner and Rummel (1996)	3.7	dry	408.4	79.4	189.066 7	329
Renner and Rummel (1996)	3.7	dry	346.8	29.8	135.466 7	317
Renner and Rummel (1996)	3.7	dry	432.5	64.5	187.166 7	368
Renner and Rummel (1996)	12.3	dry	165	50	88.3333 3	115
Renner and Rummel (1996)	11.1	dry	178	50	92.6666 7	128
Renner and Rummel (1996)	12.1	dry	62	10	27.3333 3	52
Renner and Rummel (1996)	11.9	dry	173	50	91	123
Renner and Rummel (1996)	12.5	dry	160	50	86.6666 7	110
Renner and Rummel (1996)	12.6	dry	69	10	29.6666 7	59
Renner and Rummel (1996)	12.7	dry	177	50	92.3333 3	127
Renner and Rummel (1996)	12.8	dry	237	80	132.333 3	157
Renner and Rummel (1996)	16.7	dry	154	50	84.6666 7	104
Renner and Rummel (1996)	16.3	dry	177	50	92.3333 3	127

Renner and Rummel (1996)	17.6	dry	222	80	127.333 3	142
Renner and Rummel (1996)	9.1	dry	67	10	29	57
Renner and Rummel (1996)	7.2	dry	223	50	107.666 7	173
Renner and Rummel (1996)	6.9	dry	231	50	110.333 3	181
Renner and Rummel (1996)	7.6	dry	234	50	111.333 3	184
Renner and Rummel (1996)	14.7	dry	179	50	93	129
Renner and Rummel (1996)	14.8	dry	82	10	34	72
Renner and Rummel (1996)	10.3	dry	250	50	116.666 7	200
Renner and Rummel (1996)	11.3	dry	238	50	112.666 7	188
Renner and Rummel (1996)	16.2	dry	139	50	79.6666 7	89
Renner and Rummel (1996)	9	dry	255	80	138.333 3	175
Renner and Rummel (1996)	9.8	dry	191	40	90.3333 3	151
Renner and Rummel (1996)	7.4	dry	304	80	154.666 7	224
Renner and Rummel (1996)	11.9	dry	60	10	26.6666 7	50
Renner and Rummel (1996)	7.7	dry	271	50	123.666 7	221
Renner and Rummel (1996)	12.4	dry	195	50	98.3333 3	145
Renner and Rummel (1996)	14.8	dry	182	50	94	132
Vajdova et al. (2004a)	10.4	dry	290	290	290	0

Vajdova et al. (2004a)	15.6	dry	60	60	60	0
Vajdova et al. (2004a)	18.1	dry	60	60	60	0
Vajdova et al. (2004a)	20	dry	60	60	60	0
Hugman and Friedman (1979)	0.59	dry	331	50	143.666	7
Hugman and Friedman (1979)	0.59	dry	365	100	188.333	3
Hugman and Friedman (1979)	8.43	dry	175	50	91.6666	7
Hugman and Friedman (1979)	8.43	dry	168	100	122.666	7
Hugman and Friedman (1979)	0.55	dry	335	50	145	285
Hugman and Friedman (1979)	0.55	dry	355	100	185	255
Hugman and Friedman (1979)	2.03	dry	168	33	78	135
Hugman and Friedman (1979)	2.03	dry	285	100	161.666	7
Hugman and Friedman (1979)	4	dry	380	50	160	330
Hugman and Friedman (1979)	4	dry	470	100	223.333	3
Hugman and Friedman (1979)	4	dry	440	100	213.333	3
Hugman and Friedman (1979)	2.93	dry	360	100	186.666	7
Hugman and Friedman (1979)	3.25	dry	375	50	158.333	3
Hugman and Friedman (1979)	3.25	dry	575	100	258.333	3
Hugman and Friedman (1979)	3.04	dry	434	50	178	384
Hugman and Friedman (1979)	3.04	dry	482	100	227.333	3

Hugman and Friedman (1979)	3.04	dry	600	200	333.333	3	400
Hugman and Friedman (1979)	3.04	dry	695	300	431.666	7	395
Hugman and Friedman (1979)	5.03	dry	365	100	188.333	3	265
Hugman and Friedman (1979)	1.7	dry	350	50	150		300
Hugman and Friedman (1979)	1.7	dry	475	100	225		375
Hugman and Friedman (1979)	1.7	dry	515	100	238.333	3	415
Hugman and Friedman (1979)	1.7	dry	520	100	240		420
Hugman and Friedman (1979)	1.7	dry	575	150	291.666	7	425
Hugman and Friedman (1979)	1.7	dry	792	150	364		642
Hugman and Friedman (1979)	1.7	dry	897	200	432.333	3	697
Hugman and Friedman (1979)	7.72	dry	495	100	231.666	7	395
Hugman and Friedman (1979)	7.72	dry	650	100	283.333	3	550
Hugman and Friedman (1979)	7.72	dry	435	100	211.666	7	335
Hugman and Friedman (1979)	9.58	dry	405	100	201.666	7	305
Hugman and Friedman (1979)	9.58	dry	433	100	211		333
Hugman and Friedman (1979)	9.58	dry	375	100	191.666	7	275
Hugman and Friedman (1979)	9.58	dry	430	100	210		330

Hugman and Friedman (1979)	3.05	dry	275	50	125	225
Hugman and Friedman (1979)	3.05	dry	419	100	206.333	319
Hugman and Friedman (1979)	2	dry	102	0	34	102
Hugman and Friedman (1979)	5.8	dry	85	0	28.3333	85
Hugman and Friedman (1979)	3.6	dry	253	10	3	243
Hugman and Friedman (1979)	20.9	dry	57	0	91	57
Hugman and Friedman (1979)	7.9	dry	165	7	19	158
Hugman and Friedman (1979)	4.6	dry	189	15	59.6666	174
Hugman and Friedman (1979)	4.24	dry	315	25	7	290
Hugman and Friedman (1979)	13.8	dry	153	15	73	138
Hugman and Friedman (1979)	5.4	dry	274	0	121.666	274
Hugman and Friedman (1979)	6.4	dry	174	0	7	174
Hugman and Friedman (1979)	6.8	dry	115	5	61	110
Hugman and Friedman (1979)	5.7	dry	240	10	91.3333	230
Hugman and Friedman (1979)	10	dry	172	10	3	162
Hugman and Friedman (1979)	13.2	dry	201	15	58	186
Hugman and Friedman (1979)	15.4	dry	43	0	41.6666	43
					86.6666	
					7	
					64	
					77	
					14.3333	
					3	

Hugman and Friedman (1979)	17.9	dry	57	5	22.3333	3	52
Hugman and Friedman (1979)	5.7	dry	130	10	50	50	120